



HAL
open science

Measurement of Z-boson and J/ψ Production in p-Pb and Pb-Pb Collisions at $\sqrt{s_{NN}} = 5.02$ TeV with ALICE at the LHC

Mohamad Tarhini

► **To cite this version:**

Mohamad Tarhini. Measurement of Z-boson and J/ψ Production in p-Pb and Pb-Pb Collisions at $\sqrt{s_{NN}} = 5.02$ TeV with ALICE at the LHC. High Energy Physics - Experiment [hep-ex]. Université Paris Saclay (COMUE), 2017. English. NNT : 2017SACLS283 . tel-01691725

HAL Id: tel-01691725

<https://theses.hal.science/tel-01691725>

Submitted on 24 Jan 2018

HAL is a multi-disciplinary open access archive for the deposit and dissemination of scientific research documents, whether they are published or not. The documents may come from teaching and research institutions in France or abroad, or from public or private research centers.

L'archive ouverte pluridisciplinaire **HAL**, est destinée au dépôt et à la diffusion de documents scientifiques de niveau recherche, publiés ou non, émanant des établissements d'enseignement et de recherche français ou étrangers, des laboratoires publics ou privés.

Mesure de la production du boson Z et du J/ψ dans les collisions p-Pb et Pb-Pb à $\sqrt{s_{NN}} = 5.02$ TeV avec ALICE

Thèse de doctorat de l'Université Paris-Saclay
préparée à l'Université Paris Sud

École doctorale n°576 PHENICS
Spécialité de doctorat : Physique hadronique

Thèse présentée et soutenue à Orsay, le 27/09/2017, par

Mohamad Tarhini

Composition du Jury :

M. Raphael Granier De Cassagnac Directeur de recherche, Université Paris-Saclay (LLR)	Président
M. Philippe Crochet Directeur de recherche, Université Clermont Auvergne (LPC)	Rapporteur
M. Giuseppe Bruno Professeur, Université polytechnique de Bari (INFN)	Rapporteur
M. Patrick Robbe Directeur de recherche, Université Paris-Saclay (LAL)	Examineur
M. Ingo Schienbein Maitre de conférence, Université Joseph Fourier (LPSC)	Examineur
M. Bruno Espagnon Professeur, Université Paris-Saclay (IPNO)	Directeur de thèse

Titre : Mesure de la production du boson Z et du J/ψ dans les collisions p-Pb et Pb-Pb à $\sqrt{s_{NN}} = 5.02$ TeV avec ALICE

Mots clés : Collisions d'ion lourds, plasma des quarks et gluons, J/ψ , boson Z, ALICE, LHC.

Résumé : Les collisions d'ions lourds ultra-relativistes sont considérées comme un outil unique pour produire, en laboratoire, un milieu chaud et dense interagissant fortement, le Plasma de Quarks et de Gluons (PQG). Cette thèse est dédiée à l'étude de deux sondes, les J/ψ et les bosons Z, qui peuvent aider à atteindre une meilleure compréhension des propriétés du PQG.

Dans les collisions d'ions lourds, il existe une observable importante pour étudier la formation du PQG, c'est la mesure de la production des J/ψ . L'importance des différents effets qui peuvent augmenter ou supprimer cette production varie avec l'énergie de la collision. Dans cette thèse, la production des J/ψ est mesurée avec les collisions Pb-Pb à $\sqrt{s_{NN}}=5.02$ TeV, en utilisant principalement le spectromètre à muons du détecteur ALICE. Le facteur de modification nucléaire des J/ψ est présenté en fonction de la centralité des collisions, la rapidité et l'impulsion transversale (p_T). En outre, les résultats sur le p_T moyen du J/ψ sont présentés. La comparaison entre les résultats expérimentaux et divers calculs théoriques suggère que la production du J/ψ est affectée dans le milieu par deux processus concurrents : le dissociation et le régénération.

Dans les collisions d'ions lourds, l'état initial de la collision peut aussi affecter les résultats, en l'absence de formation du PQG. La compréhension et la quantification des tels effets est crucial pour les séparer de ceux provoqués par la présence du PQG. Un de ces effets est la modification nucléaire des fonctions de distribution des partons (PDFs). La mesure de production du boson Z dans les collisions d'ions lourds est un outil puissant pour étudier la modification nucléaire des PDFs car il n'est pas affectés par la présence d'une matière en forte interaction. La seconde partie de cette thèse est dévolue à la mesure de la production des bosons Z, pour la première fois dans ALICE, avec les collisions p-Pb et Pb-Pb à $\sqrt{s_{NN}}=5.02$ TeV. Dans les collisions Pb-Pb où la précision de la mesure est plus élevée, l'accord entre les données et des calculs théoriques est meilleur lorsque ces derniers prennent en compte la modification nucléaire des PDFs.

Title : Measurement of Z-boson and J/ψ production in p-Pb and Pb-Pb collisions at $\sqrt{s_{NN}} = 5.02$ TeV with ALICE at the LHC

Keywords : Heavy-ion collisions, quark-gluon plasma, J/ψ , Z-boson, ALICE, LHC.

Abstract : Ultra relativistic heavy-ion collisions are considered as a unique tool to produce, in the laboratory, the hot and dense strongly-interacting medium, the Quark-Gluon Plasma (QGP). This thesis is dedicated to the study of two powerful probes, the J/ψ and Z-boson, that can help reaching a better understanding of the properties of the QGP.

An important observable to study the QGP formation in heavy-ion collisions is the measurement of the J/ψ production. The sizes of the different effects that can enhance or suppress this production vary with the collision energy. In this thesis, the J/ψ production is measured in Pb-Pb collisions at $\sqrt{s_{NN}} = 5.02$ TeV using mainly the muon spectrometer of the ALICE detector. The J/ψ nuclear modification factor is presented as a function of collision centrality, rapidity and transverse momentum (p_T). In addition, results on the J/ψ average p_T and squared average p_T are also obtained. The comparison between the results and various theoretical calculations suggests that the J/ψ production is affected in the medium by an interplay between dissociation and regeneration mechanisms.

In heavy-ion collisions, the initial state of the collision can affect the results even in the absence of the QGP. Understanding and quantifying such effects is crucial in order to separate them from the ones caused by the presence of the QGP. One of these effects is the nuclear modification of the parton distribution functions (PDFs). The measurement of Z-boson production in heavy-ion collisions is a powerful tool to study the nuclear modification of PDFs since it is not affected by the presence of the strongly-interacting medium. The second part of this thesis is devoted to measure the Z-boson production, for the first time with ALICE, in p-Pb and Pb-Pb collisions at $\sqrt{s_{NN}} = 5.02$ TeV. In Pb-Pb collisions where the precision of the measurement is higher, the agreement between data and theoretical calculations is better when the latter take into account the nuclear modification of the PDFs.



Acknowledgements

Without the support of some people, the work of this thesis would not have been accomplished or at least would not have been done in the same manner. I would like to thank you all and my apologies for the ones that are not mentioned on this page.

The biggest thank-you goes to the ALICE group at the IPN. To my thesis director Bruno Espagnon, I would like to thank you for every single advice you gave me, and there was a lot, and for all the fruitful discussions we had.

To my supervisors, Christophe and Zaida, as much as I am very thankful for your excellent supervision, I thank you for being my friends as well.

Cynthia, we worked together and we had useful discussions. Besides thanking you, I apologise for all the times I misspelled your family name ;)

Jana, my officemate and the dynamo of the group, thank you for the laughs we shared and for all the goodies that you used to bring with you.

Even if she arrived at the IPN in my last year (unfortunately), I am very grateful for the time I spent with Laure.

Special thanks to Philippe Crochet, Guiseppa Bruno, Raphael Granier De Cassagnac, Patrick Robbe, and Ingo Schienbein for accepting to be in my defence's jury and for all the suggestions you gave me during and after the defence.

During these three years, I have had the chance to meet and work with many people of the ALICE collaboration. Many thanks to Ginés, Benjamin, Diego, Philippe Pillot, Audrey, Hugo, Astride, Marie, Victor, Javier, Francesco Bossu, Johnson, Roberta.

To the friends I met during my stay at Orsay and with whom I shared unforgettable moments (because I rarely forget a thing and not because of the moments themselves). A thank-you as big as the number of meals we eat together, to Ayoub (who did not include my name in his thesis's acknowledgement), Fatouma (Em Youssef), Rouraaaaa, Elie(🍷), Moustapha, Dima, TaTa, the Koumayha sisters (Marwa, Zanouba), hsein, Mayla.

و بالأخرى (بالأحرى بالأول عشان عارف حتبلشوا قراية من هون) لإمي و بيبي و بطة و زنوية و زهراء و روان: دخيل ربو الللي بدعكن

TABLE OF CONTENTS

Table of Contents	vii
	Page
Introduction	1
1 From the standard model to the Quark-Gluon Plasma	3
1.1 The standard model of particle physics	3
1.1.1 QCD and confinement	5
1.2 Quark-Gluon Plasma	7
1.2.1 QGP hadron transition	7
1.3 Experimental study of the QGP	8
1.3.1 Evolution of nuclear collision	8
1.3.2 Geometry of nuclear collision	9
1.4 Probing the QGP	12
1.4.1 Soft probes	12
1.4.2 Hard probes	14
2 Z-boson and J/ψ production in heavy-ion collisions	15
2.1 Z-boson hadronic production	15
2.2 J/ψ properties and production mechanisms	17
2.2.1 Charmonium states	17
2.2.2 J/ψ hadronic production	18
2.2.3 J/ψ Photoproduction	21
2.3 Cold nuclear matter effects	22
2.3.1 Nuclear parton distribution functions	22
2.3.2 Multiple scattering and energy loss	27

TABLE OF CONTENTS

2.3.3	Nuclear absorption	28
2.4	Hot nuclear matter effects on the Z-boson production	29
2.5	Hot nuclear matter effects on the J/ψ production	30
2.5.1	Color screening and sequential dissociation	30
2.5.2	J/ψ regeneration	32
2.5.3	Interaction with comovers	33
2.5.4	Theoretical status	33
2.6	Experimental results	36
2.6.1	Z-boson production in heavy-ion collisions	36
2.6.2	J/ψ production in heavy-ion collisions	38
2.6.3	J/ψ production in small systems	41
3	Experimental apparatus	45
3.1	The LHC	45
3.1.1	LHC beams	46
3.1.2	LHC experiments	47
3.2	ALICE	48
3.2.1	Global detectors	51
3.2.2	Central barrel detectors	53
3.2.3	The MUON Spectrometer	58
3.2.4	ALICE trigger system	64
3.2.5	Data Reconstruction	65
3.3	Data Quality Assurance	66
3.3.1	Data Quality Assurance for the muon spectrometer	66
4	Z-boson and J/ψ production analyses	71
4.1	Introduction	71
4.2	Data samples and event selection	72
4.3	Event normalization	75
4.3.1	Minimum bias normalization	75
4.3.2	Luminosity	78
4.4	Single muon and dimuon selections	79
4.5	Signal extraction	80

4.5.1	Z-boson signal extraction	83
4.5.2	J/ψ signal extraction	93
4.6	Detector acceptance and efficiency Correction	107
4.6.1	MC simulations setup	108
4.6.2	$A\varepsilon$ calculation	108
4.6.3	Systematic uncertainties	112
4.7	Reference cross sections in pp collisions	122
4.7.1	J/ψ production cross section in pp collisions at $\sqrt{s} = 5.02\text{TeV}$	123
5	Z-boson production results	125
5.1	Introduction and summary from previous chapters	125
5.2	Z-boson production in p-Pb collisions at $\sqrt{s_{\text{NN}}} = 5.02\text{TeV}$	127
5.2.1	Comparison with theoretical models	128
5.2.2	Comparison with other LHC experiments	131
5.2.3	Related measurements in ALICE	131
5.2.4	Conclusions and discussion	133
5.3	Z-boson production in Pb-Pb collisions at $\sqrt{s_{\text{NN}}} = 5.02\text{TeV}$	135
5.3.1	Integrated in rapidity and centrality	136
5.3.2	Rapidity dependence	139
5.3.3	Centrality dependence	139
5.3.4	Conclusions and discussion	142
6	J/ψ production results	145
6.1	Introduction and summary from previous chapters	145
6.2	J/ψ invariant yields	148
6.2.1	J/ψ average p_{T}	148
6.3	Nuclear modification factor	155
6.3.1	Integrated R_{AA}	156
6.3.2	R_{AA} centrality dependence	157
6.3.3	R_{AA} p_{T} dependence	166
6.3.4	R_{AA} rapidity dependence	170
6.4	Conclusions and discussion	172
	Conclusions and outlooks	175

Résumé en français	179
A Signal extraction functions	187
A.1 J/ψ signal functions	187
A.2 Background functions	189
B Effect of non-prompt J/ψ on R_{AA}	191
C J/ψ invariant mass fits	195
D Numerical values of results	205
D.1 J/ψ pp cross sections at $\sqrt{s} = 5.02\text{TeV}$	205
D.2 J/ψ invariant yield in Pb-Pb collisions at $\sqrt{s_{NN}} = 5.02\text{TeV}$	206
D.3 J/ψ $\langle p_T \rangle$ and r_{AA} results at $\sqrt{s_{NN}} = 5.02\text{TeV}$	207
D.4 J/ψ R_{AA} results at $\sqrt{s_{NN}} = 5.02\text{TeV}$	207
List of Tables	211
List of Figures	215
Bibliography	221

INTRODUCTION

Our understanding of the universe has evolved over the years thanks to the progress of the experimental physics. The study of the properties and the constituents of matter under different thermodynamical conditions is the quest of subatomic physics. One of its fundamental questions addresses the behavior of the matter at high temperature and energy density. It is expected that under such conditions, the matter exists as a plasma of quarks and gluons (QGP) in contrast to what we see in the ordinary matter where these constituents are confined inside hadrons. A unique experimental tool to create these conditions in laboratories is to collide heavy nuclei at sufficiently high collision energy. Such collisions have been performed in the last 30 years at different energies. Results from different experiments have helped so far to make a good step toward understanding the QGP but there are still open questions to be answered.

Heavy-ion experiments probe the QGP by measuring different observables of different particles that are affected by the presence of the QGP (hot effects). However, in nuclear collisions, these observables might be affected due to the presence of nuclei even in the absence of the QGP (cold effects). In this manuscript, two analyses are presented. The first one is motivated by the study of some cold nuclear effects, in particular the nuclear modification of parton distribution functions. It is devoted to measure the Z-boson production in p-Pb and Pb-Pb collisions at $\sqrt{s_{\text{NN}}} = 5.02 \text{ TeV}$. In the second analysis, the J/ψ production in Pb-Pb collisions at $\sqrt{s_{\text{NN}}} = 5.02 \text{ TeV}$ is measured. The main motivation behind this measurement is to probe the confinement properties of the QGP. In the following, the contents of the chapters of this manuscript are presented.

Chapter 1 gives an introduction to the general concepts of the QGP and heavy-ion collisions. It is closed by giving brief descriptions of some of the studied QGP

probes. Chapter 2 is dedicated to describe the production mechanisms of the Z-boson and the J/ψ , before introducing the different nuclear effects on the two probes. At the end of this chapter, previous experimental results on the Z-boson and J/ψ production in heavy-ion collisions are summarized.

The experimental apparatus is described in chapter 3. In particular, the LHC operation scheme is presented before describing the different sub-detectors of the ALICE detector, focusing mainly on the muon spectrometer with which the data samples analyzed in this thesis are collected.

Chapter 4 describes in details both the Z-boson and J/ψ analyses. Their results are respectively presented in chapter 5 and chapter 6.

FROM THE STANDARD MODEL TO THE QUARK-GLUON PLASMA

This chapter provides an introduction to the general concepts that are relevant for the measurement of the Z-boson and J/ψ production in heavy-ion collisions. The standard model which describes the fundamental compositions of the matter and their interactions is introduced. The Quark-Gluon Plasma (QGP) is then presented as a state of matter at very high temperature and energy density. Finally, heavy-ion collisions are introduced as a unique experimental tool to recreate the QGP and some experimental measurements used in order to study it are presented.

1.1 The standard model of particle physics

According to the standard model, the elementary particles listed in Figure 1.1 can be classified as [1] (i) matter particles with half integer spin (fermions), (ii) force-carrier particles that have integer spin (gauge bosons), and (iii) a scalar boson (Higgs boson).

Fermions can be grouped into leptons and quarks. There are three lepton generations that include each a negative electric charged particle (e^- , μ^- , and τ^-) and its

corresponding anti-lepton with a positive electric charge (e^+ , μ^+ , and τ^+). Similarly, each lepton generation comprises three leptonic neutrinos (ν_e , ν_μ , and ν_τ) and same number of anti-neutrinos ($\bar{\nu}_e$, $\bar{\nu}_\mu$, and $\bar{\nu}_\tau$). On the quark side, there are six flavors with each one containing a quark (q) and a corresponding anti-quark (\bar{q}) with an opposite electric charge. The u, c, and t quarks have positive electric charges $+2/3$ while the d, s, b quarks have negative electric charges ($-1/3$). In addition to the electric charges, quarks have also color charges that take three values (red, blue or green). In ordinary matter, quarks are confined inside hadrons that can be categorized according to the number of constituent (valence) quarks and anti-quarks. Baryons (e.g protons) are made of three quarks while mesons (e.g pions) are made of one quark and one anti-quark. Recently, hadrons that contain more than three valence quarks were discovered. In particular the tetraquark $Z(4430)-\{c\bar{c}d\bar{u}\}$ was discovered by the Belle experiment [2], and the two pentaquark states $P_c^+(4380)$ and $P_c^+(4450)\{uudc\bar{c}\}$ were discovered by the LHCb [3].

The standard model governs so far three of the four fundamental interactions:

- **The electromagnetic interaction:** fundamental particles that have electric charges (the six charged leptons and the six quarks) can interact electromagnetically by exchanging photons. The theory of Quantum Electrodynamics (QED) is the framework to describe this interaction.
- **The weak interaction:** all fermions can interact weakly by the exchange of W^\pm or Z bosons. The weak interaction is $\sim 10^5$ times weaker than the electromagnetic one. The electroweak theory is the framework in which the electromagnetic and the weak interactions are unified.
- **The strong interaction:** particles with color charges, i.e quarks and gluons can strongly interact by exchanging gluons. This interaction is ~ 100 times stronger than the electromagnetic one. The Quantum Chromo-Dynamics (QCD) is the theoretical framework dedicated to describe this interaction.

In addition to the interactions included in the standard model, **the gravitation force** is applied on all the massive elementary particles.

In the standard model, elementary particles acquire their masses via the interaction with the Higgs field quantized by the Higgs boson which was recently discovered by the two experiments ATLAS [4] and CMS [5] at CERN in 2012.

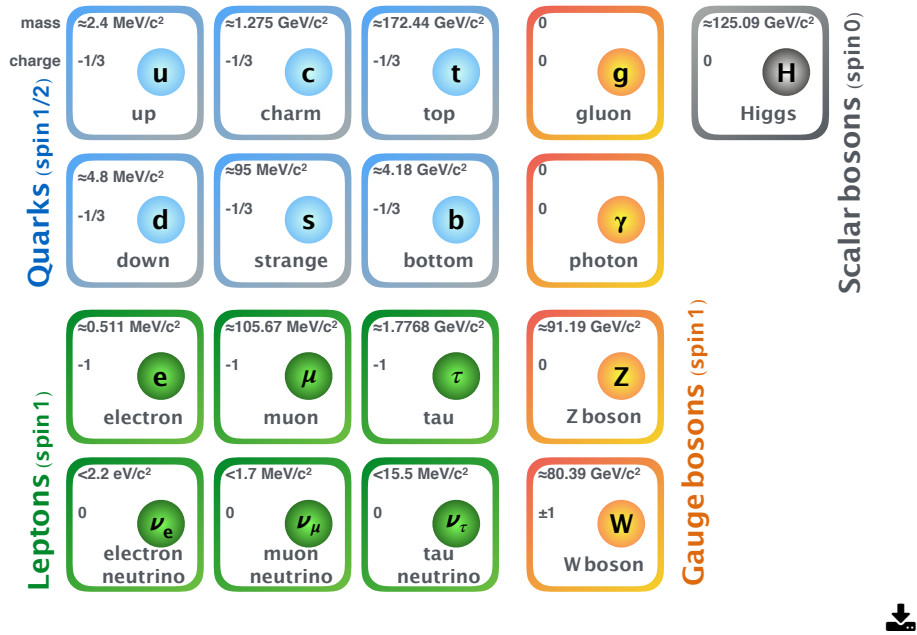


Figure 1.1: Elementary particles discovered at the time of writing this manuscript [1]. For leptons and quarks, the corresponding anti-particles mentioned in the text are not added.

1.1.1 QCD and confinement

In QED, the strength of the coupling between two charged particles decreases with increasing distance (decreasing momentum transfer Q). Indeed, a charged particle (e.g an electron) is screened by virtual e^+e^- pairs from the vacuum, which reduces the effective charge of the particle. If in analogy the QCD vacuum consists only of virtual $q\bar{q}$ pairs, the strength of the strong coupling would behave similarly. However, virtual gluon pairs exist also in this vacuum due to the fact that they have color charges (in contrast to photons which are electrically neutral). The

screening by virtual gluon pairs (known as anti-screening) enhance the effective color charge of the screened particle and consequently causes the coupling to decrease with increasing momentum transfer as shown in Figure 1.2. The strong coupling vanishes when $Q \rightarrow \infty$, this is known as asymptotic freedom. In this regime, perturbative QCD calculations are fully valid in describing the strong interaction. At Q values close to the QCD scale ($\Lambda_{QCD} \sim 200MeV$), the coupling constant becomes large and perturbative QCD breaks down. This is the case inside hadrons where the coupling becomes too strong that it is impossible to isolate a quark from a hadron. This mechanism is known as confinement. Lattice QCD (lQCD) is a non-perturbative technique to solve QCD equations. It is based on discretizing the space-time continuum in a finite number of points where the QCD equations can be solved.

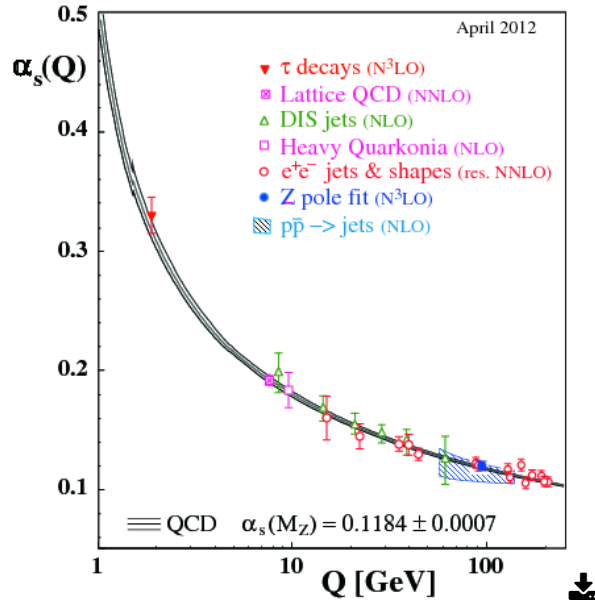


Figure 1.2: Summary of measurements of the strong coupling constant (α_s) as a function of the energy scale Q . Figure is taken from [6].

1.2 Quark-Gluon Plasma

After the big bang, as the universe was expanding and cooling down it undergoes different phase transitions. At a temperature of $\sim 10^{16}$ GeV, the gravity is expected to be separated from the other three fundamental interactions. As the temperature of the universe decreases, the strong and electroweak interactions were separated before the electroweak symmetry breaking took place and the masses of the elementary particles were generated at a temperature of ~ 100 GeV. At this stage, the matter existed as a de-confined medium of quarks and gluons. This state of matter is known as the Quark-Gluon Plasma (QGP). At lower temperature of the order of 100 MeV, the transition between the QGP and the hadronic matter, where the quarks and gluons are confined inside hadrons, is expected to be taken place.

1.2.1 QGP hadron transition

The transition from the de-confined state of matter to the hadronic one is usually characterized in the (T, μ_b) phase space, where T is the temperature and μ_b is the baryo-chemical potential which measures the baryon density of the system. A qualitative phase-space diagram is shown in Figure 1.3. At a given μ_b , the state of matter changes when the temperature reaches a critical value T_c . Latest IQCD calculations [7] predicts $180 < T_c < 200$ MeV at zero μ_b which corresponds to the conditions of the early universe.

The nature of the transition between the de-confined state and the hadronic one across all the phase diagram is still an open question. At zero μ_b , IQCD calculation shows that the transition is a smooth cross-over [8]. However, at $\mu_b \neq 0$, these calculations are still not reliable and theoretical and experimental works are ongoing in order to understand this transition. Calculations from [9] predict the existence of a critical point where the transition becomes a first order transition as shown in Figure 1.3.

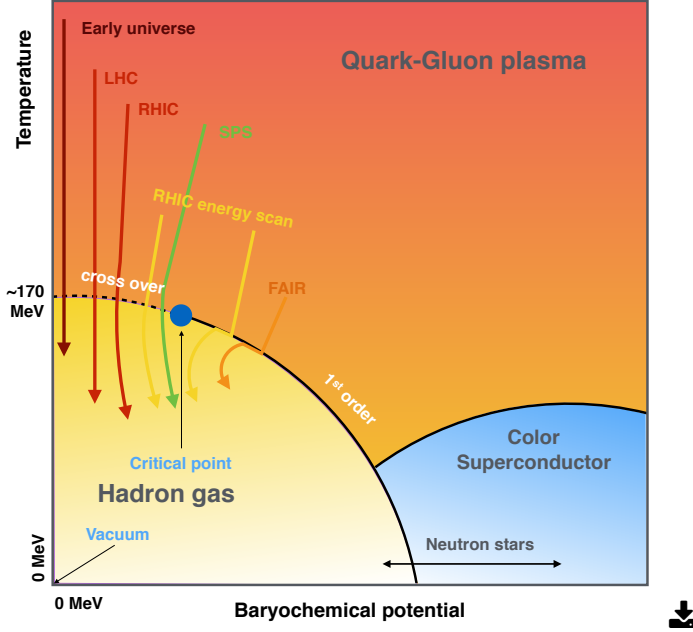


Figure 1.3: A qualitative phase-space diagram characterizing the different states of matter.

1.3 Experimental study of the QGP

By colliding heavy-ion nuclei, the conditions of high energy density and temperature, needed to create the de-confined state of matter, can be reached. Various experimental projects have been established for this purpose. They cover a wide scale of collision energy per nucleon, from ~ 20 GeV at SPS-CERN, up to 5 TeV at LHC-CERN. With increasing collision energy, T increases while μ_b decreases. This means that the different facilities with different energies probe different (T, μ_b) phase-space regions as also qualitatively indicated in the diagram of Figure 1.3.

1.3.1 Evolution of nuclear collision

In Bjorken picture [10], the evolution of the collision of two heavy nuclei can be schematized by Figure 1.4, where the indicated timescales correspond to a collision at the LHC energies and are not hard numbers but rather rough guidelines according to the Ref [11]. The following stages are listed chronologically:

- In the laboratory frame, the two incoming nuclei are Lorentz contracted. They **cross** each other at a time $\tau_{cross} = 2R/\gamma$, where R is the radius of the nucleus and γ is the Lorentz factor. Scatterings with large momentum transfers between the partons of the nuclei take place at this stage and consequently hard processes (e.g. electroweak bosons and heavy flavor quarks) are created.
- In the second stage of the collision, free partons, created from the inelastic collisions of the nucleons of the two nuclei, **thermalize** through additional scatterings. This can lead to the formation of a nuclear matter with high temperature. The system then starts to expand and cools down.
- As the system is cooling down, it reaches a critical temperature where **hadrons** start forming. The **chemical freeze-out** is reached when no further inelastic interactions take place and consequently the number of formed hadrons stays unchanged.
- The formed hadrons gas is still expanding and cooling down until its density is too low that no more elastic collisions take place. The end of this stage is known as **kinetic freeze-out** where the momenta of the formed hadrons are set.

1.3.2 Geometry of nuclear collision

The idea of colliding heavy ions in order to recreate the QGP is essentially based on the large number of involved nucleon-nucleon collisions. Therefore, these conditions may differ depending on the geometry of the initial configuration of the collided nuclei. For instance, the closer the collision is to 'head-on' (more central), the more likely the QGP formation will be. The physical observable that can characterize the initial geometry is the impact parameter (b) which for a hadronic collision can take values from 0 to the sum of the radii of the two nuclei (R_1+R_2).

The number of participating nucleons that undergo at least one inelastic collisions (N_{part}) and the number of binary nucleon-nucleon collision (N_{coll}) can be obtained using Glauber model [12]. It is a model that treats the nucleus-nucleus collision as a superposition of many independent nucleon-nucleon collisions. In

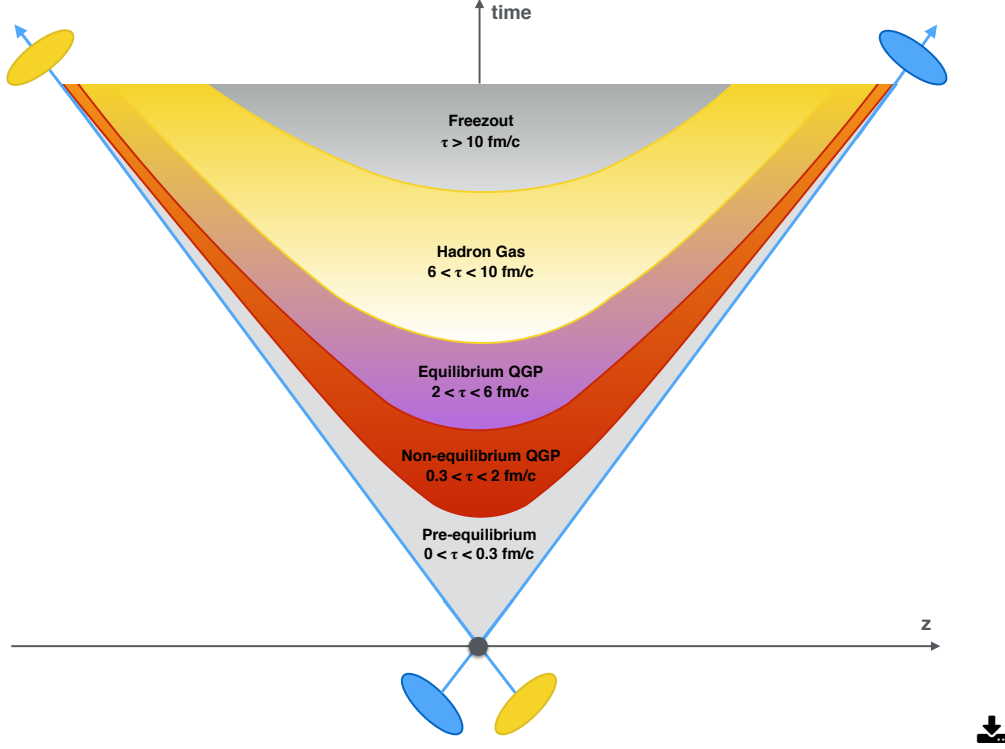


Figure 1.4: Space-time evolution of the collision of two heavy ions. The timescales correspond to a collision at the LHC energies. Figure is taken from [11].

Figure 1.5, two heavy ions A and B collide along the z -direction with an impact parameter b . If one considers the flux tube (red colored surface) located at a transverse distance s from the center of the nucleus A, the probability for a given nucleon to be located in this tube is given by:

$$T_A(s) = \int dz \rho(s, z), \quad (1.1)$$

where $\rho(s, z)$ is the nucleus density distribution. Similar probability is given for the flux tube located at a distance $(s - b)$ from the center of the nucleus B. For a given b , one can define the nuclear overlap function for A-B collision by:

$$T_{AB}(b) = \int d^2s T_A(s) T_B(s - b). \quad (1.2)$$

$T_{AB}(b)$ can be interpreted as the effective overlap area for which a specific

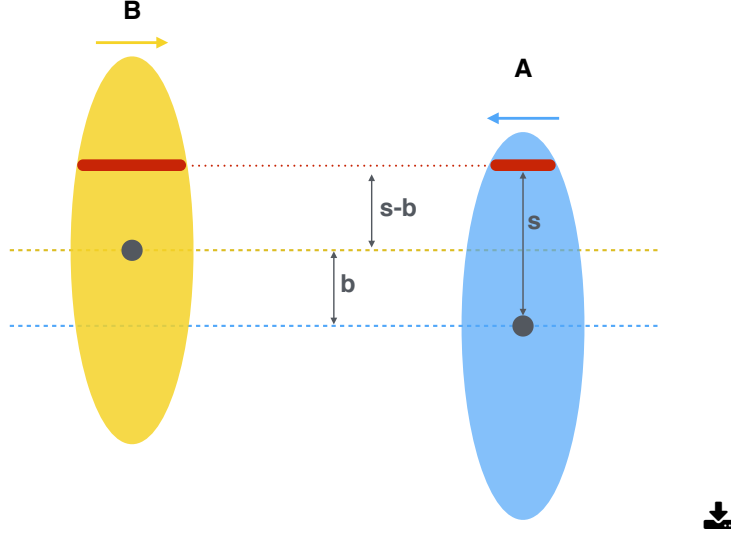


Figure 1.5: Schematic view of the initial geometry of two collided ions A and B separated by an impact parameter b . Figure is taken from [12].

nucleon in A can interact with a given nucleon in B. If σ_{inel}^{NN} is the inelastic nucleon-nucleon cross section, then N_{coll} is expressed as:

$$N_{coll}(b) = A_A \cdot A_B \sigma_{inel}^{NN} T_{AB}(b), \quad (1.3)$$

where A_A and A_B are respectively the number of nucleons in the nucleus A and B. While N_{part} is given by:

$$N_{part}(b) = A_A \cdot \int d^2s T_A \left(1 - \left[1 - \sigma_{inel}^{NN} T_B(b-s) \right]^B \right) + B_B \cdot \int d^2s T_B \left(1 - \left[1 - \sigma_{inel}^{NN} T_A(s) \right]^A \right). \quad (1.4)$$

In heavy-ion experiments, the centrality classes and the related quantities ($\langle N_{part} \rangle$, $\langle N_{coll} \rangle$, and $\langle T_{AA} \rangle$) are usually obtained by performing Monte Carlo simulations based on Glauber model of a given measurable quantity (e.g the charged particle multiplicity) and fitting it to real data.

1.4 Probing the QGP

It is not possible experimentally to directly observe the QGP due to its brief lifetime. Therefore, only indirect observations using different signatures to probe the QGP are possible. The different probes can be classified based on the involved momentum scales. Soft probes are those with relatively low momentum transfer and consequently can be created in different stages of the collision. In contrast, hard probes involve large momentum transfer and are consequently created in the early stages of the collisions. In the following, brief descriptions of some of the soft and hard probes are presented. Note that the aim of the following presentation is not to cover all the existed probes but rather to show their variety.

1.4.1 Soft probes

1.4.1.1 Particle yields and ratios

The relative production of hadrons with light (u, d, and s) quarks depend on the state of the system at the chemical freeze-out. Thus measuring the relative yields of different hadrons can be used in order to calculate the temperature of the system at the chemical freeze-out and the baryo-chemical potential. This is usually done by fitting the measured relative yields with statistical models [13].

1.4.1.2 Strangeness enhancement

In hadronic matter, the constituent quarks are dressed with gluons, thus their mass is different than the bare quark mass $m_q \sim 0$. The quark mass is restored in the de-confined matter (this is also known as the chiral symmetry restoration) [14]. As a consequence, the energy threshold of $s\bar{s}$ pair production is smaller in the presence of the QGP. Experimentally, measuring an enhancement of the production of strange hadrons in heavy-ion collisions with respect to what is expected from collisions where no QGP is formed (e.g low multiplicity proton-proton collisions) can be understood as a signature of the QGP formation. Enhanced productions of strange hadrons in heavy-ion collisions have been observed by different experiments [15, 16], [17]. Similarly, an enhancement of strange hadrons has been recently observed in high multiplicity proton-proton collisions [18]. This

is also the case for other measurements in proton-proton collisions (e.g [19, 20]) showing behaviors which are understood to be related to the formation of the QGP.

1.4.1.3 Elliptic flow of charged particles

In non-central heavy-ion collisions, the colliding matter is not symmetrically distributed around the beam axis (almond-shaped). This asymmetry causes, via multiple collisions, an anisotropic momentum distribution as shown in Figure 1.6. For a given particle, the elliptic flow (v_2) is the second order coefficient of the Fourier expansion of the azimuthal distribution of this particle with respect to the reaction plane defined by the beam axis and the impact parameter vector of the colliding nuclei. Measuring the elliptic flow can serve to study the hydrodynamical properties of the expanding medium such that the viscosity and temperature. Other v_n coefficients also exist and have been measured like v_2 by different experiments [21, 22] [23, 24]. They are in general arising from fluctuations of the nucleon positions in the overlap region.

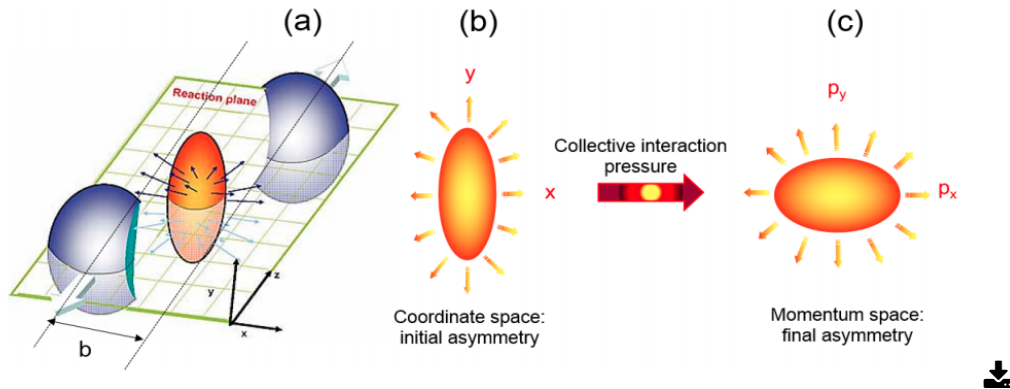


Figure 1.6: (a) A non-central collision of two nuclei leads to an almond-shaped interaction volume; (b) This initial spatial anisotropy with respect to the reaction plane translates via pressure gradients into (c) a momentum anisotropy of the produced particles. Figure is taken from [25].

1.4.2 Hard probes

1.4.2.1 Jet quenching

High energy partons lose energy by radiation when traversing the dense medium via multiple scatterings. This causes the suppression of high transverse momenta particles and known as jet quenching. Experimentally, this can be studied by comparing the yields of high momentum particle in heavy-ion collisions to the same yields measured in proton-proton collisions.

1.4.2.2 Heavy flavor production

Heavy flavor hadrons (contain charm or beauty quarks) and $c\bar{c}$ or $b\bar{b}$ resonances, known respectively as charmonia and bottomonia, are expected to probe the whole phase of the QGP due to the early production of their constituents heavy quarks. Their production can be affected by the presence of the hot medium by energy loss and/or color screening (for quarkonia). Chapter 2 describes the production mechanisms of the charmonium states, and how are used to study different nuclear effects expected to be present in heavy-ion collisions.

1.4.2.3 Electroweak bosons production

The electroweak bosons (W^\pm and Z-bosons) are created in the initial hard collisions and do not have color charges thus not affected by the presence of the strongly interacting medium. This makes the study of their production in heavy-ion collisions as clean probes of nuclear effects which are present in the absence of the QGP. In chapter 2, the production of the Z-boson and the different nuclear effects that are relevant to this production are described.

Z-BOSON AND J/ψ PRODUCTION IN HEAVY-ION COLLISIONS

As described in the previous chapter, heavy-ion collisions are the only available experimental tools to produce a strongly interacting medium, QGP. It was discussed that different probes exist to study the created medium, and those probes were classified into two categories, soft and hard depending on their momentum scales.

In this chapter, an overview of the properties and production mechanisms of two hard probes, the Z-boson and the J/ψ is presented. This will be followed by exploring various nuclear effects on the production of the two particles. Finally, a brief overview of the experimental results on Z-boson and J/ψ production in heavy-ion collisions will be given.

2.1 Z-boson hadronic production

The Z-boson is one of the four electroweak gauge bosons (alongside the W^+ , the W^- , and the photon). It was discovered at the SPS (CERN) in 1983 [26] and since then has been heavily studied in different experiments [27], [28], [29]. Its intrinsic properties (mass, width, lifetime and couplings), which are among the most precise

measurements in the standard model, were precisely measured by the experiments at the e^+e^- collider LEP [1]. Table 2.1 summarizes some of these properties.

Mass (GeV)	Width (GeV)	Decay mode fractions		
		l^+l^-	hadronic	neutrinos
91.1876 ± 0.0021	2.4952 ± 0.0023	$(3.3658 \pm 0.0023) \%$	$(69.91 \pm 0.06) \%$	$(20.00 \pm 0.06) \%$

Table 2.1: Mass, width, and the branching ratios of some decay modes of the Z-boson [1].

The precise knowledge of the mass and the width of the Z-boson makes it a powerful tool for electron and muon energy calibration for particle physics detectors [30]. The Z-boson can also serve as a benchmark for studies and searches for other particles (e.g the Higgs boson) as a known background source.

Theoretically, the Z-boson production in hadronic collisions can be calculated up to NNLO [31]. Figure 2.1 shows examples of leading order (LO), and next-to-leading order (NLO) Feynman diagrams of the Z-boson production. This production is dominated by the LO Drell-Yan (DY)¹ process which is the production of a massive lepton pair via an intermediate Z-boson or an off-mass-shell photon (γ^*) by the annihilation of a quark-antiquark pair. Based on the factorization theorem of hard processes [33], the differential cross section for a DY process in an A-B collision can be expressed as [34]:

$$\sigma_{AB} = \sum_q \frac{4\pi e_q^2 \alpha^2}{9\hat{s}} f_q(x_1, M^2) f_{\bar{q}}(x_2, M^2), \quad (2.1)$$

where $\alpha \approx 1/137$ is the QED coupling constant, e_q is the quark fractional electric charge, $\hat{s} = (p_q + p_{\bar{q}})^2$ is the partonic center-of-mass energy, and $f_{q,\bar{q}}(x, Q^2)$ is the quark (anti-quark) parton distribution functions (PDFs, described in section 2.3.1).

¹After Sidney D. Drell and Tung-Mow Yan who predicted the process in 1970 [32].

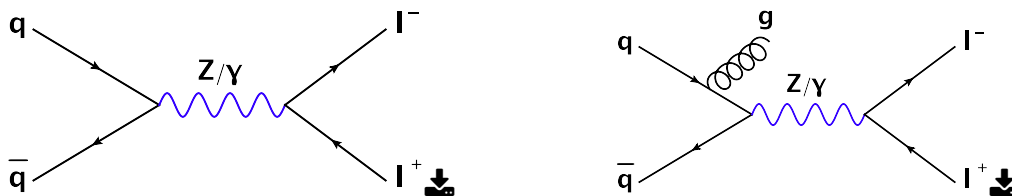


Figure 2.1: Examples of LO (left) and NLO (right) Feynman diagrams of the Z-boson production in hadronic collisions.

2.2 J/ψ properties and production mechanisms

2.2.1 Charmonium states

A charmonium state is a vector meson comprising a charm and an anti-charm quarks. The charmonium mass depends on the angular momentum of the $c\bar{c}$ pair. The spectroscopic notation of a state is given by $n^{2S+1}L_J$ where n, S, L and J are respectively the principal quantum number, the spin, the orbital momentum and the angular momentum of the state. The lowest mass charmonium states correspond to the case where $L=0$ and they are known as η_c and J/ψ . The latter was the first discovered charmonium state in 1974, simultaneously at SLAC [35] and BNL [36]².

The intrinsic properties of different charmonium states are summarized in Table 2.2. In vacuum ($T = 0$), a charmonium bound state, with a separation r between the charm and anti-charm quarks, can be described by a non-relativistic potential due to the large mass of the charm quark [37]

$$V(r, T = 0) = \sigma \cdot r - \frac{\alpha_c}{r}. \quad (2.2)$$

The $1/r$ term in equation 2.2 is Coulomb-like and governs the short distance behavior of the potential. This term represents gluon exchanges between the charm and anti-charm quarks. The coupling factor in the Coulomb-like term, α_c , can be related to the strong coupling constant α_s by a factor that accounts for the summation over color indices, $\alpha_c = (4/3)\alpha_s$ [38]. The linear term corresponds to the

²The BNL group gave the new particle the name J while the SLAC group attributed the name ψ .

confining potential obtained from lattice QCD calculations [39], where the string tension σ represents the strength of the confining.

Charmonium	$n^{2S+1}L_J$	mass (MeV/ c^2)	width (MeV/ c^2)
η_c	1^1S_0	2983.4 ± 0.5	31.8 ± 0.8
J/ψ	1^3S_1	3096.900 ± 0.006	0.0929 ± 0.0028
χ_{c0}	1^3P_0	3414.75 ± 0.31	10.5 ± 0.6
χ_{c1}	1^3P_1	3510.66 ± 0.07	0.84 ± 0.04
h_c	1^1P_1	3525.38 ± 0.11	0.7 ± 0.4
χ_{c2}	1^3P_2	3556.20 ± 0.09	1.93 ± 0.11
$\eta_c(2S)$	2^1S_0	3639.2 ± 1.2	$11.3^{+3.2}_{-2.9}$
$\psi(2S)$	2^3S_1	3686.097 ± 0.025	0.296 ± 0.008

Table 2.2: Masses and widths of some charmonium states [1].

By emitting photons or pions, heavier charmonium states can decay to lighter ones as shown in Figure 2.2. This is known as charmonium indirect production. In the J/ψ case, this is dominated by the decay of $\psi(2S)$ which has similar quantum numbers as the J/ψ except for the principal quantum number n .

2.2.2 J/ψ hadronic production

Direct and indirect J/ψ productions are both referred to as prompt production. At the LHC energy, the prompt production is dominated by the gluon fusion mechanism due to the increasing number of the gluons inside the protons with increasing collision energy. However, another J/ψ source is the weak decay of b hadrons. J/ψ from the last source are known as non-prompt. In the following, a brief description of two different models on the prompt J/ψ production, followed by a discussion on the non-prompt one are presented.

2.2.2.1 Color Singlet Model (CSM)

The CSM was proposed shortly after the J/ψ discovery [40]. It is based on the factorization approach to separate the charmonium production cross section into a perturbative and a non-perturbative steps. The former is being the production of

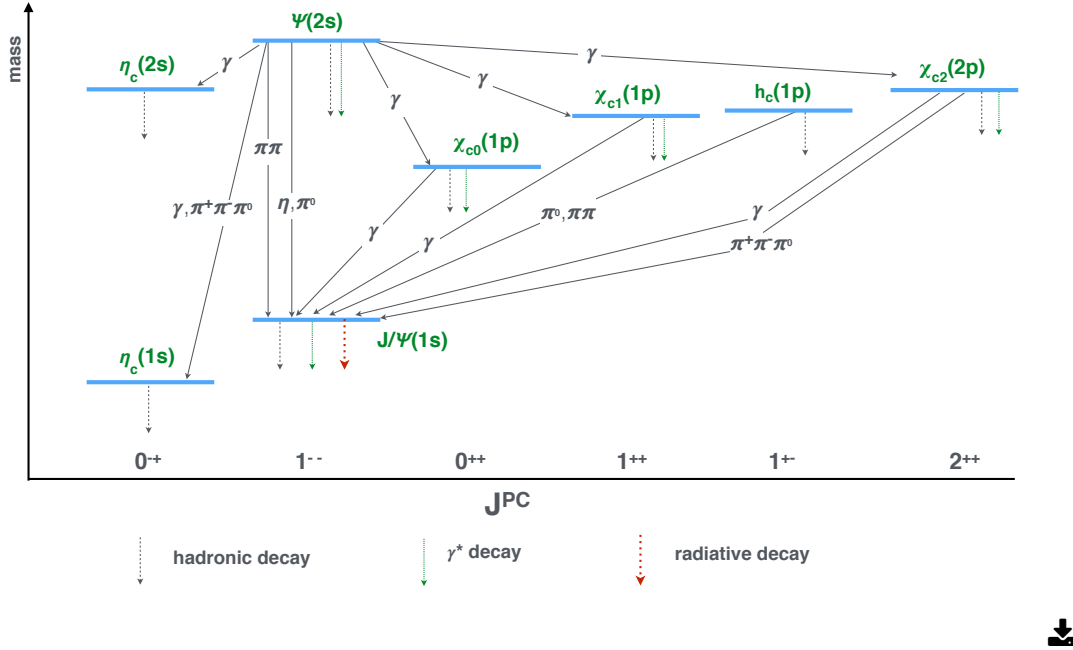


Figure 2.2: Schematic illustration for the different charmonium→charmonium decay channels. Figure is adapted from [1]

on-shell charm and anti-charm quarks, while the latter represents the process of their binding into a charmonium state. During the binding, the model assumes that the charm and anti-charm quarks are at rest in the charmonium frame. Another assumption is that the color charge and the spin of the $c\bar{c}$ pair are unchanged during the whole process, leading to the name of the model since the J/ψ is a color singlet under this assumption.

The strength of the model relies in its prediction power. Indeed, the only free parameters of the model are the absolute values of the color-singlet $c\bar{c}$ wave functions and their derivatives. These wave functions can be determined from data on decay processes or by application of potential models [41].

Predictions made by the CSM have successfully described data at low energy [42]. However, the model underestimates the prompt charmonium production cross section in $p\bar{p}$ collisions at $\sqrt{s} = 1.8\text{TeV}$ at the Tevatron [43] by more than an order of magnitude.

2.2.2.2 Non-Relativistic Quantum Chromo-Dynamics (NRQCD)

This model [44] also factorizes the charmonium production cross section into perturbative and non-perturbative steps, but unlike the CSM, it does not assume that the charm quarks are produced in their final color state. The J/ψ production cross section under this model is given by [45]:

$$d\sigma(J/\psi + X) = \sum_n d\hat{\sigma}(c\bar{c}[n] + X) \langle O^{J/\psi}[n] \rangle, \quad (2.3)$$

where the non-relativistic QCD (NRQCD) matrix elements operators $\langle O^{J/\psi}[n] \rangle$ are associated with the amplitude of producing a J/ψ from a $c\bar{c}$ pair in state $[n]$. The sizes of $\langle O^{J/\psi}[n] \rangle$ parameters are determined in powers of v , the relative velocity between c and \bar{c} . The CSM can be restored from Equation 2.3 by keeping only the color-singlet contributions of leading order in v . At large p_T the J/ψ production is dominated by color octet diagrams, while the singlet color ones dominate at low p_T which explains the success of the CSM at low energies. Such diagrams are shown schematically in Figure 2.3.

This model has been successful in describing many charmonium observables including the J/ψ production cross sections at different LHC energies measured by ALICE as will be discussed in section 2.6.3.1. However, it fails to describe the J/ψ polarization results in $p\bar{p}$ collisions at $\sqrt{s} = 1.8\text{TeV}$ at the Tevatron [46].

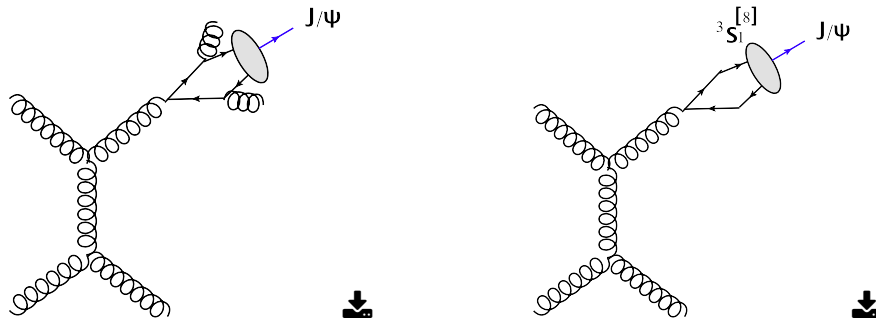


Figure 2.3: Examples of Feynman diagrams that contribute to the J/ψ production via the color singlet channel (left) and color octet channel (right) [47].

2.2.2.3 Non-prompt J/ψ production

A weak decay of a b-hadron can produce a non-prompt J/ψ as shown in the diagram of the Figure 2.4. The cross section of this process can be separated in two parts, the production of a b-hadron and its decay to a J/ψ [1]. The b-hadron cross section is theoretically factorized into two steps, perturbative one that corresponds to the b-quark production, and a non-perturbative one for the b-quark fragmentation into the hadron. The former can be evaluated using Fixed Order Next-to-Leading-Logarithm (FONLL) calculations [48], while the second one is usually extracted from e^+e^- experimental data [49].

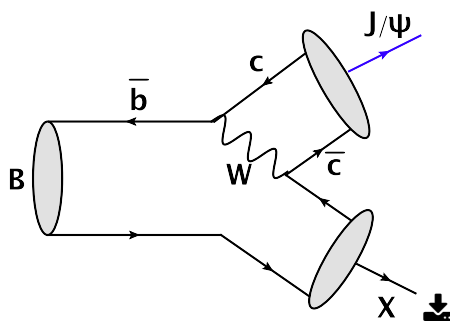


Figure 2.4: A LO contribution to the weak decay of a B hadron into a J/ψ .

2.2.3 J/ψ Photoproduction

Models and production channels discussed so far correspond all to the hadronic J/ψ production. However, photoproduction of J/ψ may also occur in nucleus-nucleus collisions due to the large involved electromagnetic field. Ultra-Peripheral Collisions (UPC), where the ions pass by each other with an impact parameter larger than the sum of their radii, allow studying the photoproduction in absence of hadronic interactions. The J/ψ production mechanism in such collisions is illustrated in Figure 2.5. One nucleus plays the role of the photon source (the photon flux grows as Z^2 , where Z is the charge of the nucleus), while the other nucleus is the target. The emitted photon fluctuates into a virtual quark-antiquark pair which then interacts with the target and produce a J/ψ .

The J/ψ p_T spectrum is dominated by the momentum transfer from the target

nucleus since the photon p_T is small. A photoproduction is said to be coherent when the quark-antiquark pair interacts in phase with the entire target nucleus. In this case, the average p_T transfer from the target nucleus is small with a scale on the order of a few times hc/R_A [45] where R_A is the radius of the nucleus. In contrast, for the incoherent case, the quark-antiquark pair interacts out of phase so that the pair effectively interacts with a single nucleon. In this case the average p_T transfer corresponding to the size of a single nucleon is larger.

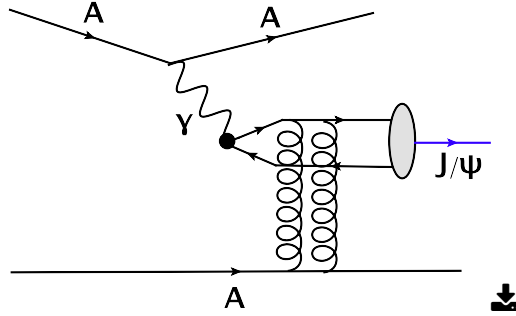


Figure 2.5: An illustration of the J/ψ photoproduction mechanism in an ultra peripheral nucleus-nucleus collision.

2.3 Cold nuclear matter effects

In this section, nuclear effects that exist even without the presence of the hot nuclear medium are discussed. Some of these effects are relevant for the production of both J/ψ and Z -boson, they will be discussed commonly. However, some of them affect only one of the probes and will be discussed within its context.

2.3.1 Nuclear parton distribution functions

Parton distribution functions (PDFs), are universal characteristics of the hadron. They are, according to the factorization theorem, the non-perturbative part of the cross sections of hard processes in hadronic collisions. They represent the probability of finding a parton with a specific flavor carrying fraction x of the hadron's longitudinal momentum at a given energy scale Q . In general, PDFs are obtained via performing global fits of different experimental datasets, using the

DGLAP evolution equation [50], [51], [52] to determine the best set of PDFs that describe the data. Experimental results included in the global fit analyses, are usually coming from Deep Inelastic Scattering (DIS) experiments. Depending on the used experimental results and the computations method, different PDF sets are available [53–55]. An example of one of them (CT14) is shown in Figure 2.6 for different partons at two different energy scales close to the mass of the charm quark and the Z-boson.

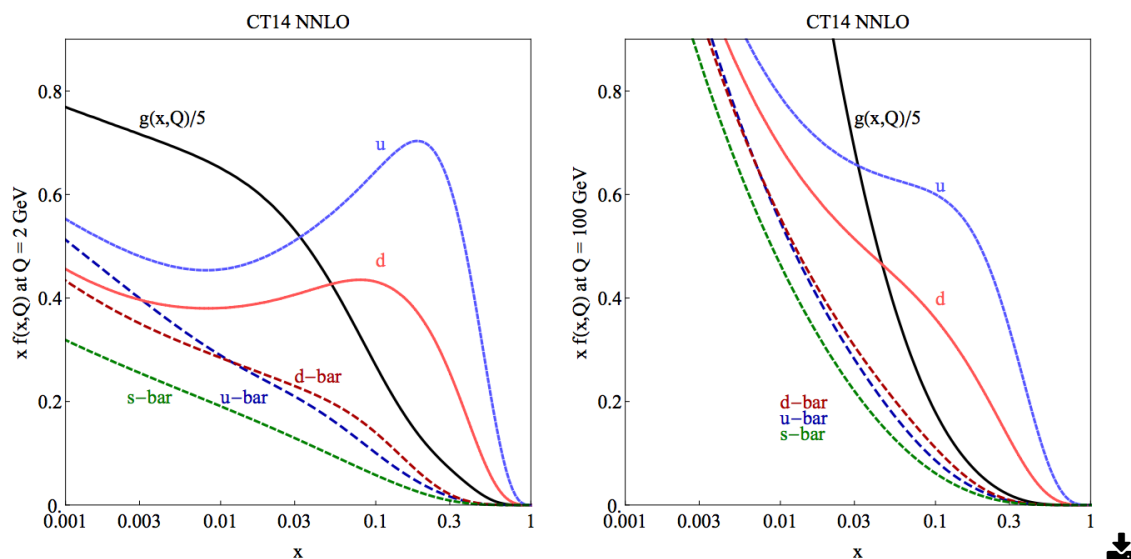


Figure 2.6: CT14 PDFs [55] for different partons (in different colors) at two different energy scales.

In 1983, the European Muon Collaboration (EMC) discovered that the partons momentum distribution in Iron (Fe) is different than the one in Deterium (De) [56] to conclude that a PDF inside a nucleus (nPDF) is different than the one in free nucleon. Since then, the phenomenon has been extensively studied, both experimentally and theoretically. The study of this subject is interesting in its own since its understanding helps to bridge the gap between nuclear and particle physics. In addition, it is crucial for other studies. In particular, precise knowledge of the nPDFs is required for predicting and understanding the results from heavy-ion collision experiments.

At a given energy scale and for a parton i that carry a fraction of longitudinal momentum x of the nucleon, the nPDF $f_i^A(x, Q^2)$ can be expressed as [57]:

$$f_i^A(x, Q^2) = R_i^A(x, Q^2) \times f_i(x, Q^2), \quad (2.4)$$

where $f_i(x, Q^2)$ is the corresponding free PDF and $R_i^A(x, Q^2)$ is its modification factor.

Similar to the free PDFs, different sets of nPDF exist [57–60]. They are also determined using global fit analyses. So far, the experimental results used in the analyses are mainly coming from lepton (charged or neutrino) DIS off nuclei, and DY production in proton-nucleus or deuteron-nucleus collisions. In contrast to the free PDFs, the nPDFs evaluation suffers from the lack of available experimental data.

Table 2.3 summarizes the characteristics of different up-to-date nPDF sets. The different sets use different free PDFs as baselines but exploit similar experimental results in their global analyses.

nPDF set	EPPS16 [61]	EPS09 [57]	DSSZ12 [58]	kA15 [59]	nCTEQ15 [60]
order in α_s	NLO	LO, NLO	NLO	NNLO	NLO
Flavor separation	Full	None	None	None	Some
Included experimental data from:					
Neutral current DIS	yes	yes	yes	yes	yes
DY dilepton $p + A/p + d$	yes	yes	yes	yes	yes
RHIC pions $d + Au/p + p$	yes	yes	yes	no	yes
Neutrino-nucleus DIS	yes	no	yes	no	no
LHC p-Pb jet data	yes	no	no	no	no
LHC p-Pb W,Z data	yes	no	no	no	no
Number of included data-points	1811	929	1579	1479	708
Number of free parameters	20	15	25	16	17
Baseline free PDFs	CT14	CTEQ6.1	MSTW2008	JR09	CTEQ6M-like

Table 2.3: Experimental status and some properties for four available nPDF sets. Table taken from [62].

A schematic illustration of a typical nPDF distribution is shown in Figure 2.7 as a function of x . One can see the different regions that correspond to different effects [63]:

- **Shadowing:** A depletion at $x \lesssim 0.1$. Usually, multiple scattering of partons in the nucleus is associated as the underlying physics explanation of this effect.

- **Antishadowing**: an excess at $0.1 \lesssim x \lesssim 0.3$. In contrast to shadowing, this can be interpreted as a result of constructive interference of amplitudes arising from the multiple scattering of partons in the nucleus.
- **EMC effect**: a depletion at $0.3 \lesssim x \lesssim 0.7$. This effect is still not totally understood. Models considering different physics processes have attempted to explain the EMC effect. These include nuclear modification of the nucleon radius and mass as well as the modification of the nucleon structure in the nuclear medium due to multi-nucleon effects (binding, pions exchange, nucleon-nucleon correlations).
- **Fermi-motion** region: an excess towards $x \rightarrow 1$ and beyond. This due to the fact that the nucleons are not stationary in the nucleus, their dynamics is known as fermi-motion.

A relevant detailed review can be found in [64].

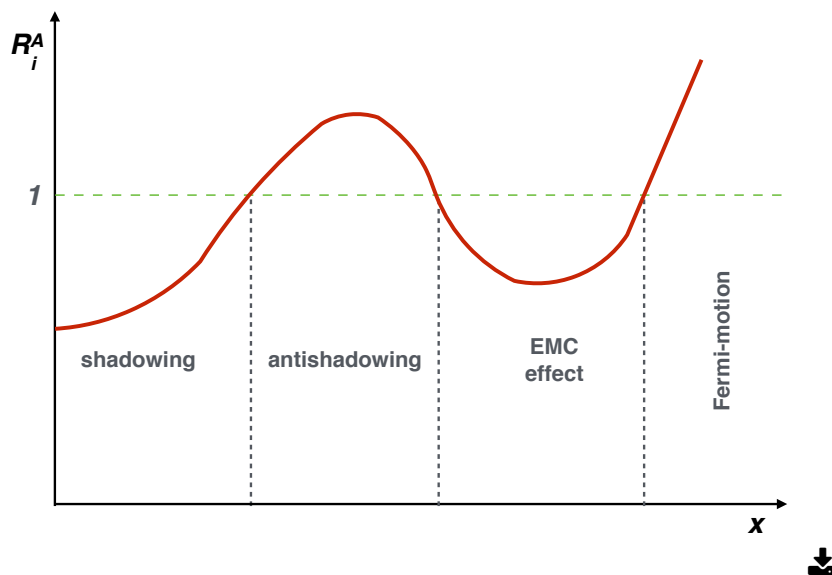


Figure 2.7: A typical nPDF distribution as a function of x [63].

As described in section 2.1 the Z-boson production at the LHC energy is dominated by the quark anti-quark annihilation process. Thus, a modification of the PDFs of the involved quarks has a direct effect on the Z-boson production.

The Z-boson production in heavy-ion collisions is considered to be a clean constraining tool of the nPDFs sets since there are no other major effects that can affect this production.

Figure 2.8 shows predictions for the modification of the Z-boson production cross section in Pb-Pb collisions with respect to pp ones at $\sqrt{s_{NN}} = 5.5$ TeV, using the EPS09 parameterization [65]. One can see the potential importance of the nPDF modification effect as well as its relatively large uncertainties. This reflects the importance of measuring the Z-boson production in heavy-ion collisions.

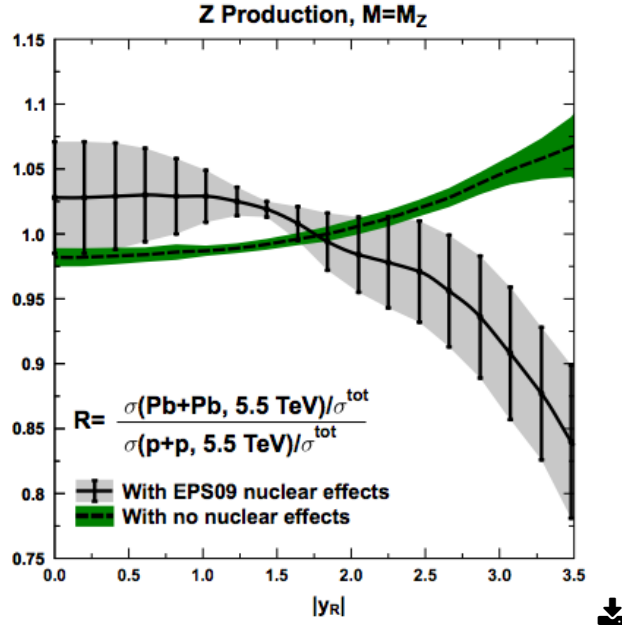


Figure 2.8: Prediction [65] for the ratio between the Z-boson cross sections in Pb-Pb and pp collisions at $\sqrt{s_{NN}} = 5.5$ TeV. The effect seen on the green band is due to the isospin effect, caused by the fact that the ratio u/d quarks is not the same in nucleus than in proton.

As described in Section 2.2, the J/ψ production cross section in hadronic collisions can be factorized in two parts, where the first one is the cross section of

producing a $c\bar{c}$ pair. This cross section can be affected by the modification of the PDFs of the involved partons. Figure 2.9 shows the nuclear modification functions at the charm mass energy scale of three partons (a valence quark, a sea quark, and a gluon) in the Pb nucleus using the EPS09 parametrisation. At the LHC energy, the J/ψ production is dominated by gluon fusion, hence it is sensitive to the gluon nuclear modification function.

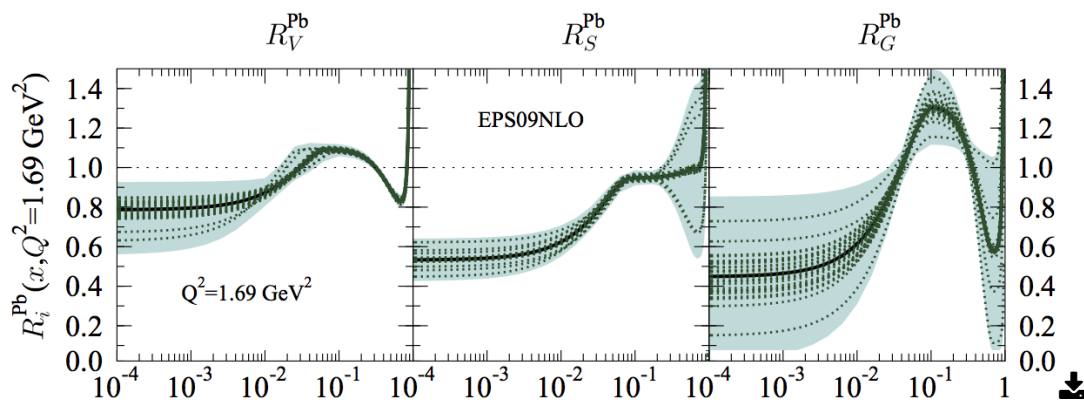


Figure 2.9: The nuclear modifications R_V , R_S , R_G for lead ion at an initial scale $Q^2 = 1.69 \text{ GeV}^2$. The thick black lines indicate the best-fit results, whereas the dotted green curves denote the error sets. Figure taken from [57].

2.3.2 Multiple scattering and energy loss

A decrease of the production cross section for a given hard probe in nuclear collisions can be caused by parton energy loss. A high energy parton traversing a nuclear medium is expected to lose energy by radiation due to multiple interactions in the target nucleus. The magnitude of this energy loss is linear with the system size L which is proportional to the nuclear size $R \sim 1.2A^{1/3} \text{ fm}$ [66]. In addition to the energy loss, the incoming parton exhibits a broadening of its transverse momentum. This effect is known as the Cronin effect and it is also expected to be proportional to the nuclear size.

2.3.2.1 Coherent energy loss

The authors of [67] suggested that gluon radiation cannot be totally attributed to parton energy loss of a well defined parton. Indeed, at small probed x , there are some hard processes where a color charge is produced colinearly with one of the incoming partons. In such cases, gluon radiation before and after the hard process is coherent. The developed model has only one free parameter which is the transport coefficient q^0 related to the nuclear broadening and the energy loss probability distribution. Originally in Ref [67], the case of J/ψ production at forward rapidity in p-A collisions was considered since it covers small x . The $c\bar{c}$ pair is assumed to be produced in a color octet state with a time scale $\tau_{c\bar{c}}$ and travel through the nucleus for a significant time $\tau_{octet} \gg \tau_{c\bar{c}}$.

In [68], a generalized picture towards AA collisions is made.

2.3.3 Nuclear absorption

Once produced, the $c\bar{c}$ pair will traverse the nuclear matter and consequently suffer absorption both in the pre-charmonium and in the charmonium stages. This so called nuclear absorption is coming from successive interactions with the target nucleons.

When discussing the nuclear absorption of a charmonium state in the nucleus, one can compare the collision time (t_{coll}) to the formation time of the state. The former is defined as $t_{coll} = 2R\gamma_{cm}$, where R is the nucleus radius and γ_{cm} is the Lorentz factor of each of the beams in the center-of-mass frame. At the LHC energy of 2.76 TeV per nucleon, t_{coll} is expected to be less than $5 \cdot 10^{-3} fm^3$, much smaller than the formation time of different charmonium states ($0.4fm - 1.2fm$). Therefore, one expects that the nuclear absorption plays no role at the LHC.

In p-A collisions, the authors of [69] have studied the J/ψ nuclear absorption cross section at different collision energies. This is shown in Figure 2.10 where a decreasing of the nuclear absorption cross section with increasing collision energy is seen.

$${}^3\gamma_{cm} = \frac{2.76TeV}{m_p=938MeV} \approx 2940$$

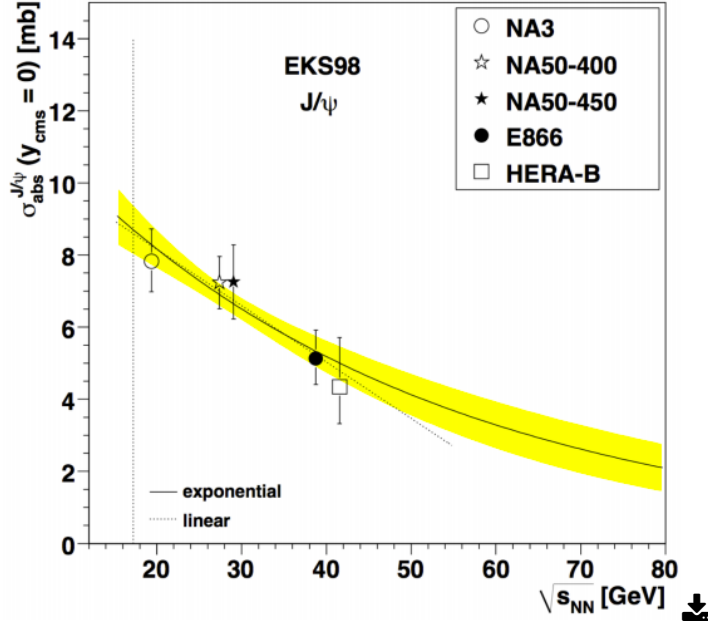


Figure 2.10: Collision energy dependence of the nuclear absorption cross section, fitted with linear and exponential function. Figure is taken from [69].

2.4 Hot nuclear matter effects on the Z-boson production

As discussed in chapter 1, a strongly interacting medium (QGP) is expected to be formed in ultra-relativistic heavy-ion collisions. In this section, induced effects on the Z-boson and its decay products are discussed.

One can see qualitatively the effects of the QGP from a timescale point of view. Indeed, due its large mass ($\sim 90 \text{ GeV}/c^2$), the Z-boson formation time is very short ($\tau_Z = 1/M_Z \sim 10^{-3} \text{ fm}/c$). The Z-boson decay time is inversely proportional to its width ($\sim 1/(2.5 \text{ GeV}/c^2) \sim 0.08 \text{ fm}/c$). On the other hand, the expected formation time of the QGP is $\sim 1 \text{ fm}/c$ and it can last after a quick thermalization up to $\sim 10 \text{ fm}/c$. So one expects no QGP effects on the Z-boson itself, but effects on its decay products should be accounted for.

The leptonic decay products⁴ pass through the medium without strong interaction

⁴There are also the hadronic decay channels where strong interaction with the hot medium has an effect.

since they carry no color charge. However, by electromagnetic interaction with the charges of the medium, they can lose energy through elastic scatterings. This energy loss depends on the lepton mean free path estimated to be $\sim 10fm/c$ in a $T = 1$ GeV medium [70] leading to an average of one elastic collision per lepton. In [71], it is shown that under such considerations, the energy loss due to lepton elastic scattering can be neglected.

This blindness of the Z-boson to the medium makes it:

- A clean constraining tool for the nPDF modifications in both nucleon-nucleus and nucleus-nucleus collisions.
- A powerful tool for validating the binary scaling of the collisions.

2.5 Hot nuclear matter effects on the J/ψ production

In this section, the various effects on the J/ψ production in nucleus-nucleus collisions where a QGP medium is created are discussed.

2.5.1 Color screening and sequential dissociation

At finite temperature, the potential in the equation 2.2 is modified due to color charge screening. This effect on the potential can be quantified by the Debye screening radius r_D . In a QGP, the quark and anti-quark of the charmonium state can no longer be bound together when the hadronic radius of the state becomes larger than r_D . Therefore a charmonium state is said to be dissociated in the QGP. The temperature at which the bound state radius, r_C , is equal to the screening length r_D , is the dissociation temperature, T_D . From the Table 2.2, one can see that the radii of the charmonium states differ, which means that some states will break up at lower temperatures than the others. Based on this picture, the authors of [72] have envisioned a hierarchy in the suppression of different charmonium states. So the observation of different charmonium states can serve as a QGP thermometer.

In order to quantitatively determine the charmonium dissociation temperature T_D in the QGP, three approaches can be followed. Two of them are based on potential models (A1, A2) and the third is based on calculation of the charmonium spectrum directly in finite temperature lattice QCD (B). In the following these approaches are described.

- (A1): at finite temperature, the potential between the quark and anti-quark becomes [73]:

$$V(r, T) = \sigma \cdot r \left(\frac{1 - e^{-\mu r}}{\mu r} \right) - \frac{\alpha}{r} e^{-\mu r}, \quad (2.5)$$

where the screening mass $\mu(T) = 1/r_D(T)$. The next step is to solve the Schrodinger equation:

$$-\frac{1}{m_c} [\nabla^2(r) + V(r, T)] \psi_i(r) = (M_i - 2m_c) \psi_i(r), \quad (2.6)$$

where m_c is the mass of the charm quark, M_i is the mass of the charmonium state "i" and ψ_i is its wave function. With increasing temperature, the bound state "i" disappears at some $\mu^i(T) = \mu(T_D^i)$. Then this approach uses the temperature dependence of the screening mass from lattice estimations, $\mu(T) = 4T$, to determine the dissociation temperatures [74].

- (A2): the second potential model approach [75] is based on assuming that the potential $V(r, T)$ is equal to the free energy $F(r, T)$. This assumption is made by neglecting the entropy term $T \left(\frac{\partial F(r, T)}{\partial T} \right)$ in the equation:

$$V(r, T) = F(r, T) - T \left(\frac{\partial F(r, T)}{\partial T} \right). \quad (2.7)$$

Then the dissociation temperatures are obtained by solving the Schrodinger equation using lattice QCD results for the free energy.

- (B): in this case, the spectrum $\sigma(\Omega, T)$ is calculated in the appropriate quantum channel, as a function of the temperature T and the $c\bar{c}$ energy Ω [76]. Then by changing the temperature in the performed simulations, one can obtain the dissociation temperature that corresponds to the disappearance of the charmonium bound state as illustrated in Figure 2.11.

The dissociation temperatures T_D for the different charmonium states and following the above approaches are summarized in Table 2.4.

State \ Approach	A1	A2	B
J/ψ	$\sim 1.2T_C$	$\sim 2T_C$	$1.5T_C < T_D < 2.3T_C$
$\psi(2S)$ and χ_c	$\sim T_C$	$\sim 1.1T_C$	$T_D > 1.1T_C$

Table 2.4: Dissociation temperature T_D for different charmonium states following the different approaches described in the text of section 2.5.1.

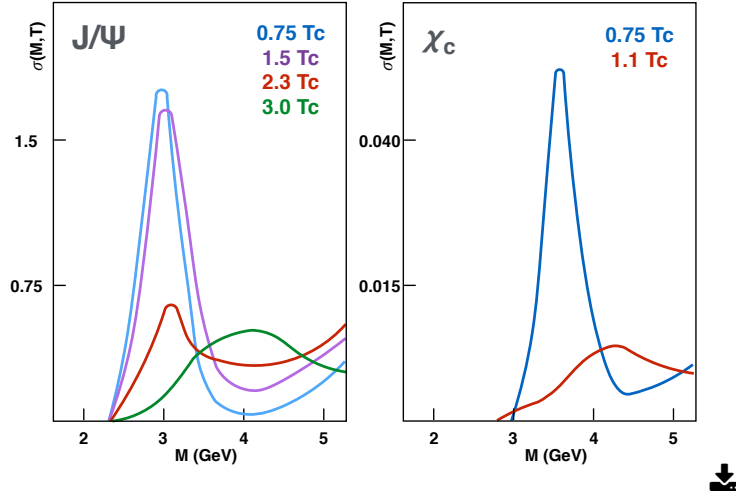


Figure 2.11: Lattice QCD simulations used for determining the dissociation temperature T_D for J/ψ (left) and χ_c (right). Figure is reproduced from [73].

2.5.2 J/ψ regeneration

At high collision energy, there is a significant number of initially produced charm and anti-charm quarks in the medium which could come close enough in phase space to form a charmonium state. This charmonium production mechanism is known as regeneration and it tends to enhance the number of observed charmonia in nucleus-nucleus collisions with respect to proton-proton collisions. The significance of this enhancement depends on the strength of the recombination between

the charm and anti-charm quarks and on the stage at which this recombination occur. Some models consider the recombination at the hadronization stage only while others consider it continuous throughout the evolution of the medium.

It is worth noting that the recombination is dominated by the initially produced charm quarks since the number of thermally produced charm quarks is too low due to the heavy mass of the charm quark.

2.5.3 Interaction with comovers

The constituents of the medium (comover particles) can scatter with the $c\bar{c}$ pair or the charmonium state (depending on their formation time compared to the charmonium one). Assuming that they interact with the $c\bar{c}$ pair, the typical reaction is $c\bar{c} + h \rightarrow D + D + X$. In this case, h stands for a comoving hadron. The probability that the bound state $c\bar{c}$ survives the interactions with comovers is given by: [77]

$$S(b) \approx \exp\left[-\int d\tau \langle \sigma_{co} v \rangle n(\tau, b)\right], \quad (2.8)$$

where v is the relative velocity of the $c\bar{c}$ with respect to the comovers, $n(\tau, b)$ is the comover density at impact parameter b and time τ , and σ_{co} is the effective charmonium-comover cross section fixed from experiments at low energy. The author of [78] admits that σ_{co} could change with energy (not dramatically) but there is no possibility to determine it so they took the known one at low energy in the calculation. One can see from the equation 2.8 that with increasing energy density (i.e collision centrality) the suppression of the charmonium due to comover interaction becomes more important.

The effects from color screening, regeneration and interaction with comovers are illustrated in the cartoon of Figure 2.12 .

2.5.4 Theoretical status

In the following, a brief description of some available theoretical models that aim to describe the J/ψ production in nucleus-nucleus collisions.

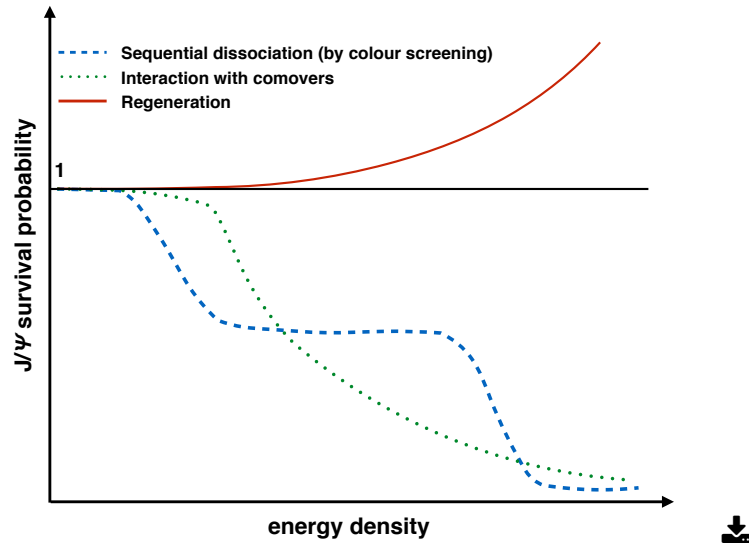


Figure 2.12: Illustration of the contribution of the color screening, interaction with comovers and regeneration to the J/ψ survival probability.

Note that other models do exist but are not described. The description is limited to the models used for the comparison with the results in chapter 6.

2.5.4.1 Statistical hadronisation model

The statistical hadronisation model was originally introduced to describe the production of hadrons with light (u, d, and s) quarks in heavy-ion collisions based on a hadro-chemical equilibrium approach [13]. This model is successful in reproducing particle ratios in a broad collision energy range (from AGS energy of ~ 10 GeV up to LHC energy). The model uses a grand canonical ensemble to describe the partition functions and hence the density of the hadrons under consideration. The only free parameters in this model are the chemical freeze out temperature and the baryo-chemical potential.

The difference with charm hadrons is that as discussed in section 2.5.2, the charm thermal rate production is negligible even at the LHC energy. Therefore, in this model, charm quarks produced in the initial hard scattering find themselves deconfined in the QGP (which means that all the produced charmonia have been color-screened). Then the charmonia and the open charm hadrons are formed

at the phase boundary according to their statistical weights (like all the other hadrons) [79, 80]. This consideration for the charm production, implies a new free parameter to the model which is the charm production cross section per rapidity unit ($d\sigma_{c\bar{c}}/dy$).

In this model all the initially produced charmonia are suppressed in the medium so the model does not include initial CNM effects on the charmonia. However, CNM effects on the $c\bar{c}$ cross section are considered.

2.5.4.2 Transport models

In models that are based on transport approach [81–83], the charmonium states (quarkonium in general) are described by the so called excitation functions f_ψ . The space-time evolution of the charmonium state in the medium is governed by the relativistic Boltzmann equation:

$$p^\mu \partial_\mu f_\psi(r, \tau, \mathbf{p}) = -E\Gamma_\psi(r, \tau, \mathbf{p})f_\psi(r, \tau, \mathbf{p}) + E\beta_\psi(r, \tau, \mathbf{p}) \quad (2.9)$$

where τ and r are respectively the time and the spacial coordinate, while Γ_ψ and β_ψ are respectively the dissociation rate and the gain term.

In transport models, charmonia can be suppressed by inelastic scattering with constituents of the medium (light quarks, gluons or light hadrons). In QGP and for a tightly bound state (e.g charmonium) the dominant process is the gluon dissociation ($g + \psi \rightarrow c + \bar{c} + X$) [84]. In such models and in contrast to the statistical hadronisation model, charmonia are continuously suppressed and generated in the QGP. Finally, nuclear absorption, nPDF modification and Cronin effect are taken into account.

2.5.4.3 Comover Interaction Model (CIM)

As the name of the model tells, it is mainly based on the notion of interaction with comovers (section 2.5.3). This model was initially introduced in [85] as an alternative to the color screening mechanism in describing the anomalous charmonium suppression observed at SPS [86]. As for the transport models, the CIM is also based on rate equations, but the difference is that the CIM does not assume a QGP formation and hence medium equilibrium.

While the first version of the model [85] does not take charmonium regeneration into account, it was included as a gain term in the rate equations in a revisited version of the model [78].

Finally, the CIM takes into account nuclear shadowing which is calculated within the Glauber-Gribov model [87].

In the early versions of the model [85], the comover medium was considered to be only hadronic and no charmonium regeneration was taken into account. However, in a revisited version of the model [78], partonic comoving medium was also considered and the regeneration was also included as a gain term in the rate equations.

2.6 Experimental results

In this section, experimental results that are related to the subjects of this manuscript will be summarized.

2.6.1 Z-boson production in heavy-ion collisions

The Z-boson production measurement in heavy-ion collisions has only become accessible at the LHC thanks to the large center of mass energies and available luminosities. chapter 5 will present the results of this production in p-Pb and Pb-Pb collisions at $\sqrt{s_{NN}} = 2.76$ TeV, measure by the ALICE detector. Below, a summary of the results of this production measure dby different experiments in different collision systems:

2.6.1.1 Pb-Pb at $\sqrt{s_{NN}} = 2.76$ TeV

The first Z-boson production measurement in heavy-ion collisions corresponds to Pb-Pb collisions at $\sqrt{s_{NN}} = 2.76$ TeV. The Z-boson yield measured by ATLAS [88] (Figure 2.13 left), is compared to model calculation using PYTHIA [89]. The model takes into account the isospin effect but it does not account for the nPDF modifications. One can see that within uncertainties, the data are well reproduced by this model.

In addition to the Z-boson yield, CMS has measured the nuclear modification factor R_{AA} ⁵ [90] which is the yield observed in nucleus-nucleus collisions relative to the one in pp collisions scaled by the number of binary nucleon-nucleon collisions (N_{coll}) as shown in Figure 2.13 right. In the calculation of R_{AA} , the Z-boson pp cross section is measured at the same energy. One can see from the flat behavior of the R_{AA} centrality dependence, within uncertainties, that the production cross section scales with the number of nucleon-nucleon collisions.

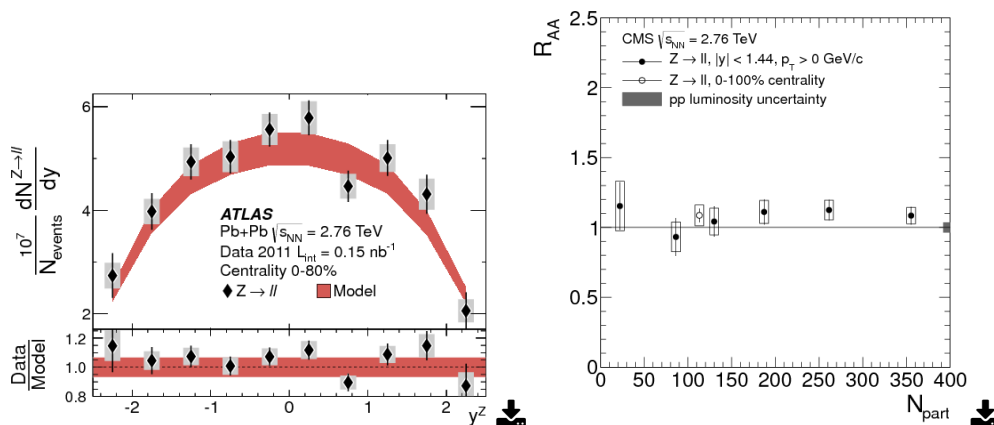


Figure 2.13: Left: Z-boson yield measured by ATLAS [88] in rapidity bins and compared to prediction based on PYTHIA. Right: Z-boson R_{AA} vs the collision centrality measured by CMS [90]. Both measurements are performed in Pb-Pb collisions at $\sqrt{s_{NN}} = 2.76$ TeV.

2.6.1.2 p-Pb at $\sqrt{s_{NN}} = 5.02$ TeV

In this collision system, the Z-boson production has been measured by the four LHC experiments. At mid-rapidity, ATLAS [91] and CMS [92] have measured it in the leptonic (combined electronic and muonic) decay channel. In Figure 2.14, the measured cross section results are compared to theoretical calculations, both with and without including nPDFs modification. Within uncertainties, both set of models are able to describe the data.

These results (among others) have been recently added to the global fit analysis by

⁵Defined in chapter 4

the EPS09 group, leading to an updated nPDF set EPPS16 [61].

At forward rapidity, the LHCb experiment has measured the Z-boson production in the dimuon decay channel [93]. Figure 2.15 shows the cross section results in two center-of-mass rapidity regions, also compared to theoretical calculation with and without including of nPDF modification. With the large statistical uncertainties, a clear conclusion could not be drawn on whether or not the agreement between the data and the theory is better with including of the modifications of nPDF.

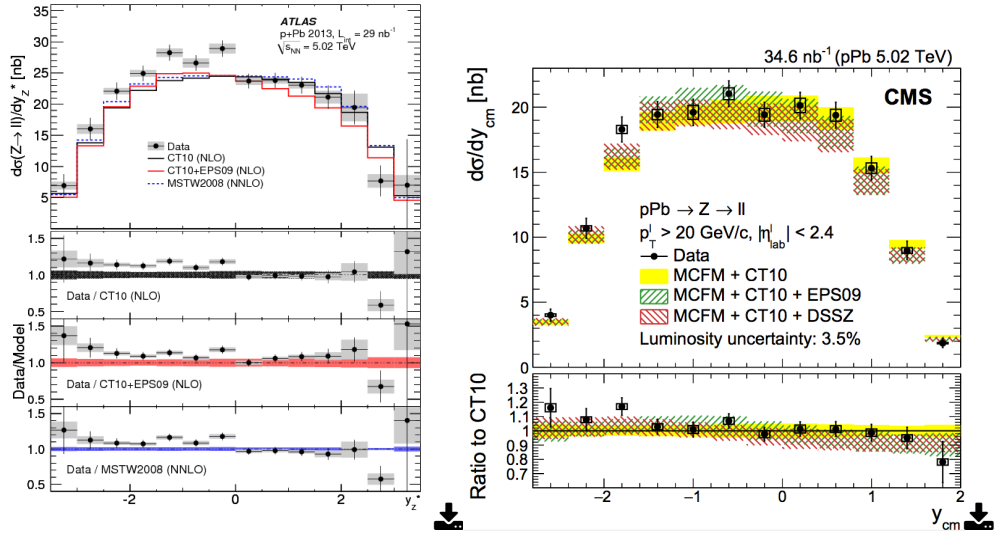


Figure 2.14: Left (right): the Z-boson cross section in p-Pb collisions measured by ATLAS [91] (CMS [92]) and compared to models with and without accounting for nPDF modification.

2.6.2 J/ψ production in heavy-ion collisions

2.6.2.1 At SPS

Nine years after the original prediction of the J/ψ suppression, the NA50 experiment at the SPS (CERN) measured the J/ψ production in Pb(158 AGeV)-Pb

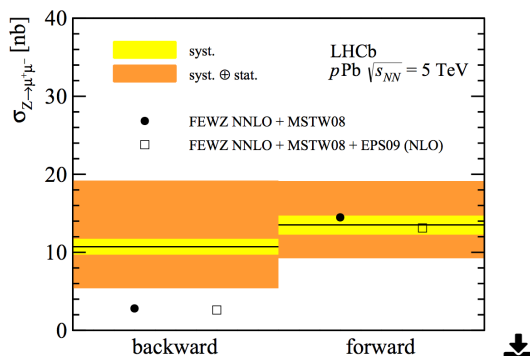


Figure 2.15: Z-boson cross section in p-Pb collisions measured by LHCb and compared to models with and without accounting for nPDF modification [93].

collisions⁶ [86]. The suppression was quantified using the J/ψ to Drell-Yan (DY) ratio since the DY production is not affected by the presence of the hot medium or by nuclear absorption. As shown in the Figure 2.16, the J/ψ suppression was found to be stronger than the one predicted by only nuclear absorption based on a Glauber model. Because of the deviation from the nuclear absorption prediction, the suppression was called "anomalous" and the NA50 experiment concluded in [94] that this suppression provides an evidence for the de-confinement of quarks and gluons in heavy-ion collisions.

2.6.2.2 At RHIC

Six years after the J/ψ anomalous suppression reported by NA50, RHIC provided the first J/ψ data in Au-Au collisions at a center of mass energy of 200 GeV [95]. The R_{AA} was introduced to quantify the J/ψ suppression. Figure 2.17 shows the comparison of the J/ψ suppression observed at SPS and RHIC in terms of an R_{AA} corrected by the CNM effects which are important at the two energies. Despite the factor of 10 higher collision energy at RHIC, the magnitude of the anomalous suppression is similar which is not expected in the picture of color screening alone. However, theoretical models that include the J/ψ regeneration component [79, 83], [96, 97] (see section 2.5.2) had anticipated a weaker J/ψ suppression at RHIC

⁶This corresponds to ~ 17 GeV of energy in the center of mass

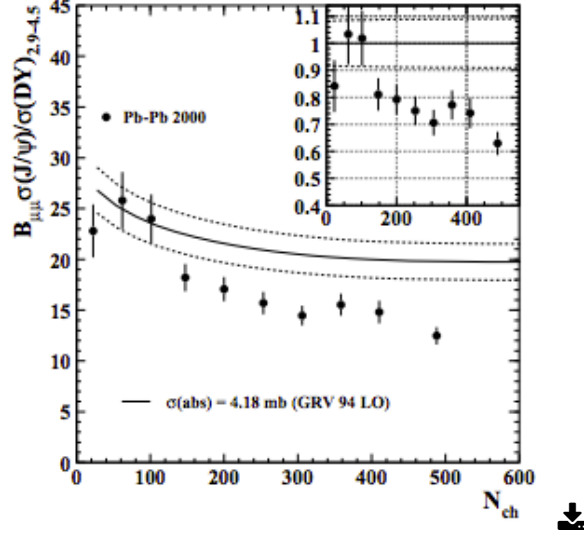


Figure 2.16: The ratio between the J/ψ and DY cross sections in Pb(158 AGeV)-Pb collisions at the SPS, measured by the NA50 experiment [86]. The dotted band corresponds to the prediction based on nuclear absorption

compared to what is predicted by color screening melting alone. This is based on the fact that the regeneration component becomes more important at RHIC due to the increase of the collision energy. Additional support for the necessity of including the regeneration component arose from the observation that J/ψ suppression at RHIC is less pronounced at mid rapidity relative to forward rapidity as shown in 2.17. It was argued that dissociation by color screening should be higher at mid-rapidity due to the larger energy density. However, this is compensated by the increasing J/ψ enhancement by regeneration at mid-rapidity due to larger charm production cross section.

2.6.2.3 At LHC

To shed light on the complexity of charmonium suppression and regeneration mechanisms in nucleus-nucleus collisions, the J/ψ production has been measured in Pb-Pb collisions, at two different center-of-mass energies $\sqrt{s_{NN}} = 2.76\text{TeV}$ and $\sqrt{s_{NN}} = 5.02\text{TeV}$. The latter is one of the main subjects of this manuscript and will be discussed in details in chapter 4 and chapter 6.

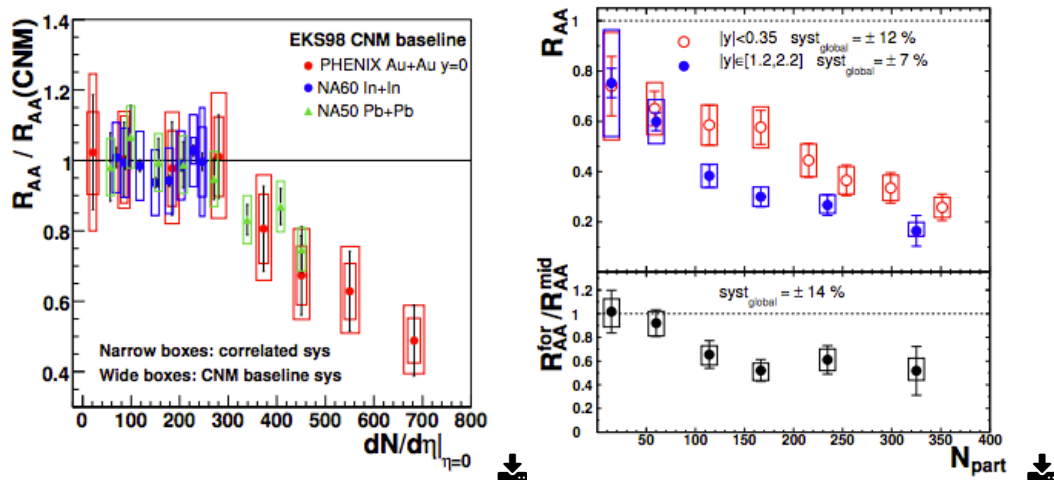


Figure 2.17: Left: the comparison between the J/ψ nuclear modification factor measured at SPS [94] and RHIC [95] (Figure taken from [45]). Right: the J/ψ R_{AA} measured at RHIC by PHENIX in two rapidity regions [95]

2.6.3 J/ψ production in small systems

In this manuscript, the focus is on the J/ψ production in Pb-Pb collisions which addresses the understanding of hot nuclear effects. However, the J/ψ production in smaller collisions systems have been studied for different motivations. In the following, some results on the J/ψ production in pp and p-Pb collisions are presented. The presentation is limited to measurements by ALICE at the LHC but results on the same topics by other LHC experiments and outside the LHC also exist.

2.6.3.1 J/ψ production in pp collisions

The study of the J/ψ production in pp collisions has two main motivations:

- A baseline for measurements of J/ψ production in heavy-ion collisions since no hot or cold nuclear effects are expected in pp collisions.
- Essential to understand the J/ψ hadronic production mechanisms.

ALICE has measured the J/ψ production in pp collisions at the different center-of-mass energies provided by the LHC (2.76, 5.02, 7, 8, and 13 TeV). Figure 2.17

shows the rapidity and p_T differential cross sections of inclusive J/ψ production at these energies. In [98], these cross sections were found in agreement with theoretical NRQCD calculations [44].

In chapter 4, more details will be presented on the J/ψ production cross section in pp collisions at $\sqrt{s} = 5.02\text{TeV}$ since it will be used as a reference for the J/ψ production in Pb-Pb collisions.

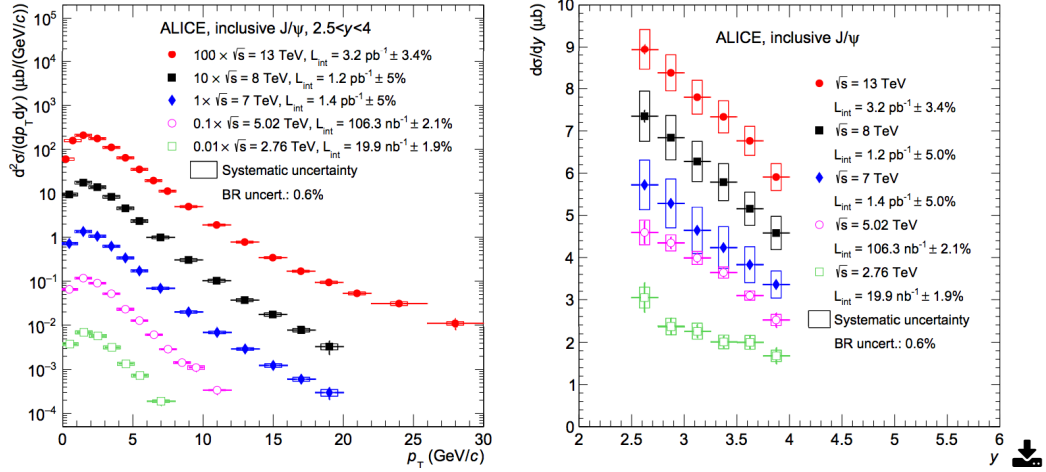


Figure 2.18: Left (right) panel: the J/ψ production cross section in pp collisions at different center-of-mass energies as a function of p_T (rapidity) measured by ALICE [98].

2.6.3.2 J/ψ production in p-Pb collisions

Hot nuclear effects are not expected to take place in p-Pb collisions. Therefore, measuring the J/ψ production in these collisions allows to quantify the cold nuclear matter effects on this production. To this date, the LHC has provided p-Pb collisions at two different center-of-mass energies, 5.02 and 8.16 TeV. At both energies, different J/ψ measurements were done. The J/ψ nuclear modification factor in p-Pb collisions (R_{pPb}) quantifies the J/ψ suppression in p-Pb collisions with respect to pp collisions. Figure 2.19 shows the R_{pPb} at $\sqrt{s_{NN}} = 5.02\text{TeV}$ as a function of rapidity. In the positive rapidity region (which probes the small Bjorken-x of the Pb ion), the measured J/ψ suppression is clear. This shows that the size of CNM effects is not negligible on the J/ψ production in heavy-ion collisions. Within uncertainties, R_{pPb}

is in agreement with theoretical calculations based on nuclear shadowing using the EPS09 parametrization [57] and coherent energy loss [67].

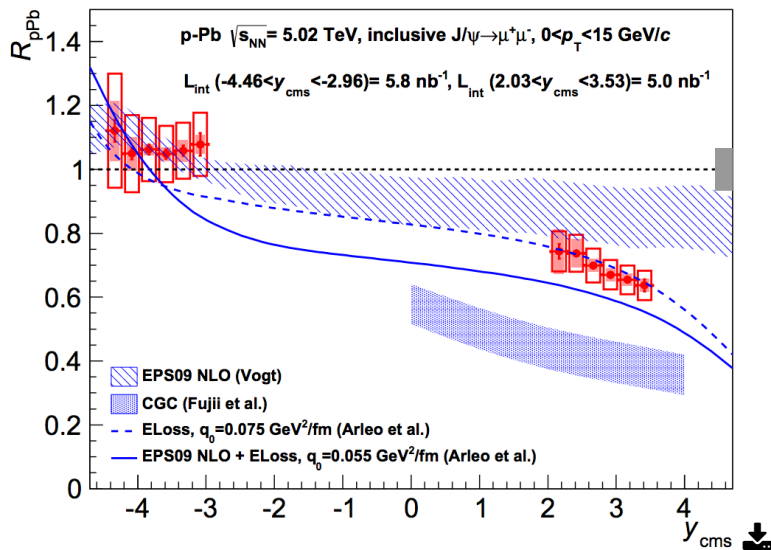


Figure 2.19: J/ψ nuclear modification factor in p-Pb collisions at $\sqrt{s_{NN}} = 5.02 \text{ TeV}$ measured by ALICE and compared to different theoretical calculations [99].

EXPERIMENTAL APPARATUS

This chapter is dedicated to the description of the experimental apparatus used to collect the analyzed data of this thesis. After a brief overview on the Large Hadron Collider, the ALICE detector and its different sub-detectors are briefly described. Data analyzed in this thesis were recorded mainly with the muon spectrometer which will be described in more details. As a service task for the collaboration, I was in co-charge of quality-assurance of data recorded by the muon spectromete. The last section of this chapter is dedicated to describe the procedure.

3.1 The LHC

The Large Hadron Collider (LHC) [100] is the largest and most powerful accelerator in the world located at CERN. Installed in a 26.7 km long tunnel underground ¹, the LHC started operating in 2008. It is optimized to run into two different modes: as a proton-proton (pp) collider and as a heavy-ion collider using fully stripped lead ions (⁸²Pb).

¹The tunnel originally built for the Large Electron-Positron collider (LEP) that was stopped in 2000.

3.1.1 LHC beams

Before reaching the LHC rings, a particle (a proton or a lead ion) passes through many accelerator facilities [101] as illustrated in Figure 3.1. In each step, the particle acquires more energy and in the Pb case, strips out more electrons². Throughout these steps, proton and Pb ions are grouped into the so-called bunches. The accelerators of the injector chain (Figure 3.1) have different lengths, which means that the entire beam of several hundred bunches cannot be injected into the LHC in one stage. Therefore, in each step, many pulses from the previous step are accumulated before acceleration and injection into the next step. The bunch spacing is defined as the time separation between two bunch injections into the PS. Bunches from the SPS are injected into the LHC in form of trains. Finally, a beam in the LHC can contain trains with a different number of bunches.

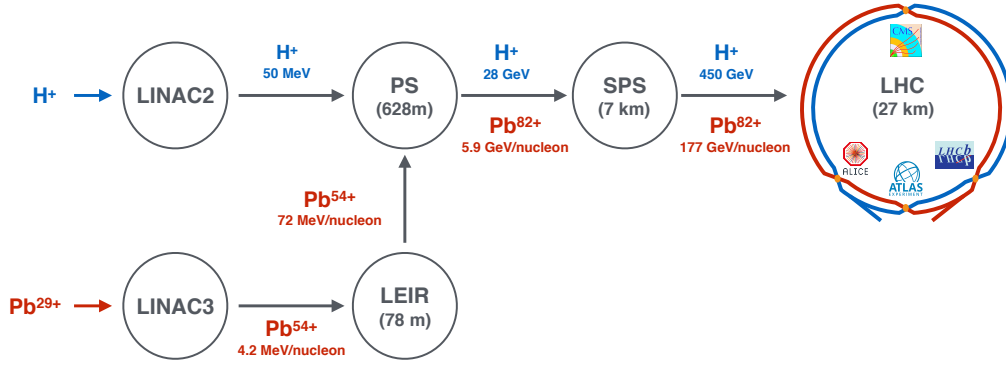


Figure 3.1: The LHC injection chain for two types of beams, protons and lead ions. For lead ions, the number of stripped electrons after each step is indicated.

For a given reaction, the instantaneous luminosity L of the collider represents the proportionality factor between the number of produced events per unit of time, dR/dt and the production cross section of the considered reaction, σ_c :

$$\frac{dR}{dt} = \sigma_c \times L \quad (3.1)$$

²The 29 outermost (weakly bound) electrons are removed electrically by evaporating Pb atoms. The obtained positive ions are then accelerated with LINAC3 and sent through a thin ($1 \mu\text{m}$) carbon target, stripping 25 electrons. The remaining 28 electrons are stripped by an aluminum foil after acceleration with PS.

In the case of a circular collider, the luminosity at a given interaction point is defined as [102]:

$$L = \frac{N_b^2 n_b f_{rev} \gamma}{4\pi \epsilon_n \beta^*} F, \quad (3.2)$$

where:

- β^* is the amplitude function at the interaction point. It is related to the width of the beams, the smaller the β^* is, the more squeezed the beams are and therefore the larger is the number of collisions,
- γ is the relativistic Lorentz factor of the accelerated particles,
- ϵ_n is the normalized transverse beam emittance. It can be interpreted as a measurement of the beam parallelism,
- n_b , N_b , and f_{rev} are respectively the number of bunches per beam, the number of particles per bunch and the revolution frequency,
- F is the geometric luminosity reduction factor due to the crossing angle at the interaction point .

By integrating over time, one can get the integrated luminosity, L_{int} .

3.1.2 LHC experiments

The two LHC beams cross in four interaction points that host the four largest CERN experiments:

- **A Large Ion Collider Experiment (ALICE)** [103] at **IP2** is a multipurpose detector optimized for the very high multiplicity environment created in central heavy-ion collisions. A detailed description of the detector is given in Section 3.2.
- **A Toroidal LHC ApparatuS (ATLAS)** [104] at **IP1** and **Compact Muon Solenoid (CMS)** [105] at **IP5** are multipurpose particle physics detectors, designed to operate in high luminosity pp mode in order to search for new particles in the standard model and beyond. Even if the two experiments are

not dedicated to heavy-ion physics, they have participated in the different LHC heavy-ions data taking periods and have been involved in various studies in this domain. In particular, they obtained results on jet quenching, quarkonia and electroweak boson measurements.

- **LHC beauty (LHCb)** [106] at **IP8** is a fully instrumented forward spectrometer focusing mainly on the beauty physics. The LHCb experiment has participated in the 2013 and 2016 p-Pb collisions data taking periods as well as in the 2015 Pb-Pb collisions one, and conducted several analyses on heavy-flavor hadrons and Z-bosons production in those collisions. However due to the high multiplicity environment in Pb-Pb collisions, LHCb still has difficulties in reconstructing tracks in the most central Pb-Pb events. The heavy-ion program of LHCb includes also a fixed-target mode by injecting nuclear gas (He, Ne, Ar) into the LHC beam pipe at the interaction point.

Depending on their dedicated physics programs, the four experiments cover different geometric acceptances. Therefore, for a given measurement, they are complementary to each other. For example, the J/ψ acceptances covered by ALICE, ATLAS, and CMS, in Pb-Pb collisions, are shown in Figure 3.2.

3.2 ALICE

ALICE is a collaboration of more than 1800 members from 42 countries at the time of writing this manuscript. In order to cover different topics in heavy-ion physics, the detector consists of 18 different sub-detectors that can be assembled in three main ensembles: (i) Global detectors for measuring general quantities such as the collision centrality, particle multiplicity, and collision time, (ii) the central barrel at mid-rapidity, which is contained in a magnetic field of 0.5 T using the magnet of the L3 experiment at LEP. The detectors of the central barrel are optimized for the reconstruction of hadrons, electrons and photons, (iii) the muon spectrometer at forward rapidity which is responsible for the reconstruction of muon decay products of heavy-flavor hadrons, quarkonia and electroweak bosons. The ALICE detector is shown entirely in Figure 3.3 and is described in details in [103].

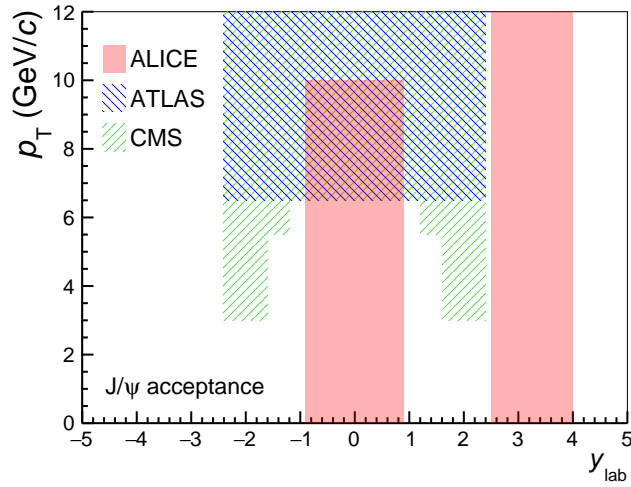


Figure 3.2: J/ψ acceptance in terms of laboratory frame rapidity (y_{lab}) and transverse momentum (p_T) for ALICE, CMS, and ATLAS in Pb-Pb collisions. The upper limits of the p_T acceptances are not hard numbers and can vary depending on the available statistics. Figure is adapted from [107].

If the beams cross at the origin of a Cartesian coordinate system, its z-axis would be parallel to the beam line such that the A-side of ALICE is in the positive direction while the C-side (where the muon spectrometer sits) in the negative one. The x-axis points to the center of the LHC ring while the y-axis points upwards. In Figure 3.4, a plot that summarizes the pseudo-rapidity coverage of the different sub-detectors is shown. In the following, a brief description of the sub-detectors of those three ensembles and their roles will be given. A detailed description of the muon spectrometer will follow.

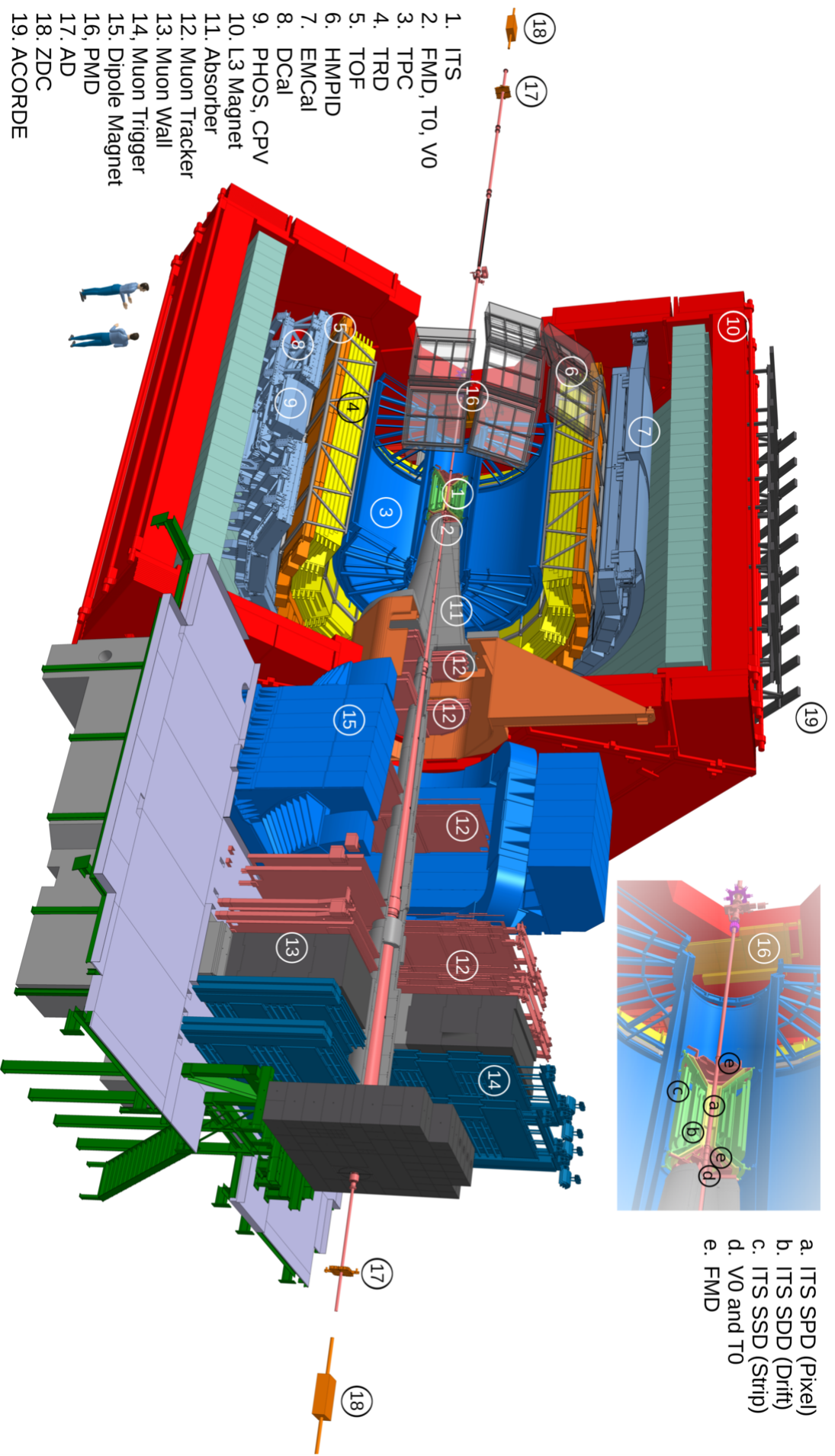


Figure 3.3: The ALICE detector with the names of its different sub-detectors. The top right panel represents a zoom-in of the region close to the interaction point. 

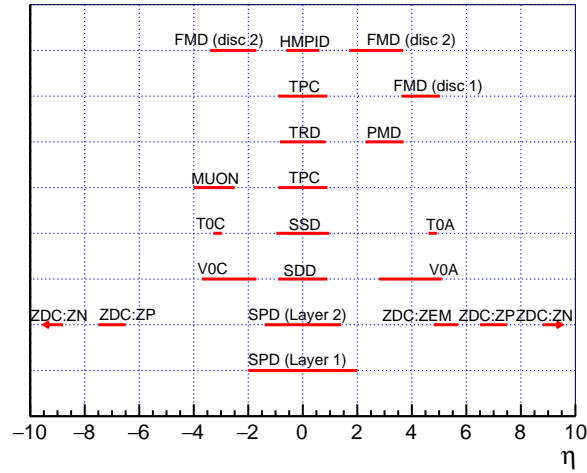


Figure 3.4: Pseudo-rapidity coverage of the different ALICE sub-detectors.

3.2.1 Global detectors

The Forward Multiplicity Detector (FMD)

The FMD [108] measures the charged particle multiplicity over a large pseudo-rapidity window. The detector has a full azimuthal coverage and it consists of about 50000 silicon strips arranged in five rings placed around the beam pipe and located at $z = 3.2$ m, 0.83 m, 0.75 m, -0.63 m and -0.75 m. The number of charged particles (i.e particle multiplicity) is obtained using the information on energy deposition in the silicon strips.

The Photon Multiplicity Detector (PMD)

The PMD [109] measures the multiplicity and spatial (η, ϕ) distribution of photons. It is positioned at 3.64 m from the interaction point and it consists of lead (Pb) converter located between two highly granular gas proportional chambers that uses a mixture of Ar/CO₂. The chamber in front of the converter is used as charged particle veto (CPV), while the second one is used for photon identification.

The T0 detector

The T0 [108] consists of 24 Cherenkov counters with quartz radiators, arranged in two units which are located around the beam line at distances of 3.75m and -0.73 m from the interaction point. With a time resolution of 25 ps, the T0 provides a collision time (time = 0) for the TOF detector, determines the vertex position within 1.5 cm, and serves as a minimum bias trigger. The T0 can also determine the particle multiplicity.

The V0 detector

The V0 [108] is composed of two arrays of scintillator counters, V0-A and V0-C, which are positioned on both sides of the interaction point at $z = 340$ cm and $z = -90$ cm respectively. Each of the V0 arrays is segmented in four rings in the radial direction, and each ring is divided in eight sections in the azimuthal one (Figure 3.5 left). Upon a hit on the scintillator, the produced light is transmitted to a Photo-Multiplier Tube (PMT) through Wave-Length-Shifting (WLS) optical fibers (Figure 3.5 right). Beam-gas events can be identified by measuring the difference of the time-of-flight between V0A and V0C with a time resolution of 1 ns, hence the V0 serves as minimum bias trigger. The V0 is also used as collision centrality estimator by measuring the particle multiplicity.

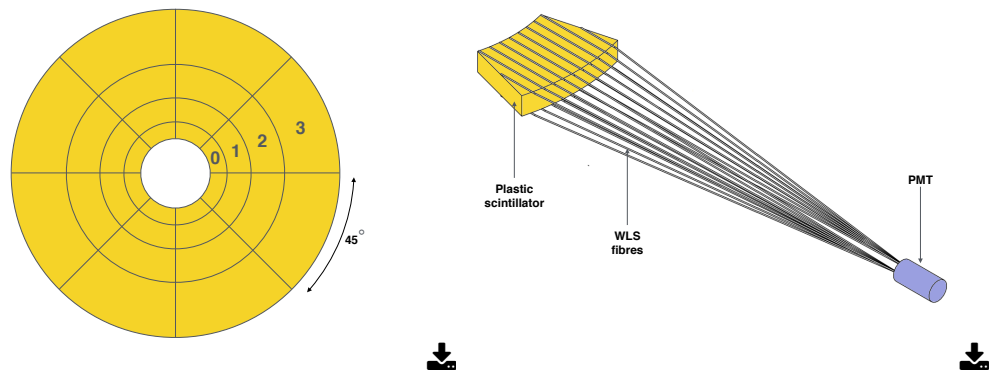


Figure 3.5: Left: a transverse view of a V0 array plane (V0-A or V0-C). Right: a schematic view of one scintillator counter. Figure is taken from [103].

The Zero-Degree Calorimeter (ZDC)

The ZDC [110] consists of two sets of hadronic calorimeters, ZP and ZN, and two electromagnetic calorimeters (ZEM). ZP and ZN are the farthest ALICE detectors from the interaction point, placed at $z = \pm 116$ m. They are quartz fibers sampling calorimeters that measure the energy deposited by spectator protons and neutrons respectively. This measurement can be related to the collision geometry since the number of spectators will decrease in most central collisions. However, the small number of spectators can also be obtained in very peripheral events where the spectators stay in the beam pipes and therefore cannot be detected by ZP and ZN. The ZEM, placed at $z = +7$ m, measures the energy deposits of particles emitted at forward rapidity (mainly photons generated from π^0 decays). This measurement can help to discriminate between most central and very peripheral events since it is monotonically increasing with centrality.

3.2.2 Central barrel detectors

The Inner Tracking System (ITS)

The ITS [111] is built up by six layers of silicon detectors, with a radial position between 3.9 to 43 cm from the beam pipe. The ITS is responsible for the reconstruction of the primary vertex of the collision and also the secondary vertices of heavy hadron decays with a resolution better than $100\mu\text{m}$. By tracking particles and measuring energy loss (dE/dx), the ITS contributes to the particle identification. The six layers of the ITS are assembled in three sub-systems as illustrated in Figure 3.6. Different detector technologies and materials are chosen for the three sub-systems, depending on the track density and the required task of each one. The two innermost layers are made of Silicon Pixel Detectors (SPD), the third and fourth layers are made of Silicon Drift Detectors (SDD) while the two outermost layers are equipped with Silicon Strip Detectors (SSD). The SPD provides a measurement of the charged-particle multiplicity. The SPD and the FMD complete each other in terms of pseudo-rapidity coverage and therefore can provide a continuous charged particle multiplicity measurement in $-3.4 < \eta < 5.1$. In contrast to the two innermost, the four outer layers have analogue readout (the SPD have binary

readout), thus taking the task of the particle identification.

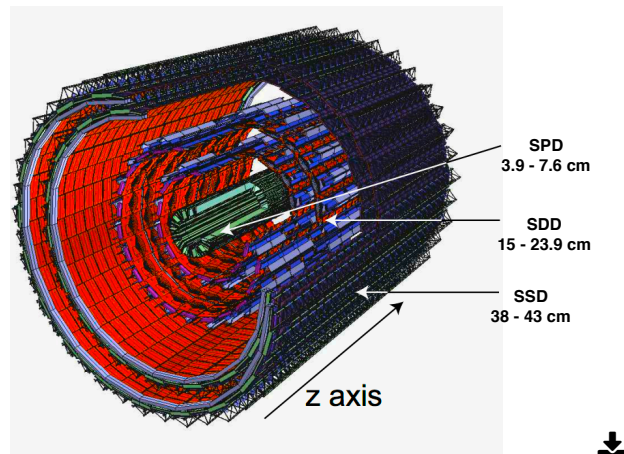


Figure 3.6: A 3D view of the ITS. The radial positions of the three sub-systems, SPD, SDD, and SSD are indicated. Figure is taken from [103].

The Time-Projection Chamber (TPC)

ALICE has the largest TPC in the world, with a cylindrical volume of about 90 m^3 . The TPC [112] is filled with a $\text{Ne}/\text{CO}_2/\text{N}_2$ gas mixture. Together with other central barrel detectors, the TPC is responsible for particle identification, vertex determination, and charged particle tracking and momentum measurements. The TPC is schematized in Figure 3.7. An electrode in the middle ($z = 0$) divides the TPC in two parts, each one ending with 18 sectors of read-out multi-wire proportional chambers mounted into the end plates at $z = \pm 2.5 \text{ m}$.

The Transition-Radiation Detector (TRD)

The TRD [113] is located between radii from 2.9 m to 3.7 m. The TRD is segmented into 18 sectors that consist each of six layers. An example of one layer is shown in Figure 3.8. The main task of the TRD is to provide electron-pion discrimination based on transition radiation mechanism. When a charged particle passes from a medium to another with a different dielectric constants, it emits a photon. The

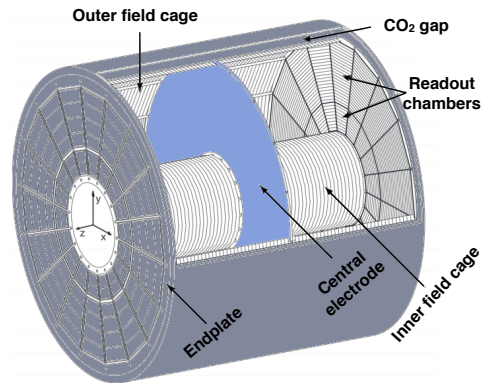


Figure 3.7: A 3D view of the ALICE TPC. Figure is taken from [103].

discrimination is then based on the probability to produce the photon which is different for pion and electrons ³.

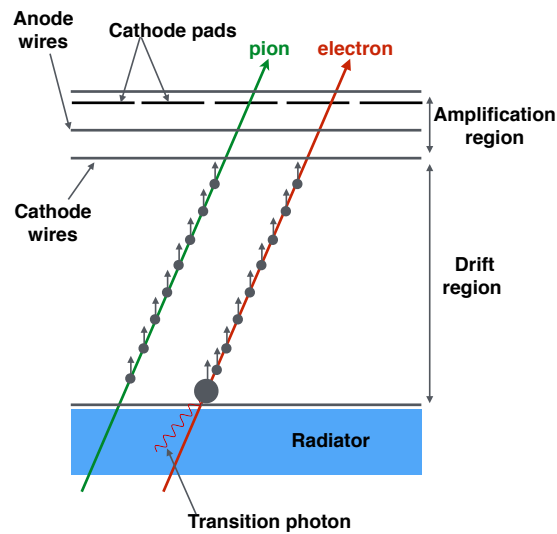


Figure 3.8: Schematic view in the $r - \phi$ direction of one TRD layer together with the clusters produced by an electron and a pion track. Figure is taken from [103].

³This probability is linear with the relativistic Lorentz factor γ . For particles with 1 GeV momentum, $\gamma_e/\gamma_\pi \sim 2000/7$

The Time-Of-Flight Detector (TOF)

By measuring the time-of-flight of charged particles that traverse the detector with a given velocity, the main task of TOF [114] is to identify protons (p), kaons (k) and pions (π). With a time resolution of about 40 ps, the TOF is able to make better than three sigma separations of K/p up to 4 GeV/c and of π /K up to 2.5 GeV/c. TOF is located at a radius of 3.8 m, it consists of Multigap Resistive Plate Chambers (MRPC) arranged in 18 sectors in azimuth. The very good time resolution is achieved by the setup of the MRPC. They feature a high and uniform electric field over the full sensitive gaseous volume, so that any traversing particle immediately triggers an avalanche, generating signals which are then observed on the pick-up electrodes. This is in contrast to other types of gaseous detectors where some time is spent by the drift of the electrons to a region of high electric field.

The High-Momentum Particle Identification Detector (HMPID)

The HMPID [115] consists of seven modules ($1.5 \times 1.5 \text{ m}^2$ each) that work as proximity-focusing Ring Imaging Cherenkov (RICH) counters. Cherenkov photons are emitted when a charged particle traversing a 15 mm thick radiator made of perfluorohexane (C_6F_{14}) and detected by a photon counter made of multi-wire pad chambers. By using information on the Cherenkov emission angle and the particle momentum, the main task of the HMPID is to identify pions, protons and kaons. The HMPID extends the PID capability of TOF, ITS and TPC, allowing the π /K and K/p separations up to 3 GeV/c and 5 GeV/c respectively.

The Photon Spectrometer (PHOS)

PHOS [116] is a high-resolution electromagnetic spectrometer, positioned on the bottom of the ALICE setup at a distance of 4.6 m from the interaction point and covering a limited acceptance domain at central rapidity. PHOS measures photons and neutral mesons (π and η) via their photonic decay, at low p_T in order to study the thermal and dynamical properties of the initial phase of the collision, and at high p_T to study jet quenching (using $\gamma - \gamma$ and $\pi - \gamma$ correlations). The main part of PHOS is the electromagnetic calorimeter made of dense scintillating crystals and lead-tungstate crystal detection cells. PHOS rejects charged particles through a

set of multi-wire proportional chambers in front of the calorimeter called Charged Particle Veto (CPV).

The ElectroMagnetic Calorimeter (EMCal)

The EMCAL [117] is a large cylindrical Pb-scintillator located at a radius of ~ 4.5 m from the beam line, between the ALICE main frame and the L3 magnet coils. Similarly to PHOS, EMCAL measures photons, and neutral mesons via their photonic decay in order to study jet quenching. Recently (after the LHC run-1), the EMCAL was completed by the installation of the Di-jet Calorimeter (DCAL) [118], forming a two-arm electromagnetic calorimeter. This enables the back-to-back correlation measurements, which are impossible with the EMCAL alone. The azimuthal acceptances of EMCAL and DCAL are respectively 110° and 70° , with both detectors covering the same pseudo-rapidity range ($-0.7 < \eta < 0.7$), providing a good acceptance for di-jets studies up to transverse momentum of $p_T \sim 150 \text{ GeV}/c$.

The ALICE electromagnetic calorimeters system (PHOS+EMCAL+DCAL) is illustrated in Figure 3.9.

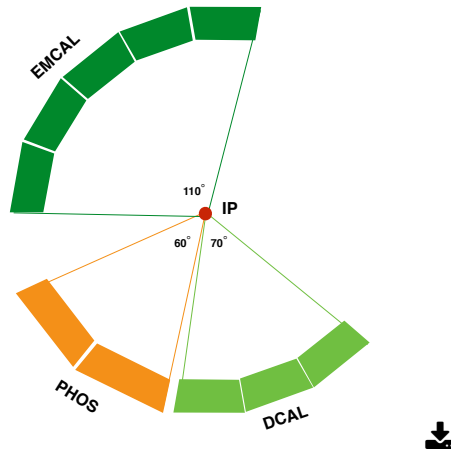


Figure 3.9: The structures and azimuthal positions of the three ALICE electromagnetic calorimeters, PHOS, EMCAL, and DCAL.

The ALICE Cosmic Ray Detector (ACORDE)

ACORDE consists of 60 plastic-scintillator counters placed on the upper surface of the L3 magnet. The scintillators are arranged two by two in the so called module in order to read-out in coincidence mode. Each scintillator has $190 \times 20 \text{ cm}^2$ effective area. Beside studying them, detected cosmic rays are used for calibration and alignments of other ALICE detectors.

3.2.3 The MUON Spectrometer

Muon decay products of low mass mesons (ρ , ϕ , ω), quarkonia, heavy-flavor hadrons and electroweak bosons are reconstructed in the muon spectrometer [119, 120]. The spectrometer is located on the C-side of the ALICE detector, covering the pseudorapidity range $-4 < \eta < -2.5$ in full azimuth. It consists of (Figure 3.10):

- A dipole magnet with an integrated magnetic field of 3 Tm
- An absorbing system
- Ten planes of high granularity tracking chambers
- Four planes of trigger chambers

In the following, the different parts of the spectrometer are described.

3.2.3.1 Dipole magnet

By deflecting a particle in a magnetic field and measuring its curvature, one can obtain its momentum and electric charge. The deflection is done using a warm magnet that provides an integral field of 3 Tm. Sitting at 7 m from the interaction point and with the dimensions, 5 m length, 6.6 m wide, and 8.6 m height, the dipole magnet contains the fifth and sixth tracking chambers. The dipole provides a horizontal magnetic field perpendicular to the beam axis, with an invertable polarity. In the following, the plane perpendicular to the magnetic field is referred to as "bending plane", while the parallel one as "non bending plane".

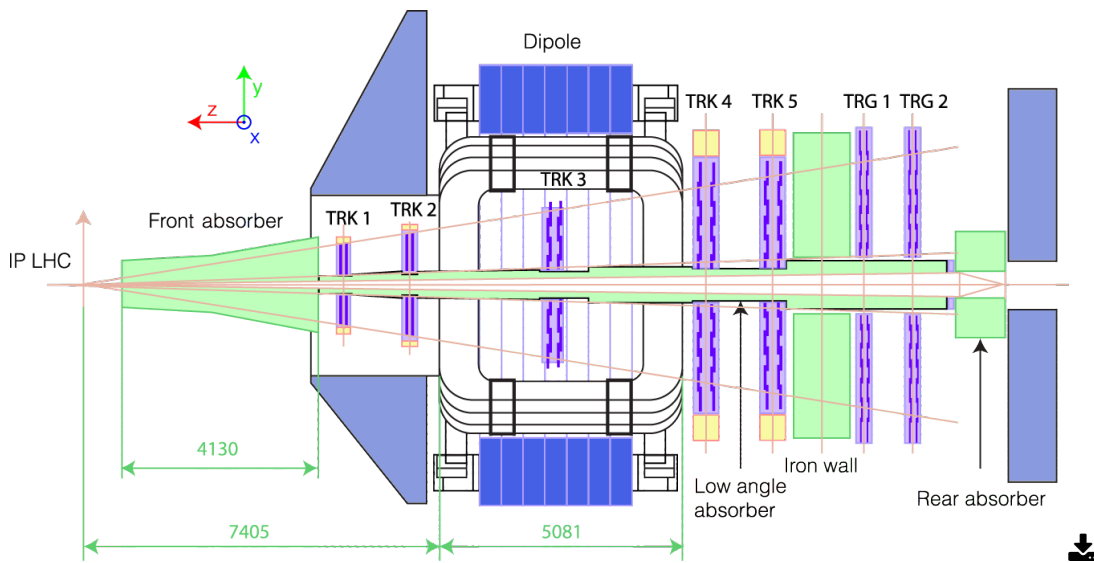


Figure 3.10: The layout of the ALICE muon spectrometer in the z - y direction. Figure is taken from [121].

3.2.3.2 Absorbing system

The first component of the absorbing system is the **front absorber** with the main task of decreasing the background of muons from the decay of pions and kaons. The distance of the front absorber from the interaction point is 90 cm and imposed by geometrical constraints from the central detectors. The front absorber is then located inside the L3 magnet with a length of 4.13 m ($\sim 60 X_0$). The design of the front absorber as well as the used materials (Figure 3.11) were chosen to achieve a good background rejection without paying a big penalty on multiple scattering which affects the spectrometer mass resolution. To lower the multiple scattering, the region of the absorber close to the interaction point is made of Carbon (low- Z material). The Carbon part is followed by concrete. In contrast, high- Z materials (Pb and polyethylene) are used for the rear end. This part has the task of absorbing the low energy photons and neutrons as well as the secondary particles produced in the front absorber itself.

The whole spectrometer is protected from secondaries coming from beam-gas interaction and from interaction of large rapidity particles with the beam pipe by the **small-angle beam shield**. It is made of dense materials (Tungsten and Pb)

and enveloped with stainless steel.

The trigger chambers are further protected by a 1.2 m **iron wall**. It acts as a muon filter since it stops the energetic hadrons and secondary particles that traverse the front absorber.

Finally, the back of the trigger chambers is protected from beam-gas interaction by the means of a **second iron wall (rear absorber)**.

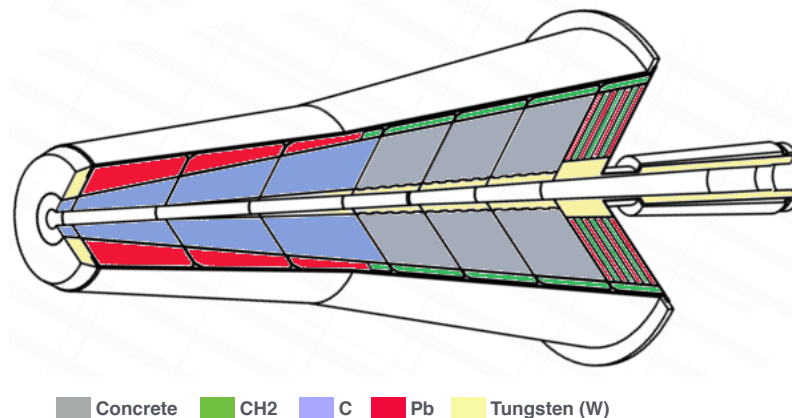


Figure 3.11: Internal structure of the front absorber with a color map that represents the used materials.

3.2.3.3 Tracking system

The tracking system consists of ten Multi-Wire-Proportional Chambers (MWPC) with a cathode readout, arranged two by two in five tracking stations. Two stations are placed before, one inside, and two after the dipole magnet. The radii of the chambers in the first two stations are defined by the angular acceptance of the spectrometer (a solid angle from 171° to 178° with an origin at the interaction point), while the chambers of the last three stations have relatively larger radii in order to detect particles after their deviation by the dipole magnet.

The chambers of the first two stations are based on a quadrant structure, with the readout electronics distributed on their surface (Figure 3.12). The other chambers have a slat structure and their electronics are implemented on the side of the slats

(Figure 3.13).

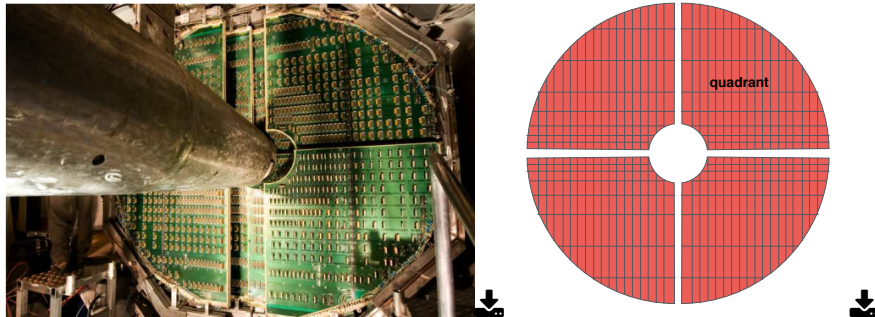


Figure 3.12: A picture of a chamber in station 2 (left) and a schematic view of the quadrant structure (right).

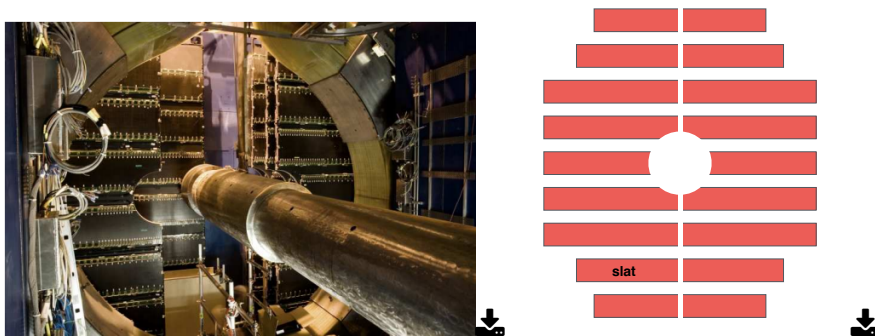


Figure 3.13: A picture of a chamber in station 4 (left) and a schematic view of the slat structure (right).

Each MWPC, schematized in Figure 3.14, consists of a central anode plane with wires equally spaced parallel to the y -axis and sandwiched between two cathode planes with different segmentation. The wires have a high voltage of 1600-1650 V, while the cathode planes are grounded. This configuration generates an electric field with its maximum value at the wire surface. The volume between the two cathodes planes is filled with a gas mixture of Argon (80%) and CO_2 (20%).

When a charged particle traverses the gaseous medium, it ionises the gas and liberates electrons which are then drifted by the electric field to the closest anode wire where they generate an avalanche of secondary electrons. This results in

an ion-cloud that induces a charge distribution on the cathode pads close to the position of the avalanche. The information from the two cathodes are used to provide bi-dimensional (x and y) hit position. The third dimension (z) is provided by the position of the chamber.

The granularity of the chambers is constrained by the particle multiplicity and by the required resolution ⁴. The multiplicity is highest in the region of the first station close to the beam line where cathode pads as small as $4.2 \times 6.3 \text{ mm}^2$ are used. Since the hit density decreases with the distance from the beam line, larger pads are used at larger radii.

Finally, the multiple scattering of the muons in the chambers is minimized by using low-Z materials (e.g. carbon fibre) resulting in a chamber thickness that corresponds to about $0.03 X_0$.

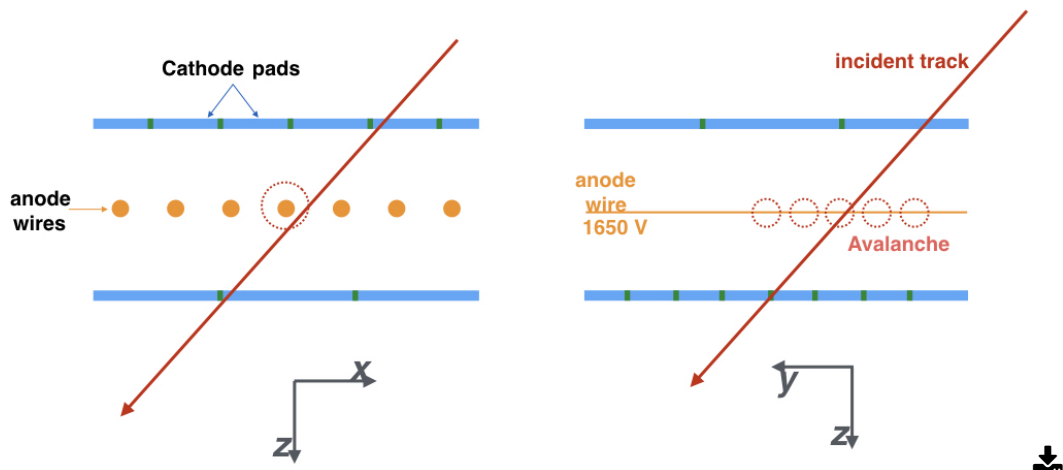


Figure 3.14: The layout and working principle of a MWPC viewed in two planes. Figure is adapted from [119].

3.2.3.4 Trigger system

To reduce the probability of triggering on events where there are no muon candidates from quarkonia, heavy-flavor or electroweak bosons decays, the muon

⁴This was mainly driven by the mass resolution needed to separate the bottomonia (Y) states: $100 \text{ MeV}/c^2$ at $10 \text{ GeV}/c^2$.

spectrometer is equipped by a trigger system. It consists of four planes of 18 Resistive Plate Chambers (RPC) arranged in two stations (MT1 and MT2), and located after the iron muon filter at $z = -16$ m and $z = -17$ m respectively. A RPC, schematized in Figure 3.15, is made up of high resistivity Bakelite electrodes separated by a gas gap of 2 mm. The outside faces of the plates are painted with graphite, one is connected to high voltage and the other is grounded. When a charged particle crosses the gas, it causes an avalanche of secondary electrons. The signals are read-out on both surfaces by orthogonal pick-up strips, providing bi-dimensional position information of the crossing particle.

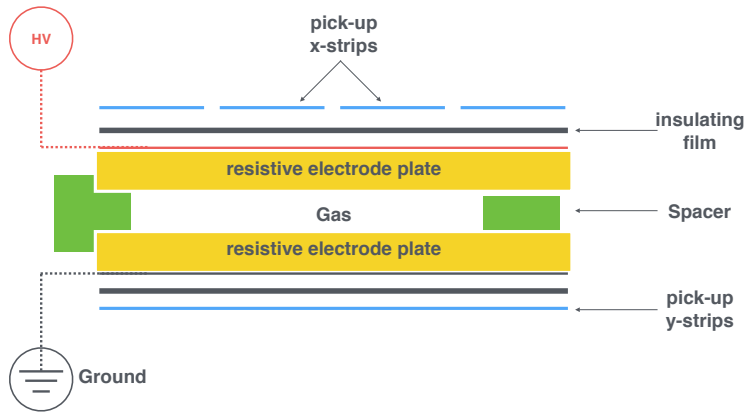


Figure 3.15: The structure of a RPC used in the muon trigger system. Figure is adapted from [103].

The trigger decision is based on the measured particle p_T since muons from pions and kaons are expected to be dominant at low p_T . The p_T cut is applied as shown in Figure 3.16 and described in the following. A muon produced at the interaction point is bent by the dipole magnetic field and crosses the trigger stations MT1 and MT2 in (x_1, y_1) and (x_2, y_2) respectively. The deviation $\delta y = y_2 - y_\infty$ is the distance between the y -coordinate of the detected muon and the hypothetical crossing point of a straight track crossing the first station at the same coordinate y_1 . The straight line corresponds to the muon if it has an infinite transverse momentum. The p_T cut can be applied through a cut on δy which is inverse proportional to the muon p_T . The sign of δy can also provide the sign of the muon.

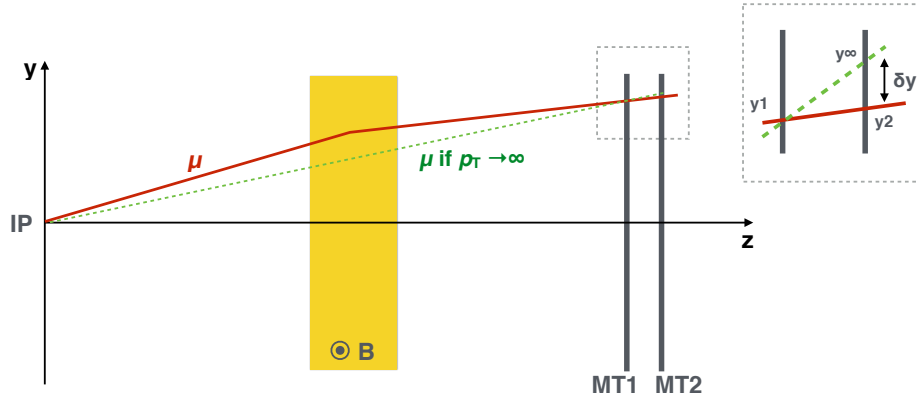


Figure 3.16: A sketch of the working principle of the muon trigger algorithm. The region inside the dotted square is zoomed-in on the top right of the figure. Figure is adapted from [122].

3.2.4 ALICE trigger system

ALICE has a three-layer trigger architecture called Central Trigger Processor (CTP) and completed by a High Level trigger (HLT).

The CTP is a hardware trigger system that combines inputs from different detectors to decide if an event is accepted for a given sub-detector and consequently read-out and written to disk. Mostly, the trigger inputs are fast calculations performed in the sub-detectors themselves. An example of such calculations is the one used to apply the muon p_T cut by the muon trigger system (Section 3.2.3.4).

Due to the difference in the response time of the different sub-detectors, an event is read-out in three trigger levels. The lowest one, called L0, is issued to the CTP and delivered to the corresponding sub-detectors after $1.2 \mu s$. A L0 trigger can be sent by V0, T0, SPD, EMCAL, PHOS and MTR. The second level trigger, called L1, is received by the sub-detector after $6.5 \mu s$. On this level, the CTP picks up input from EMCAL, TRD, and ZDC. The final level trigger, L2, is delivered after $100 \mu s$, upon completion of the drift time in the TPC. The event is finally stored only after

L2 trigger.

A trigger class is defined by a combination of different trigger inputs via logical connectors (AND, OR). As an example, the minimum bias trigger class, is defined as the logical "AND" of input signals from the two V0 arrays, V0-A and V0-C. For each trigger class, the rate is defined as the number of events that fulfill the trigger condition in a unit of time. Knowing the limitation on the total recording rate and since the rates of the different classes are very different, down scaling factors can be applied to the different trigger classes individually.

The HLT is a pure software trigger. It allows the implementation of sophisticated logic for the triggering by processing read-out data from the sub-detectors. The main tasks of the HLT are:

- To accept or reject events based on detailed online analysis.
- To select a physics region of interest within the event by performing only a partial readout.
- To reduce the event size without a loss of physics information by applying compression algorithms on the accepted and selected data.

3.2.5 Data Reconstruction

Recorded events during data taking are raw and need several cycles of reconstruction in order to be ready for physics analyses. Each reconstruction cycle is called a pass and it is done offline using the Alice offline framework. The results of a reconstruction pass are stored in Event Summary Data (ESD) files. These files includes essentially all the information from the different sub-detectors and they are ready to be used for physics analyses. After this step, the quality assurance (QA) analysis (discussed in the next section) takes place. Once the ESDs are produced, they can be filtered into Analysis Object Data (AOD) which contain less information since they are dedicated for specific analyses.

3.3 Data Quality Assurance

For each sub-detector and in every reconstruction pass, the Quality Assurance (QA) is done by looking at the trend of some observables and comparing their values to a set of reference parameters. The main tasks of the QA are:

- Spot if there are problems in the sub-detector that were not spotted during the data taking. Also check if there are no problems during data reconstruction.
- Investigate the severity of spotted problems and whether an affected run⁵ should be rejected or not. Some problems can be solved by redoing the data reconstruction. For this purpose, one must know the exact amount of affected events, regarding the non negligible resources needed for new reconstructions.
- Check the QA for other sub-detectors and investigate if there are problems that can also affect the analyses based on the investigated sub-detector. For example, in Pb-Pb collisions, informations from the ZDC detector are used in the physics selection of events. Therefore, if the ZDC has a problem during a given run, the full run needs to be rejected even if other sub-detectors work well.
- Provide lists of good runs for physics analyses.

3.3.1 Data Quality Assurance for the muon spectrometer

In the following, some observables that are used for the QA of the muon spectrometer are presented.

In order to visualize the performance of the muon trigger system, the muon trigger efficiency is monitored in the QA. The total efficiency is defined as the ratio between the number of triggerable tracks and the total number of tracks that cross the muon trigger. Each chamber has two read-out planes (in the bending and the non bending direction), a track is said to be triggerable if it fires at least three of

⁵The basic unit of data taking is known as a "run" and identified by its run number.

the four trigger chambers on both planes. An example of this efficiency is shown in Figure 3.17 left. This example corresponds to a p-Pb collisions data taking period in 2016. It shows an overall very good trigger efficiency (98-99 %) during the whole data taking period. Some bins in the distribution are empty and they correspond to runs where the muon spectrometer does not participate in the data taking. It is also shown a run with an efficiency exactly equal to unity caused by a wrong CTP configuration.

In addition to the total efficiency, the efficiency of each trigger chamber is also monitored in the QA. In case of spotted problems, this helps to understand its source. An example of the efficiency for the first trigger chamber is shown in Figure 3.17 right. The efficiency of a given chamber is calculated using tracks that fired all the other chambers in both read-out planes. In this plot, one can see an increase of the chamber efficiency with time within the same "fill" (corresponds to one LHC injection). This behavior was seen in the different data-taking periods and it is due to the fact that amount of tracks coming from beam-gas interaction decreases with time. The efficiency plotted in Figure 3.17 is calculated using tracks reconstructed in the muon trigger. However, when this efficiency is calculated using tracks reconstructed in the muon tracking system, this time-dependence of the efficiency is not seen.

The plot of Figure 3.18 shows the evolution of the track number per event as a function of run number for different type of tracks. The number of tracks per event for "all tracks" and "tracking only tracks" which represents the non triggerable tracks, decrease with time while the two others, "matched tracks" which are seen by both the tracker and the trigger and used in physics analysis, and "trigger only tracks" are more constant. This can be explained by the contribution from pile-up events. An event is qualified as pile-up when multiple interactions take place in one unit of detector read-out time. This can be either in-bunch pile-up where the interactions correspond to the same LHC bunch crossing, or out-of-bunch pile-up where they correspond to two or more bunch crossings. The muon trigger is able to distinguish between events from different bunch crossing which means that it is only sensitive to the in-bunch pile-up. However the muon tracker alone is sensitive to both types of pile-up which can explain the decreasing number of tracks

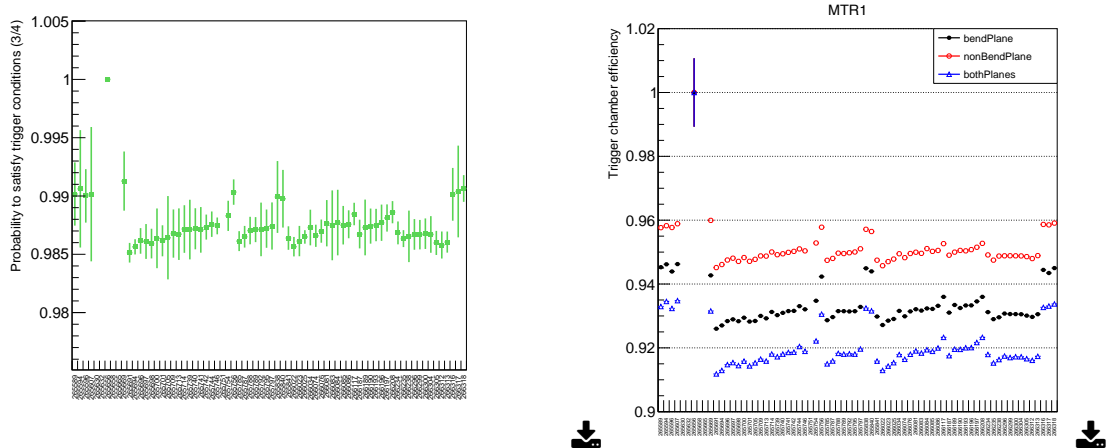


Figure 3.17: Muon trigger efficiency plots used in the QA of the 2016 p-Pb period. The left panel represents the total efficiency as a function of the run number. The right panel is the trigger efficiency of the first chamber.

reconstructed in it. Problems that can lead to a variation of the tracking or trigger efficiency can be reflected on the trend and the values of these plots.

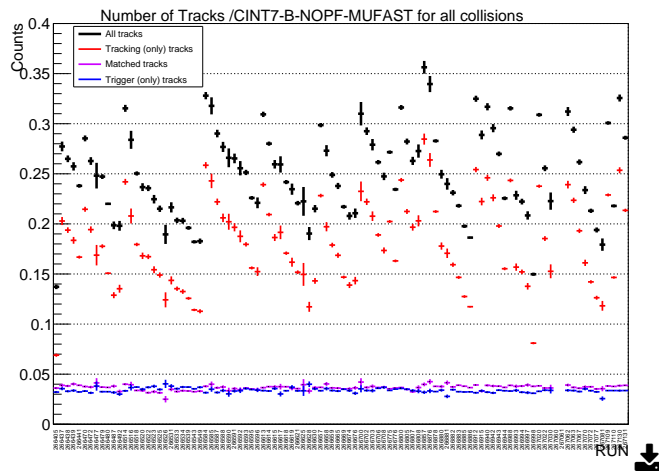


Figure 3.18: The number of track in a minimum bias event for different track types. The plot is used for the QA of the 2016 Pb-p period.

A QA plot which is more relevant for spotting hardware problems, is shown in Figure 3.19. It represents the average number of clusters reconstructed for each

tracking chamber, per track. In the ideal conditions of a tracking chamber, this average number is equal to unity. However the efficiency of a tracking chamber decreases leading to smaller number of reconstructed clusters when a part of the chamber is excluded due to hardware issue (e.g high voltage trips).

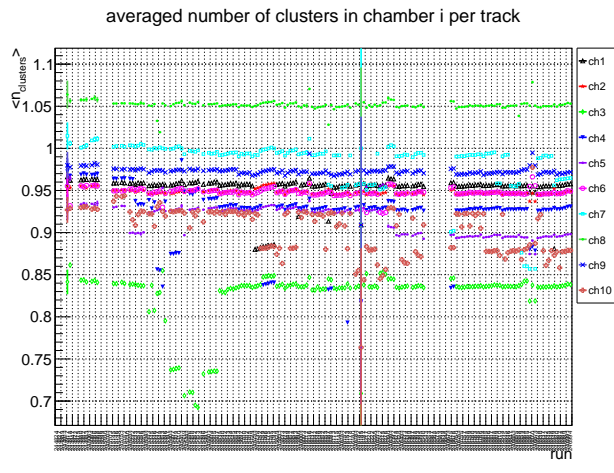


Figure 3.19: The average number of clusters in the different tracking chamber per track. The plot is used for the QA of the 2015 Pb-Pb period.

Figure 3.20 shows the fraction of accepted CMUL7-B⁶ events after the final QA check in all the data taking periods of the Run-2 of the LHC. Rejected events do not include the ones from runs having problems during the data taking and omitted before the QA check.

In addition to the checks on the reconstructed data, the QA procedure is also done on Monte-Carlo simulations. The main task, in this case, is to validate that the different plots and parameters values are reproduced from the real data.

⁶A CMUL7 trigger class is a minimum bias events where at least two opposite-charge muons fire the muon trigger chambers. More details on this point are given in the next chapter.

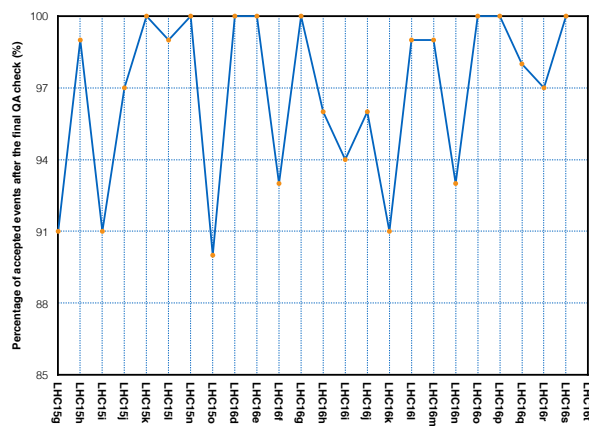


Figure 3.20: The percentage of accepted CMUL7 events after the QA check during the data taking periods of the run-2 of the LHC.

Z-BOSON AND J/ψ PRODUCTION ANALYSES

In the previous chapters, motivations for the experimental measurements of two hard probes, the Z-boson and the J/ψ meson, in heavy-ion collisions were given.

In this chapter, the steps of the analyses done in order to make such measurements are presented. After introducing the analyzed data samples, the strategy for calculating the corresponding integrated luminosities is described. This is followed by a description of the different muons and dimuons selections performed in order to improve the purity of the data samples, before presenting the Z-boson and J/ψ signal extraction procedures. Finally, the acceptance and the efficiency of the detector are introduced and the method used to calculate them in the current analyses is explained. In all these steps, a discussion on the corresponding uncertainties is done.

4.1 Introduction

The physics results presented in the next chapters correspond to three kinds of observables: yields, cross sections, and nuclear modification factors. Experimentally, for a given process "x" the production yield (Y_x) in a given collision system is given

by:

$$Y_x = \frac{N_x}{A\varepsilon(x) \times N_{MB}}, \quad (4.1)$$

where N_x is the number of observed signals, $A\varepsilon(x)$ is the Acceptance times Efficiency of the detector in measuring the process x and N_{MB} is the number of analyzed minimum bias events.

By using the integrated luminosity (L_{int}) instead of N_{MB} for normalization, the production cross section can be expressed as:

$$\sigma_x = \frac{N_x}{A\varepsilon(x) \times L_{int}}. \quad (4.2)$$

In a nuclear collision A-B, the nuclear modification factor of a given process ($R_{AB}(x)$) is defined as its yield in the given collision system divided by its production cross section in proton-proton (pp) collisions, obtained at the same energy, and the nuclear overlap function T_{AB} which is a normalization factor that quantifies the average nucleon-nucleon luminosity per A-B collision:

$$R_{AB}(x) = \frac{Y_x^{AB}}{T_{AB} \times \sigma_x^{pp}}. \quad (4.3)$$

In the following, the steps performed in order to obtain the different introduced terms in the Z-boson and J/ψ analyses are presented.

4.2 Data samples and event selection

For the Z-boson production, two sets of results will be presented in chapter 5, in p-Pb collisions and in Pb-Pb collisions, both at $\sqrt{s_{NN}} = 5.02 \text{ TeV}$. In chapter 6, the presented J/ψ production results correspond to Pb-Pb collisions at $\sqrt{s_{NN}} = 5.02 \text{ TeV}$.

Because of the asymmetry of p-Pb collisions, the rapidity of the center-of-mass (y_{cms}) is shifted with respect to the laboratory frame rapidity (y_{lab}). In a collision of two different beams with charges Z_1, Z_2 and atomic numbers A_1, A_2 , the shift in rapidity is given by:

$$\Delta y = \frac{1}{2} \ln\left(\frac{Z_1 A_2}{Z_2 A_1}\right), \quad (4.4)$$

thus $\Delta y = \pm 0.456$ in the case of p-Pb collisions. The sign of Δy is defined by the direction of the proton beam. By convention, the positive (negative) one corresponds to the case when the proton (Pb) beam is going toward the muon spectrometer and will be referred to by p-going (Pb-going) in the following. The directions of the beams with respect to ALICE in the two configurations are schematized in Figure 4.1.

In January-February 2013, two data samples were collected in the p-going configuration (LHC13d and LHC13e)¹ while one (LHC13f) was collected in the Pb-going configuration. The difference between the two p-going periods is the polarity of the dipole magnet. Since this has no effect on the Z-boson production analysis, the two periods are considered as a one data sample.

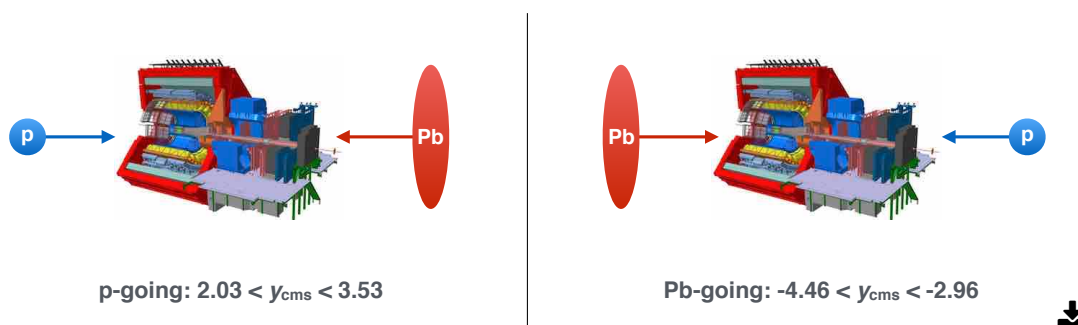


Figure 4.1: The two possible configurations of the proton and Pb beams with respect to ALICE in p-Pb collisions. The center-of-mass rapidity covered by the muon spectrometer in each configuration is indicated.

The Pb-Pb collisions at $\sqrt{s_{NN}} = 5.02 \text{ TeV}$ data sample was collected in November-December 2015 (LHC15o).

As a reminder from chapter 3, a trigger class is the logical combination of different trigger inputs. According to the condition on the triggered muons, four type of classes are defined:

- **CMSL7-B**: single muon with low- p_T trigger cut + MB trigger. In this case, at least one muon hits the trigger and the p_T trigger cut can be 0.5 or 1 GeV/c.

¹In ALICE, the name of each data taking period starts with "LHC" followed by the a number given by the year of data taking and a letter.

- **CMSH7-B**: single muon with high p_T trigger cut + MB trigger. Similar to CMSL7 but with higher p_T trigger cut set to 4.2 GeV/c.
- **CMUU7-B**: opposite-charge dimuon with low- p_T trigger cut + MB trigger. In this case, two low- p_T muons with opposite electric charges hit the trigger.
- **CMLL7-B**: same-charge dimuon with low- p_T trigger cut + MB trigger. In this case, two low- p_T muons with same electric charges hit the trigger.

In the listed trigger classes, the MB trigger is defined as the logical "AND" of two trigger inputs from V0-A and V0-C. Note that the (-B) is the ALICE nomenclature for a "beam-beam" collision.

Depending on the physics, one or several trigger classes can be used in the data analysis. In particular, for the Z-boson and J/ψ analyses which are based on dimuon reconstruction, the CMUL7 class is selected.

The first offline selection is known as Physics-Selection (PS). For the defined trigger classes, it rejects background based on information from the two V0 detectors and on the ZDC timing [123]. In the Pb-Pb collisions analyses, an additional offline cut on the collision centrality is also applied. The centrality is estimated by fitting the V0 amplitude by a MC Glauber [124]. During the 2015 data taking period, the MB trigger was fully efficient up to 90% centrality. Beyond that, a cut is applied in order to reject residual contamination from electromagnetic processes.

Table 4.1 summarizes the analyzed number of CMUL7-B events in the studied data samples, before and after applying the physics selection.

Data sample	p-Pb (p-going)	Pb-p (Pb-going)	Pb-Pb
Total CMUL7-B events	9.4M	21.4M	142.3M
PS CMUL7-B events	9.2M	20.9M	126.9M

Table 4.1: Total and physics selected (PS) CMUL7-B events in the different data samples of p-Pb and Pb-Pb collisions at $\sqrt{s_{NN}} = 5.02$ TeV. For LHC15o, the centrality selection (< 90%) is also included in the second row.

4.3 Event normalization

4.3.1 Minimum bias normalization

The fact that the analyses are based on events that already contain two opposite-charge muons introduce a bias in the data sample. This bias should be corrected for in order to fairly compare the results of a given analysis with others in different data samples or obtained by other experiments. To this purpose, for a set of events based on a given trigger selection, one needs to obtain the equivalent number of MB collisions where there is no specific selection of the final state.

For each run " i ", the number of MB collisions (N_{MB}^i) is given in terms of the number of CMUL7 triggers (N_{CMUL7}^i) by:

$$N_{MB}^i = F_{\text{norm}}^i \times N_{CMUL7}^i \quad (4.5)$$

The normalization factor F_{norm}^i can be calculated in two "different" methods.

- Using an **offline method** where the number of the offline recorded trigger classes in each event are used together with information on the CTP trigger inputs. For the run " i ", the normalization factor $F_{\text{norm}}^{\text{offline},i}$ is defined by:

$$F_{\text{norm}}^{\text{offline},i} = \frac{N_{MB}^i}{N_{MB\&0MUL}^i}, \quad (4.6)$$

where the nominator and the denominator represent respectively the total number of MB events and their number where at least one opposite-charge dimuon trigger input (0MUL) is fired.

In order to improve the statistical precision of this method, a two-steps normalization approach can be followed using the information on the single muon trigger input (0MSL). The equation 4.6 can be re-written then as:

$$F_{\text{norm}}^{\text{offline},i} = \frac{N_{MB}^i}{N_{MB\&0MSL}^i} \times \frac{N_{CMSL7}^i}{N_{CMSL\&0MUL}^i}, \quad (4.7)$$

where N_{CMSL7}^i is the number of CMSL7 events, and $N_{MB\&0MSL}^i$ ($N_{CMSL\&0MUL}^i$) is the number of MB (CMSL7) events where at least one single muon

(opposite-charge dimuon) trigger input is fired. This way is statistically better due to the fact that the number of $0MSL$ inputs is larger than the one of $0MUL$ in a MB event.

- Using an **online method** where the information of L0b counters (scalers) are used. The L0b are the L0 inputs sent from the triggers to the CTP and the index "b" stands for "before the CTP". Since the physics selection is not yet applied at this stage, one has to correct by hand for the purity of the data sample. The online normalization factor $F_{norm}^{online,i}$ is then defined as:

$$F_{norm}^{online,i} = \frac{L0b_{MB}^i \times P_{MB}^i}{L0b_{MUL}^i \times P_{MUL}^i}, \quad (4.8)$$

where $L0b_{MB}$ and $L0b_{MUL}$ are the number of counters recorded for minimum-bias and opposite-charge muon triggers respectively. P_{MB} and P_{MUL} are the purity factors of MB and CMUL7 events respectively. They are calculated as the fraction of events that satisfy the physics selection in the corresponding trigger class.

The next step in the minimum-bias normalization is to account for the pile-up effect. As explained in chapter 3, a pile-up event is when multiple interactions take place in one unit of detector read-out time. In the run "i", the pile-up correction factor can be estimated by:

$$F_{pile-up}^i = \frac{\mu^i}{1 - e^{-\mu^i}}, \quad (4.9)$$

where μ is the mean number of collisions per bunch crossing, and given by:

$$\mu^i = -\ln\left(1 - \frac{P_{MB}^i \times L0bRate_{MB}^i}{n_b^i \times f_{LHC}}\right), \quad (4.10)$$

where $L0bRate_{MB}$ is the number of minimum-bias events recorded by the L0b counter per data taking time, n_b is the number of colliding bunches and $f_{LHC} = 11245$ Hz is the revolution frequency of the LHC.

In the two data samples of p-Pb collisions at $\sqrt{s_{NN}} = 5.02$ TeV, $F_{pile-up}^i$ vary from 1.01 to 1.03, while in Pb-Pb collisions at $\sqrt{s_{NN}} = 5.02$ TeV the pile-up effect is

smaller and $F_{pile-up}^i$ was less than 1.005.

$F_{pile-up}^i$ is then taken into account as multiplicative factor in the equations 4.7 and 4.8.

The run number dependence of the minimum-bias normalization factor $F_{norm}^{offline}$ is shown for p-Pb and Pb-Pb collisions at $\sqrt{s_{NN}} = 5.02\text{TeV}$ in Figure 4.2 and Figure 4.3 respectively. For each method (offline and online), the final F_{norm} for a data taking period with N runs is obtained as the weighted average of the run-by-run ones:

$$F_{norm} = \frac{\sum_{i=1}^N F_{norm}^i \times N_{CMUL7}^i}{\sum_{i=1}^N N_{CMUL7}^i} \quad (4.11)$$

The F_{norm} values corresponding to the two methods are averaged and the difference between them is taken as a systematic uncertainty. Table 4.2 summarizes the numerical values for the three studied data samples. In p-Pb collisions at $\sqrt{s_{NN}} = 5.02\text{TeV}$, the F_{norm} in the Pb-going data sample is about twice the one in the p-going sample. This is because the muon spectrometer in the former case measures muons on the Pb fragmentation side which increases the probability to observe a muon or dimuon trigger in a MB event.

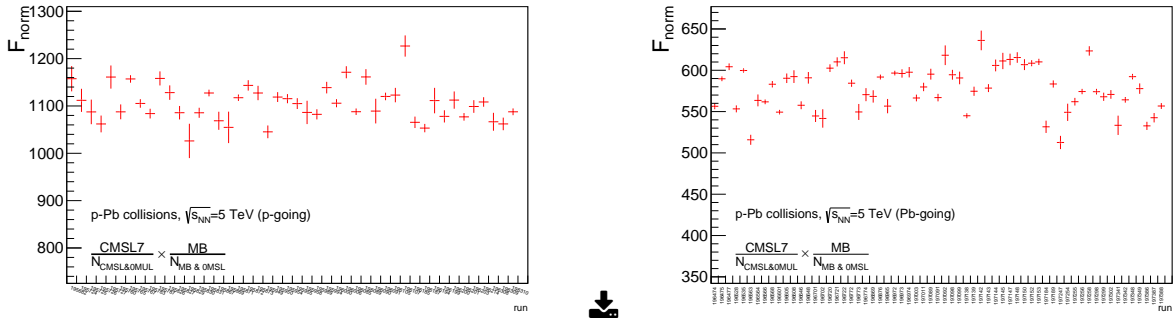


Figure 4.2: The minimum-bias normalization factor $F_{norm}^{offline}$ as a function of the run number in p-Pb collisions at $\sqrt{s_{NN}} = 5.02\text{TeV}$ for the p-going (top) and Pb-going (bottom) data samples.

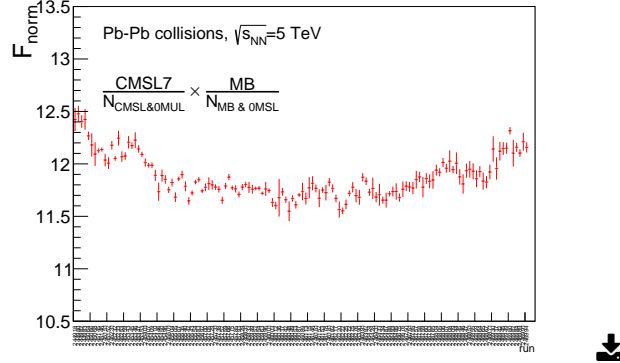


Figure 4.3: The minimum-bias normalization factor $F_{\text{norm}}^{\text{offline}}$ as a function of the run number in Pb-Pb collisions at $\sqrt{s_{\text{NN}}} = 5.02 \text{ TeV}$.

Data sample	p-Pb (p-going)	Pb-p (Pb-going)	Pb-Pb
$F_{\text{norm}}^{\text{offline}}$	1124.00	588.52	11.85
$F_{\text{norm}}^{\text{online}}$	1129.33	589.48	11.84
Average	1129.08	589.31	11.84
Systematic	0.5%	0.2%	0.5%

Table 4.2: The values of the minimum-bias normalization factor F_{norm} using two methods (offline and online) and their average in three data samples of p-Pb and Pb-Pb collisions at $\sqrt{s_{\text{NN}}} = 5.02 \text{ TeV}$.

4.3.2 Luminosity

In order to determine the production cross section of a given process, the integrated luminosity of the analyzed data sample must be known.

The measurement of the rate and cross section of a reference process allows the determination of the cross section of other processes knowing their rates. In ALICE (and in the other LHC experiments), a cross section of a reference process can be measured using the van der Meer (vdM) scan method [125]. In this method, the trigger rate of the reference process is monitored while changing the transverse separation between the two LHC beams. This provides information on the spatial convolution of the two colliding beams. Knowing the beam intensities, this can be related to the process production cross section. If the reference process is defined as a trigger signal detected by the two V0 detectors, the corresponding cross section

is the ALICE MB one (σ_{MB}).

During each new LHC configuration (a new collision system or center-of-mass energy) a vdM scan is carried out at the LHC. For the p-Pb data taking periods in 2013, two scans were done in the two beam configurations (p-going and Pb-going) [126]. The integrated luminosity in a studied data sample with a number of minimum bias events N_{MB} , is then given by:

$$L_{\text{int}} = \frac{N_{\text{MB}}}{\sigma_{\text{MB}}} \quad (4.12)$$

Table 4.3 summarizes the values of the measured MB cross sections and the collected integrated luminosities for the two data samples of p-Pb collisions at $\sqrt{s_{\text{NN}}} = 5.02 \text{ TeV}$.

Data sample	p-going	Pb-going
σ_{MB} (b)	2.09 ± 0.07	2.12 ± 0.06
L_{int} (nb^{-1})	5.03 ± 0.18	5.81 ± 0.20

Table 4.3: The ALICE MB cross sections and the collected integrated luminosities in two data samples of p-Pb collisions at $\sqrt{s_{\text{NN}}} = 5.02 \text{ TeV}$. The quoted uncertainties are systematic.

4.4 Single muon and dimuon selections

In the muon spectrometer, the background rejection is done mainly thanks to the front absorber which stops most of the hadrons entering the acceptance of the spectrometer. The front absorber also sets a minimum momentum of 4 GeV/c on tracks traversing the whole system. However, additional offline selections on the single muon tracks and the opposite-charge dimuons are needed in order to improve the purity of the analyzed data samples. In the following, the different selections are described. Unless specifying otherwise, the selections are common between the Z-boson and the J/ψ analyses.

- **A selection on the acceptance:** the geometrical acceptance of the different components of the muon spectrometer is $-4 < \eta < -2.5$. Tracks that are

reconstructed outside this window are rejected. An additional selection on the rapidity of the muon pair is also applied in order to define the acceptance of the measurement: $2.5 < y_{\mu\mu} < 4$.

- **Matched tracks:** a track candidate in the tracking system is only considered for physics analyses if it matches a track reconstructed in the trigger system.
- **Selection on the track's polar angle at the end of the front absorber:** this angle (θ_{abs}) is shown in Figure 4.4. The selection $2^\circ < \theta_{abs} < 10^\circ$ assures that the track does not traverse the part of the front absorber made entirely of high-Z materials which causes a large amount of Coulomb multiple scattering.
- **A selection on the $p \times DCA$ within 6σ :** where p is the total momentum of the track and the Distance Closest Approach (DCA) is the distance between the primary vertex and the straight extrapolation of the track exiting the front absorber (i.e. if exhibits no multiple scattering) as indicated in Figure 4.4. This selection rejects beam-induced background and particles produced in the front absorber.
- **A cut on the transverse momentum of the single muons ($p_T(\mu) > 20$ GeV/c):** this selection is only applied in the Z-boson analyses. With a small effect on the signal, it rejects most of the muon decay products of heavy flavour and quarkonia.

Table 4.4 shows the effect of the different selections on the number of opposite-charge dimuons for the three studied data samples. In Pb-Pb collisions at $\sqrt{s_{NN}} = 5.02$ TeV, the data sample is split in three centrality intervals.

4.5 Signal extraction

A common aspect of the Z-boson and the J/ψ is that they are both resonance particles. A resonance is characterized by a production peak at a particular energy that defines the pole mass of the particle. The two resonances share also the dimuon

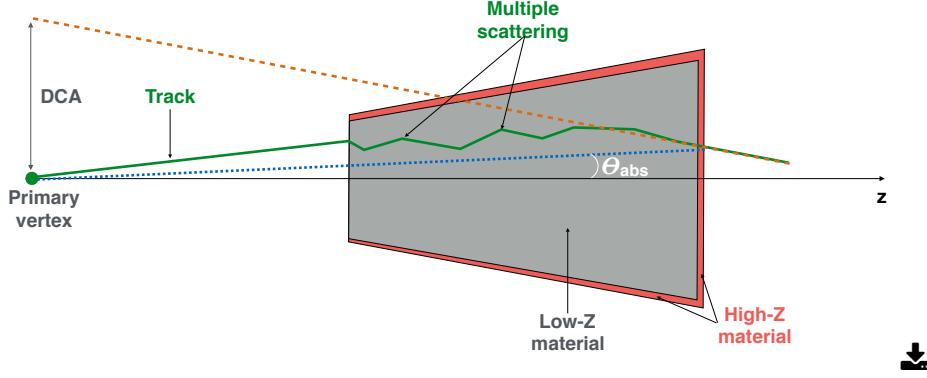


Figure 4.4: The path of a muon track through the front absorber of the muon spectrometer. The DCA and the θ_{abs} of the track are indicated.

Data sample	p-Pb (p-going)	Pb-p (Pb-going)	Pb-Pb (0-20%)	Pb-Pb (20-40%)	Pb-Pb (40-90%)
Total dimuons	$3.40 \cdot 10^6$	$5.87 \cdot 10^6$	$2.98 \cdot 10^9$	$1.83 \cdot 10^8$	$7.03 \cdot 10^6$
$2.5 < y_{\mu\mu} < 4$	$3.35 \cdot 10^6$	$5.67 \cdot 10^6$	$2.84 \cdot 10^9$	$1.56 \cdot 10^8$	$6.31 \cdot 10^6$
Matched tracks	$2.71 \cdot 10^6$	$4.02 \cdot 10^6$	$6.89 \cdot 10^7$	$7.39 \cdot 10^6$	$9.92 \cdot 10^4$
$-4 < \eta < -2.5$	$2.42 \cdot 10^6$	$3.55 \cdot 10^6$	$4.69 \cdot 10^7$	$6.41 \cdot 10^6$	$8.93 \cdot 10^4$
$2^\circ < \theta_{abs} < 10^\circ$	$2.42 \cdot 10^6$	$3.53 \cdot 10^6$	$4.57 \cdot 10^7$	$6.36 \cdot 10^6$	$8.90 \cdot 10^4$
$p \times DCA$ cut	$2.41 \cdot 10^6$	$3.51 \cdot 10^6$	$4.36 \cdot 10^7$	$6.30 \cdot 10^6$	$8.86 \cdot 10^4$
$p_T(\mu) > 20 \text{ GeV}/c$	24	2	53	25	9

Table 4.4: The cumulative decrease of the number of opposite-charge dimuon after applying the different selections on the single muon and the dimuon level in p-Pb and Pb-Pb collisions at $\sqrt{s_{NN}} = 5.02 \text{ TeV}$.

decay channel. Therefore, in a given opposite-charge dimuon invariant mass spectrum, the Z-boson and the J/ψ appear as peaks at around $M_{\mu\mu} = 91 \text{ GeV}/c^2$ and $3.1 \text{ GeV}/c^2$ respectively.

The muon spectrometer is able to reconstruct the following resonances at different invariant mass in Pb-Pb collisions:

- Low mass resonances (ρ , ω , ϕ) in the invariant mass region $0.5 < M_{\mu\mu} < 1.1 \text{ GeV}/c^2$.
- The two charmonium states J/ψ and $\psi(2S)$ in $2.8 < M_{\mu\mu} < 4 \text{ GeV}/c^2$.
- The three bottomonium states ($\Upsilon(1s)$, $\Upsilon(2s)$, $\Upsilon(3s)$) in $9 < M_{\mu\mu} < 11 \text{ GeV}/c^2$.

- The Z-boson in $60 < M_{\mu\mu} < 120 \text{ GeV}/c^2$.

A typical opposite-charge dimuon invariant mass distribution in Pb-Pb collisions at $\sqrt{s_{\text{NN}}} = 5.02 \text{ TeV}$ is shown in Figure 4.5. Due to the extended scale of the plot and the large background contribution, some of the mentioned resonances are not visually seen in this example.

in addition to the different resonances, several continuum regions are identified:

- At low mass ($M_{\mu\mu} < 2 \text{ GeV}/c^2$): uncorrelated muon pairs that are dominated by muon decay products of pions and Kaons.
- The invariant mass regions $2 < M_{\mu\mu} < 5 \text{ GeV}/c^2$ and $5 < M_{\mu\mu} < 12 \text{ GeV}/c^2$ are dominated by uncorrelated muon pairs from semi-leptonic decay of open charm and beauty hadrons respectively.
- In the invariant mass region $12 < M_{\mu\mu} < 60 \text{ GeV}/c^2$, the contribution of correlated opposite-charge dimuons from Drell-Yan decay is dominant.

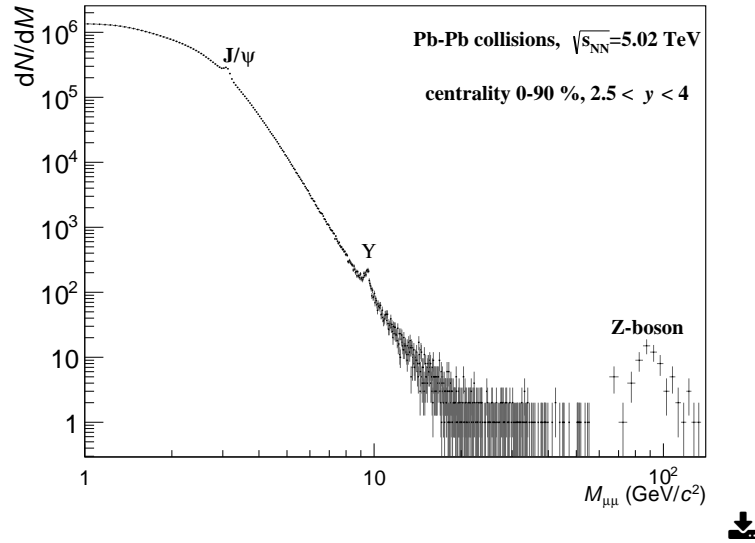


Figure 4.5: Opposite-charge dimuon invariant mass distribution in Pb-Pb collisions at $\sqrt{s_{\text{NN}}} = 5.02 \text{ TeV}$. The distribution is obtained by applying all the selections on the single muon and muon pairs of section 4.4 except the one on the muon p_{T} ($p_{\text{T}} > 20 \text{ GeV}/c$).

In the following, the Z-boson and J/ψ signal extraction procedures will be discussed. The main difference between the two signals is the amount of background in their regions, in the Z-boson case, the background is almost negligible which is not the case for the J/ψ .

4.5.1 Z-boson signal extraction

In order to justify the Z-boson signal extraction procedure used in the following, the amount of background contribution in the signal region must be checked. As already mentioned, the peak in the opposite-charge dimuon invariant mass distribution is used to identify the Z-boson signal, therefore a background contribution is an opposite-charge dimuon with an invariant mass in the range $[60 - 120] \text{ GeV}/c^2$ where the muons are not coming from a direct Z-boson decay. The signal region ($[60 - 120] \text{ GeV}/c^2$) is chosen in order to remove as much as possible the interference with the DY contribution.

In the following, brief descriptions of the possible background sources and estimation of their contribution are presented:

- **(A) Heavy flavor:** a pair of muons coming from semi-leptonic decay of c or b hadrons, $D(B) \rightarrow X\mu\nu$ (Feynman diagram of Figure 4.6), can contribute to the dimuon invariant mass signal region. This contribution is estimated using MC simulation based on PYTHIA.6 generator [89]. $D(B) \rightarrow X\mu\nu$ samples are generated and normalized to their production cross section predicted by FONLL calculations [48] and to the integrated luminosity of a given data sample. Figure 4.7 shows the dimuon invariant mass distributions of the generated samples in p-Pb collisions at $\sqrt{s_{\text{NN}}} = 5.02 \text{ TeV}$. Only dimuons in the muon spectrometer acceptance ($2.5 < y < 4$) are kept. By applying a $20 \text{ GeV}/c$ p_{T} cut on the single muons (similar to the one applied in the Z-boson data analysis), the contribution in the signal region becomes negligible. Therefore, an upper limit on the contribution of heavy flavor semi-leptonic decay is set by lowering the muon p_{T} cut down to $10 \text{ GeV}/c$. In p-Pb collisions at $\sqrt{s_{\text{NN}}} = 5.02 \text{ TeV}$, this upper limit is 1% and 0.5% in the p-going and Pb-going data samples respectively. In Pb-Pb collisions at $\sqrt{s_{\text{NN}}} = 5.02 \text{ TeV}$, this upper

limit is expected to be smaller due to the hot medium effects such that the energy loss on the heavy flavor hadrons.

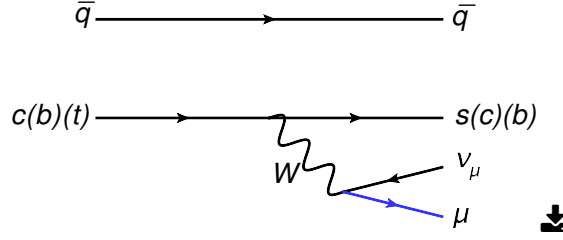


Figure 4.6: A Feynman diagram for the process of semi-leptonic decay of heavy hadrons.

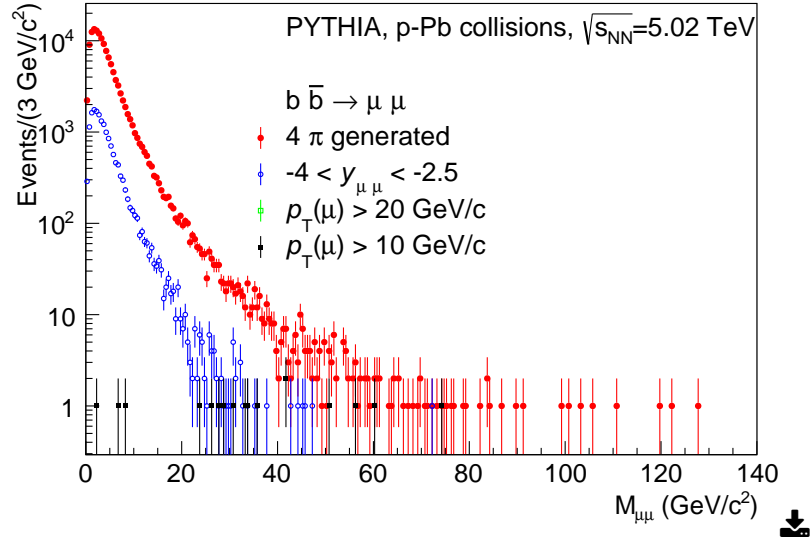


Figure 4.7: Invariant mass distributions of opposite-charge muon pairs from semileptonic decay of $b\bar{b}$ pairs at $\sqrt{s_{\text{NN}}} = 5.02 \text{ TeV}$ using PYTHIA.6. The different distributions correspond to the applying of different kinematic cuts.

- **(B)** $t\bar{t} \rightarrow \mu\mu$: another possible contribution to the background is when a pair of top quarks decay through the semi-leptonic channel to muons within the muon spectrometer acceptance. One can expect a small contribution from this source due to the corresponding dimuon rapidity distribution which is narrower than the one of dimuon from Z-boson decay. This means that going to forward rapidity regions (covered by the muon spectrometer), the $t\bar{t} \rightarrow \mu\mu$

background contribution becomes less important with respect to the signal one.

- **(C)** $Z \rightarrow \tau\tau \rightarrow \mu\mu$: a dimuon can be also obtained when a Z-boson decays to a τ pair which then decays into two muons and neutrinos. The branching ratios of the Z-boson decay to a pair of muons or a pair of τ leptons are similar, and the fraction of τ leptons decaying to muons is 0.174 [1].

The invariant mass distribution of muon pairs from this source is different from the one of those from direct Z-boson dimuon decay. This is due to the unreconstructed neutrinos taking a fraction of the energy away. The p_T cut on the single muon is more effective on this source than on the signal because the two muons are not produced back-to-back in the Z-boson rest frame in the case of double decay chain.

In order to estimate the contribution from **(B)** and **(C)**, MC simulations using the POWHEG generator [127] are used. POWHEG (Positive Weight Hardest Emission Generator) is a method for computations of different hard scattering processes at fixed next-to-leading order. The fragmentation of partons, the final state radiation, and the underlying events are simulated with a parton shower MC generator which is PYTHIA.6 [89] in this analysis. Figure 4.8 shows the dimuon invariant mass distributions that correspond to three generated MC samples, $Z/\gamma^* \rightarrow \mu\mu$, $Z/\gamma^* \rightarrow \tau\tau \rightarrow \mu\mu$, and $t\bar{t} \rightarrow \mu\mu$. The background contribution is then taken as the fraction of the two background sources to the signal one in the signal invariant mass region $[60-120] \text{ GeV}/c^2$ after applying the same muon and dimuon acceptance selections as in the data analysis. This amounts to less than 1% in both Pb-Pb and p-Pb collisions at $\sqrt{s_{NN}} = 5.02 \text{ TeV}$.

- **(D)** Uncorrelated background: muons that do not correspond the same physics process are said to be uncorrelated. Since the probabilities to obtain opposite-charge or same-charge muon pairs from this source are similar, a way to estimate the amount of uncorrelated opposite-charge dimuons is by using the rate of same-charge dimuons in the analyzed data sample.

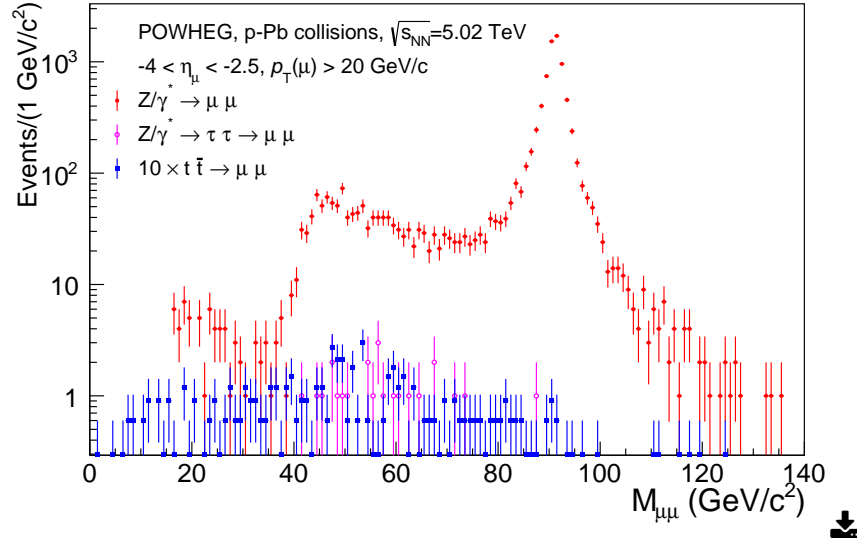


Figure 4.8: Invariant mass distributions of opposite-charge muon pairs from three processes at $\sqrt{s_{\text{NN}}} = 5.02 \text{ TeV}$, $Z/\gamma^* \rightarrow \mu\mu$, $Z/\gamma^* \rightarrow \tau\tau \rightarrow \mu\mu$, and $t\bar{t} \rightarrow \mu\mu$ using POWHEG generator.

The fact that the background contribution is negligible in the Z-boson signal region allows the signal extraction by simple counting of the opposite-charge muon pairs in the $60 - 120 \text{ GeV}/c^2$ invariant mass range that fulfill the selections of section 4.4.

The fraction of contribution from (A), (B), and (C) is assigned as a systematic uncertainty on the signal extraction results. The contribution from (D) is subtracted directly using the same-charge muon pairs distributions:

$$N_Z = N_{\mu^+\mu^-} - N_{\mu^{+(-)}\mu^{+(-)}}, \quad (4.13)$$

where N_Z is the number of Z-boson candidates and $N_{\mu^+\mu^-}$ and $N_{\mu^{+(-)}\mu^{+(-)}}$ are the number of opposite-charge and same-charge dimuons respectively.

4.5.1.1 Z-boson signal extraction in p-Pb collisions at $\sqrt{s_{\text{NN}}} = 5.02 \text{ TeV}$

In p-Pb collisions at $\sqrt{s_{\text{NN}}} = 5.02 \text{ TeV}$, the signal extraction is performed in the two center-of-mass rapidity ranges covered by the two data samples (p-going and Pb-going). The dimuon invariant mass distributions used to count the signal in the

two data samples are shown in Figure 4.9.

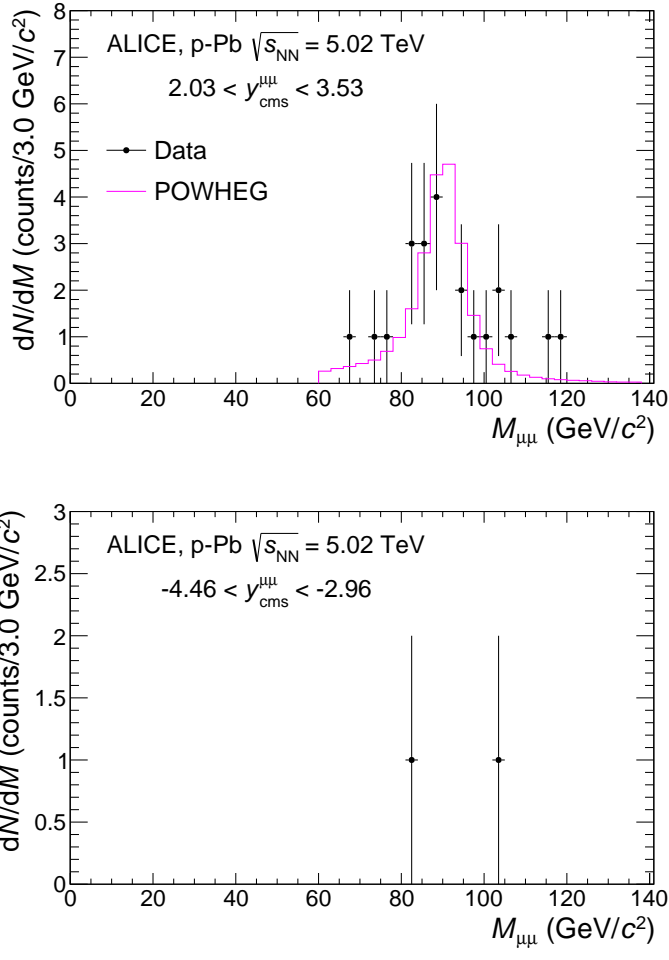


Figure 4.9: Opposite-charge dimuon invariant mass distribution in p-Pb collisions at $\sqrt{s_{NN}} = 5.02$ TeV for the p-going (top) and Pb-going (bottom) data samples. Figure taken from [128].

The number of the Z-boson candidates in the positive and negative y_{cms} regions is 22 ± 5 and 2 ± 1 respectively. The quoted uncertainties are statistical and obtained assuming that the number of Z-boson candidates follows a Poisson distribution. The smaller number of Z-boson candidates in the negative y_{cms} region is due to the smaller Acceptance \times Efficiency of the detector during the Pb-going data taking

period (see section 4.6) as well as the smaller Z-boson production cross section in this rapidity range with respect to the positive one (~ 10 times smaller).

In the positive y_{cms} region, the available statistics allows the comparison of the opposite-charge dimuon invariant mass distribution from data and Z/γ^* MC simulation obtained using POWHEG+PYTHIA. The simulated distribution reproduces well the data.

4.5.1.2 Z-boson signal extraction in Pb-Pb collisions at $\sqrt{s_{\text{NN}}} = 5.02 \text{ TeV}$

In Pb-Pb collisions at $\sqrt{s_{\text{NN}}} = 2.76 \text{ TeV}$, the integrated luminosity collected by ALICE was not sufficient to extract a Z-boson signal. This becomes possible with the collected data sample in Pb-Pb collisions at $\sqrt{s_{\text{NN}}} = 5.02 \text{ TeV}$ due to an increase of the integrated luminosity by a factor of 3 and also an increase of the Z-boson production cross section at the higher collision center-of-mass energy by about one order of magnitude.

Figure 4.10 shows the dimuon invariant mass distribution used for the signal extraction with the minimum selection on the collision centrality (centrality 0-90%). The number of Z-boson candidates is 64 ± 8 in the invariant mass range $60 - 120 \text{ GeV}/c^2$. For rapidity dependence study, the Z-boson signal in this centrality interval is also extracted in two rapidity ranges ($2.5 < y < 3$ and $3 < y < 4$).

With the available statistics, the data sample is split into two collision centrality intervals (0-20% and 20-90%). The corresponding opposite-charge dimuon invariant mass distributions are shown in Figure 4.11.

Table 4.5 summarizes the Z-boson signal extraction results in p-Pb and Pb-Pb collisions at $\sqrt{s_{\text{NN}}} = 5.02 \text{ TeV}$.

4.5.1.3 Additional background checks in Pb-Pb collisions at

$$\sqrt{s_{\text{NN}}} = 5.02 \text{ TeV}$$

Figure 4.10 shows that after applying the selections of section 4.4, the dimuon invariant mass distribution has contributions outside the signal region. One must assure that these contributions correspond to understood physics sources and are not coming from detector effects that can lead to similar contribution in the signal

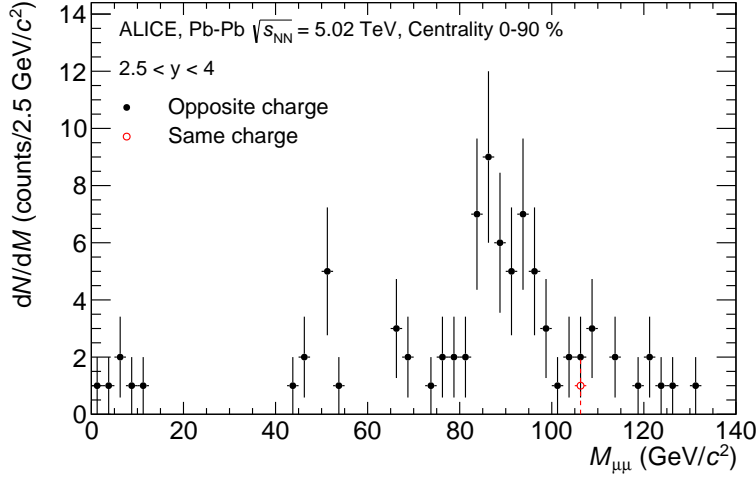


Figure 4.10: Dimuon invariant mass distribution in Pb-Pb collisions at $\sqrt{s_{NN}} = 5.02\text{TeV}$ in the 0-90% centrality interval.

rapidity/centrality range	$N_Z \pm (\text{stat})$
p-Pb collisions at $\sqrt{s_{NN}} = 5.02\text{TeV}$	
$2.03 < y_{\text{cms}} < 3.53$	22 ± 5
$-4.96 < y_{\text{cms}} < -2.46$	2 ± 1
Pb-Pb collisions at $\sqrt{s_{NN}} = 5.02\text{TeV}$	
0-90 % centrality, $2.5 < y < 4$	64 ± 8
0-90 % centrality, $2.5 < y < 3$	33 ± 6
0-90 % centrality, $3 < y < 4$	31 ± 6
0-20 % centrality, $2.5 < y < 4$	37 ± 6
20-90 % centrality, $2.5 < y < 4$	27 ± 5

Table 4.5: Number of Z-boson candidates alongside its statistical uncertainty in p-Pb and Pb-Pb collisions at $\sqrt{s_{NN}} = 5.02\text{TeV}$.

region.

A hypothesis to explain the contribution in the invariant mass region $40 < M_{\mu\mu} < 60 \text{ GeV}/c^2$ is the γ^* continuum component of the Drell-Yan. In order to test this hypothesis, an invariant mass distribution obtained from Z/γ^* POWHEG

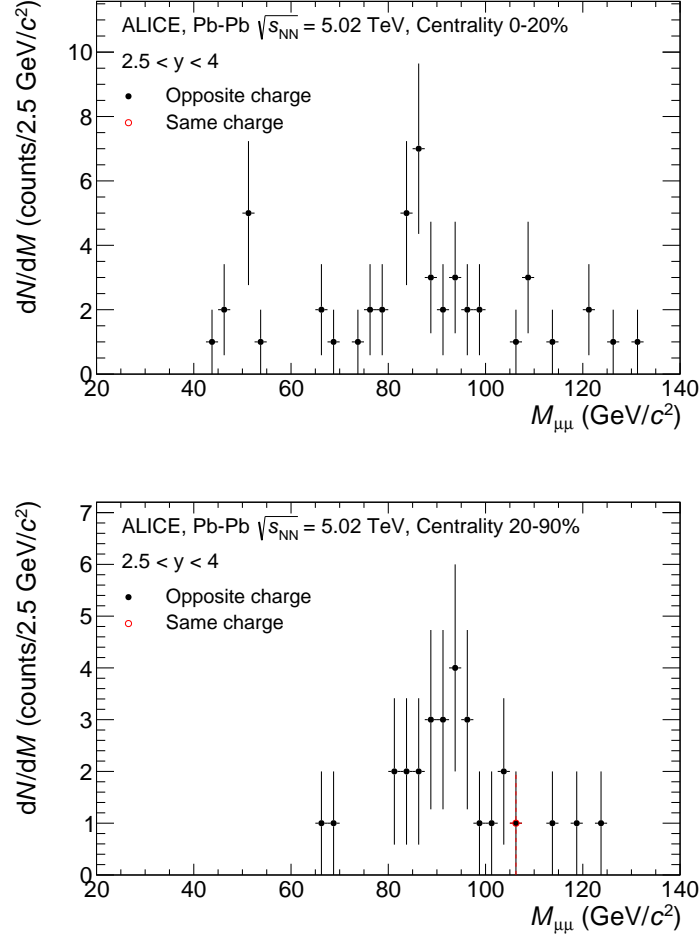


Figure 4.11: Dimuon invariant mass distribution in Pb-Pb collisions at $\sqrt{s_{NN}} = 5.02 \text{ TeV}$ with 0-20% (top) and 20-90% (bottom) centrality.

simulation is normalized and matched to the data one (Figure 4.12). A quantitative statistical test is then done by comparing the entries in the data to the ones predicted by POWHEG in three invariant mass ranges as shown in the bottom panel of Figure 4.12. The used simulation accounts for the full detector response as well as for the muon tracking chambers resolution (details on this point are presented in section 4.6.3.2). The agreement between the data and Z/γ^* POWHEG simulation in the invariant mass region $40 < M_{\mu\mu} < 120 \text{ GeV}/c^2$ is within one sigma which can explain the entries in $40 < M_{\mu\mu} < 60 \text{ GeV}/c^2$ as γ^* .

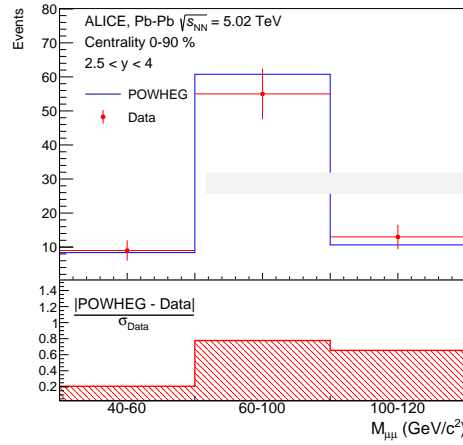
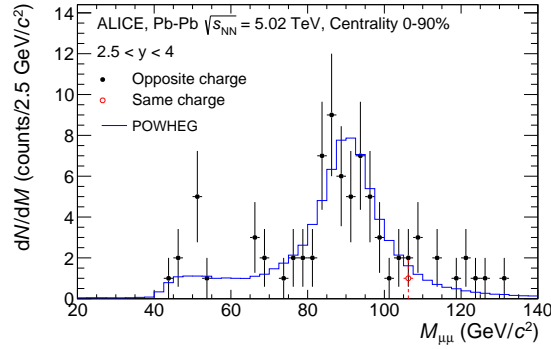


Figure 4.12: Top: comparison between the dimuon invariant mass distributions from data and Z/γ^* MC simulation using POWHEG in Pb-Pb collisions at $\sqrt{s_{NN}} = 5.02\text{TeV}$. Bottom: the comparison and ratio between the two distribution in three invariant mass intervals.

In order to have a small invariant mass and two muons with large p_T , a muon pair has to be boosted with large p_T . This is the case for the 6 entries with $M_{\mu\mu} < 12\text{ GeV}/c^2$ in Figure 4.10. A low mass resonance (ρ , ϕ) or a quarkonium (J/ψ , Υ) as well as a dimuon from semi-leptonic decay of $c\bar{c}$ or $b\bar{b}$ pairs are the possible physics explanations of these entries.

The quarkonia hypothesis was tested by estimating the expected number of J/ψ and Υ with large p_T in the analyzed data sample. The estimation procedure is explained in the following.

The measured J/ψ (Υ) p_T distribution obtained from the same studied data sample (Pb-Pb collisions at $\sqrt{s_{NN}} = 5.02$ TeV, see chapter 6) is fitted using the function $f(p_T) = C \times \frac{p_T}{(1+(p_T/p_0)^2)^n}$ commonly used to reproduce the quarkonia p_T distribution in hadronic collisions (left panels of Figure 4.13). Then the number of J/ψ (Υ) at high transverse momentum ($p_T > 40$ GeV/c) was estimated by integrating $f(p_T)$. This estimation is shown for different p_T ranges in the right panels of Figure 4.13. Within uncertainties, the expected number of quarkonia from this estimation $N_{Q\bar{Q}}(p_T > 40 \text{ GeV}/c) = 7$ is consistent with the observed number of dimuons with $p_T > 40 \text{ GeV}/c$ and $M_{\mu\mu} < 12 \text{ GeV}/c^2$.

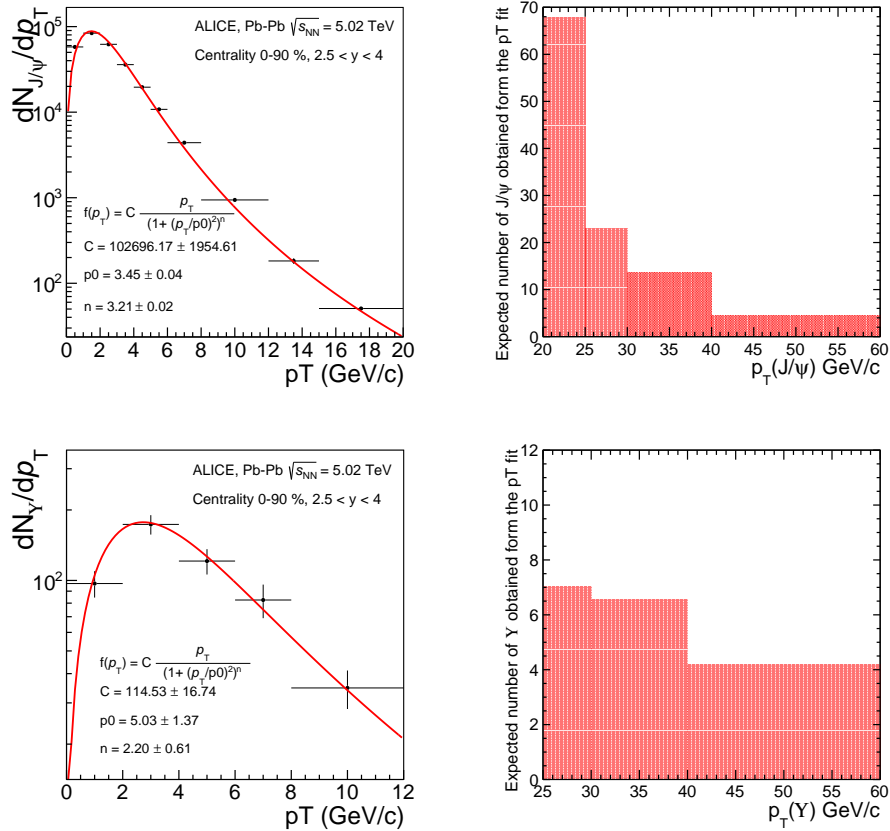


Figure 4.13: Top (bottom) left: fitted distribution of the J/ψ (Υ) yield as a function of p_T in Pb-Pb collisions at $\sqrt{s_{NN}} = 5.02$ TeV. Right: the value of the integral of the fitted functions in different p_T ranges.

4.5.2 J/ψ signal extraction

The main difference with respect to the Z-boson signal extraction is that the J/ψ signal sits in an invariant mass region where various sources of opposite-charge muon pairs can contribute. For this reason, counting the opposite-charge muon pairs in a predefined invariant mass range is an overestimation of the real J/ψ signal.

In the invariant mass region $2 < M_{\mu\mu} < 5 \text{ GeV}/c^2$, one can classify the possible sources of opposite-charge muon pairs in three different categories according to the correlation between the two muons:

- (A) A fully correlated muon pair where the muons are produced simultaneously via the decay of charmonium states (J/ψ or $\psi(2S)$).
- (B) An uncorrelated muon pair where the two muons originate from the decay of a correlated heavy quark pair ($c\bar{c}$ or $b\bar{b}$).
- (C) A fully uncorrelated muon pair where the two muons correspond to totally different physics processes. For example a muon from a kaon decay and one from a semileptonic decay of a c-hadron.

In order to extract the J/ψ signal, the amount of background contribution from (B) and (C) must be quantified and accounted for. To this aim, two methods are used:

- By estimating the size of the uncorrelated background and subtracting it from the opposite-charge dimuon invariant mass distribution.
- By directly fitting the non-subtracted opposite-charge dimuon invariant mass distribution with composite functions that account for both the signal and the full background.

In the following, the two methods are presented.

4.5.2.1 Background subtraction

Two different techniques can be used for estimating the uncorrelated dimuon background:

- **Same-charge muon pair technique:** the uncorrelated background in the opposite-charge muon pairs distribution is estimated by the number of same-charge muon pairs within each event, similarly to what is used in the Z-boson signal extraction. The benefit of this method is that the same-charge dimuon distribution is self-normalized to the opposite-charge dimuon one, since they correspond to the same events. However, this method has the disadvantage that the statistics in the background spectrum are limited to the number of available events which would affect the statistical precision of the extracted signal. This method is not used in the present analysis.
- **Event-mixing technique:** the uncorrelated background in the opposite-charge dimuon sample is given by muon pairs where the two muons correspond to two different events. On one hand, one can mix as many events as available which offers a better statistical precision than the same-charge muon pair technique. On the other hand, the obtained distributions are not self-normalized and additional steps need to be done for this purpose. In the current analysis, this method is the one used for background subtraction and will be detailed in the following.

Pools definition and mixing procedure

The first step in the event-mixing technique is to select the events to be mixed. For this purpose, events that contain at least one muon track that passes the selections of section 4.4 are stored in the so-called pools. A pool is an ensemble of events in the same run that share similar global properties such as the collision centrality and the primary vertex position. In this analysis, the pools are chosen based on the collision centrality with a width that varies from 2% to 5% from the most central to the most peripheral collisions.

The mixing is then done by combining each muon track from each event with all the other muon tracks from the next " N " events inside the pool as schematized in Figure 4.14. The value of N is chosen according to the required statistics. In this analysis, $N = 20$ was chosen.

Figure 4.15 shows the opposite-charge dimuon invariant mass distribution for mixed events in 0-10% centrality.

Figure 4.16 shows that the effect of whether or not defining pools based on the vertex position is negligible on the event-mixing results for this analysis.

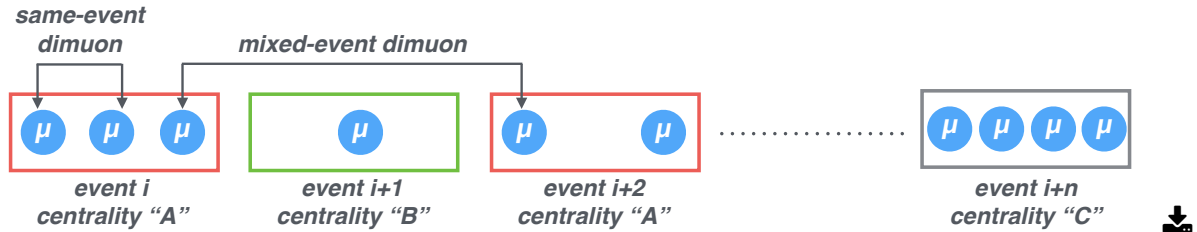


Figure 4.14: An illustration of the event-mixing procedure. The different colors of the boxes represent the different centrality pools.

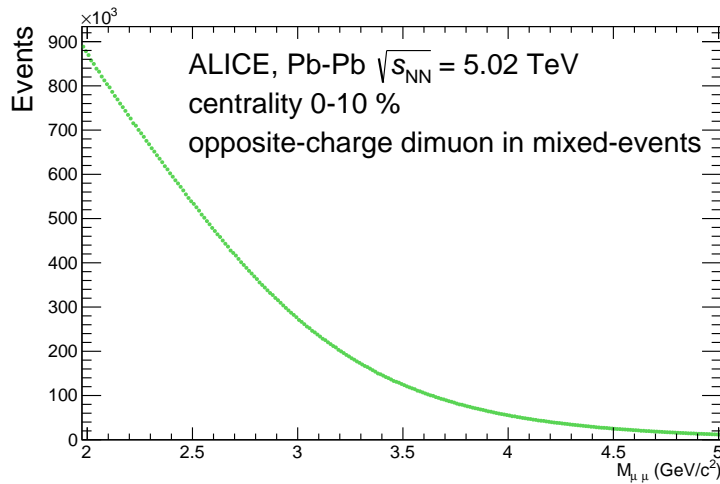


Figure 4.15: Mixed opposite-charge dimuon invariant distribution in Pb-Pb collisions at $\sqrt{s_{NN}} = 5.02 \text{ TeV}$ with 0-10% centrality.

Event-mixing normalization

The number of mixed muon pairs is different (usually larger) than the one of same-event (real) muon pairs. Therefore, in order to not over-subtract the background, the mixed muon pairs distribution must be normalized to the real one.

One can think of two normalization methods. A direct one where the normalization is done directly using the mixed and real opposite-charge dimuon invariant mass

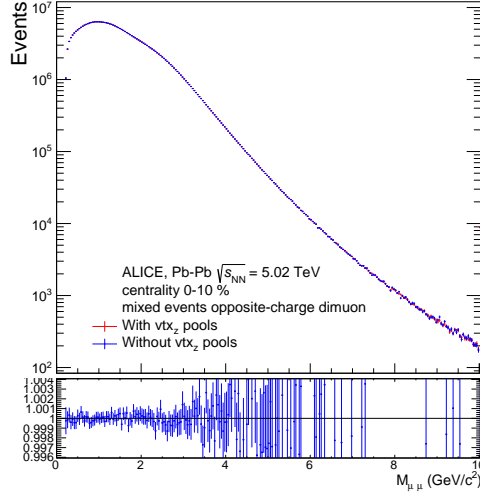


Figure 4.16: Comparison between two mixed opposite-charge dimuon invariant distribution in Pb-Pb collisions at $\sqrt{s_{NN}} = 5.02$ TeV with 0-10% centrality with an without using pools in the z-position of the primary vertex.

distributions. By construction, the mixed one is fully uncorrelated while the real one contains both correlated and uncorrelated dimuons. For this reason, the normalization in this method is done by considering only the regions of the invariant mass distributions where no correlated dimuons are expected to contribute into the real one. The region where the J/ψ and $\psi(2S)$ signals are expected to be negligible is commonly used. The fact that the signals region is excluded by hand might introduce some biases causing an overestimation of the uncorrelated background. Such biases are not introduced in the second (indirect) method which is used in this analysis. This method uses the real same-charge dimuon invariant mass distributions in the normalization. Let N_{real}^{++} and N_{real}^{--} be the number of the real same-charge dimuons in a given invariant mass bin with positive and negative charges respectively. And N_{mixed}^{+-} is the number of mixed opposite-charge dimuons in the same invariant mass bin. The normalization factor (F) is then given by:

$$F = \frac{\int_{M1}^{M2} 2R_{acc} \sqrt{N_{real}^{++} N_{real}^{--}} dM}{\int_{M1}^{M2} N_{mixed}^{+-} dM} \quad (4.14)$$

where $M1$ and $M2$ define the invariant mass range on which the normalization

is done. Unlike the direct method, there is no need to exclude a signal region. The factor R_{acc} accounts for an asymmetry due to a detector acceptance-bias relative to the charge of the muon. It can be calculated using the mixed distributions as $R_{acc} = \frac{N_{mixed}^{+-}}{2\sqrt{N_{mixed}^{++}N_{mixed}^{--}}}$. The R_{acc} factor for the 0-10% centrality interval is shown in Figure 4.17. In this analysis, the normalization is done in the invariant mass range $2 < M_{\mu\mu} < 8 \text{ GeV}/c^2$, where R_{acc} is compatible with unity.

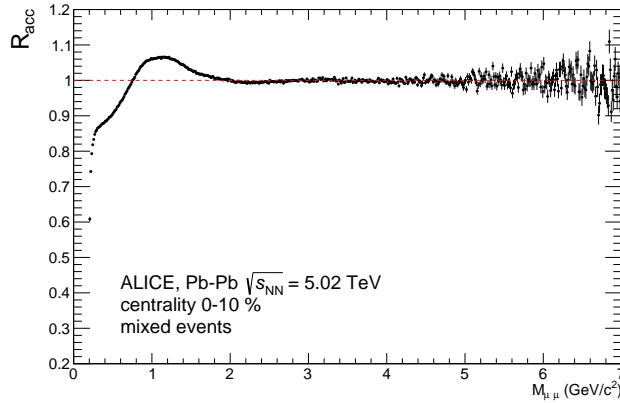


Figure 4.17: The acceptance factor $R_{acc} = \frac{N_{mixed}^{+-}}{2\sqrt{N_{mixed}^{++}N_{mixed}^{--}}}$ in Pb-Pb collisions at $\sqrt{s_{NN}} = 5.02 \text{ TeV}$ with 0-10% centrality.

Event-mixing control checks and background subtraction

Before subtracting the normalized background, the procedure is checked via different control plots. Examples of these plots are shown in Figure 4.18 for the case of 0-10% centrality interval. They represent the comparison between the mixed and real same-charge dimuon distributions in terms of invariant mass, rapidity, and transverse momentum. Since the dimuons in both cases are uncorrelated, one expects that the ratio of the compared variables is flat and compatible with unity.

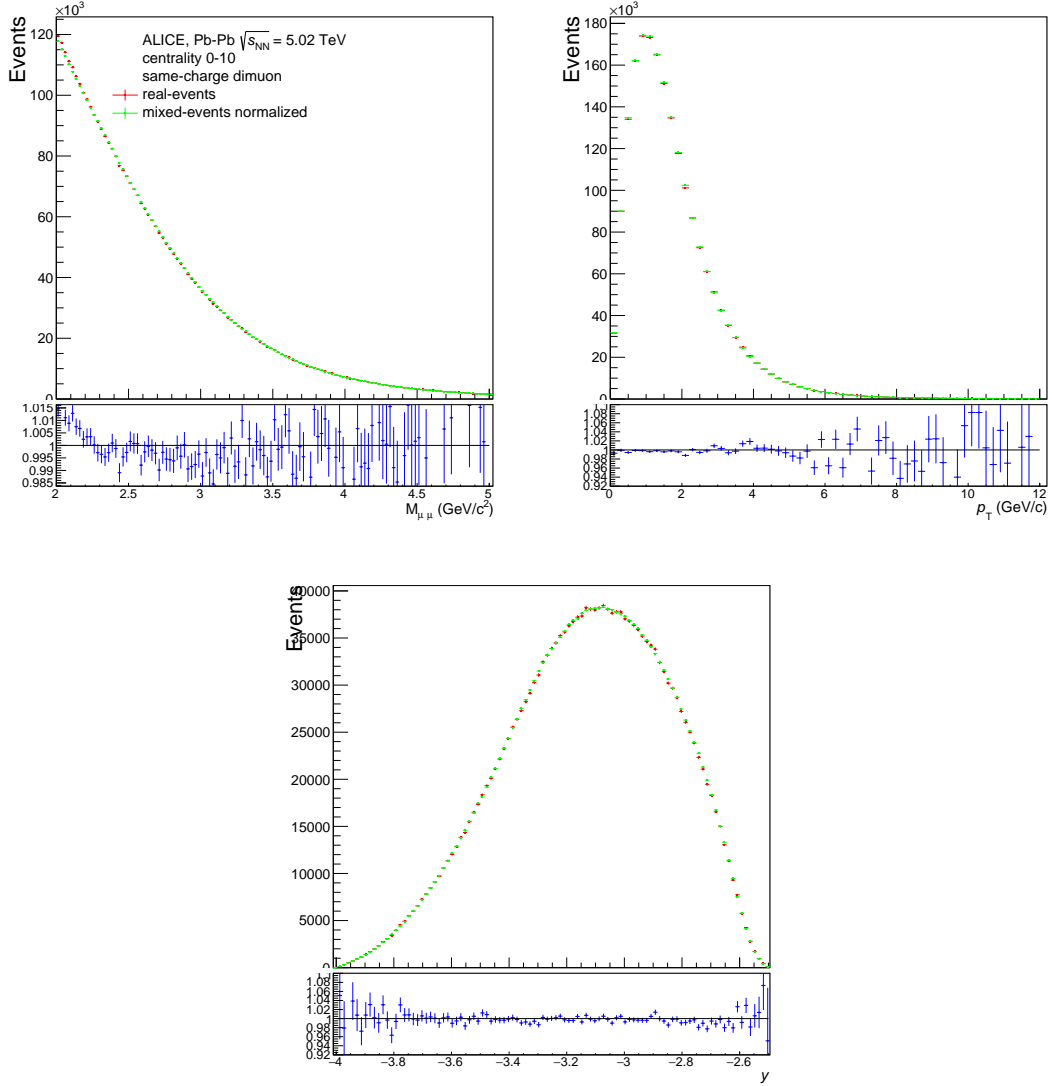


Figure 4.18: Comparison between the real and mixed same-charge dimuon distributions in Pb-Pb collisions at $\sqrt{s_{NN}} = 5.02$ TeV with 0-10% centrality for the invariant mass (top), transverse momentum (middle), and rapidity (bottom).

The mixed opposite-charge dimuon invariant mass distribution is then subtracted from the real one as shown in Figure 4.19 for the 0-10% centrality interval. In the previous paragraph about the pool definition and track selection, the discussion on the choice of the trigger class from which the mixed events are selected was omitted in purpose. The best results in terms of background reproduction were

obtained by mixing **CMSL** events.

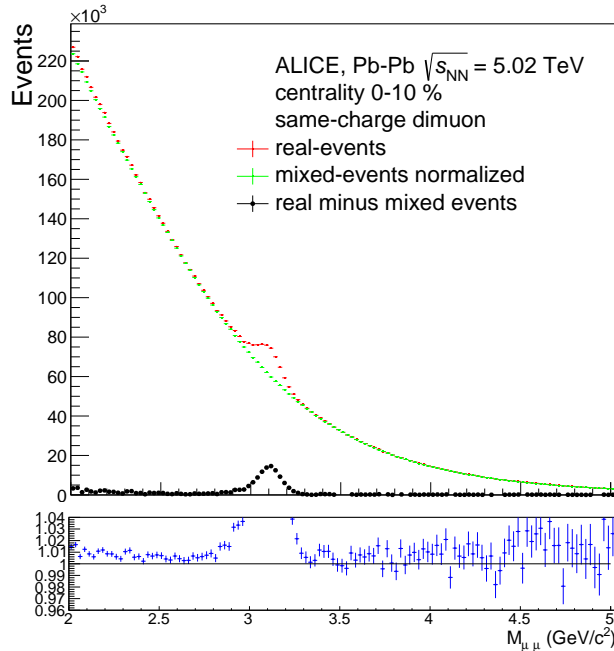


Figure 4.19: Top panel: comparison between the real (red) and mixed (green) opposite-charge dimuon invariant mass distributions in Pb-Pb collisions at $\sqrt{s_{NN}} = 5.02$ TeV. The difference between the two distributions is plotted in black in the same panel. Bottom panel: the ratio between the real and the mixed distributions.

Signal extraction after the background subtraction

After the subtraction of the uncorrelated background, the dimuon invariant mass distribution of Figure 4.19 is dominated by the contribution from the J/ψ signal. However, this is not the only contribution left since a small amount of residual correlated background exists. Therefore, a simple counting of the dimuons overestimates the signal and cannot be used. Alternatively, the distribution is fitted with a function composite of three components.

- A function that accounts for the residual background: a sum of two exponential functions is used in all the cases (different centrality, p_T and rapidity

intervals). When performing the fit, the four parameters of this function are left free.

- A function that characterizes the J/ψ signal: reconstructed resonances are in general characterized by a Gaussian distribution that models the detector resolution. This distribution is however ideal and does not take into account the detector effects on the reconstructed signals. The main effects in the case of the J/ψ reconstruction in the ALICE muon spectrometer are the muon energy loss inside the front absorber which affects the left side of the Gaussian distribution and the effect of muon tracking chambers misalignment on the resolution which affects both sides of the distribution. In order to deal with these detector effects, various functions based on a Gaussian core with additional tails exist. In this analysis, two of them, the extended Crystal-Ball² and the NA60³ functions are used. The descriptions and the formulas of the two functions can be found in Appendix A

The mean and the width of the Gaussian core of the two functions are given respectively by the pole mass of the J/ψ and the muon spectrometer resolution at the J/ψ mass. These two parameters are left free when performing the fits, while the additional tails parameters of the CB2 and the NA60 functions are fixed to predefined values. These values are either extracted by fitting simulated MC J/ψ signals, or taken from other J/ψ analyses where the J/ψ signal to background ratio is good enough to constrain them. In this analysis, three sets of tails parameters were considered, the first one is taken from the J/ψ fit results in an analysis done in pp collisions at $\sqrt{s} = 13$ TeV [98]. The two others are extracted using two MC simulations that use two different transport codes, GEANT3 [129] and GEANT4 [130] since the shape of the tails is sensitive to the description of the detector materials provided by the transport code. Figure 4.20 shows a comparison between these three sets of tails for the CB2 function.

- A function that characterizes the $\psi(2S)$ signal: this function is similar to the J/ψ one. The mean of its Gaussian core is fixed to the J/ψ one after adding

²Named after the Crystal-Ball experiment.

³Named after the NA60 experiment.

the difference between the Particle Data Group (PDG) pole masses values of the two particles ($M_{\psi(2S)} = M_{J/\psi} + (M_{\psi(2S)}^{PDG} - M_{J/\psi}^{PDG})$), while its width is fixed to the J/ψ one multiplied by the factor ($\frac{M_{\psi(2S)}^{PDG}}{M_{J/\psi}^{PDG}}$) that accounts for the evolution of the detector resolution as a function of the invariant mass. The two signals share also the same CB2 and NA60 tails parameters.

Figure 4.21 shows an example of a fitted opposite-charge dimuon invariant mass distribution after subtracting the uncorrelated background with the event-mixing technique. The number of J/ψ is then given by integrating the signal function (CB2 or NA60). The statistical uncertainty on the extracted signal is the error on the integral obtained from the fit procedure. The $\psi(2S)$ component is included in the fit function but it is almost unseen in the example due to a number of $\psi(2S)$ compatible with zero.

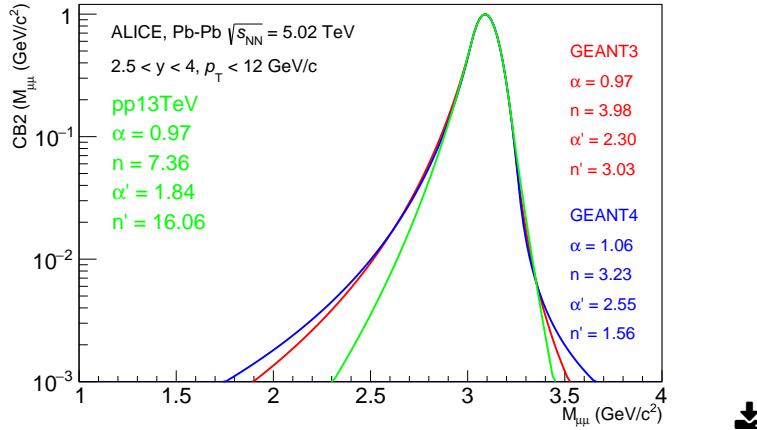


Figure 4.20: Comparison between the CB2 tails parameters of the different sets used for the J/ψ signal extraction in Pb-Pb collisions at $\sqrt{s_{NN}} = 5.02$ TeV.

4.5.2.2 Direct signal extraction

Instead of subtracting the uncorrelated background before extracting the J/ψ signal, one can alternatively perform the signal extraction procedure starting from the last step of that method, i.e. by fitting the opposite-charge dimuon invariant mass distribution with a composite model. This method cannot be applied if the

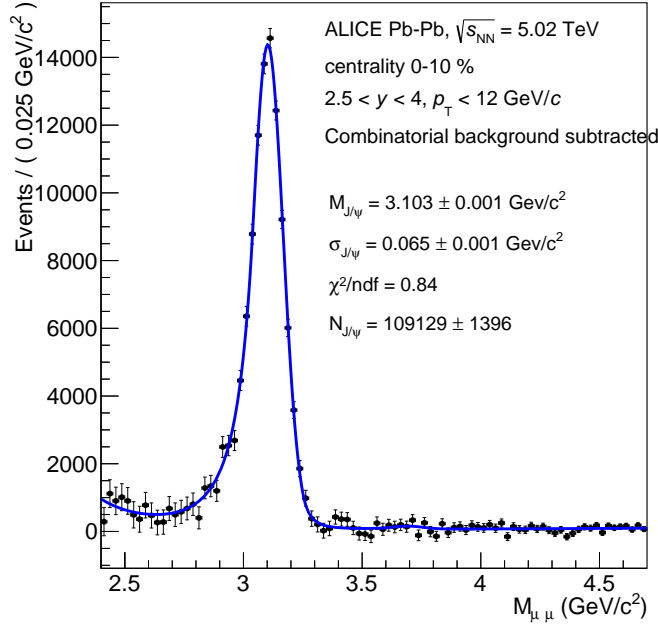


Figure 4.21: Opposite-charge dimuon invariant mass distribution in Pb-Pb collisions at $\sqrt{s_{NN}} = 5.02$ TeV with 0-10 % centrality after the subtraction of the uncorrelated background. The distribution is fitted with the sum of two exponential functions to characterize the background and two CB2 functions to characterize the J/ψ and $\psi(2S)$ signals.

J/ψ signal-to-background ratio is too small.

Similarly to the fit model presented for the previous method (section 4.5.2.1), the model used in this method is made of two signal functions to characterize the J/ψ and $\psi(2S)$ signals and one to characterize the background. The difference in this case is that the amount of background is much more important, hence more complex functions with larger numbers of parameters are needed.

Different functions that are commonly used to characterize the background distributions in particle physics are tested:

- A **linear Variable Width Gaussian (VWG)** is a Gaussian distribution with a width that varies linearly with the dimuon invariant mass. This function has four parameters.

- A **quadratic Variable Width Gaussian (VWG2)** is similar to the VWG but has an additional parameter to obtain a quadratic dependence with the invariant mass.
- A **5th order Chebyshev polynomials function (Chebyshev5)** is a sequence of orthogonal polynomials with five parameters.
- An **Exponential function multiplied by a 4th order polynomial(ExpPol4)** with six parameters.
- A **ratio of two polynomials (Pol2/Pol3)**. To avoid divergence, the order of the polynomial in the denominator must be higher than the one in the numerator. In this case they are third and second order polynomials respectively. This function has seven parameters.

The mathematical formulas for these functions can be found in Appendix A

Prior to using them in the final fit procedure, the different background functions are tested using the opposite-charge dimuon invariant mass distribution obtained from the event-mixing technique (e.g. Figure 4.15). A first check is done by fitting this distribution by the different functions and compare the resulted fit goodness. The fit goodness can be quantified by the variable χ^2/ndf , a model is said to describe a distribution ideally when the χ^2/ndf of the fit is equal to unity. As the description worsen, the χ^2/ndf increases. In the different centrality and kinematic intervals (p_T and rapidity), the two functions that have the overall best results are the VWG2 and Pol2/Pol3.

An additional check is done by injecting a simulated J/ψ signal to the mixed opposite-charge dimuon invariant mass distribution and fitting the resulted distribution with the sum of a signal function (CB2 or NA60) and one of the tested background functions. A good function combination would result in a number of J/ψ close to the known one that was injected. As for the χ^2/ndf test, the VWG2 and the Pol2/Pol3 functions are better than the others over the different centrality, p_T , and rapidity intervals.

The real opposite-charge dimuon invariant mass distribution is then fitted with a sum of a background function (VWG2 or Pol2/Pol3) and two signal ones (CB2 or NA60) for the J/ψ and $\psi(2S)$. An example of such fit is shown in Figure 4.22.

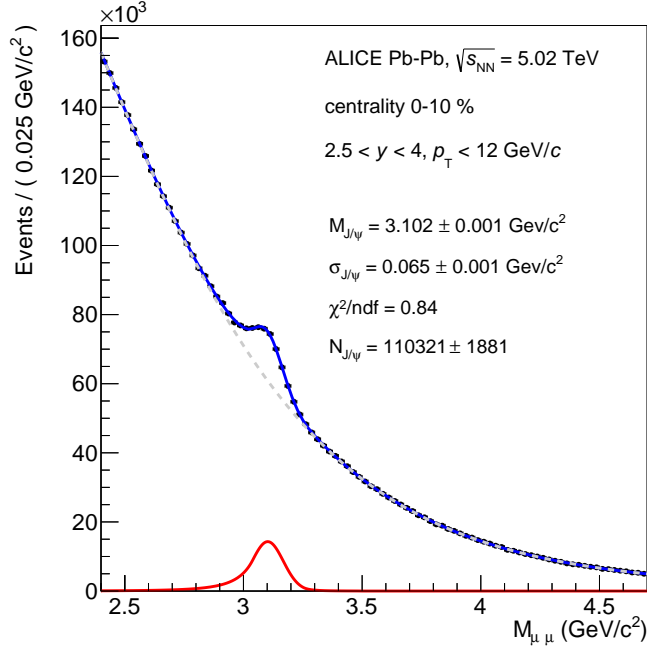


Figure 4.22: Opposite-charge dimuon invariant mass distribution in Pb-Pb collisions at $\sqrt{s_{NN}} = 5.02$ TeV with 0-10 % centrality fitted with the sum of a VWG2 function to characterize the background and two CB2 functions to characterize the J/ψ and $\psi(2S)$ signals. Signal extraction plots for the other centrality, p_T , and rapidity intervals can be found in Appendix C.

4.5.2.3 Systematic uncertainty on the J/ψ signal extraction

For each interval in centrality, p_T or rapidity, the final values of the number of J/ψ and its statistical uncertainty are obtained by averaging the values given by the 30 fit configurations that correspond to all the possible combinations of the following fit ingredients:

- **3 background functions:**
 - VWG2
 - Pol2/Pol3
 - Sum of two exponential functions after subtracting the uncorrelated background with the event-mixing technique
- **2 signal functions:**
 - CB2
 - NA60
- **3 Sets of signal functions tails parameters extracted from:**
 - J/ψ analysis in pp collisions at $\sqrt{s} = 13\text{TeV}$ (only available for CB2)
 - MC simulation using GEANT3 transport code
 - MC simulation using GEANT4 transport code
- **2 invariant mass fit ranges:**
 - 2.2-4.5 GeV/c^2
 - 2.4-4.7 GeV/c^2

The distribution of the number of extracted J/ψ as a function of the fit configuration is shown in Figure 4.23 which also shows the trend of other variables (J/ψ pole mass, signal width and the χ^2/ndf of the fit) used in order to assure the quality of the fit. The RMS of the 30 values of the number of extracted J/ψ is taken as the systematic uncertainty on the signal extraction. This uncertainty varies from 1.5% up to 4% in the different centrality, p_T , and rapidity intervals. Table 4.6

summarizes the J/ψ signal extraction results in different centrality intervals. The J/ψ signal extraction results in other centrality, p_T , and rapidity intervals can be found in Appendix D.

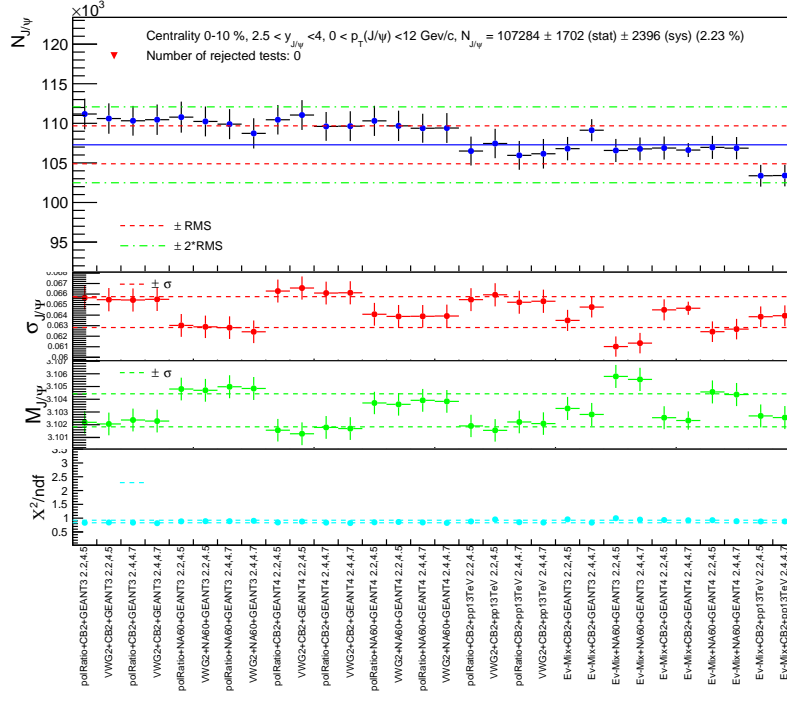


Figure 4.23: Top panel: the distribution of the extracted number of J/ψ in Pb-Pb collisions at $\sqrt{s_{NN}} = 5.02\text{TeV}$ with 0-10 % centrality as a function of the fit configurations. The horizontal solid line represents the average between the different configurations. Three bottom panels: the trend of the J/ψ pole mass, J/ψ width and the χ^2/ndf of the fit as a function of the fit configuration.

Centrality (%)	$N_{J/\psi} \pm (stat) \pm (sys)$
$2.5 < y < 4, 0 < p_T < 12 \text{ GeV}/c$	
0 , 90	$277007 \pm 2434 \pm 4806$
0 , 10	$107284 \pm 1702 \pm 2396$
10 , 20	$69808 \pm 1168 \pm 1161$
20 , 30	$45007 \pm 822 \pm 728$
30 , 40	$24876 \pm 491 \pm 630$
40 , 50	$15010 \pm 321 \pm 281$
50 , 60	$7895 \pm 190 \pm 147$
60 , 70	$4112 \pm 105 \pm 71$
70 , 80	$2042 \pm 66 \pm 34$
80 , 90	$932 \pm 37 \pm 15$

Table 4.6: The average number of J/ψ alongside its statistical and systematic uncertainties in Pb-Pb collisions at $\sqrt{s_{NN}} = 5.02 \text{ TeV}$ for different centrality intervals.

4.6 Detector acceptance and efficiency Correction

The extracted Z-boson and J/ψ signals are affected by the detector efficiency during the data taking as well as by its kinematic acceptance. In order to fairly compare the results from different experiments, with different detector efficiencies and kinematic acceptances, one needs to correct for their values. The maximum value for the Acceptance times Efficiency ($A\varepsilon$) is unity which corresponds to an ideal detector with 4π coverage.

To determine the $A\varepsilon$ of a detector for a given process in a given collision system, one can use a method based on Monte-Carlo (MC) simulation which mimics what happened in the detector during the data taking in order to understand the experimental conditions and performance. In the following, the ingredients of this method are described.

4.6.1 MC simulations setup

A full MC simulation for a given process is a three steps procedure. First of all, the primary particle is generated and decayed to a given final state (e.g. a pair of muons) using relevant particle generators. In this analysis, the Z-bosons are generated using either POWHEG interfaced with PYTHIA-6 or a standalone PYTHIA-6 generator, while the J/ψ are generated using a generator code provided by the ALICE Offline framework. This code generates J/ψ with p_T and rapidity distributions that follow a given set of input functions.

In the second step, the final state particles are fed into a transport code (e.g. GEANT3 [129], GEANT4 [130], FLUKA [131]) which characterizes the geometry of the detector and track the particles through its materials. It also has the task of creating the hits in the active detection elements. The third step is to reconstruct the final state particles using the information from the created hits.

Since the detector conditions and performance may vary during a whole data taking period, the MC simulations are done on a run basis.

In Pb-Pb collisions, the detector response is affected by its occupancy. For instance, the detector is less efficient in higher multiplicity events as it is the case of the most central collisions. In order to take this effect into account, an embedding technique was used. It is based on simulating signal particle (J/ψ or Z-boson) and embedding the detector response into the raw data of a real event. The embedded event is then reconstructed as if it was a normal real event.

4.6.2 $A\epsilon$ calculation

After performing a MC simulation of a given process, the corresponding $A\epsilon$ is calculated as:

$$A\epsilon = \frac{N_{Rec}}{N_{Gen}}, \quad (4.15)$$

where N_{Gen} is the number of the initially generated particles (Z-boson or J/ψ) and N_{Rec} is the number of reconstructed ones which must also fulfill the same selections used in the real data analysis on the single muons and dimuons (section 4.4).

For the calculation of the $A\varepsilon$ in a given interval (in centrality, p_T , or rapidity), different weights are applied and are summarized in the following.

Run number weighting

Since the detector efficiency varies from run to run, the $A\varepsilon$ must be calculated for each individual run. When calculating the average over all the runs, the $A\varepsilon$ of each run is weighted by the number of CMUL7 (the trigger class on which the data analyses are based) events in the same run.

In p-Pb collisions at $\sqrt{s_{NN}} = 5.02 \text{ TeV}$, the $A\varepsilon$ of the process $Z \rightarrow \mu\mu$ as a function of the run number is shown in the left (right) panel of Figure 4.24 for the p-going (Pb-going) data sample. The detector efficiency in the Pb-going data sample is smaller and has larger fluctuations with respect to the one in the p-going data sample. This was caused by the larger amount of high voltage trips in the muon tracking chambers during the Pb-going data taking period.

In Pb-Pb collisions at $\sqrt{s_{NN}} = 5.02 \text{ TeV}$, the $A\varepsilon$ of the processes $Z \rightarrow \mu\mu$ and $J/\psi \rightarrow \mu\mu$ as a function of the run number are shown respectively in the left and right panels of Figure 4.25.

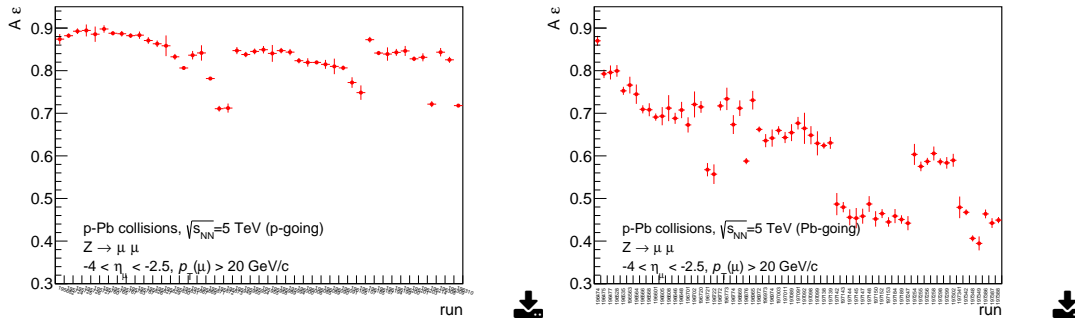


Figure 4.24: The Z -boson $A\varepsilon$ as a function of the run number in p-Pb collisions at $\sqrt{s_{NN}} = 5.02 \text{ TeV}$ for the p-going (left) and the Pb-going (right) data samples.

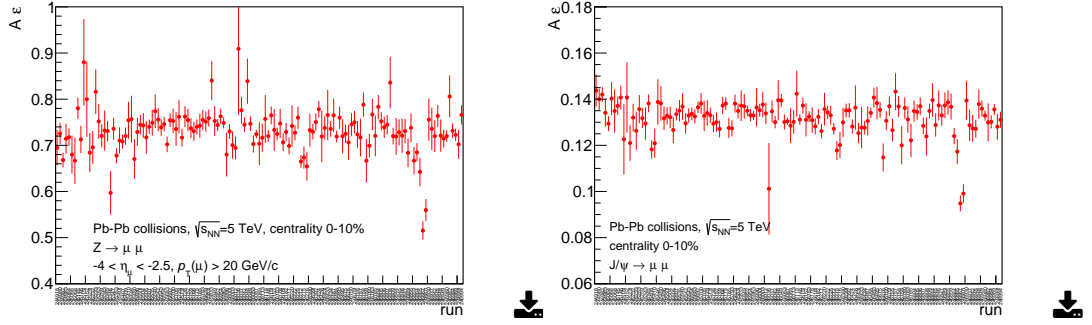


Figure 4.25: The Z-boson (left) and the J/ψ (right) $A\varepsilon$ as a function of the run number in Pb-Pb collisions at $\sqrt{s_{NN}} = 5.02\text{TeV}$ in the 0-10 % centrality interval.

Centrality weighting

In Pb-Pb collisions at $\sqrt{s_{NN}} = 5.02\text{TeV}$, the embedding technique allows the calculation of the $A\varepsilon$ as a function of the collision centrality. This dependence is shown for the Z-boson and for the J/ψ in the left and right panels of Figure 4.26 respectively. With respect to the most peripheral collisions which are equivalent to a signal-only simulation (without embedding), the detector efficiency drops by about 9% when going to the most central collisions. This drop is mainly due to the decrease of muon trigger efficiency with increasing particle multiplicity.

In order to calculate the J/ψ $A\varepsilon$ in a given centrality interval, the values of the $A\varepsilon$ in 10% centrality sub-intervals within that interval are averaged after assigning a weight given by the reconstructed number of J/ψ in each sub-interval. For example, the $A\varepsilon$ in the 0-90% centrality interval is given by:

$$A\varepsilon_{0-90\%} = \frac{\sum_{i=0-10\%}^{80-90\%} N_{J/\psi}^i \cdot A\varepsilon_i}{N_{J/\psi}^{0-90\%}}, \quad (4.16)$$

where $N_{J/\psi}^i$ and $A\varepsilon_i$ are respectively the number of reconstructed J/ψ and the $A\varepsilon$ in the centrality interval "i".

In the Z-boson analysis case, the same averaging procedure is done but by taking the number of CMUL7 events in a centrality sub-interval as a weight instead of the number of Z-bosons due to the lack of statistics on the latter.

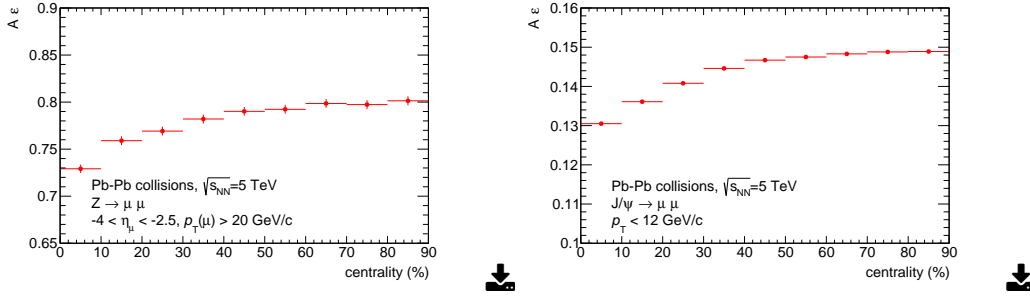


Figure 4.26: The Z-boson (left) and the J/ψ (right) $A\varepsilon$ as a function of the centrality in Pb-Pb collisions at $\sqrt{s_{NN}} = 5.02$ TeV.

J/ψ input functions weighting

The J/ψ generator needs p_T and rapidity input functions because the p_T and rapidity dependence of the detector $A\varepsilon$ is not constant as shown in Figure 4.27. These input functions can be obtained using an iterative data-driven method. A first $A\varepsilon$ obtained using a given set of input functions is used to correct the p_T and rapidity J/ψ raw distributions. Those $A\varepsilon$ corrected yields are fitted and the resulted fit functions are fed as inputs to the next generator. This procedure is repeated using the new $A\varepsilon$ values until the obtained input functions in two steps are similar.

In Pb-Pb collisions, the p_T and rapidity distributions vary from a given centrality interval to another due to the different dominant sources of J/ψ in the different centrality intervals (see chapter 6).

Due to technical limitations, the iterative procedure to determine the input functions was done using the J/ψ distributions of the 0-90% centrality interval (dashed black lines in Figure 4.28) and not for each centrality interval. This would affect the results of the $A\varepsilon$ calculated in the different centrality intervals. To clarify this, one can consider the example of calculating the $A\varepsilon$ in the 60-90% centrality interval with $0 < p_T < 12$ GeV/c. The J/ψ p_T distribution in the 60-90% centrality interval is harder than the one in 0-90% centrality interval which means that in the former case, the fraction of J/ψ at high p_T , that has higher $A\varepsilon$, is larger. Therefore using a J/ψ generator based on the p_T distribution of the 0-90% centrality interval would result in an $A\varepsilon$ smaller than the real one for the 60-90% centrality interval.

A correction is carried out by applying two independent p_T and rapidity weights

(w_{p_T}, w_y) to each generated and reconstructed dimuon. The weight is given by the ratio of the p_T or rapidity functions (f_{p_T}, f_y) in a given centrality interval "i" to the corresponding one in the 0-90% centrality interval:

$$w_{p_T(y)}^i = \frac{f_{p_T(y)}^i}{f_{p_T(y)}^{0-90\%}} \quad (4.17)$$

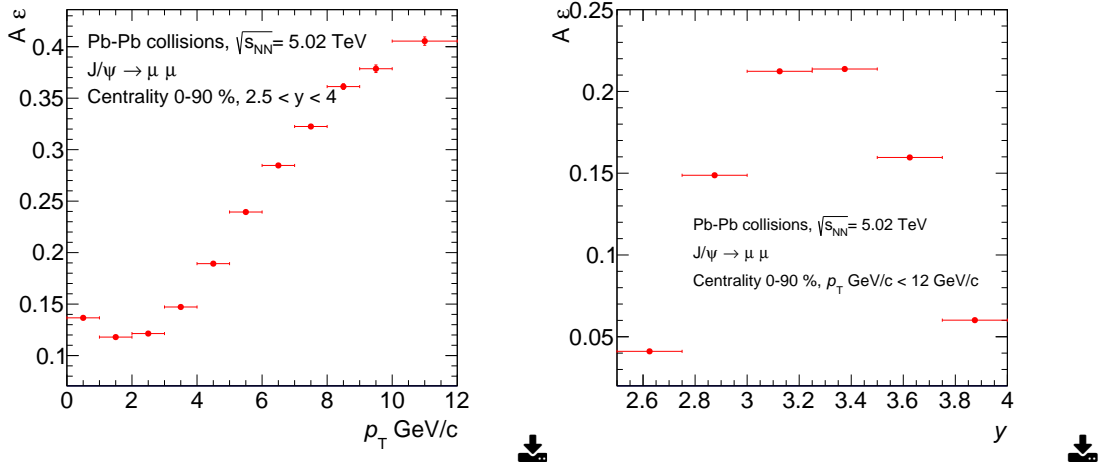


Figure 4.27: J/ψ $A\varepsilon$ distribution as a function of p_T (left) and rapidity (right) in Pb-Pb collisions at $\sqrt{s_{NN}} = 5.02$ TeV in 0-90% centrality interval.

4.6.3 Systematic uncertainties

Several sources contribute to the systematic uncertainty on the $A\varepsilon$ calculation. Some of them are muon-related uncertainties which means that they are shared by the Z-boson and J/ψ analyses while others are only relevant to one of them. In the following, these different sources with the sizes of their systematic uncertainties are discussed.

4.6.3.1 Muon tracking efficiency

The aim of a MC simulation is to reproduce the real conditions of the detector and their evolution with time. Concerning the tracking chambers, the detection

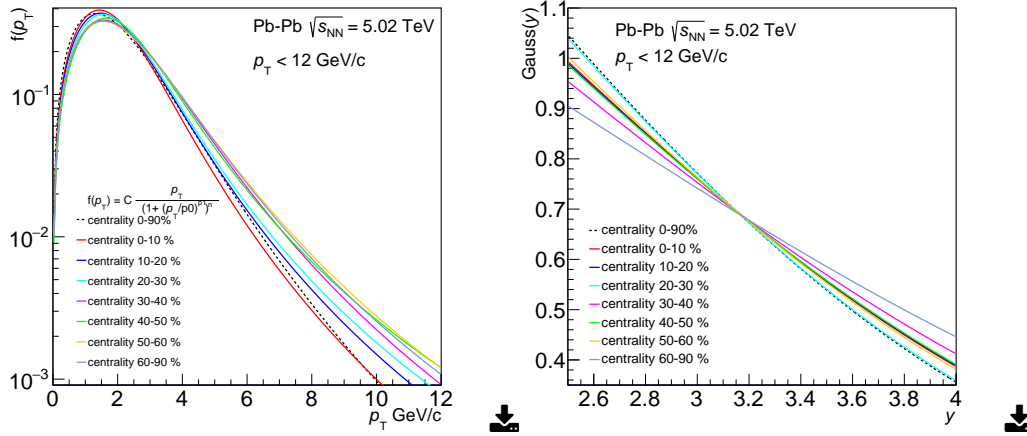


Figure 4.28: J/ψ yield distribution as a function of p_T (left) and rapidity (right) in Pb-Pb collisions at $\sqrt{s_{NN}} = 5.02$ TeV for different centrality intervals.

efficiency can be affected by problems like high voltage trips, electronic noise, etc. For each run, these problems are taken into account during a MC simulation.

In order to cross-check the realism of the simulations, one must find a quantity that can be calculated using both real data or MC simulations and compare their results. For this purpose, a method has been developed to measure the tracking efficiency of the single muons using the reconstructed tracks [132]. This method is applicable on both real data and simulations. In the following, a description of the method is presented and followed by the results obtained in p-Pb and Pb-Pb collisions at $\sqrt{s_{NN}} = 5.02$ TeV.

In order to reconstruct a track in the muon tracking system, it must have at least one reconstructed cluster in each one of the first three stations and at least three reconstructed clusters in the last two stations. The method used to calculate the tracking efficiency of each chamber is explained by considering as an example one of the first three stations.

Figure 4.29 schematizes a tracking station composed of two chambers i and j ; and the different possibilities for a passing tracks in terms of reconstructed clusters in the two chambers. The configuration "i-j" corresponds to the case when clusters in both chambers are reconstructed while the configurations "i-0" and "0-j" represent respectively the cases when only one cluster is reconstructed in the

chamber i or j. Finally, the configuration "0-0" is when no clusters are reconstructed in the station. The last configuration exists but cannot be observed since it does not fulfill the tracking algorithm.

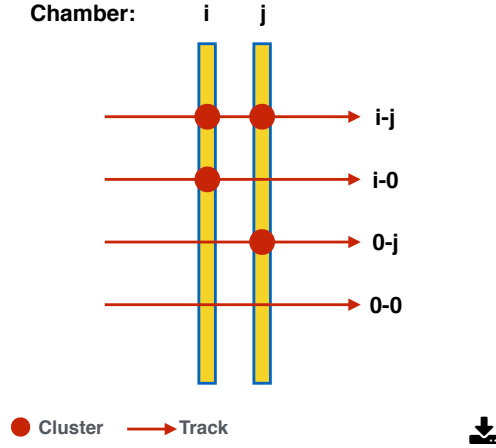


Figure 4.29: Possible configurations for a track going through a muon tracking station composed of two chambers i and j.

The total number of tracks (N_{tot}) is the sum over the different configurations:

$$N_{tot} = N_{ij} + N_{i0} + N_{0j} + N_{00} \quad (4.18)$$

Considering that the individual tracking efficiencies of the chamber i and j (ϵ_i^{trk} and ϵ_j^{trk} respectively) are independents, the ingredients of equation 4.18 can be expressed as:

$$N_{ij} = \epsilon_i^{trk} \cdot \epsilon_j^{trk} \cdot N_{tot} \quad , \quad N_{i0} = \epsilon_i^{trk} \cdot (1 - \epsilon_j^{trk}) \cdot N_{tot} \quad , \quad N_{0j} = (1 - \epsilon_i^{trk}) \cdot \epsilon_j^{trk} \cdot N_{tot} \quad (4.19)$$

The equation 4.19 can be re-arranged as:

$$\epsilon_i^{trk} = \frac{N_{ij}}{N_{ij} + N_{0j}} \quad \text{and} \quad \epsilon_j^{trk} = \frac{N_{ij}}{N_{ij} + N_{i0}} \quad (4.20)$$

allowing the calculation of ϵ_i^{trk} and ϵ_j^{trk} with no need to determine N_{00} .

After calculating the tracking efficiency of each chamber, the one of the stations are obtained according to their tracking algorithm. For the first three stations, the station tracking efficiency " $\epsilon_{st1|2|3}^{trk}$ " is defined as:

$$\epsilon_{st1|2|3}^{trk} = \epsilon_i^{trk} + \epsilon_j^{trk} - \epsilon_i^{trk} \epsilon_j^{trk} \quad (4.21)$$

while in the case of the last two stations, their tracking efficiency is calculated as one quantity:

$$\epsilon_{st4,5}^{trk} = \sum_{i=7}^{10} (1 - \epsilon_i^{trk}) \prod_{j=7, j \neq i}^{10} \epsilon_j^{trk} \quad (4.22)$$

Finally the total tracking efficiency is given by:

$$\epsilon_{tot}^{trk} = \epsilon_{st1}^{trk} \epsilon_{st2}^{trk} \cdot \epsilon_{st3}^{trk} \cdot \epsilon_{st4,5}^{trk} \quad (4.23)$$

Figure 4.30 shows two distributions of ϵ_{tot}^{trk} as a function of the run number in Pb-Pb collisions at $\sqrt{s_{NN}} = 5.02 \text{ TeV}$. The first distribution (blue) is obtained using reconstructed real tracks while the second (red) corresponds to the use of reconstructed tracks from a single muon MC simulation. This simulation uses a generator similar to the one used in the J/ψ MC simulation.

The relative integrated difference between the two tracking efficiencies computed in the data and MC simulations is taken as systematic uncertainty on single muon tracking efficiency. The uncertainty on the dimuon tracking efficiency is taken as twice the one on single muons assuming the two muons are fully independent. In p-Pb collisions at $\sqrt{s_{NN}} = 5.02 \text{ TeV}$, the uncertainty on the dimuon level amounts to 4% and 6% in the p-going and Pb-going data samples respectively. In Pb-Pb collisions at $\sqrt{s_{NN}} = 5.02 \text{ TeV}$, this uncertainty is 3% in both the Z-boson and the J/ψ analyses.

4.6.3.2 Muon chambers misalignment and resolution effect

The alignment of the muon chambers is a crucial step in order to obtain the required track momentum resolution. Figure 4.31 illustrates the effect of misaligned detector elements on a track reconstruction, considering a simple scenario with one translation degree of freedom and without the presence of a magnetic field.

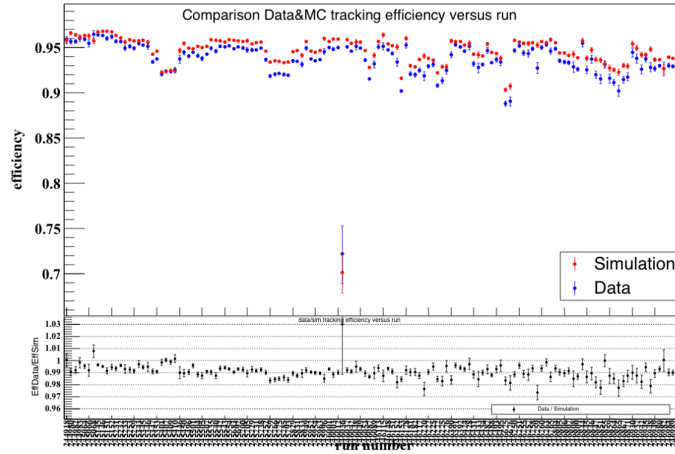


Figure 4.30: Comparison between the single muon tracking efficiency calculated using reconstructed tracks from data (blue) and MC simulation (red) as a function of the run number in Pb-Pb collisions at $\sqrt{s_{NN}} = 5.02$ TeV. The bottom panel shows the ratio between the two distributions [133].

The left panel shows an ideally aligned detector where the real position of each detector element is exactly as the assumed one in the offline detector geometry used for reconstruction. This leads to reconstructed clusters positions similar to the real ones, and therefore a reconstructed track identical to the real one. In the right panel of Figure 4.31, the real positions of the detector elements are different than the assumed ones, leading to a bias in the reconstructed clusters positions and the track.

An alignment procedure aims to correct the assumed positions of the detector elements to match the real ones during a given data taking period. For the muon spectrometer, this is done using information of physics tracks from dedicated runs with and without the presence of a magnetic field.

For each detector element, the true alignment can be determined by scanning the assumed position and refitting the track accordingly until the minimum in the observed χ^2 is reached. The χ^2 represents the goodness of the track fit. However, due to the large number (156) of detector elements and the fact that for each one, the misalignment is a 3D transformation with six degrees of freedom, approximations are needed to minimize a χ^2 function with many parameters. These approximations require that the alignment procedure is iterated several times

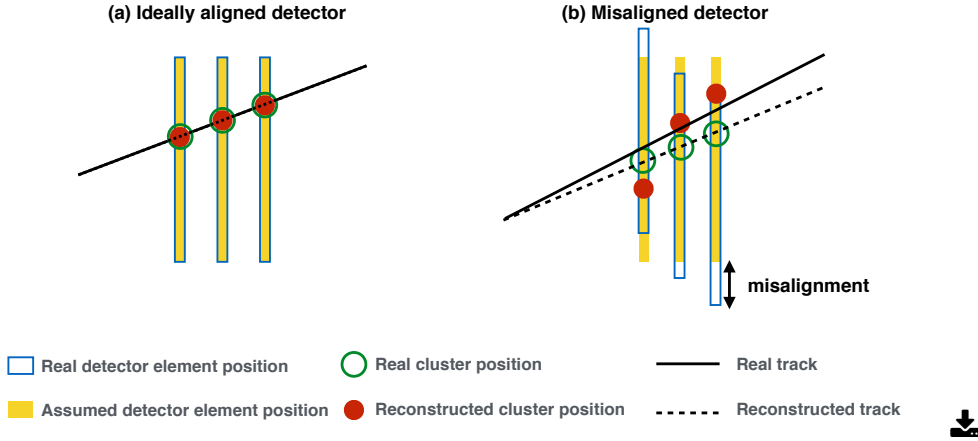


Figure 4.31: A cartoon showing the effect of the misalignment of detector elements on the track reconstruction.

until the best geometry is reached. In each iteration the measured misalignments are used to update the detector geometry which is then used as input for the next iteration.

In order to mimic the effect of the residual misalignment in MC simulations, different misalignment parameter sets are usually generated by randomly transforming (shifting or rotating) each detector element position after the alignment procedure within the resolution of the detector element.

Since the signal extraction of the Z-boson and hence the $A\varepsilon$ calculation is performed in a limited invariant mass range ($60 < M_{\mu\mu} < 120 \text{ GeV}/c^2$), the variation of the shape of Z-boson reconstructed invariant mass peak due to the residual misalignment affects the value of the $A\varepsilon$. This is shown in Figure 4.32 for p-Pb and Pb-Pb collisions at $\sqrt{s_{\text{NN}}} = 5.02 \text{ TeV}$ using POWHEG simulations. A systematic uncertainty is taken as the difference between the Z-boson $A\varepsilon$ calculated using different misalignment sets. This uncertainty amounts to about 2% (0.5%) in p-Pb (Pb-Pb) collisions at $\sqrt{s_{\text{NN}}} = 5.02 \text{ TeV}$. The uncertainty is larger in p-Pb collisions at $\sqrt{s_{\text{NN}}} = 5.02 \text{ TeV}$ because one of the used sets was fine tuned in order to reproduce the width of the Υ signal in the data which is not needed in Pb-Pb collisions at

$$\sqrt{s_{\text{NN}}} = 5.02 \text{ TeV.}$$

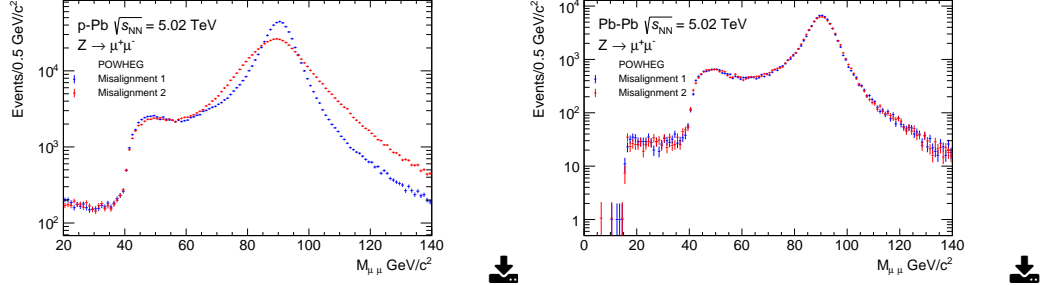


Figure 4.32: The comparison between the reconstructed MC dimuon invariant mass distributions using different misalignment parameters in p-Pb (left) and Pb-Pb (right) collisions at $\sqrt{s_{\text{NN}}} = 5.02 \text{ TeV}$.

Another detector effect that can smear the reconstructed Z-boson invariant mass peak and hence affect the $A\varepsilon$ calculation is the parametrization of the cluster resolution of the muon tracking chambers. During the reconstruction, the cluster resolution is characterized by a distribution having Gaussian tails. A more realistic description of the tails can be achieved by using Crystal-Ball function instead of the Gaussian one. Such tails were better in describing the single muon p_T shape in p-Pb collisions at $\sqrt{s_{\text{NN}}} = 5.02 \text{ TeV}$.

Figure 4.33 shows the effect of changing the parametrization of the cluster resolution on the dimuon invariant distribution. By using a more realistic function (Crystal-Ball), the peak becomes wider which means that the $A\varepsilon$ computed in the range $60 < M_{\mu\mu} < 120 \text{ GeV}/c^2$ would decrease. The systematic uncertainty due to this effect is calculated, similarly to the one on the alignment, as the difference between the Z-boson $A\varepsilon$ calculated using the two different cluster resolution parametrizations. This uncertainty amounts to about 2% (3.5%) in p-Pb (Pb-Pb) collisions at $\sqrt{s_{\text{NN}}} = 5.02 \text{ TeV}$.

The effect of the muon chambers misalignment and cluster resolutions is present also for the J/ψ but it is much smaller since such effects are more important for the high p_T muons. It is also worth noting that these effects do not have an impact on the J/ψ $A\varepsilon$ calculation where no invariant mass region is specified.

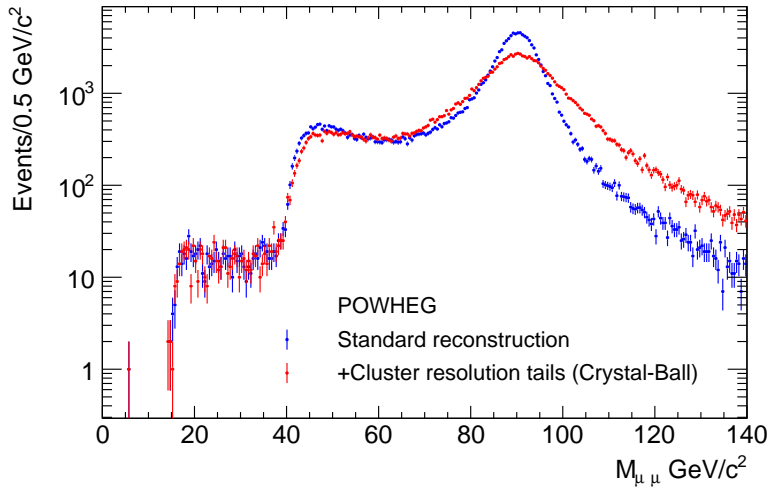


Figure 4.33: The comparison between the reconstructed MC dimuon invariant mass distributions obtained from a standard simulation (blue) or by characterizing the tails of the muon tracking chamber cluster resolution with a Crystal-Ball function (red) in Pb-Pb collisions at $\sqrt{s_{NN}} = 5.02\text{TeV}$.

4.6.3.3 Trigger efficiency

There are two sources that contribute to the systematic uncertainty on the muon trigger efficiency:

- **The uncertainty on the intrinsic trigger efficiency:** each muon trigger chamber contains 234 local board which are its smallest detection units. When performing a MC simulation, the values of the trigger efficiency of each local board is taken similar to what was estimated during the data taking. The trigger board efficiency is estimated from the data in a similar way to what is used for the chamber tracking efficiency (section 4.6.3.1). The obtained efficiency is then used in the MC simulation. The systematic uncertainty on the muon trigger efficiency is estimated as the variation of the single muon $A\varepsilon$ when varying the trigger efficiency of each board by a factor α . This factor corresponds to the average uncertainty on the trigger board efficiency obtained by changing the selections (e.g muon p_T cut) on the tracks used to estimate the intrinsic efficiency. This uncertainty is related

to the single muon and it is independent of the muon p_T which means that it is identical in the Z-boson and J/ψ analyses. In p-Pb (Pb-Pb) collisions at $\sqrt{s_{NN}} = 5.02$ TeV, it amounts to 2% (1.5%) on the dimuon level [134].

- **The uncertainty due to the muon trigger threshold:** the muon p_T cut, on which the muon trigger is based (see chapter 3), is not a sharp cut. Muons with a lower p_T still have a probability to pass this cut. The muon trigger is programmed to perform three different levels of p_T cut known as: **All- p_T** ($p_T > 0.5$ GeV/c), **Low- p_T** ($p_T > 1$ GeV/c), and **High- p_T** ($p_T > 4.2$ GeV/c). The **Low- p_T (High- p_T)** trigger response is defined as the ratio between the p_T distribution of the muons that fulfill the **Low- p_T (High- p_T)** to the one of muons that fulfill the **All- p_T** condition.

In Pb-Pb collisions at $\sqrt{s_{NN}} = 5.02$ TeV, as shown in Figure 4.34, the **Low- p_T** trigger response is not similar for muons from real data and the ones from MC simulations. The difference between the two distributions is important in the region close to the **Low- p_T** threshold which was set to 1 GeV/c. In order to estimate the systematic uncertainty due to this difference, two dedicated J/ψ MC simulations were done. In the first one, the muons are weighted by the MC trigger response while in the second by the one from data. The difference between the calculated $A\varepsilon$ is taken as a systematic uncertainty. This uncertainty amounts to 4.5% for J/ψ with $p_T < 1$ GeV/c and it starts decreasing when going to larger p_T to become negligible for $p_T > 8$ GeV/c [135].

In Figure 4.34, going to higher muon p_T (> 4 GeV/c) the difference between the two response functions becomes negligible, which means that this uncertainty is not relevant to the Z-boson analysis where muons with $p_T > 20$ GeV/c are selected.

4.6.3.4 Trigger-tracking matching efficiency

During the reconstruction, muon tracks in the trigger and the tracking systems are matched together. Only matched tracks that pass a given selection on the track fit-goodness are considered for analysis. A systematic uncertainty due to the difference behaviors of this cut in real data and MC simulation contributes to the

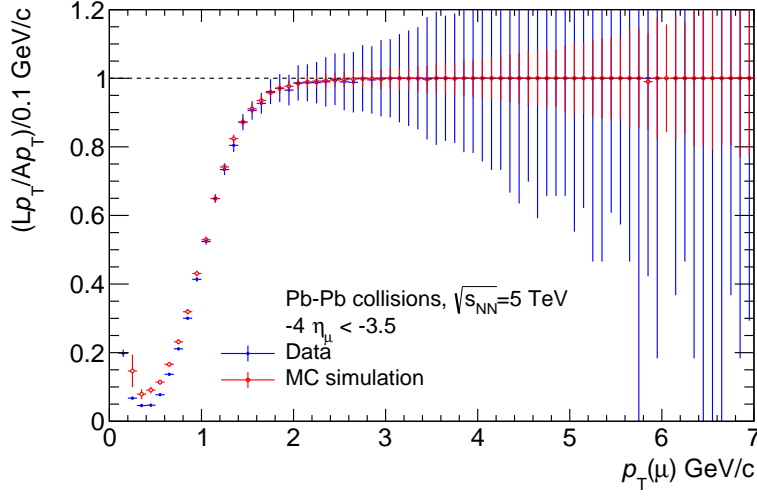


Figure 4.34: The comparison between the **Low- p_T** single muon trigger responses for data and MC in Pb-Pb collisions at $\sqrt{s_{NN}} = 5.02\text{TeV}$.

total uncertainty on the $A\varepsilon$ calculation. This systematic is usually estimated by looking at the effect of changing the value of the cut on the matching in both real data and MC simulation.

In p-Pb and Pb-Pb collisions at $\sqrt{s_{NN}} = 5.02\text{TeV}$, this systematic uncertainty amounts to 0.5% at the single muon level which is equivalent to 1% at the dimuon one [133].

4.7 Reference cross sections in pp collisions

The nuclear modification factor of a hard process at a given center-of-mass energy is usually normalized using a cross section of this process in pp collisions at the same energy. In November 2015, the LHC provided pp collisions at $\sqrt{s} = 5.02$ TeV and the data sample collected by ALICE corresponds to an integrated luminosity of about 106 nb^{-1} .

Figure 4.35 shows the opposite-charge dimuon invariant mass distribution in pp collisions at $\sqrt{s} = 5.02$ TeV. This distribution is obtained by applying the selections on the single muon and muon pairs of section 4.4 except the selection on the muon p_T ($p_T > 20 \text{ GeV}/c$). A clear J/ψ signal can be identified while the statistics is not sufficient in order to extract a Z-boson signal from this data sample. Alternatively, a theoretical Z-boson cross section obtained using perturbative QCD (pQCD) calculation [65] will be used for the evaluation of the R_{AA} in chapter 5.

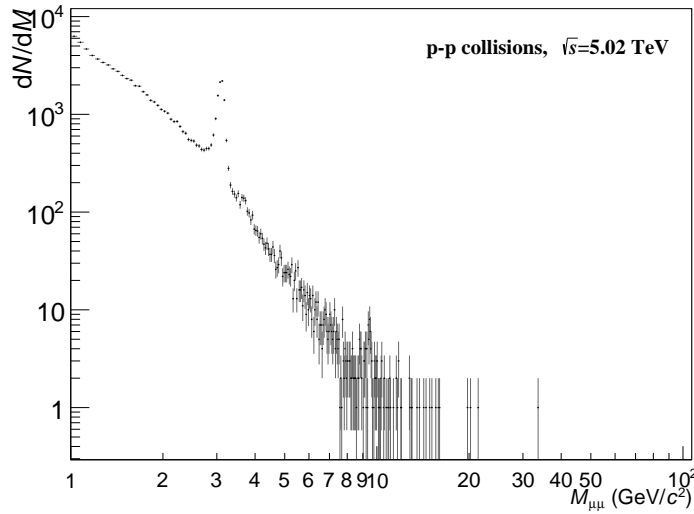


Figure 4.35: Opposite-charge dimuon invariant mass distribution in pp collisions at $\sqrt{s} = 5.02$ TeV.

4.7.1 J/ψ production cross section in pp collisions at

$$\sqrt{s} = 5.02 \text{ TeV}$$

The J/ψ production cross section at $\sqrt{s} = 5.02 \text{ TeV}$ was obtained using similar analysis steps to what is described for the J/ψ analysis in Pb-Pb collisions at $\sqrt{s_{\text{NN}}} = 5.02 \text{ TeV}$ (previous sections of this chapter). The p_{T} and rapidity differential cross section is calculated as:

$$\frac{d^2\sigma_{J/\psi}^{pp}}{dy dp_{\text{T}}} = \frac{N_{J/\psi}^{pp}(\Delta y, \Delta p_{\text{T}})}{BR_{J/\psi \rightarrow \mu\mu} \cdot L_{int}^{pp} \cdot A\varepsilon_{pp}(\Delta y, \Delta p_{\text{T}}) \cdot \Delta y \cdot \Delta p_{\text{T}}}, \quad (4.24)$$

where

- Δy and Δp_{T} are respectively the width of the rapidity and p_{T} ranges.
- $N_{J/\psi}^{pp}(\Delta y, \Delta p_{\text{T}})$ is the number of extracted J/ψ in the kinematic range $(\Delta y, \Delta p_{\text{T}})$. To extract the J/ψ signal, the opposite-charge dimuon invariant mass distribution is fitted with a composite model that accounts for the background, and the J/ψ and $\psi(2S)$ signals as shown in Figure 4.36 for $2.5 < y < 4$ and $p_{\text{T}} < 12 \text{ GeV}/c$.
- $BR_{J/\psi \rightarrow \mu\mu} = 5.96 \pm 0.03\%$ is the dimuon branching ratio of the J/ψ decay [1].
- $L_{int}^{pp} = 106.3 \pm 2.2$ (syst) nb^{-1} is the integrated luminosity obtained similarly to what is presented in section 4.3.2 using a MB cross section measured by the van der Meer scan method [136]. The quoted uncertainty reflects the van der Meer scan uncertainty.
- $A\varepsilon_{pp}(\Delta y, \Delta p_{\text{T}})$ is the detector Acceptance times Efficiency in the kinematic range $(\Delta y, \Delta p_{\text{T}})$. It is obtained using MC simulation as described in section 4.6.

The cross section value, integrated over the interval $2.5 < y < 4$ and $p_{\text{T}} < 12 \text{ GeV}/c$ is $\sigma_{pp}^{J/\psi} = 5.61 \pm 0.08 \pm 0.28 \mu b$ where the first quoted uncertainty is statistical and the second one is systematic and it corresponds to the contribution of the uncertainties on the signal extraction, $A\varepsilon$ calculation, the branching ratio and the integrated luminosity determination.

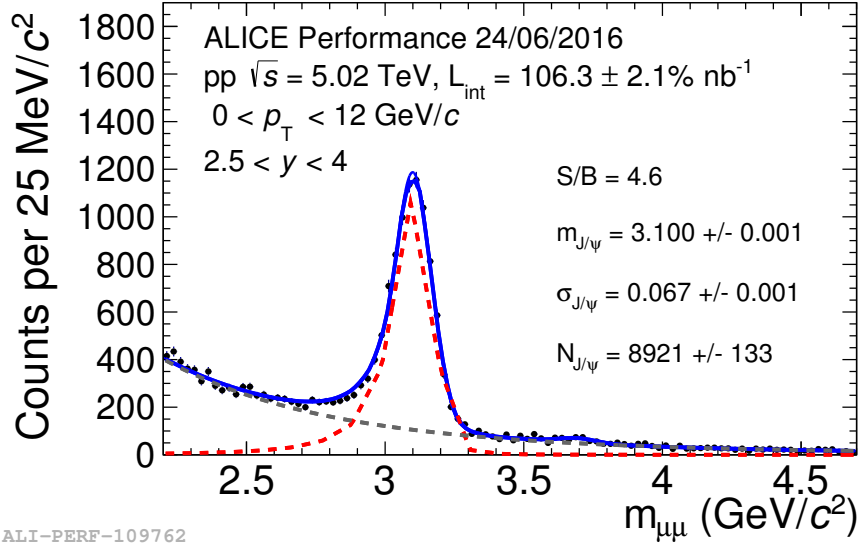


Figure 4.36: Opposite-charge dimuon invariant mass distribution in pp collisions at $\sqrt{s} = 5.02\text{ TeV}$ fitted with the sum of a VWG function to characterize the background and two CB2 functions to characterize the J/ψ and $\psi(2S)$ signals.

The left and right panel of Figure 4.37 show respectively the J/ψ p_T and rapidity differential cross sections in pp collisions at $\sqrt{s} = 5.02\text{ TeV}$.

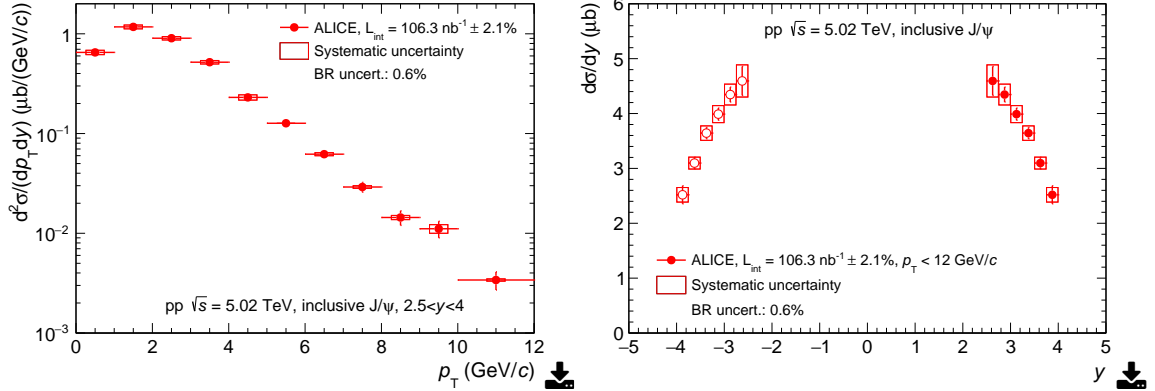


Figure 4.37: Left (right) panel: the J/ψ production cross section in pp collisions at $\sqrt{s} = 5.02\text{ TeV}$ as a function of p_T (rapidity) [98].

Z-BOSON PRODUCTION RESULTS

This chapter presents the results of the Z-boson production analyses in two collision systems. In p-Pb collisions at $\sqrt{s_{\text{NN}}} = 5.02\text{TeV}$, the Z-boson production cross section is calculated in two center-of-mass rapidity regions and compared to results from other LHC experiments. In Pb-Pb collisions at $\sqrt{s_{\text{NN}}} = 5.02\text{TeV}$, the Z-boson production invariant yield divided by the nuclear overlap function is presented as a function of rapidity and of the collision centrality. The nuclear modification factor is also evaluated in this collision system. As discussed previously, the motivation behind measuring the Z-boson production in heavy-ion collisions is to test and constrain the available parametrizations of the nuclear modification of the parton distribution functions. For this purpose, all the presented results are compared to different theoretical models with and without accounting for nuclear modifications.

5.1 Introduction and summary from previous chapters

The Z-boson production analysis was presented in chapter 4 in the two collision systems. The signal extraction was performed by counting the dimuon candidates

that pass different selections on the muon and the dimuon acceptance as well as on the muon transverse momentum with an invariant mass in the range $60 < M_{\mu\mu} < 120 \text{ GeV}/c^2$. The extracted signals were further corrected by the Acceptance times Efficiency ($A\epsilon$) of the detector using MC simulations.

Parton Distribution Functions (PDFs) as well as the nuclear modified ones (nPDFs) are calculated in the phase space (Q^2, x) where Q is the energy scale of the studied hard process given by the mass of the Z-boson in this case, and x is the fraction of the longitudinal momentum carried by the interacting partons. In a collision of two hadrons $h_1 - h_2$ at a given center-of-mass energy ($\sqrt{s_{\text{NN}}}$) The value of x is related to the rapidity y covered by the measurement. At LO, this relation is given by the following formula:

$$x_{1,2} = \frac{M_Z}{\sqrt{s_{\text{NN}}}} e^{\pm y}, \quad (5.1)$$

where the indexes (1,2) represent the probed x regions in the hadrons h_1 and h_2 respectively.

Figure 5.1 summarizes the probed x regions in the Pb ion by studying the Z-boson production in the different data samples of p-Pb and Pb-Pb collisions at $\sqrt{s_{\text{NN}}} = 5.02 \text{ TeV}$ within the muon spectrometer acceptance.

The p-going data sample in p-Pb collisions at $\sqrt{s_{\text{NN}}} = 5.02 \text{ TeV}$ cover the center-of-mass rapidity range $2.03 < y_{\text{cms}} < 3.53$ probing the small x regions in the Pb ion which correspond mainly to the sea quarks while in the Pb-going data sample, the covered center-of-mass rapidity range is $-4.46 < y_{\text{cms}} < -2.96$ which probes the large x regions in the Pb ion dominated by valence quarks.

In the case of the symmetric Pb-Pb collisions at $\sqrt{s_{\text{NN}}} = 5.02 \text{ TeV}$, the muon spectrometer covers the rapidity region $2.5 < y < 4$ probing at the same time large and small x regions of the Pb ions. Note that in the following, the center-of-mass rapidity is expressed as y_{cms} (y) for p-Pb (Pb-Pb) collisions. This is just to match the appearance of this symbol in the corresponding publications.

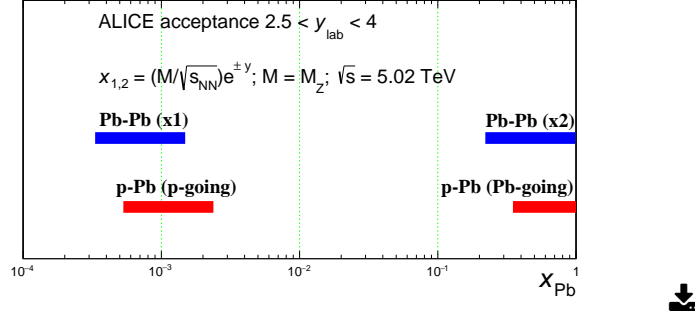


Figure 5.1: The probed x (calculated at LO) regions in the Pb ions by measuring the Z-boson production with the ALICE muon spectrometer in p-Pb and Pb-Pb collisions at $\sqrt{s_{NN}} = 5.02\text{TeV}$.

5.2 Z-boson production in p-Pb collisions at $\sqrt{s_{NN}} = 5.02\text{TeV}$

The differential Z-boson production cross section is calculated using the following formula:

$$\frac{d\sigma}{dy_{\text{cms}}} = \frac{N_Z}{L_{\text{int}} \cdot \Delta y_{\text{cms}} \cdot A\epsilon}, \quad (5.2)$$

where N_Z is the number of Z-boson candidates, L_{int} is the integrated luminosity, Δy_{cms} is the width of the rapidity range, and $A\epsilon$ is the Acceptance times Efficiency of the detector. The calculation is done in the following fiducial region:

$$\begin{cases} -4 < \eta_\mu < -2.5 \\ p_T(\mu) > 20 \text{ GeV}/c \\ 60 < M_{\mu\mu} < 120 \text{ GeV}/c^2 \end{cases}$$

The results of the Z-boson production cross section are shown in Figure 5.2 for the two y_{cms} regions. The statistical uncertainties coming from the ones on the number of Z-boson candidates are represented by vertical error bars, while the boxes around the points represent the total systematic uncertainties given by the quadratic sum of the different contributions summarized in Table 5.1.

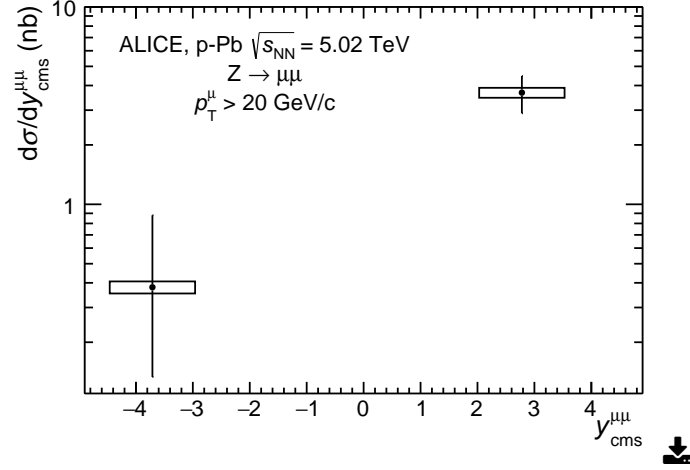


Figure 5.2: The measured Z-boson cross section in p-Pb collisions at $\sqrt{s_{\text{NN}}} = 5.02 \text{ TeV}$ as a function of the center-of-mass rapidity **[This thesis]**.

y_{cms}	$2.03 < y_{\text{cms}} < 3.53$	$-4.46 < y_{\text{cms}} < -2.96$
Signal extraction	< 1	< 1
F_{norm}	1	1
σ_{MB}	3.2	3
$A\varepsilon$ calculation		
Tracking efficiency	4	6
Trigger efficiency	2	2
Matching efficiency	1	1
Misalignment effect	1	2
Cluster resolution effect	2	2
Total	5.7	7.6

Table 5.1: The different contributions to the total systematic uncertainties (%) on the Z-boson production cross section in p-Pb collisions at $\sqrt{s_{\text{NN}}} = 5.02 \text{ TeV}$.

5.2.1 Comparison with theoretical models

In order to test the EPS09 nPDF (NLO) parametrization [57], the results of the Z-boson production cross section in p-Pb collisions at $\sqrt{s_{\text{NN}}} = 5.02 \text{ TeV}$ are compared to two different sets of calculations with and without taking into account the different nuclear effects on the PDFs from EPS09.

The first set of calculations is based on NLO perturbative QCD (pQCD) [65] using CT10 (NLO) [54] as a baseline PDF. The second one is obtained with the NNLO calculator FEWZ [31] and uses the MSTW2008 (NNLO) PDF set [53] as a baseline. The comparison between the data and the calculations from pQCD and FEWZ are shown in the top and bottom panels of Figure 5.3 respectively. In both cases, the filled (hatched) boxes represent the calculation with (without) including the nuclear modifications from EPS09. Independently from the baseline PDFs, the EPS09 parametrization predicts a decrease of the Z-boson production cross section. This decrease is relatively small with respect to the statistical precision of the data and all the calculations are in agreement with the measurement.

The numerical values of the measured cross sections, as well as the predicted ones by pQCD and FEWZ calculations, are summarized in Table 5.2.

y_{cms}	$2.03 < y_{\text{cms}} < 3.53$	$-4.46 < y_{\text{cms}} < -2.96$
Data	3.68 ± 0.78 (stat) ± 0.21 (sys)	$0.38^{+0.50}_{-0.25}$ (stat) ± 0.03 (sys)
pQCD: CT10	3.52 ± 0.14	0.44 ± 0.02
pQCD: CT10 + EPS09	3.07 ± 0.25	0.39 ± 0.03
FEWZ: MSTW2008	3.68 ± 0.08	0.39 ± 0.01
FEWZ: MSTW2008 + EPS09	3.33 ± 0.07	0.30 ± 0.01

Table 5.2: Comparison between the measured Z-boson cross sections (nb) in p-Pb collisions at $\sqrt{s_{\text{NN}}} = 5.02\text{TeV}$ and different theoretical calculations in two center-of-mass rapidity regions.

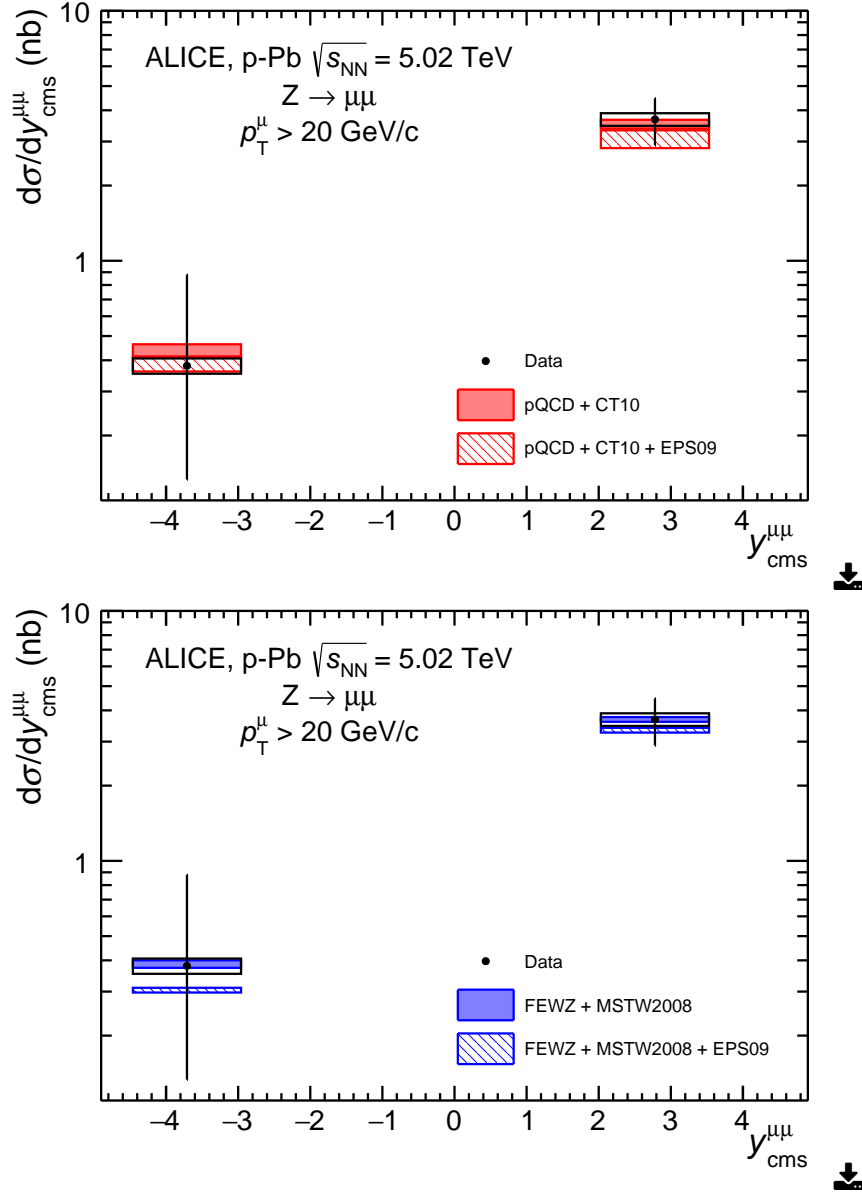


Figure 5.3: The measured Z-boson cross section in p-Pb collisions at $\sqrt{s_{\text{NN}}} = 5.02$ TeV as a function of the center-of-mass rapidity compared to theoretical calculations from pQCD (top) and FEWZ (bottom) performed both with and without including the nuclear modification of the PDFs using the EPS09 parametrization. Figure adapted from [128].

5.2.2 Comparison with other LHC experiments

As mentioned in chapter 2, the Z-boson production cross section in p-Pb collisions at $\sqrt{s_{\text{NN}}} = 5.02\text{TeV}$ has been also measured by the other LHC experiments. It was also discussed that every experiment covers different acceptances. Therefore, a correction by their acceptances must be done before comparing their results. Since the deviation of the measured cross section from the theoretical calculations is more relevant to the aim of the studies than the absolute value of the cross section itself, and to avoid the acceptance corrections, the comparison between the experimental results is carried out by comparing all the results to the same theoretical calculation. The upper panel of Figure 5.4 show the Z-boson production cross sections in p-Pb collisions at $\sqrt{s_{\text{NN}}} = 5.02\text{TeV}$ measured by the four LHC experiments, divided by the corresponding pQCD calculation including the nuclear modifications from EPS09 [57]. The calculation describes all the data within uncertainties. However, none of the experiments can exclude the calculations without accounting for nuclear modifications as it is shown in the bottom panel of Figure 5.4.

5.2.3 Related measurements in ALICE

Another analysis was performed in ALICE to measure the W-boson production cross section in p-Pb collisions at $\sqrt{s_{\text{NN}}} = 5.02\text{TeV}$. This measurement has the same motivation as the Z-boson one in testing and constraining the nuclear modifications of the PDFs.

The left and right panels of Figure 5.5 shows the production cross sections for the W^+ and the W^- bosons respectively. The statistical uncertainties are represented by vertical error bars, while the systematic ones are represented by black boxes around the points. The measurement was done using muon tracks that have transverse momenta larger than $10\text{ GeV}/c$ in the two center-of-mass of rapidity regions $2.03 < y_{\text{cms}} < 3.53$ and $-4.46 < y_{\text{cms}} < -2.96$. The W-bosons production cross sections were compared to the same calculations as for the Z-boson ones. Both the NLO pQCD calculations with the CT10 PDFs (blue hatched boxes) and the NNLO FEWZ calculations using the MSTW2008 PDF set (blue filled boxes) describe the data within uncertainties. The inclusion of a parameterisation of the nuclear modification of the PDFs in the calculations (red hatched boxes for pQCD and

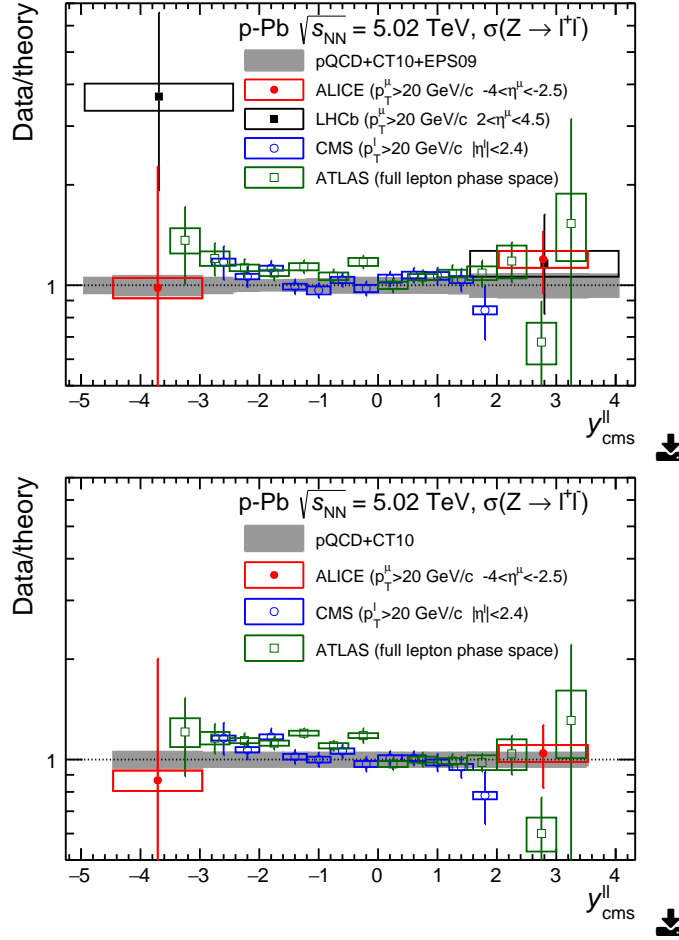


Figure 5.4: Z-boson production cross section measured by the four LHC experiments in p-Pb collisions at $\sqrt{s_{NN}} = 5.02$ TeV and divided by theoretical calculations from pQCD+CT10+EPS09 (top) and pQCD+CT10 (bottom). The LHCb points in the top panel have been shifted by +0.02 units of rapidity for better visibility. The ATLAS cross sections are measured in a slightly smaller invariant mass range ($66 < M_{ll} < 116$ GeV/ c^2) compared to the other experiments ($60 < M_{ll} < 120$ GeV/ c^2). Figure taken from [128].

red filled boxes for FEWZ) results in a slightly lower value of the cross section, especially at forward rapidity. This variation, however, is of the same order as the theoretical and/or experimental uncertainties, thus limiting the discriminating power of the measured cross sections.

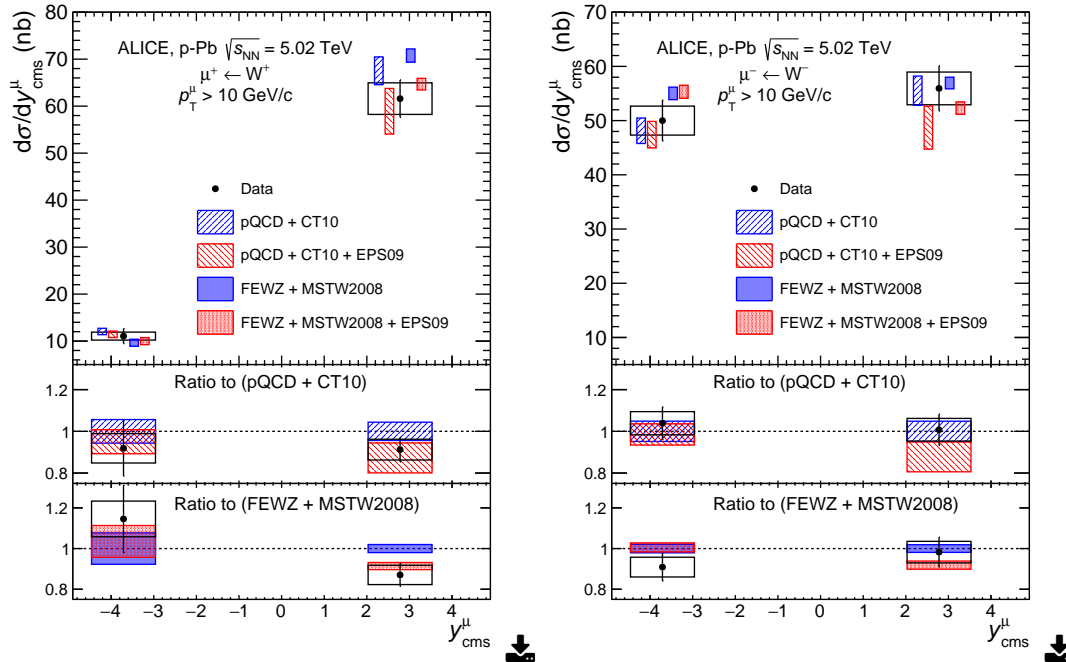


Figure 5.5: Left (right) panel: W^- (W^+) boson production cross section as a function of the center-of-mass rapidity measured in p-Pb collisions at $\sqrt{s_{NN}} = 5.02\text{TeV}$. The results are compared to theoretical calculations performed both with and without including the nuclear modification of the PDFs using the EPS09 parametrization. In the top panels, the calculations are shifted along the x-axis to improve the visibility. The middle (bottom) panel shows the data and pQCD (FEWZ) calculations divided by the pQCD (FEWZ) calculations without nuclear modification of the PDFs. Figure taken from [128].

5.2.4 Conclusions and discussion

The inclusive Z-boson production cross section has been measured via the dimuon decay channel in two center-of-mass rapidity regions for the first time with ALICE in p-Pb collisions at $\sqrt{s_{NN}} = 5.02\text{TeV}$. With respect to similar measurements from the other LHC experiments at the same center-of-mass energy, this cross section has smaller uncertainties than the corresponding LHCb one which is computed in similar rapidity regions as ALICE. It is complementary to the ATLAS and CMS ones measured at mid-rapidity.

The measured cross sections are in agreement with different theoretical pre-

dictions from pQCD and FEWZ calculations with and without accounting for the modification nuclear of the PDFs using the EPS09 parametrization. In the two studied rapidity regions, the size of the nuclear modification of the cross section is smaller than the statistical uncertainty of the measurement which limits the constraining power of the measurement.

5.3 Z-boson production in Pb-Pb collisions at

$$\sqrt{s_{NN}} = 5.02\text{TeV}$$

In Pb-Pb collisions at $\sqrt{s_{NN}} = 5.02\text{TeV}$, the Z-boson invariant yield is calculated in the same fiducial region as in p-Pb collisions at $\sqrt{s_{NN}} = 5.02\text{TeV}$ using the formula:

$$dN/dy = \frac{N_Z}{N_{MB} \cdot \Delta y \cdot A\varepsilon}, \quad (5.3)$$

where N_Z , N_{MB} and $A\varepsilon$ are respectively the number of Z-boson candidates, the equivalent number of minimum-bias events and the Acceptance times Efficiency of the detector. In the following, the results of the Z-boson invariant yield are presented as a function of rapidity as well as a function of the collision centrality. In order to compare the results to cross section calculations from theoretical models, the invariant yield is divided by the average nuclear overlap function ($\langle T_{AA} \rangle$). The values of $\langle T_{AA} \rangle$ in the different studied centrality intervals are summarized in Table 5.3.

Dividing by the Z-boson production cross section in pp collisions at the same center-of-mass energy, one can get the nuclear modification factor R_{AA} :

$$R_{AA} = \frac{dN/dy}{\langle T_{AA} \rangle \cdot \sigma_{pp}} \quad (5.4)$$

As it was discussed in chapter 4, the collected statistics by ALICE in pp collisions at $\sqrt{s} = 5.02\text{TeV}$ was not sufficient to measure a Z-boson production cross section. Alternatively, a theoretical pp cross section is used in the evaluation of the R_{AA} . This cross section is calculated in the pQCD framework [65] using the CT14 PDF (NLO) set [55]. Table 5.4 summarizes the values of the cross sections in the different studied rapidity ranges. It is worth noting that the pQCD cross section, in $2.5 < y < 4$, calculated using the CT10 PDF (NLO) set [54] is $\sigma_{Z \rightarrow \mu^+ \mu^-}^{pp, CT10} = 11.93 \pm 0.54$ pb and compatible within uncertainty with the one calculated using the CT14 PDF set in the same pQCD framework.

Centrality	$\langle T_{AA} \rangle$ (mb)	$\langle N_{\text{part}} \rangle$	$\langle N_{\text{coll}} \rangle$	$\langle N_{\text{part}} \rangle N_{\text{coll}}$
0-90%	6.2 ± 0.2	126 ± 2	435 ± 41	263 ± 3
0-20%	18.8 ± 0.6	311 ± 3	1318 ± 130	322 ± 3
20-90%	2.61 ± 0.09	73 ± 1	183 ± 15	141 ± 2

Table 5.3: Values of the average nuclear overlap factor, $\langle T_{AA} \rangle$ the number of participating nucleons, $\langle N_{\text{part}} \rangle$, and the number of binary nucleon-nucleon collisions, $\langle N_{\text{coll}} \rangle$, for each centrality interval. The average number of participants as weighted by the average number of collisions, $\langle N_{\text{part}} \rangle N_{\text{coll}}$, is also reported.

y range	$\sigma_{Z \rightarrow \mu^+ \mu^-}^{pp, CT14} \pm$ (pb)
$2.5 < y < 3$	5.56 ± 0.19
$3 < y < 4$	6.36 ± 0.26
$2.5 < y < 4$	11.92 ± 0.43

Table 5.4: Z-boson production cross section in pp collisions at $\sqrt{s} = 5.02$ TeV obtained from pQCD calculation using the CT14 PDF set in different rapidity ranges.

5.3.1 Integrated in rapidity and centrality

In the 0-90% centrality interval, the invariant yield divided by $\langle T_{AA} \rangle$ is measured to be $\frac{dN/dy}{\langle T_{AA} \rangle} = 6.11 \pm 0.76$ (stat) ± 0.38 (sys) pb. The first uncertainty is of statistical origin while the second one is systematic and corresponds to the contribution of the different uncertainty sources summarized in Table 5.5.

Figure 5.6 shows the measured invariant yield (black point) with the statistical uncertainty represented by the horizontal error bar and the systematic one by a yellow band. In the same figure, the invariant yield is compared to different theoretical calculations (colored boxes). From top to bottom, the calculations correspond to the following models:

- **CT14:** calculation in this model is similar to the one in simple pp collisions, but in addition, it takes into account the isospin effect coming from the difference between proton-proton, proton-neutron and neutron-neutron binary collisions¹. With respect to the pp case, an increase of the Z-boson invariant

¹The bound neutron PDFs are obtained from the bound proton PDFs by assuming isospin symmetry which implies that (i) the PDF of a u (d) quark in the proton is similar to the one of d (u)

yield by about 6% is observed. This calculation overestimates the measured invariant yield by about 2.3σ calculated by considering both the statistical and systematic uncertainties of the measurement.

- **CT14+EPS09:** in this model, the PDFs from CT14 are modified using the EPS09 parametrization. Within uncertainties, this model is in agreement with the measured invariant yield.
- **CT14+EPPS16:** the EPPS16 nPDF (NLO) set [61] supersedes the EPS09 (NLO) [57] by adding new experimental results in the global fit analysis. The new datasets include results on neutrino-nucleus DIS [137], as well as new LHC data such that the electroweak bosons production in p-Pb collisions at $\sqrt{s} = 5.02\text{TeV}$ measured by ATLAS [91] and CMS [92, 138] and the dijet measurement in the same collision system measured by CMS [139]. It is worth noting that the included LHC electroweak data provide small constraints on the nPDFs at the current perturbative order of the calculation (NLO). Also with respect to EPS09, the new analysis allows more freedom for the flavour dependence of nuclear effects which results in larger uncertainties. This model is also in agreement within uncertainties with the measured invariant yield.
- **nCTEQ15:** the nPDFs from the nCTEQ15 (NLO) parametrization [140] are obtained by fitting the nuclear data in an analogous way as done for free proton data, but using a parameterisation that depends on the atomic mass of the nucleus. The recent data used in EPPS16 (neutrino-nucleus DIS, and LHC electroweak and dijet measurements) are not yet included in the nCTEQ15 analysis. However, it is shown in Ref [141] that including the LHC electroweak data in the analysis has a small impact on the nCTEQ15 parametrization. Within uncertainties, the calculated Z-boson invariant yield from this model agrees with the calculations from EPS09 and EPPS16 as well as with the measurement.

The R_{AA} is then obtained by dividing the invariant yield by the pp cross section predicted by CT14 (Table 5.4). This is shown in the right panel of Figure 5.6 where

quark in the neutron, and (ii) the PDFs of other flavors are similar in protons and neutrons.

the R_{AA} is deviated from unity by 2.1σ .

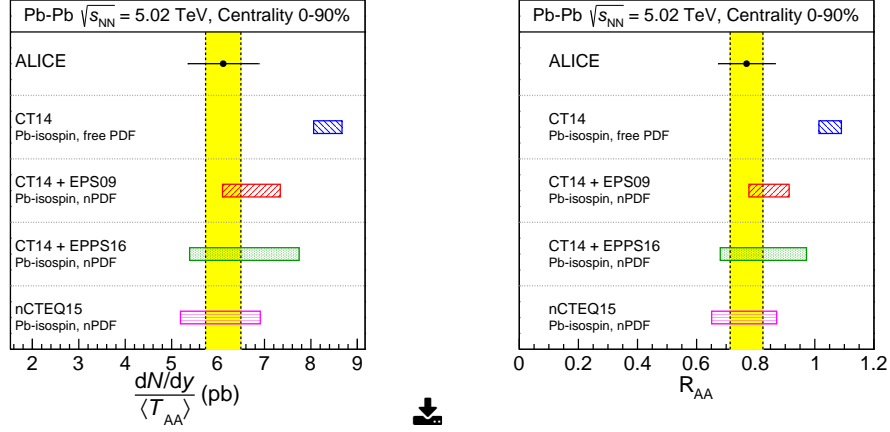


Figure 5.6: The invariant yield (left) and the R_{AA} (right) of the Z-boson production in $2.5 < y < 4$ divided by the average nuclear overlap function in the 0 – 90% centrality interval. The results are compared to theoretical calculations with and without including the nuclear modification of the PDFs [142].

Signal extraction	< 1
F_{norm}	$0.5^{*\dagger}$
$\langle T_{AA} \rangle$	$3.2-3.5^*$
pp cross section	$3.6-4^\dagger$
$A\varepsilon$ calculation	
Muon tracking efficiency	3^\dagger
Muon trigger efficiency	1.5^\dagger
Muon matching efficiency	1^\dagger
Cluster resolution effect	3.5^\dagger

Table 5.5: The different contributions to the total systematic uncertainties (in %) on the invariant yield and R_{AA} of the Z-boson in Pb-Pb collisions at $\sqrt{s_{NN}} = 5.02$ TeV. The uncertainty on the pp cross section affects only the R_{AA} . Uncertainties marked with * (\dagger) are correlated as a function of rapidity (centrality) and they are added to the global uncertainty in Figure 5.7 (Figure 5.8).

5.3.2 Rapidity dependence

Similar to the integrated case, the rapidity dependence of the invariant yield and the R_{AA} are determined. The collected statistics allows to perform the measurement in two rapidity ranges, $2.5 < y < 3$ and $3 < y < 4$.

The measured invariant yields in these two ranges are shown in the top panel of Figure 5.7. They are compared to theoretical calculations based on the PDF set CT14 with and without including the nuclear effects from EPPS16. The calculation that does not include nuclear effects systematically overestimates the measured invariant yields. The value of this calculation is separated by 2σ from the results in the rapidity interval $3 < y < 4$.

Using the CT14 pp cross section as a reference, the rapidity dependence of the R_{AA} is also obtained and shown in the bottom panel of Figure 5.7. The R_{AA} rapidity dependence is well reproduced by EPPS16 calculation within uncertainties.

5.3.3 Centrality dependence

Finally, the invariant yield and the R_{AA} are computed in two centrality intervals (0-20% and 20-90%). In heavy-ion collision measurements, the centrality of the collision is commonly quantified by the average number of nucleons participating in the interaction ($\langle N_{\text{part}} \rangle$). As the Z-boson production is a hard process, it scales with the average number of colliding nucleons ($\langle N_{\text{coll}} \rangle$), therefore the average centrality at which they are produced is better quantified by the average number of participant nucleons scaled by the number of colliding nucleons ($\langle N_{\text{part}} \rangle_{N_{\text{coll}}}$).

The measured invariant yield and the R_{AA} as a function of $\langle N_{\text{part}} \rangle_{N_{\text{coll}}}$ are shown respectively in the top and bottom panels of Figure 5.8. A hint of a decrease of the invariant yield toward most central collisions can be seen, even if the values in the two centrality intervals are compatible within uncertainties. The R_{AA} is compatible with unity in the most peripheral collisions, but it is smaller than unity by 2.6σ in the most central events. The data are compared to calculations including a centrality-dependent nuclear modification of the PDFs using the EPS09 parametrization: the obtained centrality dependence is small and the calculations describe data within uncertainties.

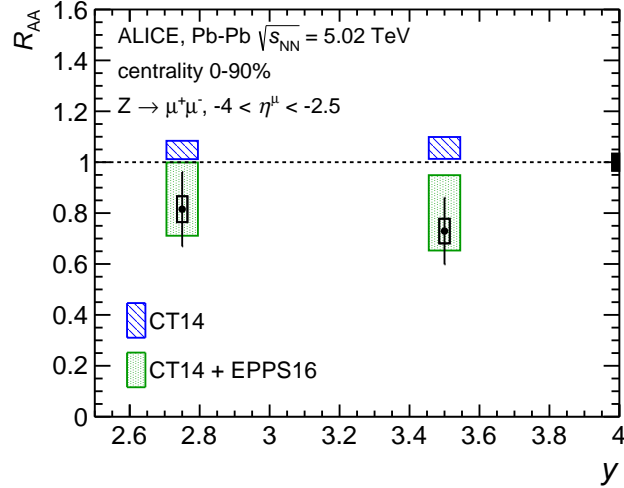
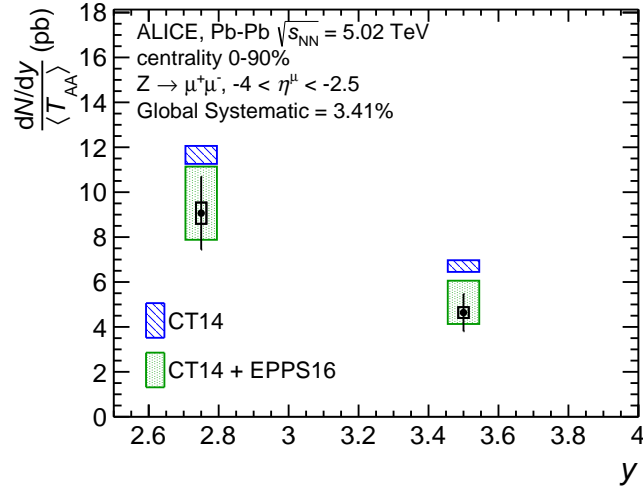


Figure 5.7: The invariant yield (top) and the R_{AA} (bottom) of the Z-boson production as a function of rapidity and divided by the average nuclear overlap function in the 0 – 90% centrality interval. The results are compared to theoretical calculations with and without including the nuclear modification of the PDFs from the EPPS16 parametrization [142].

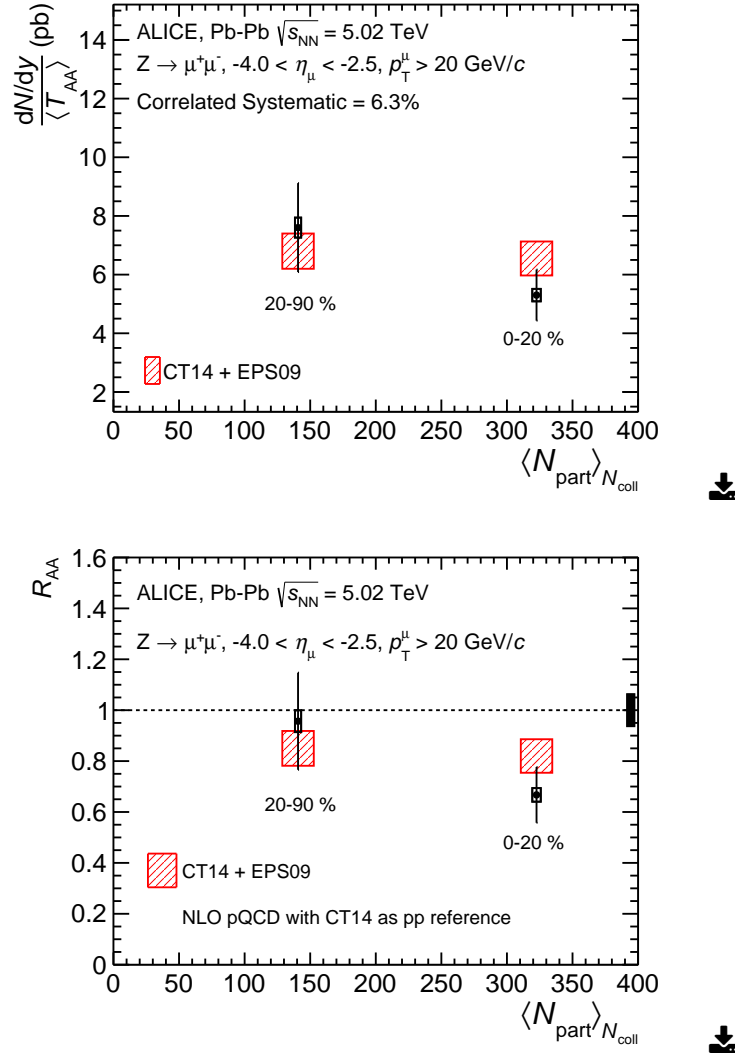


Figure 5.8: The invariant yield (top) and the R_{AA} (bottom) of the Z-boson production as a function of the collision centrality and divided by the average nuclear overlap functions. The results are compared to theoretical calculations with and without including the nuclear modification of the PDFs from the EPS09 parametrization [142].

The numerical values of the measured invariant yields and the R_{AA} as well as the ones from different theoretical calculations in the different studied rapidity and centrality intervals are summarized in Table 5.6, Table 5.7, and Table 5.8.

Centrality 0-90%, $2.5 < y < 4$		
	$\frac{dN/dy}{\langle T_{AA} \rangle}$ (pb)	R_{AA}
Data	$6.11 \pm 0.76 \pm 0.38$	$0.77 \pm 0.10 \pm 0.05$
CT14	8.36 ± 0.31	1.05 ± 0.04
CT14+EPPS16	6.57 ± 1.18	0.83 ± 0.15
CT14+EPS09	6.72 ± 0.62	0.85 ± 0.07
nCTEQ15	6.05 ± 0.86	0.76 ± 0.11

Table 5.6: Comparison between the integrated Z-boson invariant yield and R_{AA} in Pb-Pb collisions at $\sqrt{s_{NN}} = 5.02$ TeV and different theoretical calculations.

Centrality 0-90% vs y (correlated sys: 3.4%)				
	$2.5 < y < 3$		$3 < y < 4$	
	$\frac{dN/dy}{\langle T_{AA} \rangle}$ (pb)	R_{AA}	$\frac{dN/dy}{\langle T_{AA} \rangle}$ (pb)	R_{AA}
Data	$9.07 \pm 1.63 \pm 0.47$	$0.82 \pm 0.15 \pm 0.05$	$4.64 \pm 0.83 \pm 0.24$	$0.73 \pm 0.13 \pm 0.05$
CT14	11.66 ± 0.40	1.05 ± 0.04	6.71 ± 0.26	1.06 ± 0.04
CT14+EPPS16	9.51 ± 1.63	0.86 ± 0.14	5.10 ± 0.97	0.80 ± 0.15

Table 5.7: Comparison between the Z-boson invariant yield and R_{AA} in Pb-Pb collisions at $\sqrt{s_{NN}} = 5.02$ TeV and different theoretical calculations in two rapidity intervals.

$2.5 < y < 4$, vs centrality (correlated sys: 5.1% (yield), 6.3% (R_{AA}))				
	0-20%		20-90%	
	$\frac{dN/dy}{\langle T_{AA} \rangle}$ (pb)	R_{AA}	$\frac{dN/dy}{\langle T_{AA} \rangle}$ (pb)	R_{AA}
Data	$5.30 \pm 0.87 \pm 0.21$	$0.67 \pm 0.11 \pm 0.03$	$7.60 \pm 1.51 \pm 0.34$	$0.96 \pm 0.19 \pm 0.04$
CT14+EPS09	6.55 ± 0.58	0.82 ± 0.07	6.80 ± 0.60	0.85 ± 0.07

Table 5.8: Comparison between the Z-boson invariant yield and R_{AA} in Pb-Pb collisions at $\sqrt{s_{NN}} = 5.02$ TeV and theoretical calculation using the EPS09 parametrization in two centrality intervals.

5.3.4 Conclusions and discussion

The Z-boson production is measured for the first time at forward rapidity in Pb-Pb collisions at $\sqrt{s_{NN}} = 5.02$ TeV. The invariant yields divided by the average nuclear overlap functions are evaluated as a function of the rapidity and of the collision centrality. The corresponding nuclear modification factor values are estimated by dividing the measured invariant yields in Pb-Pb collisions by the expected cross-sections in pp collisions at the same center-of-mass energy estimated with NLO pQCD calculations that use the CT14 free PDFs. In the 0-90% centrality interval, the measured invariant yield is in a good agreement with pQCD calcula-

tions that include the modification of the PDFs in the nuclei using three different parametrizations, EPS09, EPPS16, and nCTEQ15. Without accounting for the nuclear modification, the CT14 alone overestimates the measurement by 2.3σ . The EPPS16 calculations describe also well the rapidity dependence of the measured invariant yield.

As a function of centrality, the R_{AA} is compatible with unity in the 20-90% centrality interval, while it is smaller than unity by 2.6σ in the 0-20% most central collisions. The results are described by theoretical calculations that include nuclear modifications of the PDFs using the EPS09 parametrizations.

J/ψ PRODUCTION RESULTS

This chapter reports the results of the inclusive J/ψ production in Pb-Pb collisions at $\sqrt{s_{\text{NN}}} = 5.02\text{TeV}$. First, the J/ψ invariant yields as a function of p_{T} in different centrality intervals are presented. Using these yields, the centrality dependence of the J/ψ average p_{T} and average squared p_{T} are extracted. Then the nuclear modification factor is presented as a function of centrality, p_{T} and rapidity. Results of the different observables are compared to results at lower collision energy and to available theoretical calculations.

6.1 Introduction and summary from previous chapters

The J/ψ production analysis strategy was presented in chapter 4. The signal extraction was performed by fitting the opposite-charge dimuon invariant mass distribution by functions that account for the J/ψ signal as well as for the background contribution. The extracted yields were further corrected by the acceptance times efficiency ($A\varepsilon$) of the detector obtained using a MC where J/ψ were embedded into real events.

The systematic uncertainties that affect the determination of the J/ψ invariant

yields and nuclear modification factor (R_{AA}) were also discussed in chapter 4. In the following, these uncertainties and their sizes in this analysis are summarized:

- Systematic uncertainty on the J/ψ signal extraction: this corresponds to the variation of the number of J/ψ obtained using different fit configurations. As a function of centrality, rapidity, and p_T , this uncertainty contributes to the uncorrelated uncertainty of the invariant yield and R_{AA} .
- The uncertainty on the centrality limits is due to the resolution of the centrality determination. It can affect the number of J/ψ extracted in different centrality intervals. For each centrality interval, this uncertainty corresponds to the variation of the extracted number of J/ψ when varying the used centrality estimators which have an impact on the definition of the centrality intervals. A maximum uncertainty of 5% is obtained in the most peripheral centrality interval (85–90%) vanishing toward the most central events. This uncertainty contributes to the uncorrelated (correlated) uncertainty of the R_{AA} centrality (p_T and y) dependence.
- The systematic uncertainty on the $A\varepsilon$ calculation includes the contribution from uncertainties on the tracking efficiency, trigger efficiency, matching efficiency, and on the MC input functions. These uncertainties contribute to the uncorrelated (correlated) uncertainty of the R_{AA} p_T and y (centrality) dependence.
For the tracking and trigger efficiency, an additional uncertainty related to the collision centrality is added. It is negligible in peripheral collisions and increases up to 1% when going to the most central ones.
- The uncertainty on the MB normalization is due to the uncertainty on the calculation of F_{norm} and it is added to the R_{AA} correlated uncertainty.
- The systematic uncertainty on the determination of the J/ψ pp cross section (σ^{pp}) is in three sources, a statistical one, an uncorrelated systematic one and a correlated one that corresponds to the uncertainty on the branching ratio and luminosity. The correlated one is added to the correlated uncertainties in the R_{AA} results, while the statistical and systematic ones are added in

quadrature and contribute either to the R_{AA} correlated uncertainty when determining the R_{AA} centrality dependence or to the uncorrelated ones when determining the p_T or rapidity dependence of the R_{AA} .

- The uncertainty on the calculation of $\langle T_{AA} \rangle$. This uncertainty varies from $\sim 3\%$ in the most central events to $\sim 6\%$ in the most peripheral ones and contributes to the uncorrelated (correlated) uncertainty of the R_{AA} centrality (p_T and y) dependence.

Table 6.1 summarizes these uncertainties as a function of centrality, p_T , and rapidity.

source	vs centrality	vs p_T	vs y
Signal extraction	1.5–3.6	1.5–3.6	1.5–5
MB normalization	0.5*	0.5*	0.5*
$\langle T_{AA} \rangle$	3.1–6	3.2–4.5*	3.2–4.5*
Centrality limits	0.1–3.5	0–1.4*	0–1.4*
$A\varepsilon$ calculation			
Tracking efficiency	$3^* \oplus 0-1$	$3 \oplus 0-1^*$	$3 \oplus 0-1^*$
Intrinsic trigger efficiency	1.5*	1.5	1.5
Trigger response	$0-2.2^* \oplus 0-1$	$0-3.8 \oplus 0-1^*$	$0-1.9 \oplus 0-1^*$
Matching efficiency	1*	1	1
MC parametrization	2*	2–3	0.5–2.5
pp cross section			
Statistical	1.4–10*	2.5–20	3–6
Uncorrelated systematic	3.5–4.5*	3–9	4–7.5
Correlated systematic	2.1*	2.1*	2.1*

Table 6.1: Summary of the systematic uncertainties (in %) on the J/ψ yields and R_{AA} calculation as a function of centrality, p_T and rapidity. Values with an asterisk correspond to the cases where the systematic uncertainties are fully correlated as a function of the given variable.

Throughout the following sections, a p_T cut ($p_T > 300 \text{ MeV}/c^2$) has been applied in the J/ψ analysis. The motivation behind it is to reduce the possible contamination

from J/ψ photo-production. Indeed, at $\sqrt{s_{NN}} = 2.76$ TeV, ALICE has reported a J/ψ excess at very low p_T [143] and photo-production was identified as the most likely source of this excess. At $\sqrt{s_{NN}} = 5.02$ TeV [144], this cut would reject $\sim 80\%$ of the photo-produced J/ψ assuming that the relative contribution of the incoherent over coherent components is the same as the one estimated in ultra-peripheral collisions.

6.2 J/ψ invariant yields

The differential J/ψ invariant yields $\left(\frac{d^2Y_{J/\psi}^i}{dydp_T}\right)$ are obtained in a centrality interval "i" using the formula:

$$\frac{d^2Y_{J/\psi}^i}{dydp_T} = \frac{N_{J/\psi}^i}{\Delta p_T \cdot \Delta y \cdot BR_{J/\psi \rightarrow \mu\mu} \cdot A\varepsilon^i(p_T, y) \cdot N_{MB}^i}, \quad (6.1)$$

where Δp_T and Δy are respectively the widths of the p_T and rapidity intervals, $N_{J/\psi}^i$ is the number of extracted J/ψ , $BR_{J/\psi \rightarrow \mu\mu} = 5.96 \pm 0.03\%$ is the dimuon branching ratio of the J/ψ dimuon decay [1], N_{MB}^i is the equivalent number of minimum-bias events and $A\varepsilon^i$ is the Acceptance times efficiency of the detector. The p_T dependence of the J/ψ invariant yields is shown in Figure 6.1 in seven centrality intervals. For each distribution, the statistical uncertainties are represented by vertical error bars while the systematic uncertainties uncorrelated as a function of p_T are shown as open boxes around the points. The correlated systematic uncertainties versus p_T are not shown.

The J/ψ photo-production contamination can be responsible for the relative increase of the yield at low p_T ($p_T < 0.5$ GeV/c) in the most peripheral collisions (60–90%) with respect to other centrality intervals.

6.2.1 J/ψ average p_T

The hardness of the different yields vary from one centrality interval to another. This hardness can be quantified by the average p_T . In order to calculate the J/ψ average p_T , the p_T distributions are fitted (Figure 6.2) with the function:

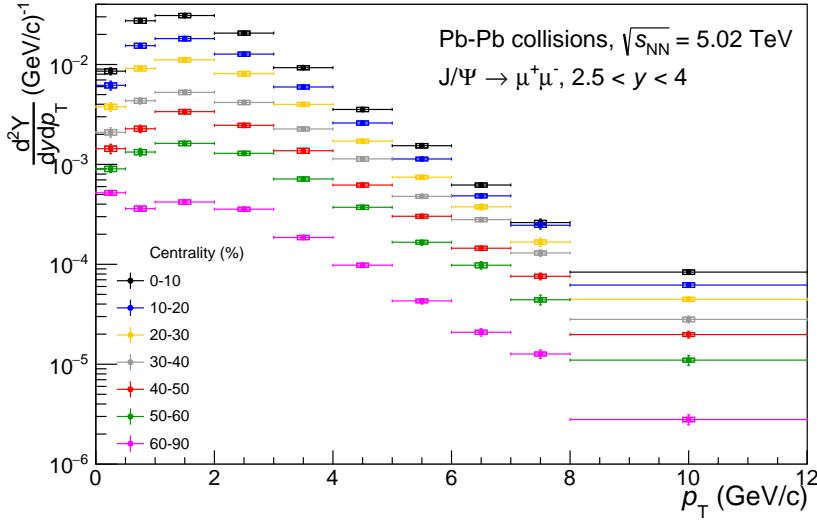


Figure 6.1: Inclusive J/ψ invariant yields as a function of p_T in Pb-Pb collisions at $\sqrt{s_{NN}} = 5.02\text{TeV}$ for seven centrality intervals and in the rapidity range $2.5 < y < 4$. The vertical error bars represent the statistical uncertainties while the uncorrelated systematic ones are represented by open boxes around the points [This thesis].

$$f(p_T) = C \cdot \frac{p_T}{\left(1 + (p_T/p_0)^2\right)^n}, \quad (6.2)$$

where the three parameters C , p_0 and n are left free when performing the fits. This function is commonly used to reproduce the quarkonia p_T distribution in hadronic collisions, so it cannot reproduce the J/ψ photo-production component. For this reason, the p_T interval that contains the largest fraction of photo-produced J/ψ ($0 < p_T < 0.5\text{ GeV}/c$) is excluded from the fit. The plotted dashed lines in this interval are the extrapolations of the fitted functions.

The average p_T ($\langle p_T \rangle$) and the average squared p_T ($\langle p_T^2 \rangle$) are then calculated as the first and second order momentum of $f(p_T)$ respectively. In general the k^{th} order momentum (M_k) of $f(p_T)$ is given by:

$$M_k = \frac{\int p_T^k \cdot f(p_T) dp_T}{\int f(p_T) dp_T}. \quad (6.3)$$

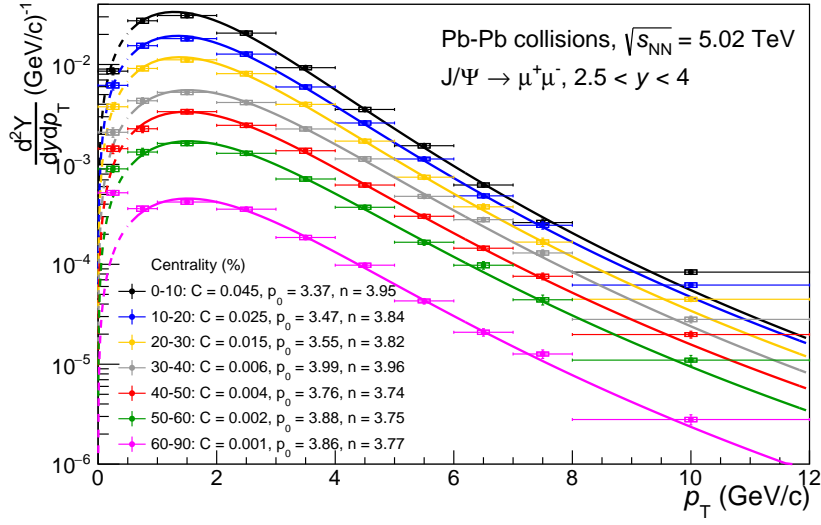


Figure 6.2: Inclusive J/ψ invariant yields as a function of p_T in Pb-Pb collisions at $\sqrt{s_{\text{NN}}} = 5.02 \text{ TeV}$ for seven centrality intervals and in the rapidity range $2.5 < y < 4$. The distributions are fitted with the function $f(p_T) = C \cdot \frac{p_T}{(1+(p_T/p_0)^2)^n}$. The values of the three parameters C , p_0 , and n are shown for each centrality interval in the legend [This thesis].

In a given centrality interval, the central values of $\langle p_T \rangle$ and $\langle p_T^2 \rangle$ are obtained by fitting the p_T distribution in which the statistical and uncorrelated systematic uncertainties are summed in quadrature. The statistical (systematic) uncertainties on $\langle p_T \rangle$ and $\langle p_T^2 \rangle$ correspond to fitting distributions that contain only statistical (uncorrelated systematic) uncertainties. Since the $\langle p_T \rangle$ is only related to the shape of the distribution and not to its magnitude, the correlated uncertainties versus p_T are not considered in the fits.

The top panel of Figure 6.3 shows the J/ψ $\langle p_T \rangle$ in Pb-Pb collisions at $\sqrt{s_{\text{NN}}} = 5.02 \text{ TeV}$ as a function of $\langle N_{\text{part}} \rangle$. Statistical uncertainties are represented by vertical error bars while the systematic ones are represented by open boxes around the points. For the two most peripheral centrality intervals (50–60 % and 60–90 %), the plotted brackets represent the possible range of variation of the hadronic J/ψ $\langle p_T \rangle$ for two extreme hypotheses on J/ψ the photo-production contamination. The lower limit bracket corresponds to the assumption that no contribution from

photo-produced J/ψ , while the upper one corresponds to the hypothesis that all the J/ψ with p_T smaller than 300 MeV/c are photo-produced.

In the four most peripheral centrality intervals ($\langle N_{\text{part}} \rangle < 150$), the J/ψ $\langle p_T \rangle$ distribution is constant and compatible with the measurement in pp collisions at $\sqrt{s} = 5.02$ TeV ($\langle p_T \rangle_{pp} = 2.31 \pm 0.02$ (stat) ± 0.02 (sys) [98]). A significant decrease is observed when going to more central collisions. The values of the J/ψ $\langle p_T \rangle$ in the most central (0–10 %) and most peripheral collisions (60–90%) are separated by more than 5σ .

The variable r_{AA} is defined by:

$$r_{AA} = \frac{\langle p_T^2 \rangle_{AA}}{\langle p_T^2 \rangle_{pp}}, \quad (6.4)$$

where the numerator and denominator are respectively the J/ψ $\langle p_T^2 \rangle$ measured in AA (Pb-Pb in the present analysis) and pp collisions [98]. The centrality dependence of the r_{AA} at $\sqrt{s_{NN}} = 5.02$ TeV is shown in the bottom panel of Figure 6.3. The vertical error bars represent the quadratic sum of the statistical and uncorrelated systematic uncertainties while the correlated one, which accounts for the uncertainty on $\langle p_T^2 \rangle_{pp}$, is represented by a filled box around unity. Similar to the $\langle p_T \rangle$, the r_{AA} decreases significantly from peripheral to central collisions. To understand this decrease, one can list the different hot and cold nuclear effects on the J/ψ production in heavy-ion collisions that may affect the centrality dependence of the $\langle p_T \rangle$ and r_{AA} :

- **Color screening dissociation:** this effect is expected to make the J/ψ p_T shape harder since high p_T J/ψ can escape without being suppressed by the QGP. In addition, the more central the collision, the larger this effect is expected to be, which means that one expects an increase of the J/ψ $\langle p_T \rangle$ from peripheral to central collisions due to this effect.
- **The Cronin effect:** this effect, due to gluon multiple scatterings with the constituents of the medium, has a direct influence on the p_T distributions and hence on the J/ψ $\langle p_T \rangle$. The more important this effect, the broader the p_T distribution is expected to be. In heavy-ion collisions, the size of the medium increases toward the most central collisions which means that Cronin effect

is more important in central collisions than it is in peripheral ones. Therefore, due to this effect alone, the $\langle p_T \rangle$ would be larger in central collisions than in peripheral ones.

- **J/ψ regeneration:** this effect is more important when going toward the most central collisions due to the increasing number of $c\bar{c}$ pairs in the collision. Moreover, the regeneration favors low p_T J/ψ , thus increases the yield at low p_T . As a result of this effect, the J/ψ $\langle p_T \rangle$ is expected to decrease when going from peripheral collisions toward central ones as is qualitatively observed in the data.

The r_{AA} at $\sqrt{s_{NN}} = 5.02\text{TeV}$ (red points) is compared to the one measured at $\sqrt{s_{NN}} = 2.76\text{TeV}$ (blue) [145] in Figure 6.4. The number of J/ψ reconstructed in Pb-Pb collisions at $\sqrt{s_{NN}} = 5.02\text{TeV}$ is about seven times the one at $\sqrt{s_{NN}} = 2.76\text{TeV}$. This allows having the centrality dependence in finer centrality intervals. Within uncertainty, the results at two energies are compatible with each other and compatible with unity in the most peripheral collisions. In Ref [145], the r_{AA} results in Pb-Pb collisions at $\sqrt{s_{NN}} = 2.76\text{TeV}$ were compared to other experimental results at lower collision energies ($\sqrt{s_{NN}} = 200\text{ GeV}$ at RHIC [146] and $\sqrt{s_{NN}} = 17\text{ GeV}$ at SPS [147]). A very different centrality dependence was seen as the r_{AA} increases (especially at SPS energy) toward more central collisions. The different behaviors of r_{AA} at different energies can be explained by the increasing amount of J/ψ regeneration with energy.

The r_{AA} results at $\sqrt{s_{NN}} = 5.02\text{TeV}$ are also compared in Figure 6.4 to theoretical calculations based on a transport model [81]. This model is briefly described in Section 6.3.2 together with other models used for the comparison of the R_{AA} results. Similarly to the measurement, the r_{AA} obtained by these calculations decreases with centrality. However, this model systematically underestimates the measured r_{AA} . The tension between the data and the model is maximum in semi-central collisions ($\langle N_{\text{part}} \rangle \sim 120$) where the separation between them reaches $\sim 3\sigma$.

The numerical values of $\langle p_T \rangle$, $\langle p_T^2 \rangle$, and r_{AA} in pp and Pb-Pb collisions at $\sqrt{s_{NN}} = 5.02\text{TeV}$ can be found in Appendix D.

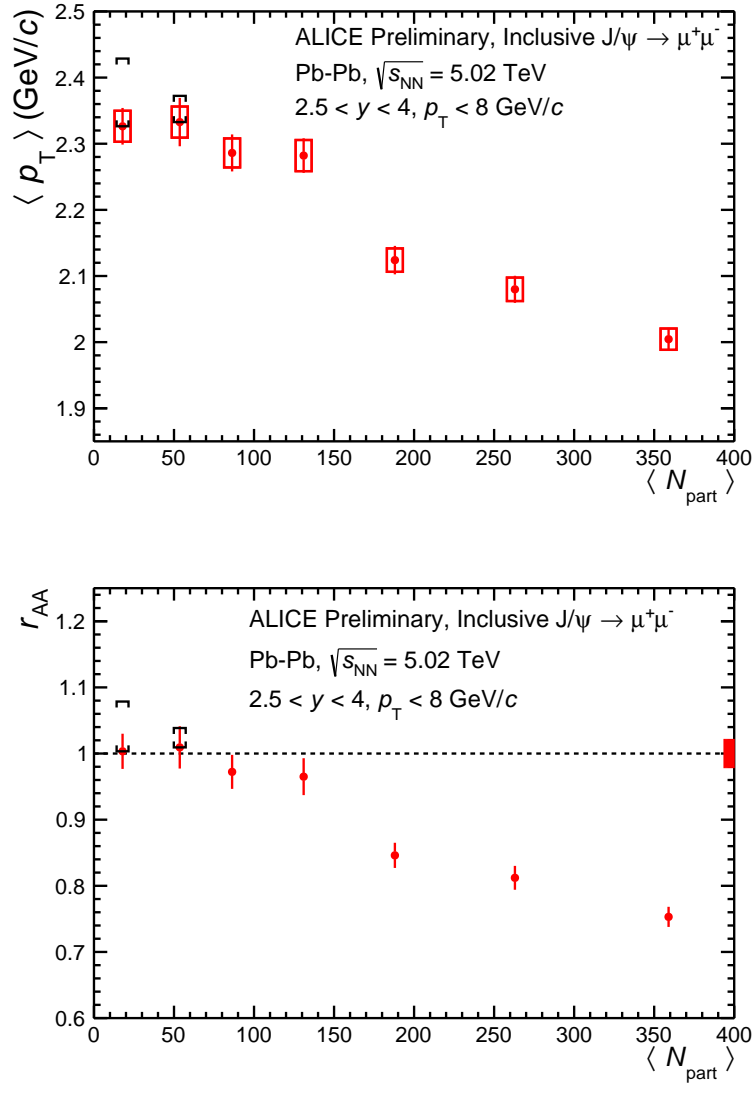


Figure 6.3: The inclusive J/ψ $\langle p_T \rangle$ (top) and r_{AA} (bottom) as a function of $\langle N_{part} \rangle$ in Pb-Pb collisions at $\sqrt{s_{NN}} = 5.02$ TeV.

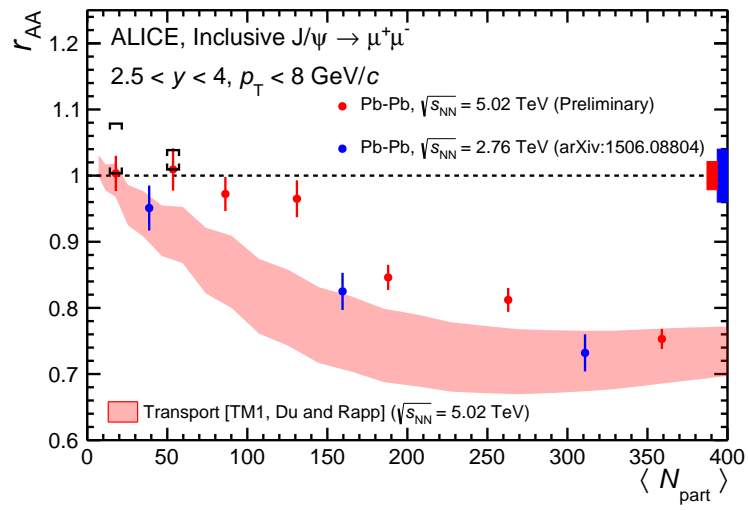


Figure 6.4: The inclusive J/ψ r_{AA} as a function of $\langle N_{\text{part}} \rangle$ measured by ALICE in Pb-Pb collisions at $\sqrt{s_{NN}} = 5.02 \text{ TeV}$ (red points) and compared to results at $\sqrt{s_{NN}} = 2.76 \text{ TeV}$ [145] (blue points) and to theoretical calculations based on a transport model [81] (red band).

6.3 Nuclear modification factor

In order to quantify the nuclear effects on the J/ψ production in heavy-ion collisions at a given collision energy, the nuclear modification factor (R_{AA}) can be used. In a centrality interval i and a kinematic range defined by a rapidity and p_T intervals Δy and Δp_T , the R_{AA} is defined as:

$$R_{AA} = \frac{N_{J/\psi}^i(\Delta y, \Delta p_T)}{\sigma_{J/\psi}^{pp}(\Delta y, \Delta p_T) \cdot BR_{J/\psi \rightarrow \mu\mu} \cdot N_{MB}^i \cdot A\varepsilon_{J/\psi}^i(\Delta y, \Delta p_T) \cdot \langle T_{AA} \rangle^i}, \quad (6.5)$$

where in addition to the terms used in the J/ψ invariant yield calculation (Equation D.1), $\langle T_{AA} \rangle^i$ is the average of the nuclear overlap function in the centrality interval i (Table 6.2) and $\sigma_{J/\psi}^{pp}(\Delta y, \Delta p_T)$ is the J/ψ cross section in the kinematic range $(\Delta y, \Delta p_T)$ measured in pp collisions at $\sqrt{s} = 5.02\text{TeV}$ with ALICE [98].

Centrality %	$\langle N_{part} \rangle$	$\langle T_{AA} \rangle$ (mb $^{-1}$)
0-10	359.0 ± 3.0	23.40 ± 0.08
10-20	263.0 ± 4.0	14.30 ± 0.05
20-30	188.0 ± 3.0	8.60 ± 0.03
30-40	131.0 ± 3.0	4.92 ± 0.02
40-50	86.3 ± 1.7	2.61 ± 0.01
50-60	53.6 ± 1.2	1.28 ± 0.06
60-70	30.4 ± 0.8	0.57 ± 0.03
70-80	15.6 ± 0.5	0.23 ± 0.02
80-90	7.6 ± 0.2	0.09 ± 0.01
0-20	311.0 ± 3.0	18.80 ± 0.61
20-40	159.6 ± 2.6	6.75 ± 0.22
40-90	38.7 ± 1.1	0.96 ± 0.04
60-90	17.7 ± 0.5	0.30 ± 0.02
0-90	126.1 ± 1.8	6.22 ± 0.20

Table 6.2: Values of the average nuclear overlap factor $\langle T_{AA} \rangle$ and the number of participating nucleons, $\langle N_{part} \rangle$ for different centrality intervals.

In the following, the R_{AA} results are presented in different centrality, p_T , and rapidity intervals. Wherever corresponding results in Pb-Pb collisions at

$\sqrt{s_{\text{NN}}} = 2.76\text{TeV}$ are available, a comparison between the R_{AA} at two energies is made. The R_{AA} results are also compared to available theoretical calculations.

It is worth noting that with the muon spectrometer, the prompt and non-prompt J/ψ cannot be discriminated, hence the presented results refer to inclusive J/ψ (prompt + non-prompt). However, the size of the variation of the prompt R_{AA} ($R_{\text{AA}}^{\text{prompt}}$) can be obtained by assuming two extreme hypotheses on the non-prompt R_{AA} ($R_{\text{AA}}^{\text{non-prompt}}$) using the relation:

$$R_{\text{AA}}^{\text{prompt}} = \frac{R_{\text{AA}} - F_B \cdot R_{\text{AA}}^{\text{non-prompt}}}{1 - F_B}, \quad (6.6)$$

where F_B is the ratio between the non-prompt and the inclusive J/ψ cross sections in pp collisions. It is obtained by an interpolation of the LHCb measurements in pp collisions at $\sqrt{s} = 2.76\text{TeV}$ [148] and $\sqrt{s} = 7\text{TeV}$ [149] as described in Appendix B. The two extreme hypotheses correspond to the total suppression of b-hadrons ($R_{\text{AA}}^{\text{non-prompt}} = 0$) and to no medium effects on the b-hadrons ($R_{\text{AA}}^{\text{non-prompt}} = 1$).

In the following presented results, similar to the $\langle p_T \rangle$ case, a double bracket plotted around a R_{AA} point represents the possible range of variation of the hadronic J/ψ R_{AA} for two extreme hypotheses on the photo-production contamination. The upper limit bracket corresponds to the assumption that no contribution from photo-produced J/ψ , while the lower one corresponds to the hypothesis that all the J/ψ with p_T smaller than 300 MeV/c are photo-produced.

6.3.1 Integrated R_{AA}

The J/ψ R_{AA} in Pb-Pb collisions at $\sqrt{s_{\text{NN}}} = 5.02\text{TeV}$ integrated over the centrality interval 0-90%, and in the kinematic range ($2.5 < y < 4$, $p_T < 12\text{ GeV}/c$) is equal to $0.65 \pm 0.01 \pm 0.05$. The first quoted uncertainty is statistical while the second one is systematic. This R_{AA} is smaller than unity by more than 6σ showing a significant J/ψ suppression.

In Pb-Pb collisions at $\sqrt{s_{\text{NN}}} = 2.76\text{TeV}$, the integrated R_{AA} was measured in the

p_T range $0 < p_T < 8$ GeV/c [150]. The R_{AA} values at the two energies in this p_T range are summarized in Table 6.3. The R_{AA} increases with energy by about 15 % but this increase is within the total uncertainties. The systematic uncertainty in Pb-Pb collisions at $\sqrt{s_{NN}} = 5.02$ TeV is about twice smaller than the one in Pb-Pb collisions at $\sqrt{s_{NN}} = 2.76$ TeV. This is mainly due to the large uncertainties on the tracking efficiency and the pp cross section at $\sqrt{s} = 2.76$ TeV. The R_{AA} differential calculations presented in the following sections can serve to determine if the two R_{AA} have more significance differences in specific centrality/kinematic ranges.

$R_{AA}(p_T < 8 \text{ GeV}/c, \sqrt{s_{NN}} = 5.02 \text{ TeV})$	$0.66 \pm 0.01 \text{ (stat)} \pm 0.05 \text{ (sys)}$
$R_{AA}(p_T < 8 \text{ GeV}/c, \sqrt{s_{NN}} = 2.76 \text{ TeV})$	$0.58 \pm 0.01 \text{ (stat)} \pm 0.09 \text{ (sys)}$

Table 6.3: J/ψ R_{AA} in the kinematic range ($2.5 < y < 4$, $p_T < 8$ GeV/c) in Pb-Pb collisions at $\sqrt{s_{NN}} = 5.02$ TeV and $\sqrt{s_{NN}} = 2.76$ TeV in the centrality interval 0–90%.

6.3.2 R_{AA} centrality dependence

All the hot medium effects on the J/ψ production presented in chapter 2 are expected to vary as a function of the energy density of the medium. In heavy-ion collisions, this density is related to the collision centrality. Figure 6.5 shows the centrality dependence of the J/ψ R_{AA} in Pb-Pb collisions at $\sqrt{s_{NN}} = 5.02$ TeV compared to the one measured in Pb-Pb collisions at $\sqrt{s_{NN}} = 2.76$ TeV [150] in the integrated kinematic range ($2.5 < y < 4$, $p_T < 8$ GeV/c). For both R_{AA} distributions, the statistical uncertainties are represented by vertical error bars and the uncorrelated systematic ones by open boxes around the points, while the correlated ones are represented by filled boxes around the unity axis. The decrease of the J/ψ R_{AA} with centrality is similar at both energies and saturates beyond $\langle N_{part} \rangle \sim 100$ which corresponds to the centrality interval 40–50 %. The central values of $R_{AA}(\sqrt{s_{NN}} = 5.02 \text{ TeV})$ are systematically larger than the ones of $R_{AA}(\sqrt{s_{NN}} = 2.76 \text{ TeV})$ but the two measurements remain compatible within uncertainties.

At $\sqrt{s_{NN}} = 5.02$ TeV, R_{AA}^{prompt} would be about 10% higher if $R_{AA}^{\text{non-prompt}} = 0$ and about 5% (1%) smaller if $R_{AA}^{\text{non-prompt}} = 1$ for central (peripheral) collisions.

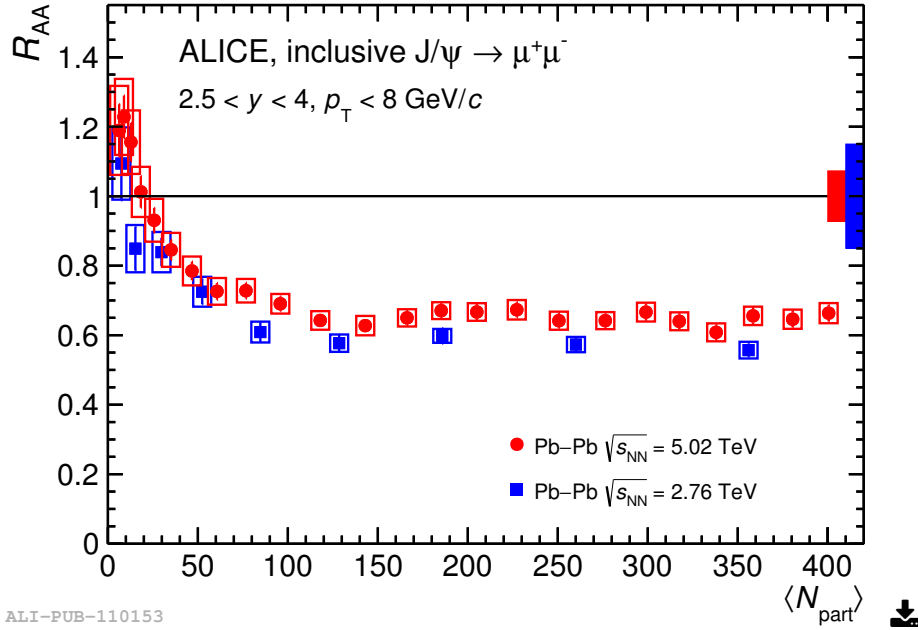


Figure 6.5: The inclusive J/ψ R_{AA} as a function of $\langle N_{\text{part}} \rangle$ at $\sqrt{s_{NN}} = 5.02$ TeV [144] (red) and $\sqrt{s_{NN}} = 2.76$ TeV [150] (blue). The error bars represent statistical uncertainties, the boxes around the points uncorrelated systematic uncertainties, while the centrality-correlated global uncertainties are shown as a filled box around unity.

In the two distributions of Figure 6.5, an excess ($R_{AA} > 1$) is seen in the two most peripheral centrality intervals due to a potential contribution from J/ψ photo-production. Figure 6.6 shows the effect of applying a p_T cut ($p_T > 300$ MeV/c) on the R_{AA} results in Pb-Pb collisions at $\sqrt{s_{NN}} = 5.02$ TeV. The excess in the most peripheral events is not seen anymore while the effect of this cut on the R_{AA} results in semi-central and most-central events is negligible.

The centrality dependence of the R_{AA} at $\sqrt{s_{NN}} = 5.02$ TeV is compared to different theoretical calculations as shown in the four panels of Figure 6.7. In the following, a brief description of these models and their ingredients are presented.

- **Transport model-1 (TM1) [81]:** this model is based on a thermal rate equation, which includes continuous dissociation and regeneration of the J/ψ ,

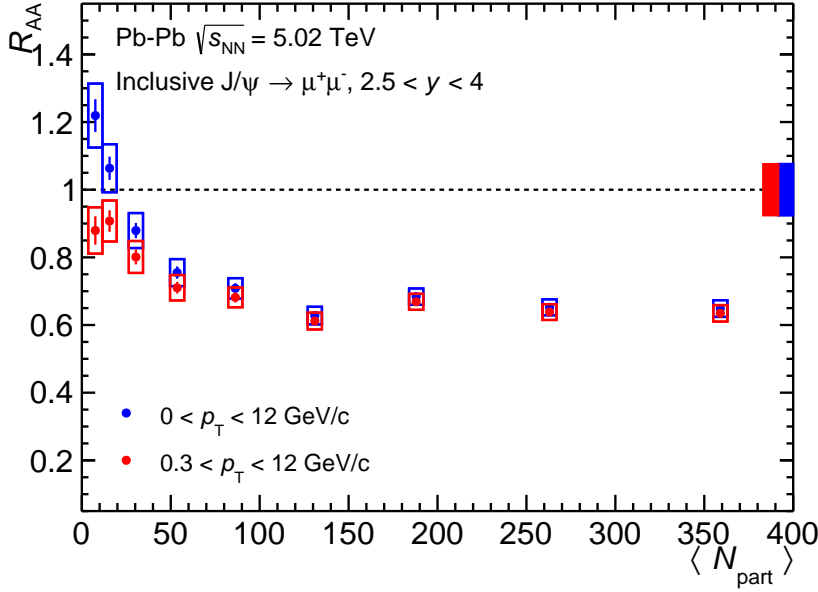


Figure 6.6: The inclusive J/ψ R_{AA} as a function of $\langle N_{\text{part}} \rangle$ at $\sqrt{s_{\text{NN}}} = 5.02$ TeV for $p_T > 0$ (blue) and $p_T > 0.3$ GeV/c (red) **[This thesis]**.

both in the QGP and at the hadronization stage. The $c\bar{c}$ cross section needed as an input to the regeneration component is taken as $d\sigma_{c\bar{c}}/dy = 0.57$ mb, consistent with FONLL calculations [48]. The upper (lower) limit of the band representing this model corresponds to including 10% (25%) shadowing. A 5% uncertainty on the $c\bar{c}$ cross section is also added. Within uncertainties, this model is able to describe the measurement. In the next sections, calculations from this model that are available in more differential intervals will be also compared to data.

- **Transport model-2 (TM2): [82]** this model mainly differs from TM1 in the rate equation that controls the fractions of J/ψ dissociation and regeneration. The used $c\bar{c}$ cross section is $d\sigma_{c\bar{c}}/dy = 0.82$ mb and corresponds to the upper limit of FONLL calculations. The upper and lower error bands of this model correspond respectively to the choice of no shadowing and a shadowing effect estimated with the EPS09 parametrization [57]. This model is also able to

describe the data within uncertainties.

- **Statistical hadronization model:** [13] in this model, all the J/ψ are dissociated in the medium and the observed ones are created, like all other hadrons, only at the chemical freeze-out. $d\sigma_{c\bar{c}}/dy = 0.45$ mb is extrapolated from LHCb pp measurements at $\sqrt{s} = 7$ TeV [149]. The error bands of this model correspond to the uncertainty on the extrapolated $c\bar{c}$ cross section and on the EPS09 parametrization used to account for the shadowing effect on it. Data are also described by this model within uncertainties.
- **Comover interaction model** [78]: in this model the J/ψ are dissociated via interactions with partons and hadrons produced in the same rapidity range using an effective interaction cross section $\sigma_{co} = 0.65$ mb, from low-energy data. The J/ψ regeneration is included by adding a gain term proportional to σ_{co} and to the number of produced c and \bar{c} quarks. Shadowing effects are included in this model using the Glauber-Gribov theory [87]. The error bands of this model correspond to the choice of $d\sigma_{c\bar{c}}/dy$ ranging from 0.45 to 0.7 mb. The measured R_{AA} can be described within uncertainties by this model.

By dividing the R_{AA} at the two energies, the uncertainty on the $\langle T_{AA} \rangle$ is assumed to cancel out as well as some theoretical uncertainties. This ratio ($R_{AA}^{\frac{5.02}{2.76}} = R_{AA}(\sqrt{s_{NN}} = 5.02 \text{ TeV})/R_{AA}(\sqrt{s_{NN}} = 2.76 \text{ TeV})$) is shown in Figure 6.8 where the statistical, uncorrelated systematic (without the one the $\langle T_{AA} \rangle$) and the correlated systematic uncertainties of the two distributions are summed in quadrature. Within uncertainties, this ratio is compatible with unity. The variation range of R_{AA}^{prompt} at $\sqrt{s_{NN}} = 2.76$ TeV was estimated using the same procedure used in this analysis. Therefore one can estimate this variation for $R_{AA}^{\frac{5.02}{2.76}}$. For prompt J/ψ , $R_{AA}^{\frac{5.02}{2.76}}$ would be about 2% (1–2%) higher if beauty hadrons were fully (not) suppressed by the medium. This ratio is also compared to the same theoretical calculations as for R_{AA} . The four models are able to describe the data within uncertainties.

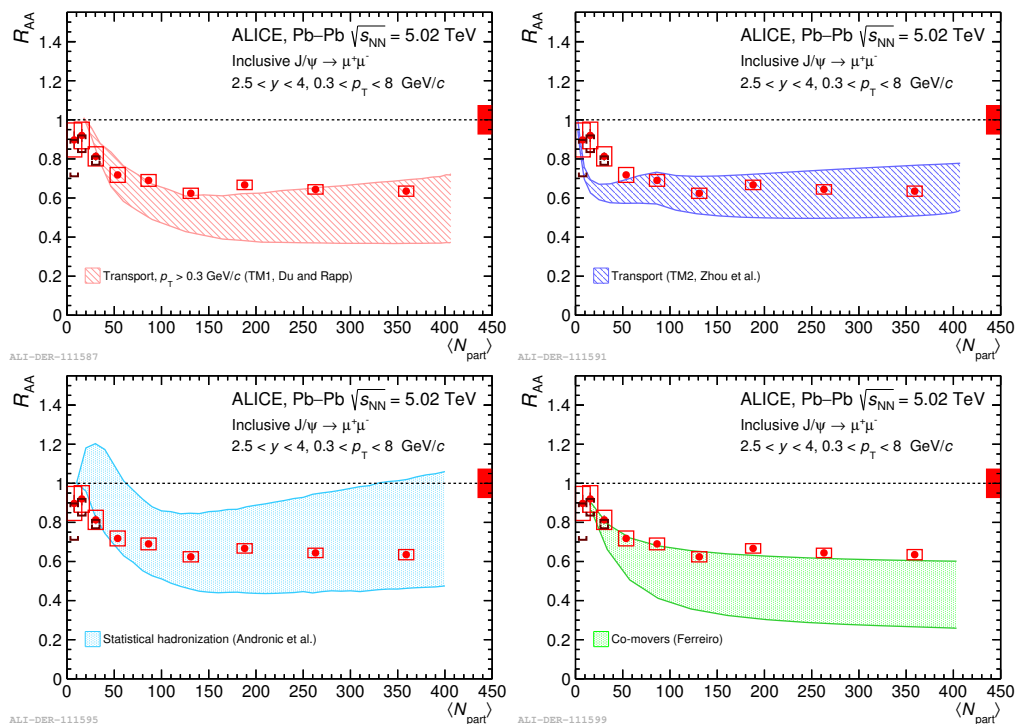


Figure 6.7: The inclusive J/ψ R_{AA} as a function of $\langle N_{part} \rangle$ at $\sqrt{s_{NN}} = 5.02$ TeV measured with ALICE and compared to theoretical calculations based on two transport models [81, 82] (top), a statistical hadronization model [13] (bottom left), and a comover interaction model [78] (bottom right).

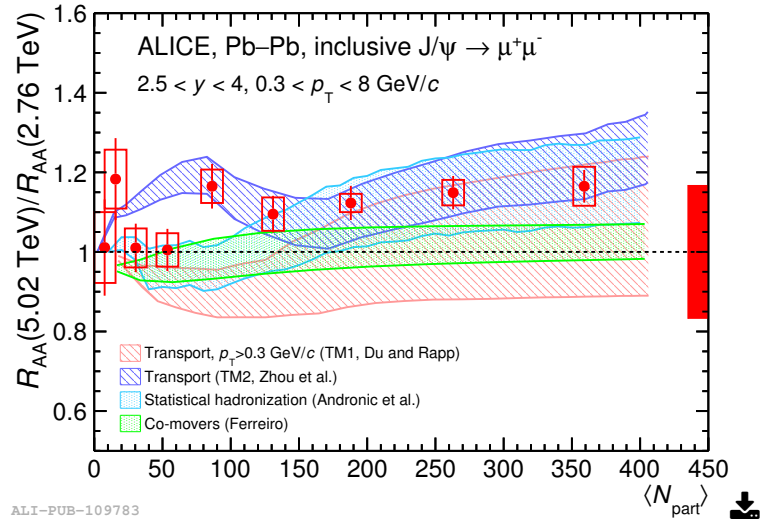


Figure 6.8: The ratio of the inclusive J/ψ R_{AA} as a function of $\langle N_{\text{part}} \rangle$ for $0.3 < p_T < 8 \text{ GeV}/c$ between $\sqrt{s_{NN}} = 5.02 \text{ TeV}$ and $\sqrt{s_{NN}} = 2.76 \text{ TeV}$, compared to the theoretical models described in the text. The vertical error bars represent the statistical uncertainties and the boxes around the data points the uncorrelated systematic uncertainties. The centrality-correlated global uncertainty is shown as a filled box around unity.

6.3.2.1 R_{AA} centrality dependence in different p_T intervals

According to the models, the suppression and regeneration patterns have different p_T dependence. This can be confirmed by studying the J/ψ R_{AA} centrality dependence in different p_T intervals. Figure 6.9 shows the R_{AA} as a function of $\langle N_{\text{part}} \rangle$ in Pb-Pb collisions at $\sqrt{s_{\text{NN}}} = 5.02$ TeV for the four p_T intervals 0.3–2, 2–5, 5–8, and 8–12 GeV/c. Going from low to high p_T , the J/ψ suppression becomes larger and the centrality dependence of the R_{AA} becomes stronger. The shapes and values of the J/ψ R_{AA} in the two highest p_T intervals ($5 < p_T < 8$ and $8 < p_T < 12$ GeV/c) are similar. In this kinematic region, and in contrast to low p_T ranges, the J/ψ regeneration is expected to be negligible and other effects, mainly the energy loss, become dominant.

Available calculations from the transport model TM1 [81] are compared to the results as shown in the four panels of Figure 6.10 for the four p_T ranges. The model is able to qualitatively describe the results in all the p_T intervals. However, some discrepancies between the calculations and the measurements are seen, mainly at intermediate p_T (2–5 GeV/c) in semi-central collisions ($100 \lesssim \langle N_{\text{part}} \rangle \lesssim 250$) where the model calculation is separated from the calculation by $\sim 1.7 \sigma$. Such discrepancies are already seen when comparing the r_{AA} results (Section 6.2.1) to calculations from this model.

Except for the last p_T interval (8–12 GeV/c), the double ratio $R_{AA}^{\frac{5.02}{2.76}}$ is shown in the bottom of the first three panels of Figure 6.10. In all the p_T intervals, this ratio is flat as a function of centrality. Within uncertainties, it is also compatible with unity. One can spot an increase with energy of the central values of the R_{AA} at intermediate p_T (2–5 GeV/c) but this increase is within one σ .

The estimation of the variation range of the prompt R_{AA}^{prompt} is also done for the four p_T ranges. The corresponding numerical values are summarized in Table 6.4, where as expected the higher the J/ψ p_T , the larger is the variation range since the contribution from b-hadron decay increases with p_T .

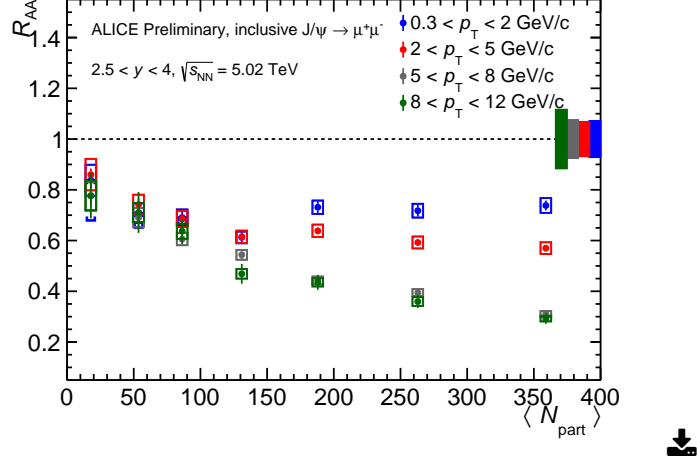


Figure 6.9: The inclusive J/ψ R_{AA} as a function of $\langle N_{part} \rangle$ at $\sqrt{s_{NN}} = 5.02$ TeV in four p_T intervals (0.3-2, 2-5, 5-8, and 8-12 GeV/c).

p_T (GeV/c)	Assumption	Most peripheral collisions		Most central collisions	
		$R_{AA}(5.02 \text{ TeV})$	$R_{AA}^{\frac{5.02}{2.76}}$	$R_{AA}(5.02 \text{ TeV})$	$R_{AA}^{\frac{5.02}{2.76}}$
0.3-2	$R_{AA}^{\text{non-prompt}} = 0$	+8%	+1%	+8%	+1%
	$R_{AA}^{\text{non-prompt}} = 1$	+1%	-2%	-3%	-1%
2-5	$R_{AA}^{\text{non-prompt}} = 1$	+10%	+2%	+10%	+2%
	$R_{AA}^{\text{non-prompt}} = 1$	-4%	+2%	-11%	+4%
5-8	$R_{AA}^{\text{non-prompt}} = 0$	+15%	+3%	+15%	+3%
	$R_{AA}^{\text{non-prompt}} = 1$	-9%	+2%	-45%	-4%
8-12	$R_{AA}^{\text{non-prompt}} = 1$	+24%	N.A.	+24%	N.A.
	$R_{AA}^{\text{non-prompt}} = 1$	-13%	N.A.	-69%	N.A.

Table 6.4: Variation of the prompt R_{AA} and $R_{AA}^{\frac{5.02}{2.76}} = R_{AA}(\sqrt{s_{NN}} = 5.02 \text{ TeV})/R_{AA}(\sqrt{s_{NN}} = 2.76 \text{ TeV})$ under the two assumptions on $R_{AA}^{\text{non-prompt}}$ in different p_T intervals.

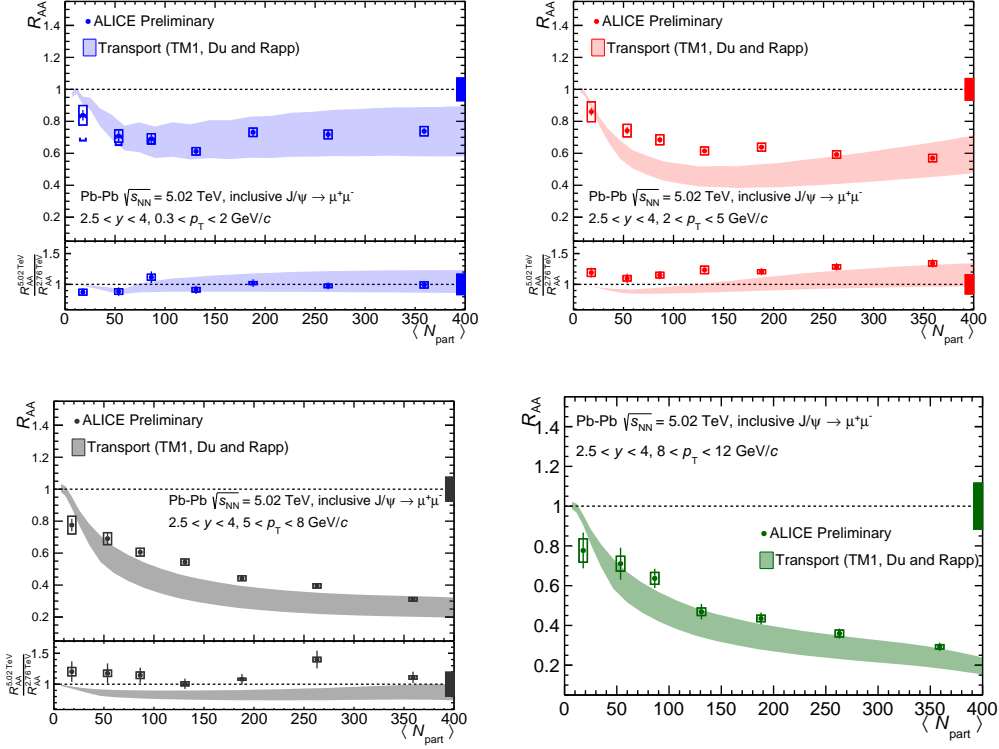


Figure 6.10: The inclusive J/ψ R_{AA} as a function of $\langle N_{part} \rangle$ in four p_T intervals (0.3-2, 2-5, 5-8, and 8-12 GeV/c) in Pb-Pb collisions at $\sqrt{s_{NN}} = 5.02$ TeV measured with ALICE and compared to theoretical calculations based on transport model [81]. Except for the last p_T interval (8-12 GeV/c), the bottom panel of each plot shows the ratio $R_{AA}(\sqrt{s_{NN}} = 5.02 \text{ TeV}) / R_{AA}(\sqrt{s_{NN}} = 2.76 \text{ TeV})$ and the comparison to the same calculations. For each distribution, the vertical error bars represent statistical uncertainties, the boxes around the points uncorrelated systematic uncertainties, while the centrality-correlated global uncertainties are shown as a filled box around unity.

6.3.3 R_{AA} p_T dependence

The p_T dependence of the J/ψ R_{AA} offers another way to study the different effects on the J/ψ production. Figure 6.11 shows the R_{AA} as a function of p_T in Pb-Pb collisions at $\sqrt{s_{NN}} = 5.02$ TeV for three centrality intervals, 0–20%, 20–40%, and 40–90%. In the last one, the first p_T bin is 0.3–1 GeV/c instead of 0–1 GeV/c in order to reduce the possible J/ψ photo-production contamination. In the 0–20% centrality interval, the value of the J/ψ R_{AA} decreases to the half from low (0–1 GeV/c) to high p_T (5–6 GeV/c). Beyond 6 GeV/c, where the dominant effect on the J/ψ production is expected to be the energy loss, the R_{AA} is approximately constant. The p_T dependence of the R_{AA} becomes weaker in the centrality interval 20–40% and negligible in the centrality interval 40–90% where the R_{AA} is constant at ~ 0.8 . As concluded from the centrality dependence of the R_{AA} in different p_T intervals, this behavior can be explained by an interplay between J/ψ dissociation and regeneration mechanisms.

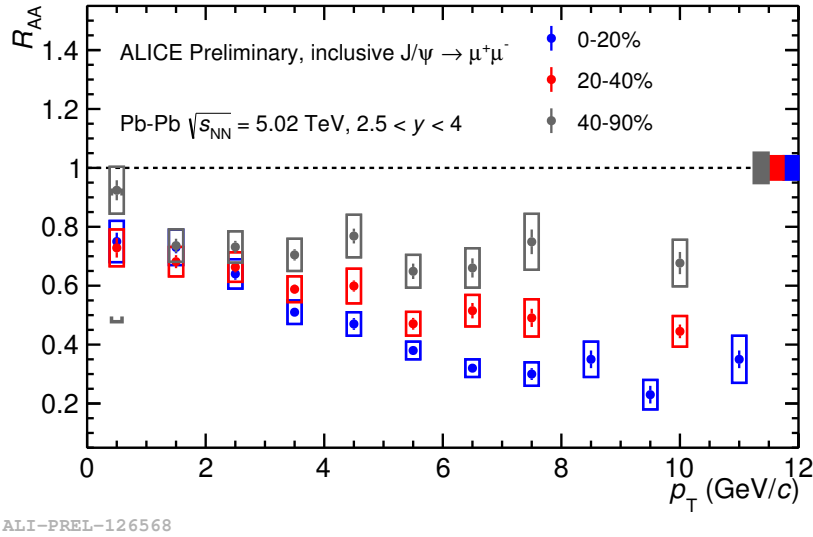


Figure 6.11: The inclusive J/ψ R_{AA} as a function of p_T at $\sqrt{s_{NN}} = 5.02$ TeV in three centrality intervals, 0–20%, 20–40%, and 40–90%.

The results are compared to the ones measured at $\sqrt{s_{NN}} = 2.76$ TeV in Fig-

ure 6.12 and Figure 6.13, where for all the centrality intervals, similar R_{AA} patterns are observed at both energies. The bottom panel of each plot of Figure 6.12 and Figure 6.13 shows the p_T dependence of the ratio $R_{AA}^{\frac{5.02}{2.76}}$ in the given centrality interval. When doing this ratio, the uncertainty on the $\langle T_{AA} \rangle$ is assumed to cancel out from the correlated uncertainties (filled boxes around unities). An increase with energy of the central values of the R_{AA} can be observed in the intermediate p_T region ($2 < p_T < 6$ GeV/c) for the most central collisions (0–20%) and the semi central ones (20–40%) even if the two measurements are compatible within uncertainties. The variation ranges of the prompt R_{AA} and $R_{AA}^{\frac{5.02}{2.76}}$ under the two assumptions of full and no beauty suppression are summarized in Table 6.5 for the three centrality intervals. For each centrality interval, the effect is maximum for the highest p_T range and starts to decrease toward lower p_T . The results of R_{AA} at $\sqrt{s_{NN}} = 5.02$ TeV and $R_{AA}^{\frac{5.02}{2.76}}$ are also compared to available calculations based on the transport model TM1 [81]. Similar to the case of centrality dependence, the model is able to describe the data within uncertainties but it underestimates the results in the intermediate p_T region for the centrality interval 20–40% by $\sim 2 \sigma$.

		$p_T < 1$ GeV/c		$8 < p_T < 12$ GeV/c	
centrality	Assumption	$R_{AA}(5.02 \text{ TeV})$	$R_{AA}^{\frac{5.02}{2.76}}$	$R_{AA}(5.02 \text{ TeV})$	$R_{AA}^{\frac{5.02}{2.76}}$
0–20%	$R_{AA}^{\text{non-prompt}} = 0$	+7%	0%	+30%	0%
	$R_{AA}^{\text{non-prompt}} = 1$	-2%	0%	-55%	+15%
20–40%	$R_{AA}^{\text{non-prompt}} = 0$	+7%	+1%	+24%	+3%
	$R_{AA}^{\text{non-prompt}} = 1$	-2%	0%	-30%	-5%
40–90%	$R_{AA}^{\text{non-prompt}} = 0$	+7%	+1%	+24%	+3%
	$R_{AA}^{\text{non-prompt}} = 1$	-1%	0%	-12%	0%

Table 6.5: Variation of the prompt R_{AA} and $R_{AA}^{\frac{5.02}{2.76}} = R_{AA}(\sqrt{s_{NN}} = 5.02 \text{ TeV})/R_{AA}(\sqrt{s_{NN}} = 2.76 \text{ TeV})$ under the two assumptions on $R_{AA}^{\text{non-prompt}}$ in different centrality intervals.

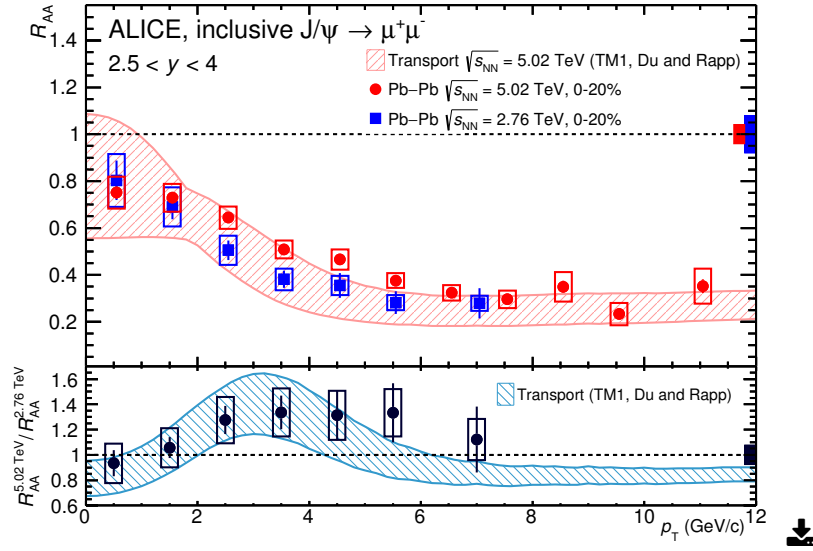


Figure 6.12: The inclusive J/ψ R_{AA} as a function of p_T in Pb-Pb collisions at $\sqrt{s_{NN}} = 5.02$ TeV [144] and $\sqrt{s_{NN}} = 2.76$ TeV [145] in the 0-20% centrality interval. The one measured at $\sqrt{s_{NN}} = 5.02$ TeV is compared to calculation based on transport model. The bottom panel shows the ratio $R_{AA}(\sqrt{s_{NN}} = 5.02 \text{ TeV})/R_{AA}(\sqrt{s_{NN}} = 2.76 \text{ TeV})$ and also compared to the same calculations.

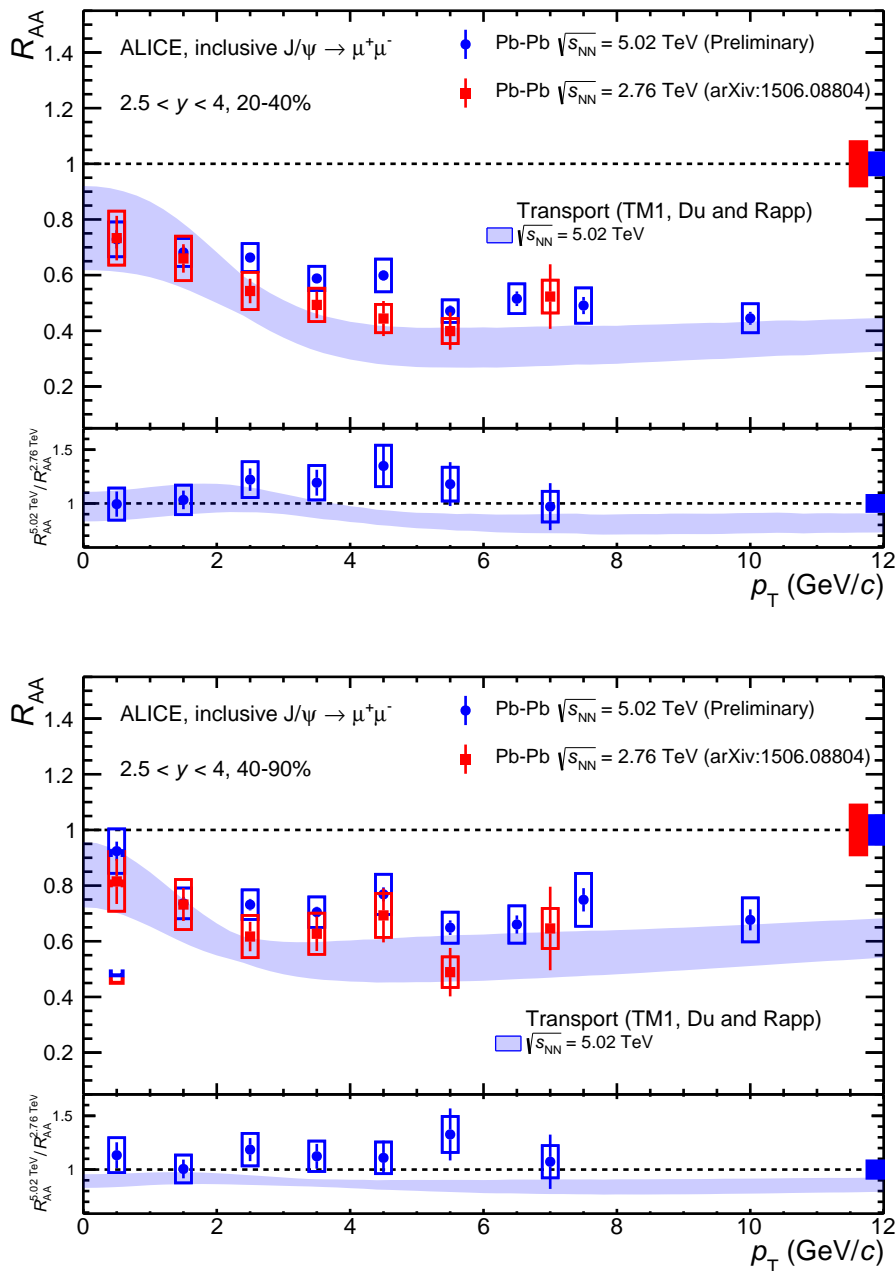


Figure 6.13: The inclusive J/ψ R_{AA} as a function of p_T in Pb-Pb collisions at $\sqrt{s_{NN}} = 5.02$ TeV and $\sqrt{s_{NN}} = 2.76$ TeV [145] in two centrality intervals, 20-40% (top), and 40-90% (bottom). The ones measured at $\sqrt{s_{NN}} = 5.02$ TeV are compared to calculation based on transport model. The bottom panel of each plot shows the ratio $R_{AA}(\sqrt{s_{NN}} = 5.02 \text{ TeV})/R_{AA}(\sqrt{s_{NN}} = 2.76 \text{ TeV})$ and also compared to the same calculations.

6.3.4 R_{AA} rapidity dependence

The rapidity dependence of the J/ψ R_{AA} was also measured in Pb-Pb collisions at $\sqrt{s_{NN}} = 5.02$ TeV and shown in the top panel of Figure 6.14 for the centrality interval 0–90%. Even if the central values of the R_{AA} monotonically decreases by about 20% from the less forward rapidity bin (2.5–2.75) to the most forward one (3.75–4), the distribution is compatible with a constant within the statistical and uncorrelated systematic uncertainties. Theoretically speaking, both the dissociation and the regeneration mechanisms are expected to be more important when going from forward to mid-rapidity regions. Concerning the dissociation mechanism, this is due to the increasing density of the medium and it would result in a smaller R_{AA} at smaller rapidity. For the J/ψ regeneration, this is due the increasing number of the initially produced $c\bar{c}$ pairs when going toward mid-rapidity regions and would result in a larger R_{AA} at smaller rapidity.

The rapidity dependence of $R_{AA}^{\frac{5.02}{2.76}}$ is also shown in Figure 6.14. Except for the last rapidity bin (3.75–4) where a deviation is observed (1.5σ), $R_{AA}^{\frac{5.02}{2.76}}$ is consistent with unity within uncertainties.

Since this dependence is measured in the integrated p_T range, the contribution from the non-prompt J/ψ is small. At $\sqrt{s_{NN}} = 5.02$ TeV, R_{AA}^{prompt} would be about 10% (8%) larger for the rapidity interval 2.5–2.75 (3.75–4) under the assumption of $R_{AA}^{\text{non-prompt}} = 0$, and about 7% (9%) smaller for the rapidity interval 2.5–2.75 (3.75–4) under the assumption of $R_{AA}^{\text{non-prompt}} = 1$. The values of the variation of R_{AA}^{prompt} at $\sqrt{s_{NN}} = 5.02$ TeV are similar to the ones estimated at $\sqrt{s_{NN}} = 2.76$ TeV [145] which means that the effect on their ratio is small.

The rapidity dependence of the J/ψ R_{AA} in Pb-Pb collisions at $\sqrt{s_{NN}} = 5.02$ TeV is also measured in the three centrality intervals 0–20%, 20–40%, and 40–90%. The corresponding results are shown in the bottom panel of Figure 6.14. Similarly to the 0–90% centrality case, the distribution is approximately constant with similar values for the three centrality intervals.

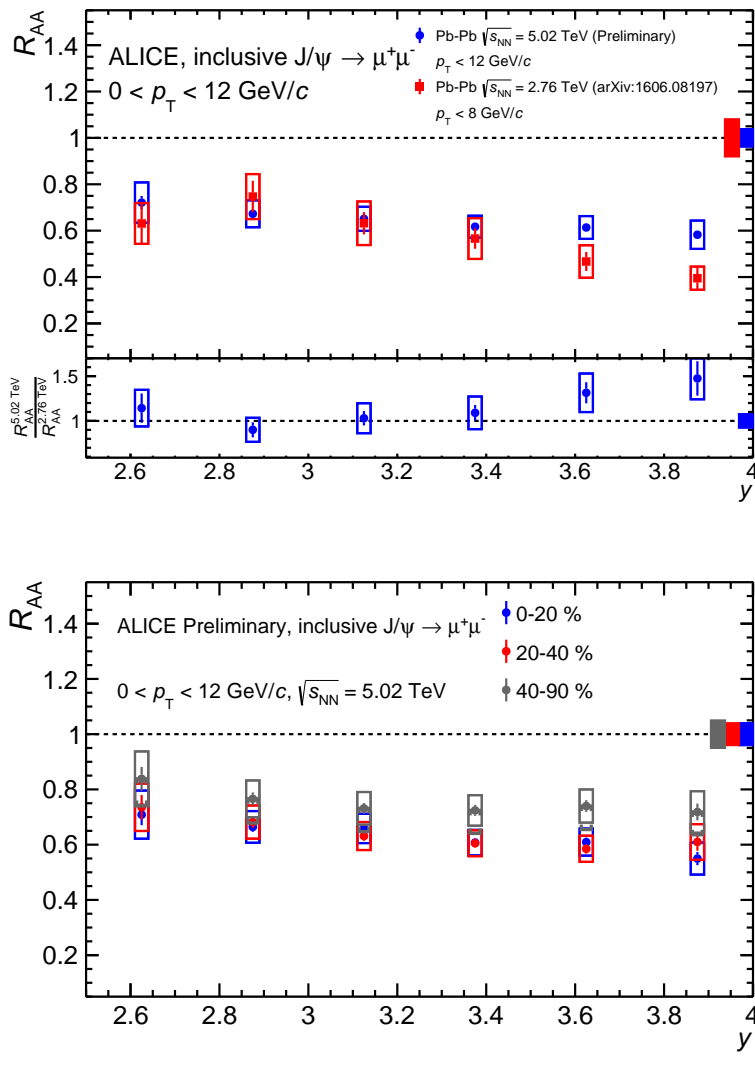


Figure 6.14: Top: the inclusive J/ψ R_{AA} as a function of rapidity in Pb-Pb collisions at $\sqrt{s_{NN}} = 5.02$ TeV and $\sqrt{s_{NN}} = 2.76$ TeV [145] in the 0-90 % centrality interval. The ratio of the two distributions is shown in the bottom panel of the plot. Bottom: the inclusive J/ψ R_{AA} as a function of rapidity in Pb-Pb collisions at $\sqrt{s_{NN}} = 5.02$ TeV in three centrality intervals (0-20%, 20-40%, and 40-90%).

6.4 Conclusions and discussion

This chapter presented the results of this thesis on the J/ψ production in Pb-Pb collisions at $\sqrt{s_{\text{NN}}} = 5.02 \text{ TeV}$ at forward rapidity ($2.5 < y < 4$):

- **The inclusive J/ψ $\langle p_{\text{T}} \rangle$:** a significant decrease (by more than 5σ) from peripheral to central collisions is measured. The ratio $r_{\text{AA}} = \frac{\langle p_{\text{T}}^2 \rangle_{\text{AA}}}{\langle p_{\text{T}}^2 \rangle_{\text{pp}}}$ is also calculated and shows a similar decrease with values smaller than unity.
- **The inclusive J/ψ R_{AA} :** the centrality dependence is clear and independent from the J/ψ kinematic up to $\langle N_{\text{part}} \rangle \sim 100$. For $\langle N_{\text{part}} \rangle > 100$, the centrality dependence and the size of the J/ψ suppression starts to vary with p_{T} . At low p_{T} (0–2 GeV/c), the centrality dependence is negligible. Going toward higher p_{T} , the centrality dependence of the R_{AA} becomes more pronounced and the suppression becomes larger. As a function of rapidity, the R_{AA} is compatible with constant within uncertainties.

In addition, other results of related measurements in Pb-Pb collisions at $\sqrt{s_{\text{NN}}} = 5.02 \text{ TeV}$ can be listed in order to formulate a more complete conclusion:

- **The inclusive J/ψ R_{AA} at mid-rapidity ($-0.8 < y < 0.8$):** the measured R_{AA} is compatible within uncertainty with the one at forward rapidity with a similar centrality dependence [151]. The results were compared to the same theoretical models of Section 6.3.2: all the models can describe the data within uncertainties.
- **The J/ψ elliptic flow (v_2) at forward rapidity:** a non zero v_2 with a 6.6σ significance in semi central collisions is measured [152]. The J/ψ v_2 is expected to vary depending on the production mechanism. For regeneration, the v_2 acquired by the thermalized charm quarks can be further transferred to the produced J/ψ . In contrast, primordial J/ψ which are initially produced by hard processes are not directly sensitive to this effect. However, they are sensitive to another effect related to their path in the medium. In particular, J/ψ emitted out-of-plane traverse a longer path through the medium than those emitted in-plane resulting in a small apparent v_2 . This effect is expected to be dominant at high p_{T} , thus, at low p_{T} , the measured J/ψ v_2 can

be explained as an inheritance of the charm quarks one.

All these results can be explained by an interplay of different mechanisms that affect differently the J/ψ production and take the lead at different p_T regions. The J/ψ enhancement at low p_T and the clear J/ψ elliptic flow give together a strong indication on the presence of the J/ψ regeneration.

The R_{AA} results at $\sqrt{s_{NN}} = 5.02\text{TeV}$ are compared to different model calculations ([13, 78, 81, 82]). In general, the large theoretical uncertainties did not allow to discriminate between the models. Reproducing different observables simultaneously is a crucial test for the models. This was shown in this chapter for a transport model [81] which has available calculations for the r_{AA} , the R_{AA} in different centrality, rapidity, and p_T intervals, as well as for the v_2 [152]. This model is able to describe qualitatively these observables but some tensions are visible between the calculation and the results.

CONCLUSIONS AND OUTLOOKS

The Z-boson production in heavy-ion collisions is a powerful tool to study cold nuclear matter effects that are not caused by the presence of hot and dense medium created in the collisions. Notably among such effects, the nuclear modification of parton distribution functions (PDFs). The PDFs represent the non-perturbative part of hard-processes cross sections in hadronic collisions. Understanding this modification relies strongly on the availability of experimental data that can be used to constrain the different parametrizations. The Z-boson production in heavy-ion collisions has only become possible with the LHC thanks to its high collision energies. In this manuscript, I presented the first measurement of the Z-boson production with the ALICE experiment. ALICE covers an acceptance that allows the Z-boson production in Pb-Pb collisions to probe the nuclear PDFs in small Bjorken-x regions that are not probed by ATLAS and CMS experiments at the LHC.

The measured Z-boson production cross section in p-Pb collisions at $\sqrt{s_{\text{NN}}} = 5.02\text{TeV}$ agrees within uncertainties with different theoretical calculations. However, its precision is not sufficient to conclude on the presence of cold nuclear matter effects in the studied collision system. This is consistent with what the other LHC experiments have reported on this measurement.

With the higher statistics collected by ALICE in Pb-Pb collisions at $\sqrt{s_{\text{NN}}} = 5.02\text{TeV}$, the results presented in this thesis showed a suppression of the Z-boson production with respect to what is expected from a collision without nuclear effects with a 2.3σ significance. The measurement agrees within uncertainties with expectations from two available nuclear PDFs parametrizations.

To address hot nuclear matter effects that take place in heavy-ion collisions,

I also presented in this thesis my contribution to the study of the J/ψ production in Pb-Pb collisions at $\sqrt{s_{\text{NN}}} = 5.02 \text{ TeV}$. The J/ψ production in heavy-ion collisions has been extensively studied by different experiments at different energies. It can probe the whole evolution of the collision due to the short formation time of the charm quarks. Among the other LHC experiments involved in heavy-ion physics, ALICE has a unique capability of measuring the J/ψ down to zero p_{T} , allowing a complete study for the different expected effects. At $\sqrt{s_{\text{NN}}} = 5.02 \text{ TeV}$, the J/ψ production shows a clear suppression but considerably lower than what has been measured at lower energies at RHIC and SPS. This is not expected according to a simple picture of J/ψ dissociation by color screening. To this purpose, this thesis also presented a set of differential studies which showed that the decrease of the J/ψ suppression is predominant at low p_{T} . In addition, the centrality dependence of the suppression becomes more pronounced when going from low to high p_{T} . The J/ψ suppression was also found to be constant as a function of rapidity. From the current theoretical knowledge, this behavior is most likely coming from the J/ψ regeneration which is expected to increase with the collision energy as a consequence of the increasing number of $c\bar{c}$ pairs created in the collision. This is also supported by the measured non zero J/ψ elliptic flow in the same data sample, which at low p_{T} can be inherited from regenerated charm quarks. The discrimination between the different effects in different kinematic regions must be done by comparing the experimental results to theoretical calculations. This was presented in this manuscript considering different models which have unfortunately relatively large uncertainties preventing a discrimination between them.

The two analyses presented in this thesis were not performed as one study but rather as independent with different motivations. Though, one can learn from the results obtained in one to better understand the other. For instance, among the different effects on the J/ψ production in Pb-Pb collisions at $\sqrt{s_{\text{NN}}} = 5.02 \text{ TeV}$, the cold nuclear matter effects are not negligible. This is supported by the suppression of the Z-boson production in the same data sample (Figure 7.1) even if knowing that the different cold nuclear matter effects do not act similarly on the two particles.

In the near future, the two presented analyses will benefit from the ALICE

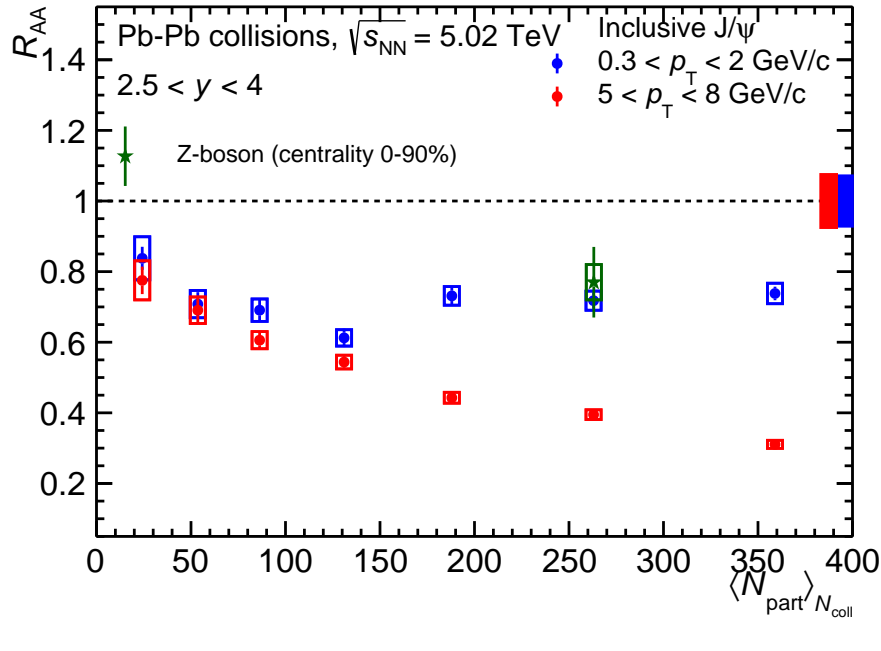


Figure 7.1: R_{AA} of Z-boson and J/ψ (in two p_{T} intervals) as a function of $\langle N_{\text{part}} \rangle$ weighted by $\langle N_{\text{coll}} \rangle$ in Pb-Pb collisions at $\sqrt{s_{\text{NN}}} = 5.02$ TeV **[This thesis]**.

upgrade program foreseen during the next long shutdown of the LHC (2019-2020). Concerning the study of the Z-boson production, the major gain will be on the statistics which represent the main limitation of the present study. The improvement of the electronic readout capability of the muon spectrometer would reflect in an increase of the collected luminosity by an order of magnitude. This will surely improve the precision of the Z-boson (same for the W-boson) measurement and therefore contribute more to the constraining of nuclear PDFs parametrizations.

Concerning the J/ψ analysis, the main benefit will come from the installation of the Muon Forward Tracker [153]. This will allow the separation between the prompt and non-prompt J/ψ , which is not possible at forward rapidity using the current experimental setup. A particularly important measurement would be the total charm cross section by separating the charm and beauty muon decays. This measurement is crucial for different theoretical models considering J/ψ regeneration

since this ingredient represents a major source of their uncertainties.

RÉSUMÉ EN FRANÇAIS

Chapitre 1 et 2 : contexte théorique

Les quarks et les gluons sont les constituants fondamentaux des hadrons tels que les protons et les neutrons. À des températures et des densités d'énergie extrêmement élevées, on s'attend à la formation d'un état de la matière connu sous le nom de Plasma de Quarks et de Gluons (PQG) où les quarks et les gluons ne sont plus confinés dans les hadrons. Expérimentalement, les conditions extrêmes nécessaires à la création du PQG sont atteintes en effectuant des collisions entre d'ions lourds. Plusieurs sondes existent pour étudier les différentes propriétés du PQG. Ces sondes sont dites douces (dures) lorsque le transfert d'impulsion impliqué est relativement petit (grand). Dans cette thèse, la production de deux sondes dures lors des collisions d'ions lourds est étudiée. La première est le méson J/ψ et la deuxième est le boson Z .

Le J/ψ est l'état de charmonium ¹ de masse la plus basse. En raison de la formation du PQG, la production de J/ψ est affectée par différents mécanismes. Un d'entre eux est l'écrantage de couleur où les quarks et gluons dans le PQG réduisent le potentiel de liaison entre le charme et l'anticharme, empêchant la formation de J/ψ . Cet effet pourrait conduire à une réduction relative de la production de J/ψ dans les collisions d'ions lourds par rapport aux collisions où aucun effet nucléaire n'est attendu (par exemple des collisions proton-proton). Un autre effet est la régénération du J/ψ quand deux quarks charme et anticharme se rencontrent dans le milieu et forment un J/ψ . Contrairement à l'écrantage de couleur, cet effet conduit à une augmentation de la production de J/ψ dans les collisions d'ions lourds. La régénération devient plus importante avec l'augmentation de l'énergie de collision

¹état lié d'un pair charm-anticharm.

puisque le nombre de quarks de charme et anticharme, produit dans la collision, augmente. La production de J/ψ dans les collisions d'ions lourds peut également être modifiée par d'autres effets qui présents dès l'état initial de la collision et qui ne sont pas liés à la formation du PQG. La quantification de tels effets est cruciale afin de les séparer des effets causés par la présence du PQG. Parmi ces effets, un effet important concerne la modification des fonctions de distribution de partons (PDFs) dans le noyau par rapport aux nucléons. La paramétrisation de cette modification est effectuée en ajustant certaines données expérimentales obtenus à différentes énergies. L'étude de la production du boson Z dans les collisions d'ions lourds peut aider à contraindre les différentes paramétrisations en bénéficiant principalement du fait que le boson Z ne porte pas de charge de couleur et n'est donc pas affecté par la présence du PQG.

Chapitre 3 : environnement expérimental

Les données analysées dans cette thèse sont collectées par l'expérience ALICE². Elle est située au LHC³ et dédiée à l'étude des collisions d'ions lourds. Elle se compose de 17 sous-détecteurs qui peuvent être regroupés en deux grandes parties, les détecteurs de la partie centrale autour du point d'interaction du LHC et le spectromètre à muons vers l'avant. Dans cette thèse, le détecteur principal est le spectromètre à muons où les produits de désintégration (deux muons) des J/ψ et des bosons Z sont reconstruits. Il se compose d'un absorbeur frontal épais filtrant les muons devant cinq stations de trajectographie comprenant chacune deux plans de chambres à fils à cathodes segmentées. La troisième station se trouve à l'intérieur d'un aimant dipolaire avec un champ magnétique intégré de 3 Tm. Le système de trajectographie est complété par un système de déclenchement constitué de quatre plans de détection devant un mur de fer de 1,2 m d'épaisseur, qui absorbe les hadrons secondaires s'échappant de l'absorbeur frontal. Le LHC peut fournir des collisions entre des faisceaux des protons (p) et/ou des ions de plomb (Pb). Deux lots de données ont été analysés dans cette thèse. Le premier lot porte sur les collisions p-Pb collectées en 2013, tandis que le deuxième porte sur

²A Large Ion Collider Experiment.

³Large Hadron Collider.

les collisions Pb-Pb collecté fin 2015. Dans les deux systèmes, l'énergie par collision nucléon-nucléon est $\sqrt{s_{NN}} = 5.02 \text{ TeV}$.

En tant que tâche de service pour la collaboration, durant ma thèse j'étais en charge de contrôler la qualité des données collectées par le spectromètre à muons de 2015 à 2016. Cela inclut des données collectées dans trois systèmes de collision différents, pp, p-Pb et Pb-Pb.

Chapitre 4 : l'analyse

Dans les collisions p-Pb à $\sqrt{s_{NN}} = 5.02 \text{ TeV}$, la section efficace de production du boson Z est mesurée dans deux intervalles de rapidité. Trois ingrédients principaux sont nécessaires pour obtenir la section efficace :

- Le nombre de candidats de bosons Z obtenus en comptant les dimuons dans un intervalle de masse invariante prédéfini (60-120 GeV/c^2), en supposant que le bruit de fond dans cette région de signal est négligeable.
- Un facteur de correction qui tient en compte l'acceptance et l'efficacité du détecteur. Ce facteur est calculé en utilisant une simulation Monte-Carlo (MC) du détecteur ALICE.
- La luminosité intégrée du lot de données qui représente le nombre d'événements analysés.

Afin de tester la validité de l'hypothèse de bruit de fond négligeable, la contribution de différentes sources physiques possibles dans la région du signal est estimée en utilisant deux générateurs de particules POWHEG [127] et PYTHIA [89]. La contribution estimée est inférieure à 1% et a été prise en compte en tant qu'incertitude systématique sur la mesure. D'autres incertitudes systématiques sur le calcul d'acceptance et d'efficacité du détecteur ainsi que sur la luminosité sont prises en compte et sont expliquées en détail dans le manuscrit.

Dans les collisions Pb-Pb à $\sqrt{s_{NN}} = 5.02 \text{ TeV}$, le taux de production du boson Z est calculé d'une manière similaire à celle de la section efficace en normalisant par la fonction de recouvrement nucléaire liée au nombre de collisions nucléon-nucléon dans une collision Pb-Pb. Aussi, le facteur de modification nucléaire (R_{AA}) du

boson Z est évalué dans ce système de collision. Il est obtenu en divisant le taux de production dans les collisions Pb-Pb par la section efficace de production dans les collisions proton-proton (pp) à la même énergie. Dans les collisions Pb-Pb, les événements sont généralement classés dans différents intervalles de centralité. Cette dernière variable est liée au paramètre d'impact de la collision. L'analyse du boson Z est effectuée dans deux intervalles de centralité, les 0-20% et les 20-90% des collisions les plus centrales.

L'autre partie de cette thèse a été consacrée à mesurer la production de J/ψ dans les collisions Pb-Pb à $\sqrt{s_{NN}} = 5.02 \text{ TeV}$. La différence principale par rapport à l'analyse du boson Z est la contribution relativement importante du bruit de fond dans la région du signal. Par conséquent, le comptage des candidats dimuons dans un intervalle de masse invariante donné n'est pas suffisant. Pour cela, l'extraction du signal du J/ψ est réalisée en utilisant deux méthodes différentes. La première consiste à estimer le bruit de fond et à le soustraire en utilisant une technique qui s'appelle le mixage d'événements, puis à extraire le signal du J/ψ en ajustant la distribution de masse invariante des dimuons par une fonction de signal dédiée qui prend en compte les effets du détecteur sur la forme du signal du J/ψ . La deuxième méthode consiste à ajuster directement (sans soustraction de bruit de fond) la distribution de masse invariante des dimuons avec des fonctions composées qui tiennent en compte à la fois des contributions du signal et du bruit de fond. La différence entre les résultats obtenus par les deux méthodes, et aussi en modifiant les configurations d'ajustement (fonctions de signal et de bruit de fond, intervalle en masse d'ajustement ...) est considéré comme une incertitude systématique. Quant à l'analyse du boson Z, d'autres sources d'incertitudes systématiques sur la détermination d'efficacité et d'acceptance du détecteur et aussi sur la normalisation sont étudiées et prises en compte.

Chapitre 5 : Résultats du boson Z

Les résultats de la section efficace de production du boson Z dans les collisions p-Pb à $\sqrt{s_{NN}} = 5.02 \text{ TeV}$ sont montrés sur la Figure 8.1 dans deux intervalles de rapidité. Les résultats sont comparés à deux ensembles de calculs théoriques basés sur la QCD perturbative [65] et le programme FEWZ [31]. Les deux ensembles

Dans les collisions Pb-Pb à $\sqrt{s_{NN}} = 5.02 \text{ TeV}$, le taux de production et le R_{AA} ont été mesurés dans deux intervalles de centralité et de rapidité. La Figure 8.2 montre le taux de production intégrée en centralité et rapidité. Alors que les données sont bien reproduites, dans la limite des incertitudes, par les modèles théoriques qui comprennent des modifications nucléaires des PDFs, elles sont séparées par environ 2,6 écarts-types du modèle qui ne prend pas en compte des modifications des PDFs (free PDF-bande bleue). Ces résultats sont publiés dans [142].

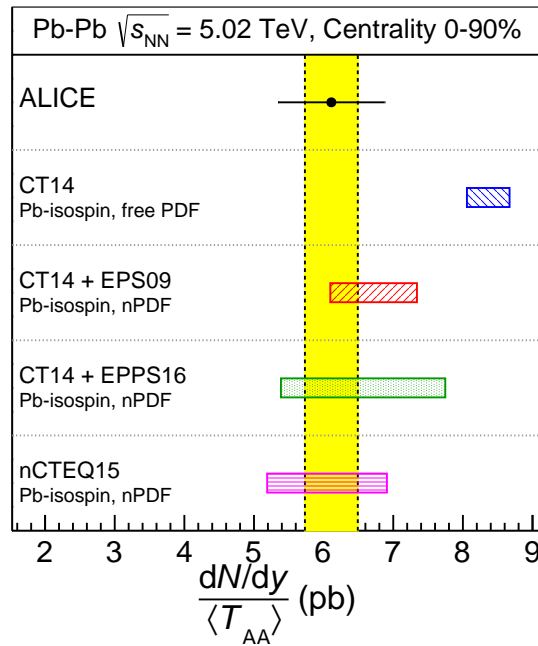


Figure 8.2: Taux de production du boson Z dans les collisions Pb-Pb à $\sqrt{s_{NN}} = 5.02 \text{ TeV}$. L'incertitude statistique (systématique) est représentée par une barre horizontale (bande jaune). Les résultats sont comparés à différents calculs théoriques (boîtes colorées) [142].

Chapitre 6 : Résultats du J/ψ

Concernant la production du J/ψ dans les collisions Pb-Pb à $\sqrt{s_{NN}} = 5.02 \text{ TeV}$, deux observables sont mesurées, (i) la valeur moyenne de l'impulsion transverse

($\langle p_T \rangle$) ainsi que la valeur moyenne du carré de l'impulsion transverse ($\langle p_T^2 \rangle$) (ii) le facteur de modification nucléaire (R_{AA}). Les premières observables expriment la dureté du taux de production en fonction de p_T qui peut être modifié par différents mécanismes. Une observable qui nous permet de quantifier les effets nucléaires sur la dureté du taux de production est la r_{AA} . Cette observable est le $\langle p_T^2 \rangle$ mesuré à Pb-Pb et divisée par la même quantité mesurée dans les collisions pp à la même énergie. La Figure 8.3 montre la distribution de r_{AA} , en fonction du nombre moyen de particules participantes dans la collision ($\langle N_{part} \rangle$). Dans les collisions périphériques (petites valeurs de $\langle N_{part} \rangle$), le r_{AA} est compatible avec l'unité ce qui n'est pas le cas pour les collisions plus centrales. Parmi les effets qui peuvent conduire à une diminution du $\langle p_T^2 \rangle$, il y a la régénération du J/ψ , car ce mécanisme favorise la production de J/ψ à bas p_T et par conséquent adoucit le taux de production en fonction de p_T . Les résultats sont comparés à des calculs théoriques basés sur un modèle de transport où la production est affectée par la dissociation et la régénération dans le milieu. Le modèle décrit qualitativement la tendance des données, mais certains désaccords peuvent être observés.

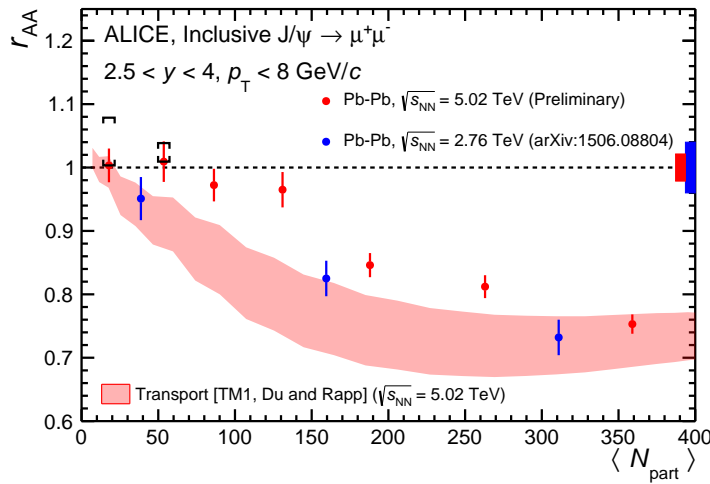


Figure 8.3: r_{AA} du J/ψ mesuré dans les collisions Pb-Pb à $\sqrt{s_{NN}} = 5.02$ TeV (rouge) et $\sqrt{s_{NN}} = 2.76$ TeV (bleu) [145]. Les incertitudes (statistiques + systématiques) sont représentées par des barres verticales. Les résultats sont comparés à un calcul théorique basé sur un modèle de transport [81].

Le R_{AA} du J/ψ est déterminé dans différents intervalles en centralité, rapidité et p_T du J/ψ . La Figure 8.4 montre les résultats en fonction de $\langle N_{part} \rangle$ dans différents intervalles en p_T . Pour tous les intervalles, une suppression claire du J/ψ par rapport aux collisions pp est observée. Cependant, cette suppression est plus faible pour les intervalles de bas p_T . En effet, à bas p_T , l'effet de régénération devrait être plus important, ce qui peut expliquer l'augmentation du R_{AA} observée. Tandis qu'à haut p_T , la régénération devient moins importante et les effets de dissociation du J/ψ deviennent dominants. Dans le manuscrit, les résultats du R_{AA} du J/ψ sont comparés à différents calculs théoriques qui sont capables de reproduire les données dans les incertitudes. Les résultats du J/ψ dans les collisions Pb-Pb à $\sqrt{s_{NN}} = 5.02 \text{ TeV}$ font partie de deux papiers, l'une des deux est [144] déjà publiée et l'autre est en cours de préparation.

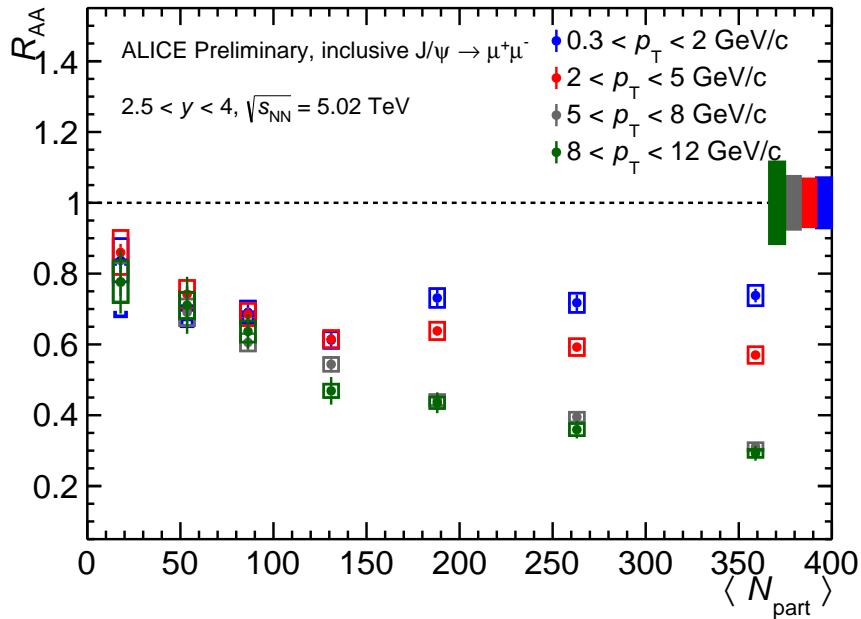
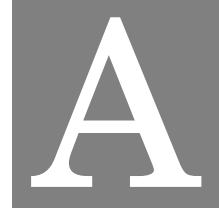


Figure 8.4: R_{AA} du J/ψ mesuré dans les collisions Pb-Pb à $\sqrt{s_{NN}} = 5.02 \text{ TeV}$ dans différents intervalles en p_T . Les incertitudes statistiques (systématiques) sont représentées par des barres verticales (boîtes ouvertes).



SIGNAL EXTRACTION FUNCTIONS

This appendix gives the analytic description of the functions used in the J/ψ signal extraction procedure. A complete fit function contains two components, one that describe J/ψ signal and the other describes the continuum background.

A.1 J/ψ signal functions

In experimental particle physics, the production peaks of resonance particles is usually described by Gaussian distribution. However due to different detector effects, these distributions are usually modified so that they can take those effects into account. The following two functions are based on a Gaussian core and contain additional parameters to adjust their tails.

Extended Crystal-Ball (CB2)

This function has a normalization factor N , two Gaussian core parameters (\bar{x} and σ) and four tail parameters (α , n , α' and n'). An example of this function is shown in Fig.2 where the different parameters are indicated. This function is defined by:

$$CB2(x) = N \cdot \begin{cases} \exp\left(-\frac{(x-\bar{x})^2}{2\sigma^2}\right) & \text{for } \alpha' > \frac{x-\bar{x}}{\sigma} > -\alpha \\ A \cdot \left(B - \frac{x-\bar{x}}{\sigma}\right)^{-n} & \text{for } \frac{x-\bar{x}}{\sigma} \leq -\alpha \\ C \cdot \left(D + \frac{x-\bar{x}}{\sigma}\right)^{-n'} & \text{for } \frac{x-\bar{x}}{\sigma} \geq \alpha' \end{cases}$$

with

$$A = \left(\frac{n}{|\alpha|}\right)^n \cdot \exp\left(-\frac{|\alpha|^2}{2}\right), B = \frac{n}{|\alpha|} - |\alpha|$$

$$C = \left(\frac{n'}{|\alpha'|}\right)^{n'} \cdot \exp\left(-\frac{|\alpha'|^2}{2}\right), D = \frac{n'}{|\alpha'|} - |\alpha'|$$

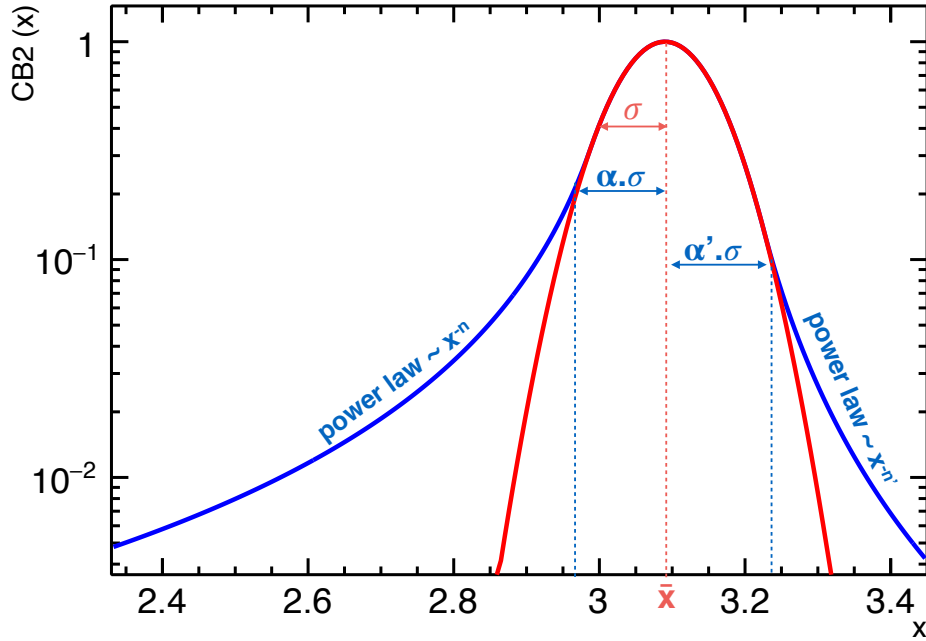


Figure A.1: Typical CB2 function (blue) compared to a gaussian function (red) with the same normalization, mean (\bar{x}) and width (σ). The four other parameters refer to the ones described in the text.

NA60 function

This function is similar to the CB2 one but it contains more parameters to describe the left and right tails. So in addition to the normalization factor N , and the two

Gaussian core parameters (\bar{x} and σ), there are eight tail parameters ($\alpha^L, p_1^L, p_2^L, p_3^L, \alpha^R, p_1^R, p_2^R$ and p_3^R). The function is defined by:

$$NA60(x) = N \cdot \exp\left(-0.5 \left(\frac{t}{t_0}\right)^2\right)$$

with

$$t = \frac{x - \bar{x}}{\sigma}$$

and

$$\begin{cases} t_0 = 1 + p_1^L(\alpha^L - t)^{(p_2^L - p_3^L)\sqrt{\alpha^L - t}} & \text{for } t < \alpha^L \\ t_0 = 1 & \text{for } \alpha^L < t < \alpha^R \\ t_0 = 1 + p_1^R(t - \alpha^R)^{(p_2^R - p_3^R)\sqrt{t - \alpha^R}} & \text{for } t > \alpha^R \end{cases}$$

A.2 Background functions

Signals in particle physics are usually accompanied with background contribution. For this reason, empirical functions that can describe the background continuum in the absence of the signal are used. Below is the definition of the two functions used for this purpose in the J/ψ signal extraction.

Variable Width Gaussian (VWG2)

This function has a normalization factor N , and four parameters ($\bar{x}, \alpha, \beta, \gamma$):

$$VWG2(x) = N \cdot \exp\left(\frac{-(x - \bar{x})^2}{2\sigma^2}\right), \text{ where } \sigma = \alpha + \beta \left(\frac{x - \bar{x}}{\bar{x}}\right) + \gamma \left(\frac{x - \bar{x}}{\bar{x}}\right)^2$$

Polynomials ratio (Pol2/Pol3)

In addition to the normalization factor N , this function has 5 parameters (a_1, a_2, b_1, b_2, b_3) and it is defined by:

$$Pol2/Pol3(x) = N \cdot \frac{1 + a_1x + a_2x^2}{b_1x + b_2x^2 + b_3x^3}$$

EFFECT OF NON-PROMPT J/ψ ON R_{AA}

The muon spectrometer detector is not able to separate the prompt and non-prompt J/ψ . Although R_{AA}^{prompt} cannot be directly accessed, it can be evaluated starting from R_{AA}^{incl} , provided hypothesis on (i) the fraction of J/ψ coming from B-hadron decays in pp collisions at $\sqrt{s_{NN}} = 5.02$ TeV, in the kinematic coverage of the muon spectrometer, (ii) the suppression of B-hadron production in Pb-Pb collisions due to initial and final state nuclear effects. As a function of p_T , $R_{AA}^{prompt}(p_T)$ can be

obtained starting from $R_{AA}^{incl}(p_T)$ as:

$$\begin{aligned}
 \frac{Y_{AA}^{inc}}{T_{AA}\sigma_{pp}^{inc}} &= R_{AA}^{inc} \\
 Y_{AA}^{pro} + Y_{AA}^{npro} &= R_{AA}^{inc} T_{AA}(\sigma_{pp}^{pro} + \sigma_{pp}^{npro}) \\
 Y_{AA}^{pro} &= R_{AA}^{inc} T_{AA} \sigma_{pp}^{pro} + R_{AA}^{inc} T_{AA} \sigma_{pp}^{npro} - Y_{AA}^{npro} \\
 \frac{Y_{AA}^{pro}}{T_{AA}\sigma_{pp}^{pro}} &= \frac{1}{T_{AA}\sigma_{pp}^{pro}}(R_{AA}^{inc} T_{AA} \sigma_{pp}^{pro} + R_{AA}^{inc} T_{AA} \sigma_{pp}^{npro} - Y_{AA}^{npro}) \\
 R_{AA}^{pro} &= R_{AA}^{inc} + \frac{R_{AA}^{inc} T_{AA} \sigma_{pp}^{npro}}{T_{AA}\sigma_{pp}^{pro}} - \frac{Y_{AA}^{npro}}{T_{AA}\sigma_{pp}^{pro}} \\
 R_{AA}^{pro} &= R_{AA}^{inc} + R_{AA}^{inc} f_B - \frac{Y_{AA}^{npro} \sigma_{pp}^{npro}}{T_{AA}\sigma_{pp}^{pro} \sigma_{pp}^{npro}} \\
 R_{AA}^{pro} &= R_{AA}^{inc} + R_{AA}^{inc} f_B - R_{AA}^{npro} f_B,
 \end{aligned} \tag{B.1}$$

where f_B is the fraction of non-prompt J/ψ to prompt J/ψ measured in pp collisions, and R_{AA}^{npro} is the suppression factor of B-hadron production in Pb-Pb collisions. The fraction of non-prompt J/ψ to prompt J/ψ $F_b = \frac{f_B}{1+f_B}$ is more commonly used. The subscripts *inc*, *pro* and *npro* refer to the inclusive, prompt and non-prompt production of J/ψ .

The differential cross-sections of non-prompt and prompt J/ψ cross-sections as a function of p_T and y have been measured by the LHCb collaboration in pp collisions $\sqrt{s_{NN}} = 7$ TeV [149] in a kinematic range overlapping with the muon spectrometer. Thus one can extract f_B very precisely from these data as shown on Fig. B.1 where a fit of the p_T and y dependence of this ratio is also given. The integrated measurement, for unpolarized J/ψ is $f_B(\sqrt{s} = 7$ TeV, $p_T < 14$ GeV/c, $2.0 < y < 4.5$) = $(10.84 \pm 0.04 \pm 1.41)\%$ and $f_B(\sqrt{s} = 7$ TeV, $p_T < 13$ GeV/c, $2.5 < y < 4.0$) = $(10.67 \pm 0.04 \pm 1.41)\%$. More recently, the LHCb collaboration completed the previous measurement with a lower energy at $\sqrt{s} = 2.76$ TeV [148]. The quoted value for unpolarized J/ψ is $f_B(\sqrt{s} = 2.76$ TeV, $p_T < 12$ GeV/c, $2.0 < y < 4.5$) = $(7.7 \pm 0.7 \pm 0.8)\%$. At $\sqrt{s} = 5.02$ TeV f_B can be calculated from the interpolated cross sections of prompt and non-prompt [154] J/ψ , resulting in $f_B(\sqrt{s} = 5.02$ TeV, $p_T < 12$ GeV/c, $2.5 < y < 4.0$) = $(9.8 \pm 0.8)\%$.

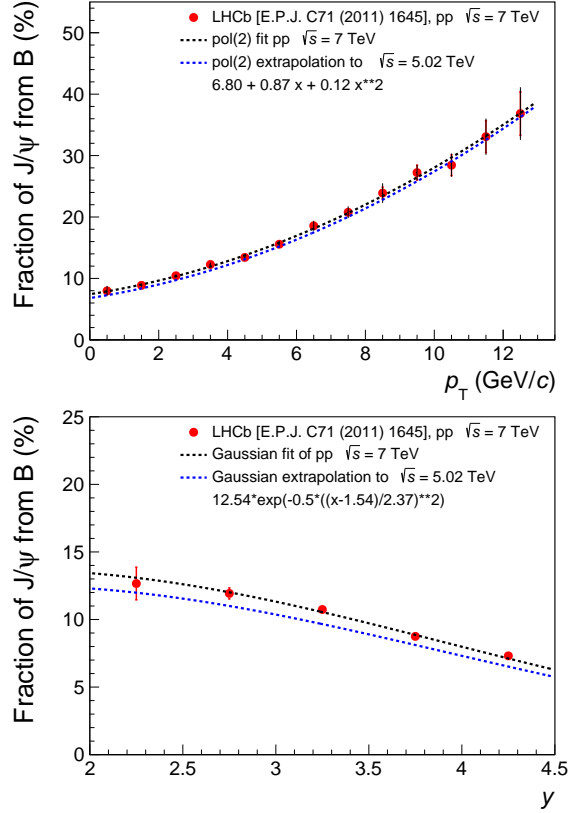


Figure B.1: Fraction of non-prompt J/ψ to prompt J/ψ , f_B , measured as a function of p_T (left) and rapidity (right). See text for details.

Thus, one can extract a reduction factor in the f_B of 1.41 going from $\sqrt{s} = 7$ TeV to $\sqrt{s} = 2.76$ TeV and of 1.09 from 7 to 5.02 TeV. Assuming that (i) this \sqrt{s} scaling factor is independent of p_T and y for the considered kinematic range (ii) the p_T dependence of f_B can be parametrized with a pol(2) function and (iii) the y dependence of f_B can be parametrized with a Gaussian function. One can obtain the extrapolation of f_B down to $\sqrt{s} = 5.02$ TeV (blue dashed lines in Fig. B.1). The p_T and y parametrizations of f_B can now be injected in equation B.1.

A reliable determination of the B-quenching factor R_{AA}^{npro} presents more difficulties since it is not available in the p_T and rapidity intervals in which the R_{AA} is determined in ALICE. Therefore, it is only possible to consider extreme hypotheses on this quenching inspired from measurements in other kinematic domains.

At high- p_T for $y < 2.4$, the CMS collaboration has measured the non-prompt J/ψ suppression [155] in Pb-Pb collisions. For J/ψ $\langle p_T \rangle \approx 9$ GeV/ c , a $R_{AA} = 0.37 \pm 0.08$ (stat.) ± 0.02 (syst.) has been measured. In Ref [156], a decrease of the R_{AA} of non-prompt J/ψ with increasing p_T is observed.

Another input is coming from theoretical prediction coupled with the ALICE measurement of D meson R_{AA} . Radiative energy loss theoretical predictions suggest different suppression factor for heavy quarks according to $R_{AA}^B > R_{AA}^D$. The ALICE measurement [157] shows that D mesons can be suppressed down to $R_{AA} \sim 0.2$ in most central Pb-Pb collisions. This, together with the non-prompt J/ψ suppression results from CMS, can tell that the hypothesis of a full b-hadrons suppression is really extreme. Concerning the hypothesis of no-nuclear effects on b-hadrons ($R_{AA}^{npro} = 1$), it could be not the extreme case since the no-prompt R_{AA} can exceed unity, but since there are no indications on the value, unity is taken.

J/ψ INVARIANT MASS FITS

This appendix presents examples of opposite-charge dimuon invariant distributions fitted in the *J/ψ* region. As described in chapter 4, different background and signal functions are used. In this appendix, one combination is considered for all the centrality, rapidity, and p_T intervals. It is the sum of a variable width gaussian (VWG2) and a crystal ball function (CB2). The fit in these examples is performed in the invariant mass range 2.2-4.5 GeV/ c^2 .

In different centrality intervals. $2.5 < y < 4$ and $0 < p_T < 8$

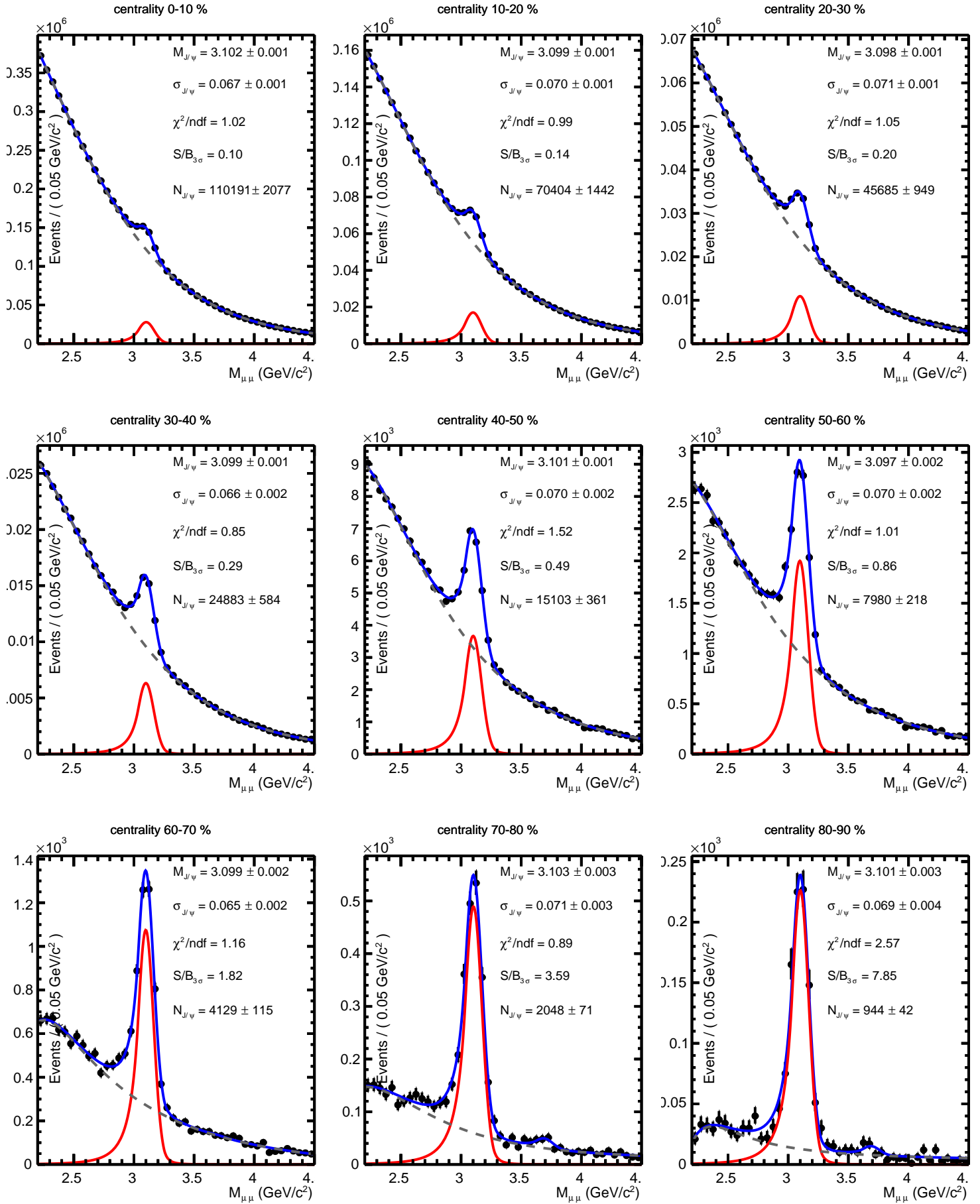


Figure C.1:

In different centrality intervals. $2.5 < y < 4$ and $0.3 < p_T < 8$

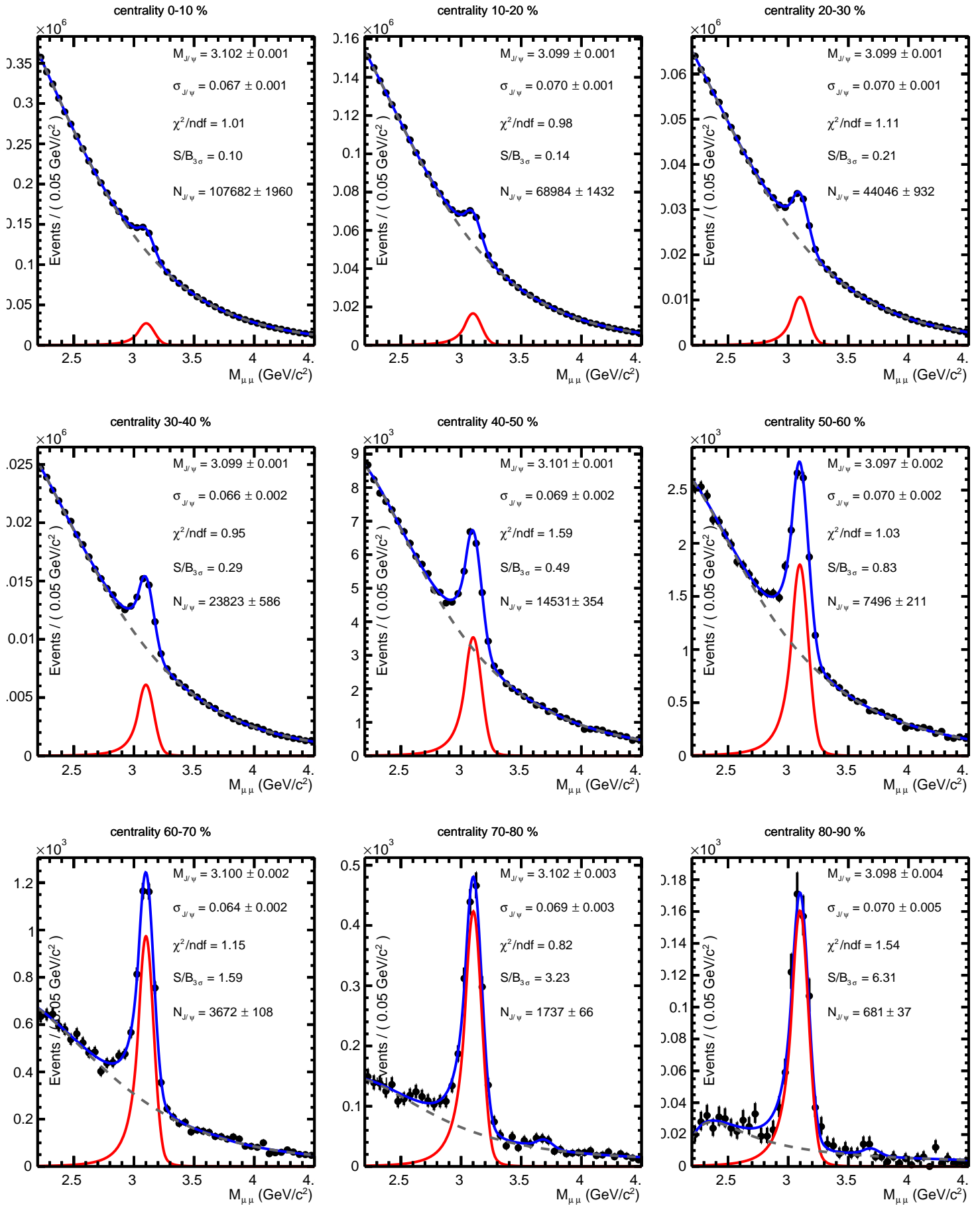


Figure C.2:

In different centrality intervals. $2.5 < y < 4$ and $0 < p_T < 2$

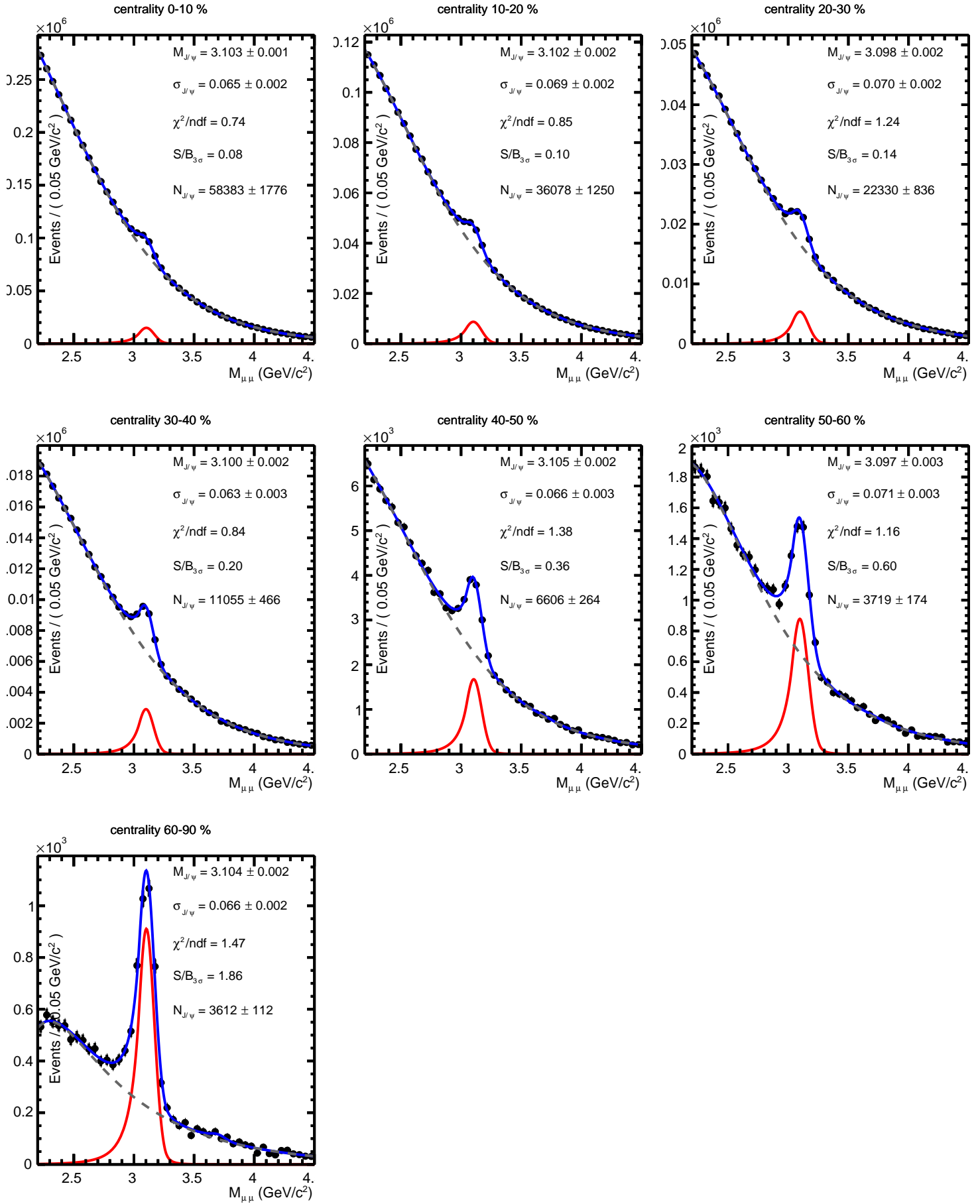


Figure C.3:

In different centrality intervals. $2.5 < y < 4$ and $2 < p_T < 5$

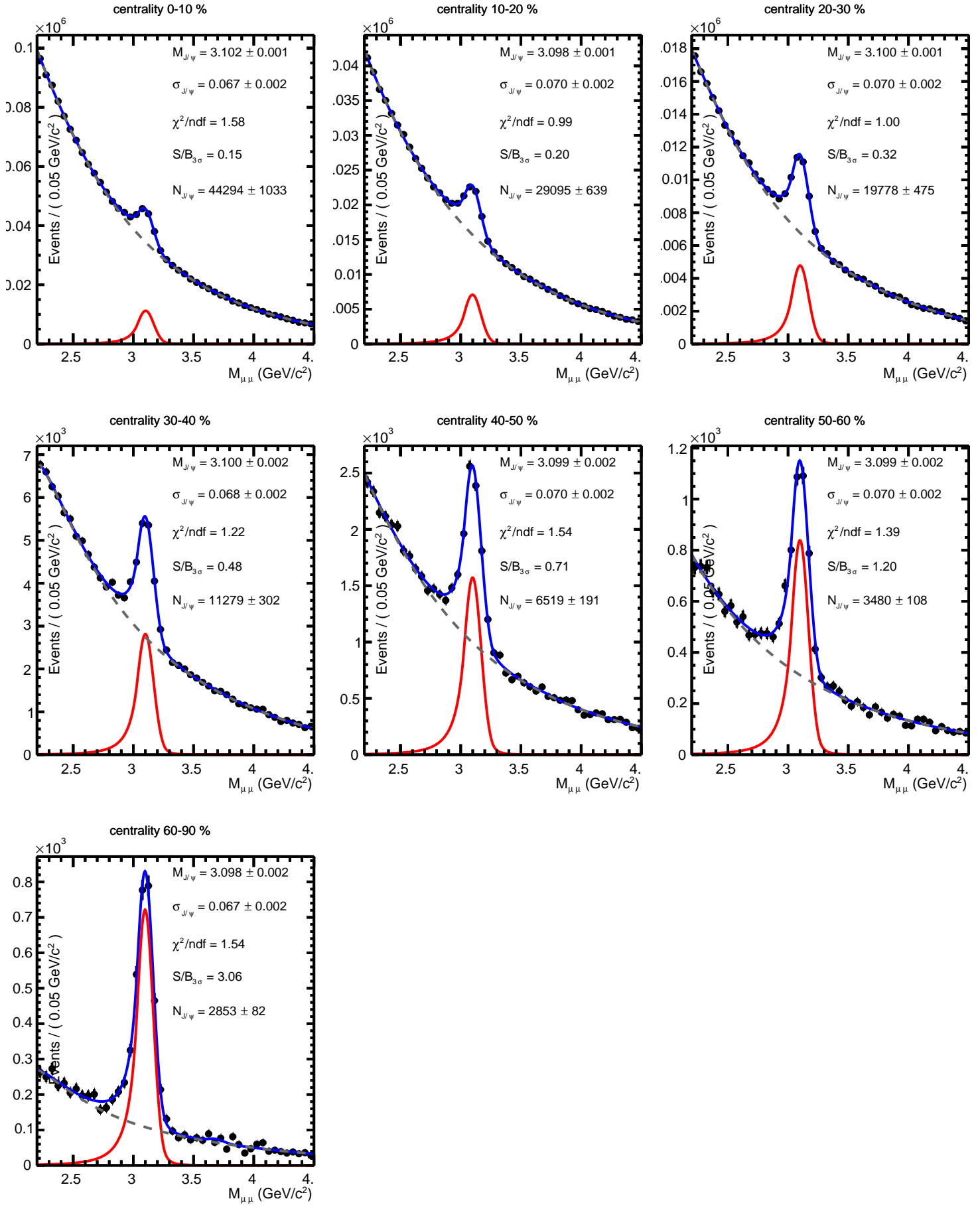


Figure C.4:

In different centrality intervals. $2.5 < y < 4$ and $5 < p_T < 8$

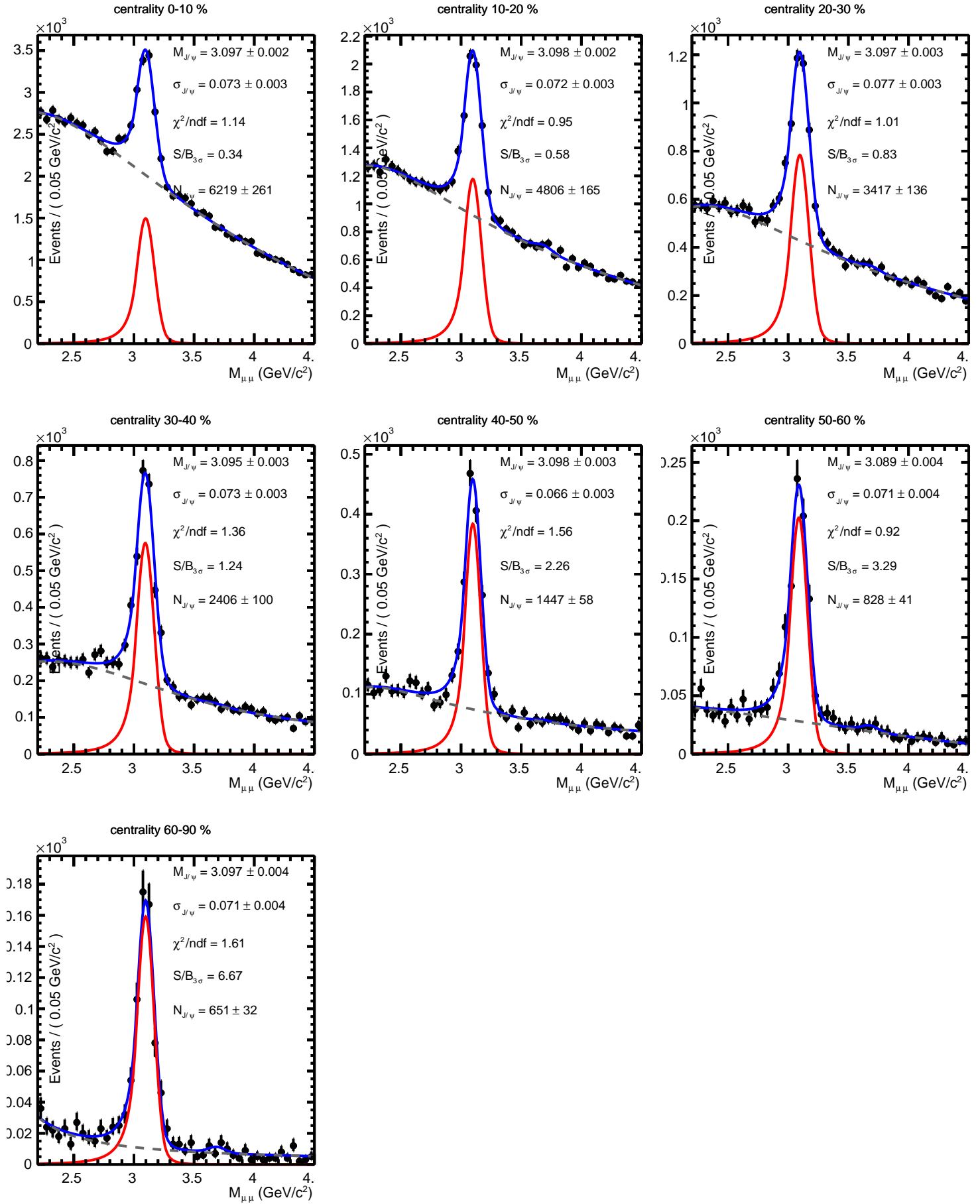


Figure C.5:

In different centrality intervals. $2.5 < y < 4$ and $8 < p_T < 12$

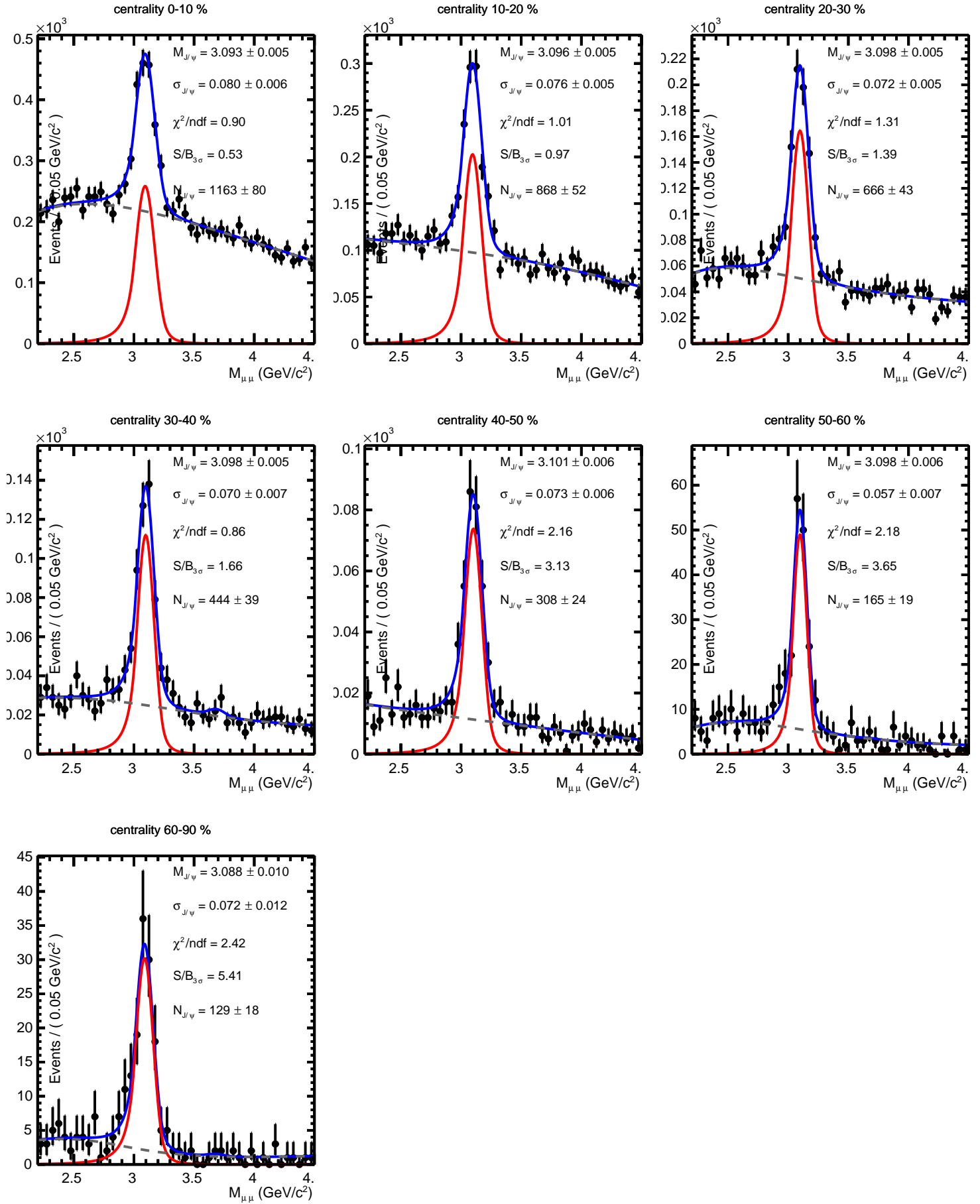


Figure C.6:

In different p_T intervals. $2.5 < y < 4$ and centrality 0–20 %

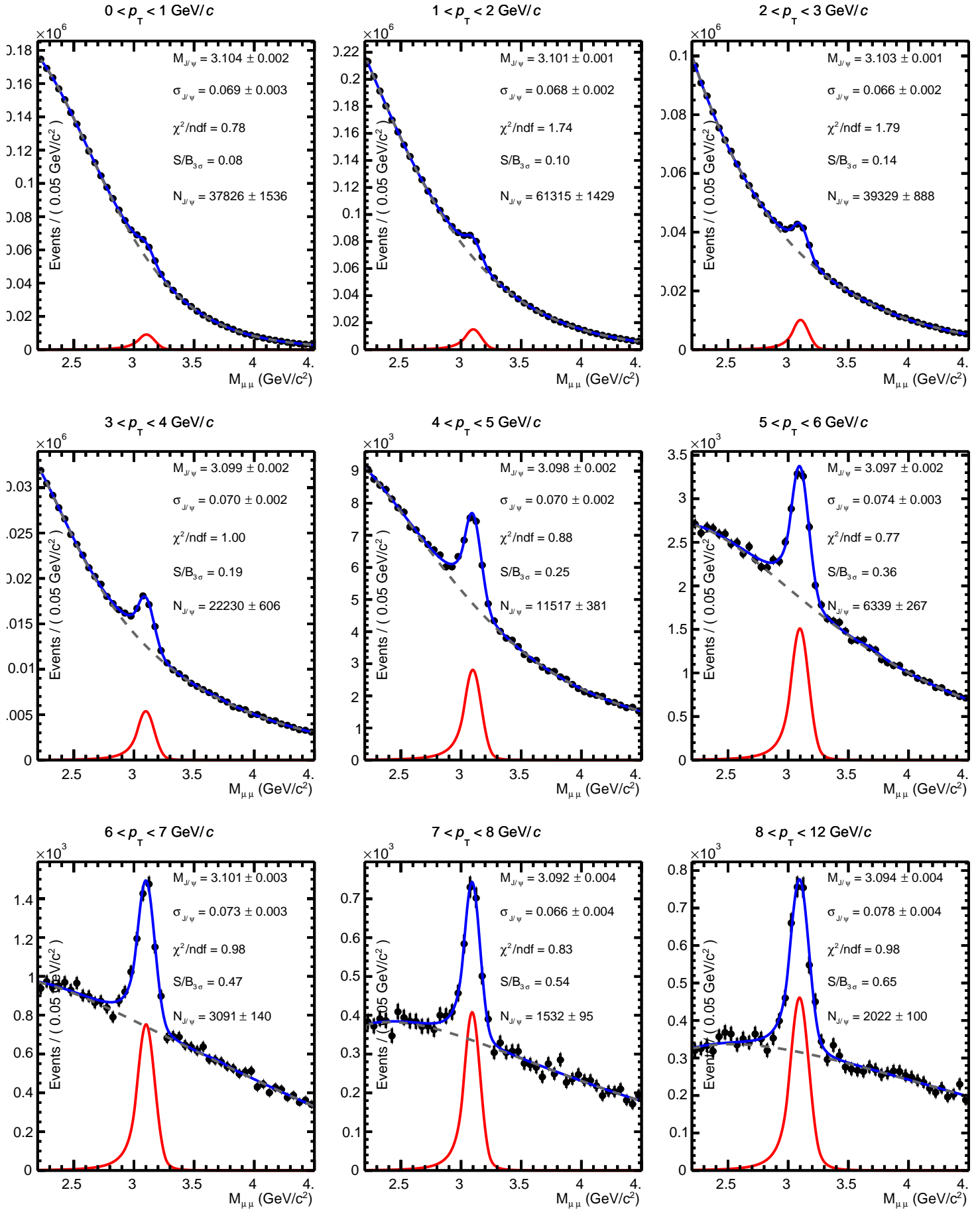


Figure C.7:

In different rapidity intervals. Centrality 0–90 % and $0 < p_T < 12$

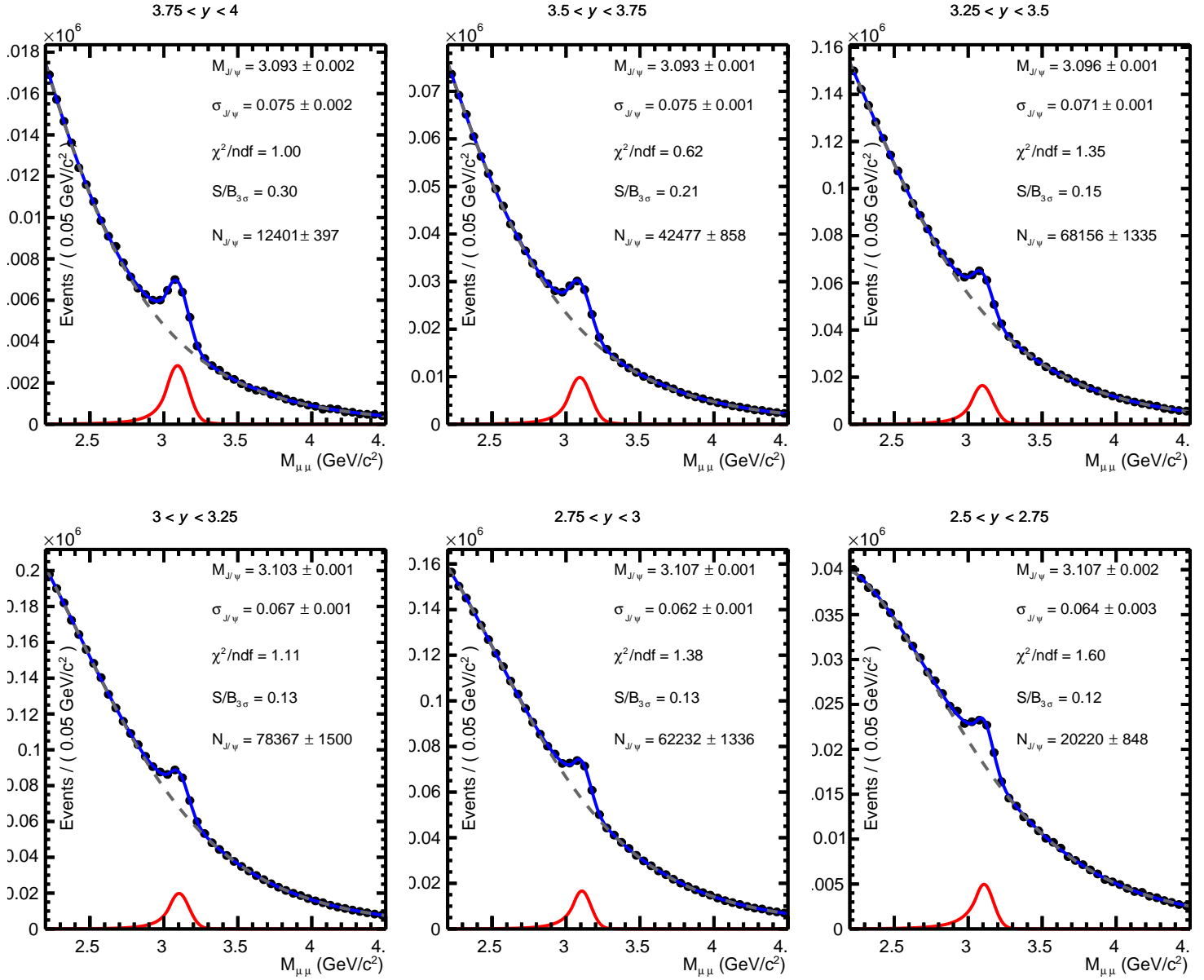


Figure C.8:

NUMERICAL VALUES OF RESULTS

This appendix gives the numerical values for the different presented quantities in the previous chapters and related to the J/ψ production analysis. In particular, the values of the J/ψ pp cross section, the signal extraction, and $A\epsilon$ results, and the R_{AA} and $\langle p_T \rangle$ results.

D.1 J/ψ pp cross sections at $\sqrt{s} = 5.02$ TeV

p_T differential cross sections in different rapidity intervals

p_T (GeV/c)	$2.5 < y < 4$	$2.5 < y < 3.25$	$3.25 < y < 4$
0–1	$0.6509 \pm 0.0238 \pm 0.0331$	$0.7506 \pm 0.0447 \pm 0.0461$	$0.5560 \pm 0.0290 \pm 0.0300$
0.3–1	$0.8529 \pm 0.0330 \pm 0.0439$	$1.0076 \pm 0.0548 \pm 0.0627$	$0.7050 \pm 0.0395 \pm 0.0380$
1–2	$1.1731 \pm 0.0311 \pm 0.0517$	$1.2930 \pm 0.0490 \pm 0.0674$	$1.0520 \pm 0.0390 \pm 0.0521$
2–3	$0.9033 \pm 0.0273 \pm 0.0361$	$1.0717 \pm 0.0445 \pm 0.0522$	$0.7466 \pm 0.0354 \pm 0.0364$
3–4	$0.5192 \pm 0.0193 \pm 0.0213$	$0.6259 \pm 0.0301 \pm 0.0353$	$0.4223 \pm 0.0250 \pm 0.0217$
4–5	$0.2304 \pm 0.0126 \pm 0.0134$	$0.2870 \pm 0.0196 \pm 0.0150$	$0.1746 \pm 0.0144 \pm 0.0101$
5–6	$0.1268 \pm 0.0076 \pm 0.0049$	$0.1472 \pm 0.0117 \pm 0.0071$	$0.1082 \pm 0.0095 \pm 0.0061$
6–7	$0.0621 \pm 0.0051 \pm 0.0022$	–	–
7–8	$0.0291 \pm 0.0033 \pm 0.0009$	–	–
6–8	$0.0450 \pm 0.0040 \pm 0.0015$	$0.0634 \pm 0.0052 \pm 0.0029$	$0.0280 \pm 0.0038 \pm 0.0017$
8–12	$0.0080 \pm 0.0008 \pm 0.0003$	$0.0089 \pm 0.0013 \pm 0.0004$	$0.0067 \pm 0.0010 \pm 0.0004$
0–2	$0.9160 \pm 0.0202 \pm 0.0418$	–	–
0.3–2	$1.0439 \pm 0.0232 \pm 0.0477$	–	–
2–5	$0.5527 \pm 0.0122 \pm 0.0248$	–	–
5–8	$0.0732 \pm 0.0034 \pm 0.0028$	–	–
0–12	$0.4600 \pm 0.0060 \pm 0.0230$	–	–
0.3–12	$0.4720 \pm 0.0068 \pm 0.0230$	–	–

Table D.1: The inclusive p_T differential J/ψ production cross section in different rapidity ranges in pp collisions at $\sqrt{s} = 5.02$ TeV measured with ALICE [98]. The first quoted uncertainty is statistical while the second one is the uncorrelated systematic. All the values are affected by a 2.1% correlated uncertainty.

rapidity differential cross sections

y	$0 < p_T < 12 \text{ GeV}/c$	$0 < p_T < 12 \text{ GeV}/c$
3.75–4	$2.5190 \pm 0.1650 \pm 0.1500$	$2.4597 \pm 0.1725 \pm 0.1420$
3.5–3.75	$3.0970 \pm 0.1070 \pm 0.1500$	$3.0293 \pm 0.1104 \pm 0.1210$
3.25–3.5	$3.6430 \pm 0.1040 \pm 0.1500$	$3.6001 \pm 0.1061 \pm 0.1420$
3–3.25	$3.9890 \pm 0.1120 \pm 0.1700$	$3.9622 \pm 0.1102 \pm 0.1670$
2.75–3	$4.3460 \pm 0.1360 \pm 0.2000$	$4.2972 \pm 0.1340 \pm 0.1912$
2.5–2.75	$4.5940 \pm 0.2640 \pm 0.3500$	$4.5775 \pm 0.2661 \pm 0.2881$

Table D.2: The inclusive rapidity differential J/ψ production cross section in different p_T ranges in pp collisions at $\sqrt{s} = 5.02 \text{ TeV}$ measured with ALICE [98]. The first quoted uncertainty is statistical while the second one is the uncorrelated systematic. All the values are affected by a 2.1% correlated uncertainty.

D.2 J/ψ invariant yield in Pb-Pb collisions at $\sqrt{s_{\text{NN}}} = 5.02 \text{ TeV}$

$$\frac{d^2 Y_{J/\psi}^i}{dy dp_T} = \frac{N_{J/\psi}^i}{\Delta p_T \cdot \Delta y \cdot BR_{J/\psi \rightarrow \mu\mu} \cdot A \varepsilon^i(p_T, y) \cdot N_{MB}^i}, \quad (\text{D.1})$$

$p_T \text{ (GeV}/c)$	0–10 %	10–20 %	20–30 %	30–40 %
0–0.5	$56.752 \pm 4.593 \pm 3.430$	$40.927 \pm 4.192 \pm 2.552$	$24.993 \pm 2.464 \pm 1.574$	$13.872 \pm 1.499 \pm 0.915$
0.5–1	$181.308 \pm 10.267 \pm 11.299$	$102.113 \pm 5.916 \pm 6.157$	$60.416 \pm 3.827 \pm 3.553$	$28.686 \pm 2.104 \pm 1.749$
1–2	$204.643 \pm 5.869 \pm 11.075$	$120.168 \pm 4.147 \pm 6.656$	$73.725 \pm 2.802 \pm 4.014$	$34.830 \pm 1.685 \pm 1.913$
2–3	$136.433 \pm 3.862 \pm 7.225$	$84.111 \pm 2.842 \pm 4.433$	$53.602 \pm 1.804 \pm 3.003$	$27.576 \pm 1.144 \pm 1.459$
3–4	$61.503 \pm 2.153 \pm 3.193$	$39.427 \pm 1.427 \pm 2.034$	$26.415 \pm 0.939 \pm 1.329$	$14.978 \pm 0.596 \pm 0.760$
4–5	$23.484 \pm 1.059 \pm 1.245$	$17.190 \pm 0.739 \pm 0.904$	$11.324 \pm 0.484 \pm 0.548$	$7.515 \pm 0.312 \pm 0.428$
5–6	$10.183 \pm 0.529 \pm 0.570$	$7.499 \pm 0.367 \pm 0.353$	$4.931 \pm 0.251 \pm 0.239$	$3.171 \pm 0.176 \pm 0.155$
6–7	$4.117 \pm 0.249 \pm 0.216$	$3.206 \pm 0.180 \pm 0.158$	$2.490 \pm 0.178 \pm 0.128$	$1.852 \pm 0.108 \pm 0.094$
7–8	$1.732 \pm 0.144 \pm 0.097$	$1.628 \pm 0.138 \pm 0.086$	$1.105 \pm 0.106 \pm 0.062$	$0.860 \pm 0.063 \pm 0.046$
8–12	$0.553 \pm 0.035 \pm 0.031$	$0.410 \pm 0.026 \pm 0.024$	$0.296 \pm 0.019 \pm 0.015$	$0.186 \pm 0.015 \pm 0.010$

Table D.3: Inclusive J/ψ invariant yields (Equation D.1 and multiplied by 10^4) as a function of p_T in Pb-Pb collisions at $\sqrt{s_{\text{NN}}} = 5.02 \text{ TeV}$ for four centrality intervals and in the rapidity range $2.5 < y < 4$. The first quoted uncertainty is statistical while the second one is systematic.

$p_T \text{ (GeV}/c)$	40–50 %	50–60 %	60–90 %
0–0.5	$9.511 \pm 1.023 \pm 0.625$	$5.971 \pm 0.478 \pm 0.383$	$3.442 \pm 0.139 \pm 0.200$
0.5–1	$15.053 \pm 1.300 \pm 0.964$	$8.800 \pm 0.799 \pm 0.563$	$2.388 \pm 0.156 \pm 0.153$
1–2	$22.325 \pm 1.055 \pm 1.247$	$10.748 \pm 0.618 \pm 0.597$	$2.782 \pm 0.116 \pm 0.153$
2–3	$16.290 \pm 0.729 \pm 0.863$	$8.548 \pm 0.457 \pm 0.451$	$2.359 \pm 0.101 \pm 0.120$
3–4	$9.071 \pm 0.373 \pm 0.562$	$4.729 \pm 0.236 \pm 0.253$	$1.228 \pm 0.054 \pm 0.065$
4–5	$4.114 \pm 0.204 \pm 0.207$	$2.464 \pm 0.127 \pm 0.129$	$0.649 \pm 0.032 \pm 0.034$
5–6	$2.003 \pm 0.110 \pm 0.098$	$1.101 \pm 0.075 \pm 0.055$	$0.285 \pm 0.020 \pm 0.014$
6–7	$0.959 \pm 0.061 \pm 0.050$	$0.648 \pm 0.056 \pm 0.039$	$0.138 \pm 0.012 \pm 0.007$
7–8	$0.502 \pm 0.039 \pm 0.026$	$0.292 \pm 0.033 \pm 0.016$	$0.084 \pm 0.008 \pm 0.004$
8–12	$0.131 \pm 0.010 \pm 0.006$	$0.073 \pm 0.008 \pm 0.004$	$0.019 \pm 0.002 \pm 0.001$

Table D.4: Inclusive J/ψ invariant yields (Equation D.1 and multiplied by 10^4) as a function of p_T in Pb-Pb collisions at $\sqrt{s_{\text{NN}}} = 5.02 \text{ TeV}$ for three centrality intervals and in the rapidity range $2.5 < y < 4$.

centrality (%)	$\langle p_T \rangle \pm (\text{stat}) \pm (\text{sys})$	$\langle p_T^2 \rangle \pm (\text{stat}) \pm (\text{sys})$	$r_{AA} \pm (\text{stat} + \text{syst})$
Pb-Pb collisions at $\sqrt{s_{NN}} = 5.02 \text{ TeV}$			
0–10	$2.004 \pm 0.017 \pm 0.016$	$5.588 \pm 0.082 \pm 0.077$	0.753 ± 0.015
10–20	$2.080 \pm 0.020 \pm 0.018$	$6.027 \pm 0.102 \pm 0.087$	0.812 ± 0.018
20–30	$2.124 \pm 0.022 \pm 0.018$	$6.279 \pm 0.110 \pm 0.089$	0.846 ± 0.019
30–40	$2.282 \pm 0.026 \pm 0.024$	$7.161 \pm 0.140 \pm 0.152$	0.965 ± 0.028
40–50	$2.286 \pm 0.028 \pm 0.022$	$7.215 \pm 0.150 \pm 0.118$	0.972 ± 0.026
50–60	$2.333 \pm 0.037 \pm 0.024$	$7.490 \pm 0.200 \pm 0.128$	1.009 ± 0.032
60–90	$2.326 \pm 0.028 \pm 0.023$	$7.446 \pm 0.151 \pm 0.127$	1.003 ± 0.027
pp collisions at $\sqrt{s} = 5.02 \text{ TeV}$			
N.A.	$2.310 \pm 0.019 \pm 0.024$	$7.421 \pm 0.120 \pm 0.110$	–

Table D.5: The inclusive J/ψ $\langle p_T \rangle$, $\langle p_T^2 \rangle$, and r_{AA} measured by ALICE in pp collisions at $\sqrt{s} = 5.02 \text{ TeV}$ [98] and in different centrality intervals in Pb-Pb collisions at $\sqrt{s_{NN}} = 5.02 \text{ TeV}$. The first quoted uncertainties are statistical while the second ones are systematic.

D.3 J/ψ $\langle p_T \rangle$ and r_{AA} results at $\sqrt{s_{NN}} = 5.02 \text{ TeV}$

D.4 J/ψ R_{AA} results at $\sqrt{s_{NN}} = 5.02 \text{ TeV}$

In the following, the R_{AA} results in different centrality, rapidity, and p_T intervals are summarized. For each interval, the columns in order represent:

- $N_{J/\psi}$ is the number of J/ψ in this interval, the first quoted uncertainty is statistical while the second is systematic.
- $A\epsilon$ is the acceptance times efficiency of the detector in (%).
- R_{AA} is the nuclear modification factor. The first quoted uncertainty is statistical while the second is uncorrelated systematic. The correlated one is reported in the header of each table.
- $R_{AA}^{Prompt,Max}$ and $R_{AA}^{Prompt,Min}$ represents the variation range of the prompt J/ψ R_{AA} according to two hypotheses on the b-hadrons.
- $R_{AA}^{\frac{5.02}{2.76}}$ is the ratio between the inclusive J/ψ R_{AA} at $\sqrt{s_{NN}} = 5.02 \text{ TeV}$ and $\sqrt{s_{NN}} = 2.76 \text{ TeV}$. The first quoted uncertainty is statistical while the second is uncorrelated systematic. The correlated one is reported in the header of each table.

In different centrality intervals. $2.5 < y < 4$ and $0.3 < p_T < 8$

centrality (%)	$N_{J/\psi}$	$A\epsilon$	$R_{AA}(7.90\% \text{ corr. sys})$	$R_{AA}^{Prompt,Max}$	$R_{AA}^{Prompt,Min}$	$R_{AA}^{\frac{5.02}{2.76}}(16.20\% \text{ corr. sys})$
0,10	$104304 \pm 1739 \pm 1999$	12.89	$0.630 \pm 0.010 \pm 0.030$	+9%	-4%	$1.170 \pm 0.040 \pm 0.050$
10,20	$67311 \pm 1187 \pm 1094$	13.51	$0.641 \pm 0.010 \pm 0.020$	+9%	-4%	$1.150 \pm 0.040 \pm 0.030$
20,30	$43265 \pm 799 \pm 701$	13.80	$0.670 \pm 0.010 \pm 0.020$	+9%	-4%	$1.120 \pm 0.040 \pm 0.020$
30,40	$23775 \pm 481 \pm 581$	14.45	$0.619 \pm 0.010 \pm 0.030$	+9%	-5%	$1.090 \pm 0.050 \pm 0.040$
40,50	$14128 \pm 313 \pm 272$	14.55	$0.690 \pm 0.020 \pm 0.030$	+9%	-3%	$1.170 \pm 0.060 \pm 0.040$
50,60	$7256 \pm 180 \pm 137$	14.63	$0.721 \pm 0.020 \pm 0.040$	+9%	-2%	$1.000 \pm 0.050 \pm 0.040$
60,70	$3672 \pm 101 \pm 65$	14.74	$0.810 \pm 0.020 \pm 0.050$	+9%	0%	$1.010 \pm 0.060 \pm 0.050$
70,80	$1701 \pm 61 \pm 28$	14.85	$0.921 \pm 0.030 \pm 0.070$	+9%	+1%	$1.180 \pm 0.100 \pm 0.070$
80,90	$660 \pm 32 \pm 11$	14.84	$0.902 \pm 0.040 \pm 0.090$	+9%	+2%	$1.010 \pm 0.120 \pm 0.090$

Table D.6:

In different centrality intervals. $2.5 < y < 4$ and $0.3 < p_T < 2$

centrality (%)	$N_{J/\psi}$	$A\epsilon$	$R_{AA}(7.14\% \text{ corr. sys})$	$R_{AA}^{Prompt,Max}$	$R_{AA}^{Prompt,Min}$	$R_{AA}^{5.02/2.76}(16.61\% \text{ corr. sys})$
0,10	$54593 \pm 1420 \pm 1137$	12.00	$0.738 \pm 0.019 \pm 0.029$	+7%	-2%	$0.991 \pm 0.060 \pm 0.050$
10,20	$33492 \pm 1074 \pm 664$	12.39	$0.718 \pm 0.023 \pm 0.027$	+7%	-3%	$0.975 \pm 0.057 \pm 0.028$
20,30	$20666 \pm 662 \pm 364$	12.50	$0.731 \pm 0.023 \pm 0.026$	+7%	-2%	$1.021 \pm 0.063 \pm 0.024$
30,40	$10192 \pm 434 \pm 196$	12.85	$0.612 \pm 0.026 \pm 0.023$	+7%	-4%	$0.913 \pm 0.067 \pm 0.036$
40,50	$6099 \pm 268 \pm 153$	12.85	$0.691 \pm 0.030 \pm 0.032$	+7%	-2%	$1.116 \pm 0.095 \pm 0.048$
50,60	$3084 \pm 147 \pm 71$	12.93	$0.708 \pm 0.034 \pm 0.039$	+7%	-2%	$0.884 \pm 0.069 \pm 0.046$
60,90	$2576 \pm 100 \pm 53$	13.08	$0.838 \pm 0.033 \pm 0.061$	+7%	0%	$0.873 \pm 0.062 \pm 0.047$

Table D.7:

In different centrality intervals. $2.5 < y < 4$ and $2 < p_T < 5$

centrality (%)	$N_{J/\psi}$	$A\epsilon$	$R_{AA}(6.79\% \text{ corr. sys})$	$R_{AA}^{Prompt,Max}$	$R_{AA}^{Prompt,Min}$	$R_{AA}^{5.02/2.76}(15.56\% \text{ corr. sys})$
0,10	$43119 \pm 854 \pm 1011$	13.14	$0.570 \pm 0.011 \pm 0.023$	+10%	-7%	$1.341 \pm 0.066 \pm 0.043$
10,20	$28649 \pm 637 \pm 671$	13.75	$0.592 \pm 0.013 \pm 0.024$	+10%	-7%	$1.285 \pm 0.060 \pm 0.034$
20,30	$18941 \pm 416 \pm 425$	14.05	$0.638 \pm 0.014 \pm 0.025$	+10%	-5%	$1.206 \pm 0.057 \pm 0.031$
30,40	$10826 \pm 282 \pm 240$	14.55	$0.615 \pm 0.016 \pm 0.024$	+10%	-6%	$1.235 \pm 0.070 \pm 0.060$
40,50	$6469 \pm 182 \pm 160$	14.72	$0.685 \pm 0.019 \pm 0.031$	+10%	-4%	$1.151 \pm 0.066 \pm 0.045$
50,60	$3411 \pm 102 \pm 60$	14.60	$0.742 \pm 0.022 \pm 0.039$	+10%	-3%	$1.099 \pm 0.076 \pm 0.044$
60,90	$2798 \pm 78 \pm 51$	14.81	$0.860 \pm 0.024 \pm 0.062$	+10%	-1%	$1.191 \pm 0.080 \pm 0.062$

Table D.8:

In different centrality intervals. $2.5 < y < 4$ and $5 < p_T < 8$

centrality (%)	$N_{J/\psi}$	$A\epsilon$	$R_{AA}(7.52\% \text{ corr. sys})$	$R_{AA}^{Prompt,Max}$	$R_{AA}^{Prompt,Min}$	$R_{AA}^{5.02/2.76}(19.51\% \text{ corr. sys})$
0,10	$6060 \pm 232 \pm 93$	25.58	$0.311 \pm 0.012 \pm 0.011$	+15%	-34%	$1.110 \pm 0.094 \pm 0.029$
10,20	$4803 \pm 181 \pm 64$	26.11	$0.395 \pm 0.015 \pm 0.014$	+15%	-24%	$1.400 \pm 0.144 \pm 0.036$
20,30	$3345 \pm 127 \pm 49$	27.00	$0.443 \pm 0.017 \pm 0.015$	+15%	-19%	$1.080 \pm 0.087 \pm 0.017$
30,40	$2367 \pm 97 \pm 34$	27.15	$0.544 \pm 0.022 \pm 0.019$	+15%	-13%	$1.007 \pm 0.084 \pm 0.034$
40,50	$1436 \pm 57 \pm 16$	27.88	$0.606 \pm 0.024 \pm 0.024$	+15%	-10%	$1.145 \pm 0.124 \pm 0.053$
50,60	$796 \pm 45 \pm 18$	27.66	$0.691 \pm 0.040 \pm 0.038$	+15%	-7%	$1.177 \pm 0.161 \pm 0.051$
60,90	$631 \pm 31 \pm 9$	28.01	$0.775 \pm 0.039 \pm 0.055$	+15%	-4%	$1.204 \pm 0.167 \pm 0.067$

Table D.9:

In different centrality intervals. $2.5 < y < 4$ and $8 < p_T < 12$

centrality (%)	$N_{J/\psi}$	$A\epsilon$	$R_{AA}(11.59\% \text{ corr. sys})$	$R_{AA}^{Prompt,Max}$	$R_{AA}^{Prompt,Min}$	$R_{AA}^{5.02/2.76}(11.59\% \text{ corr. sys})$
0,10	$1194 \pm 84 \pm 21$	36.77	$0.292 \pm 0.021 \pm 0.011$	+24%	-53%	---
10,20	$898 \pm 62 \pm 31$	36.83	$0.359 \pm 0.025 \pm 0.017$	+24%	-36%	---
20,30	$681 \pm 46 \pm 13$	38.37	$0.435 \pm 0.029 \pm 0.016$	+24%	-30%	---
30,40	$448 \pm 37 \pm 10$	40.93	$0.469 \pm 0.039 \pm 0.019$	+24%	-20%	---
40,50	$315 \pm 24 \pm 8$	40.04	$0.637 \pm 0.049 \pm 0.030$	+24%	-15%	---
50,60	$168 \pm 19 \pm 2$	39.05	$0.711 \pm 0.080 \pm 0.037$	+24%	-10%	---
60,90	$132 \pm 15 \pm 3$	40.15	$0.777 \pm 0.090 \pm 0.059$	+24%	-7%	---

Table D.10:

In different p_T intervals. $2.5 < y < 4$ and 0–20 % centrality

p_T (GeV/c)	$N_{J/\psi}$	A_ϵ	$R_{AA}(3.82\% \text{ corr. sys})$	$R_{AA}^{Prompt,Max}$	$R_{AA}^{Prompt,Min}$	$R_{AA}^{5.02}_{2.76}$ (nan% corr. sys)
0,1	$36836 \pm 1292 \pm 760$	13.41	$0.750 \pm 0.030 \pm 0.070$	+7%	-2%	$0.930 \pm 0.100 \pm 0.160$
1,2	$55865 \pm 1256 \pm 1022$	11.63	$0.730 \pm 0.020 \pm 0.060$	+8%	-3%	$1.060 \pm 0.080 \pm 0.150$
2,3	$39081 \pm 932 \pm 769$	11.91	$0.640 \pm 0.020 \pm 0.050$	+9%	-4%	$1.280 \pm 0.110 \pm 0.180$
3,4	$21576 \pm 540 \pm 451$	14.44	$0.510 \pm 0.010 \pm 0.040$	+11%	-8%	$1.340 \pm 0.130 \pm 0.190$
4,5	$11227 \pm 365 \pm 210$	18.50	$0.470 \pm 0.020 \pm 0.040$	+13%	-10%	$1.310 \pm 0.200 \pm 0.190$
5,6	$6299 \pm 242 \pm 77$	23.44	$0.380 \pm 0.010 \pm 0.030$	+15%	-18%	$1.330 \pm 0.230 \pm 0.190$
6,7	$3176 \pm 125 \pm 68$	28.24	$0.320 \pm 0.010 \pm 0.030$	+17%	-23%	---
7,8	$1535 \pm 112 \pm 29$	31.38	$0.300 \pm 0.020 \pm 0.040$	+20%	-32%	---
6,8	$4672 \pm 167 \pm 78$	29.30	---	---	---	$1.120 \pm 0.260 \pm 0.160$
8,9	$998 \pm 71 \pm 28$	35.00	$0.350 \pm 0.030 \pm 0.060$	+22%	-23%	---
9,10	$551 \pm 60 \pm 17$	37.53	$0.230 \pm 0.030 \pm 0.050$	+25%	-53%	---
10,12	$0 \pm 0 \pm 0$	39.65	$0.350 \pm 0.030 \pm 0.080$	+30%	-44%	---

Table D.11:

In different p_T intervals. $2.5 < y < 3.25$ and 0–20 % centrality

p_T (GeV/c)	$N_{J/\psi}$	A_ϵ	$R_{AA}(3.82\% \text{ corr. sys})$	$R_{AA}^{Prompt,Max}$	$R_{AA}^{Prompt,Min}$
0,1	$19303 \pm 991 \pm 486$	12.13	$0.760 \pm 0.039 \pm 0.082$	+8%	-2%
1,2	$31133 \pm 1030 \pm 674$	10.59	$0.815 \pm 0.027 \pm 0.069$	+9%	-1%
2,3	$21798 \pm 679 \pm 525$	11.08	$0.658 \pm 0.021 \pm 0.055$	+10%	-5%
3,4	$12895 \pm 417 \pm 397$	13.64	$0.542 \pm 0.018 \pm 0.050$	+12%	-10%
4,5	$6773 \pm 297 \pm 180$	17.50	$0.484 \pm 0.021 \pm 0.049$	+13%	-14%
5,6	$3755 \pm 181 \pm 70$	22.53	$0.406 \pm 0.020 \pm 0.043$	+15%	-22%
6,8	$2756 \pm 129 \pm 47$	28.33	$0.275 \pm 0.013 \pm 0.029$	+19%	-51%
8,12	$1336 \pm 76 \pm 11$	36.05	$0.373 \pm 0.021 \pm 0.060$	+26%	-45%

Table D.12:

In different p_T intervals. $3.25 < y < 4$ and 0–20 % centrality

p_T (GeV/c)	$N_{J/\psi}$	A_ϵ	$R_{AA}(3.82\% \text{ corr. sys})$	$R_{AA}^{Prompt,Max}$	$R_{AA}^{Prompt,Min}$
0,1	$17050 \pm 722 \pm 606$	15.46	$0.711 \pm 0.030 \pm 0.069$	+6%	-2%
1,2	$24586 \pm 798 \pm 573$	13.29	$0.631 \pm 0.020 \pm 0.051$	+7%	-4%
2,3	$17116 \pm 507 \pm 324$	13.23	$0.621 \pm 0.018 \pm 0.053$	+8%	-5%
3,4	$8699 \pm 368 \pm 185$	15.72	$0.470 \pm 0.020 \pm 0.044$	+9%	-10%
4,5	$4590 \pm 234 \pm 113$	20.10	$0.469 \pm 0.024 \pm 0.053$	+10%	-11%
5,6	$2483 \pm 136 \pm 51$	24.86	$0.331 \pm 0.018 \pm 0.038$	+12%	-24%
6,8	$1944 \pm 89 \pm 42$	30.73	$0.405 \pm 0.019 \pm 0.064$	+14%	-21%
8,12	$727 \pm 63 \pm 14$	37.95	$0.256 \pm 0.022 \pm 0.043$	+19%	-57%

Table D.13:

In different p_T intervals. $2.5 < y < 4$ and 20–40 % centrality

p_T (GeV/c)	$N_{J/\psi}$	A_ϵ	$R_{AA}(3.96\% \text{ corr. sys})$	$R_{AA}^{Prompt,Max}$	$R_{AA}^{Prompt,Min}$	$R_{AA}^{5.02}_{2.76}$ (7.52% corr. sys)
0,1	$13375 \pm 606 \pm 256$	14.07	$0.728 \pm 0.033 \pm 0.060$	+7%	-2%	$0.994 \pm 0.117 \pm 0.148$
0,3,1	$11649 \pm 565 \pm 241$	13.96	$0.697 \pm 0.034 \pm 0.059$	+7%	-2%	---
1,2	$19233 \pm 622 \pm 375$	12.00	$0.682 \pm 0.022 \pm 0.048$	+8%	-3%	$1.033 \pm 0.087 \pm 0.136$
2,3	$14947 \pm 402 \pm 468$	12.45	$0.663 \pm 0.018 \pm 0.048$	+9%	-4%	$1.221 \pm 0.104 \pm 0.165$
3,4	$9292 \pm 250 \pm 166$	15.18	$0.588 \pm 0.016 \pm 0.042$	+11%	-7%	$1.193 \pm 0.121 \pm 0.158$
4,5	$5431 \pm 170 \pm 182$	19.64	$0.599 \pm 0.019 \pm 0.057$	+12%	-8%	$1.349 \pm 0.196 \pm 0.191$
5,6	$2958 \pm 125 \pm 36$	24.73	$0.471 \pm 0.020 \pm 0.039$	+14%	-16%	$1.180 \pm 0.204 \pm 0.155$
6,7	$1825 \pm 92 \pm 47$	28.47	$0.515 \pm 0.026 \pm 0.052$	+17%	-16%	---
7,8	$971 \pm 61 \pm 26$	33.93	$0.491 \pm 0.031 \pm 0.062$	+19%	-19%	---
6,8	$2773 \pm 108 \pm 31$	30.29	$0.507 \pm 0.020 \pm 0.054$	+18%	-17%	$0.970 \pm 0.219 \pm 0.143$
8,12	$1119 \pm 58 \pm 15$	39.24	$0.445 \pm 0.023 \pm 0.051$	+24%	-30%	---

Table D.14:

In different p_T intervals. $2.5 < y < 4$ and 40–90 % centrality

p_T (GeV/c)	$N_{J/\psi}$	$A\epsilon$	$R_{AA}(4.97\% \text{ corr. sys})$	$R_{AA}^{Prompt,Max}$	$R_{AA}^{Prompt,Min}$	$R_{AA}^{5.02, 2.76} (8.03\% \text{ corr. sys})$
0,1	$6122 \pm 225 \pm 126$	14.35	$1.386 \pm 0.051 \pm 0.115$	+7%	0%	$1.701 \pm 0.180 \pm 0.241$
0.3,1	$4155 \pm 206 \pm 104$	14.21	$0.690 \pm 0.034 \pm 0.059$	+7 %	0%	---
1,2	$7563 \pm 240 \pm 186$	12.34	$0.736 \pm 0.023 \pm 0.053$	+8%	-2%	$1.006 \pm 0.087 \pm 0.128$
2,3	$6045 \pm 171 \pm 138$	12.89	$0.732 \pm 0.021 \pm 0.051$	+9%	-3%	$1.186 \pm 0.107 \pm 0.149$
3,4	$4008 \pm 109 \pm 112$	15.44	$0.705 \pm 0.019 \pm 0.052$	+11%	-4%	$1.124 \pm 0.115 \pm 0.139$
4,5	$2509 \pm 82 \pm 43$	19.97	$0.769 \pm 0.025 \pm 0.070$	+12%	-3%	$1.109 \pm 0.159 \pm 0.145$
5,6	$1475 \pm 59 \pm 19$	25.27	$0.649 \pm 0.026 \pm 0.054$	+14%	-7%	$1.327 \pm 0.242 \pm 0.165$
6,7	$869 \pm 42 \pm 11$	29.87	$0.660 \pm 0.033 \pm 0.065$	+17%	-8%	---
7,8	$525 \pm 29 \pm 6$	33.98	$0.749 \pm 0.042 \pm 0.094$	+19%	-6%	---
6,8	$1384 \pm 55 \pm 17$	31.28	$0.693 \pm 0.028 \pm 0.074$	+18%	-7%	$1.073 \pm 0.253 \pm 0.150$
8,12	$611 \pm 34 \pm 6$	39.80	$0.677 \pm 0.038 \pm 0.078$	+24%	-11%	---

Table D.15:

In different rapidity intervals. $0 < p_T < 12$ and 0–90 % centrality

rapidity	$N_{J/\psi}$	$A\epsilon$	$R_{AA}(3.80\% \text{ corr. sys})$	$R_{AA}^{Prompt,Max}$	$R_{AA}^{Prompt,Min}$	$R_{AA}^{5.02, 2.76} (7.60\% \text{ corr. sys})$
2.5,2.75	$18837 \pm 743 \pm 830$	4.11	$0.721 \pm 0.028 \pm 0.086$	+11%	-4%	$1.143 \pm 0.164 \pm 0.203$
2.75,3	$60195 \pm 1191 \pm 1343$	14.87	$0.673 \pm 0.013 \pm 0.055$	+11%	-5%	$0.901 \pm 0.084 \pm 0.132$
3,3.25	$76310 \pm 1343 \pm 1366$	21.23	$0.651 \pm 0.011 \pm 0.048$	+10%	-5%	$1.030 \pm 0.080 \pm 0.165$
3.25,3.5	$66497 \pm 1191 \pm 1231$	21.37	$0.617 \pm 0.011 \pm 0.044$	+10%	-6%	$1.090 \pm 0.087 \pm 0.179$
3.5,3.75	$41995 \pm 765 \pm 659$	15.96	$0.614 \pm 0.011 \pm 0.046$	+8%	-5%	$1.314 \pm 0.118 \pm 0.212$
3.75,4	$12213 \pm 371 \pm 379$	6.01	$0.582 \pm 0.018 \pm 0.060$	+8%	-6%	$1.474 \pm 0.192 \pm 0.232$

Table D.16:

In different rapidity intervals. $0 < p_T < 12$ and 0–20 % centrality

rapidity	$N_{J/\psi}$	$A\epsilon$	$R_{AA}(3.82\% \text{ corr. sys})$	$R_{AA}^{Prompt,Max}$	$R_{AA}^{Prompt,Min}$
2.5,2.75	$12029 \pm 648 \pm 600$	3.97	$0.709 \pm 0.038 \pm 0.086$	+11%	-4%
2.75,3	$38988 \pm 1041 \pm 902$	14.53	$0.664 \pm 0.018 \pm 0.054$	+11%	-6%
3,3.25	$50347 \pm 1260 \pm 1059$	20.61	$0.659 \pm 0.016 \pm 0.049$	+10%	-5%
3.25,3.5	$42698 \pm 1100 \pm 644$	20.76	$0.607 \pm 0.016 \pm 0.042$	+10%	-6%
3.5,3.75	$27130 \pm 729 \pm 464$	15.46	$0.609 \pm 0.016 \pm 0.046$	+8%	-5%
3.75,4	$7486 \pm 323 \pm 250$	5.81	$0.550 \pm 0.024 \pm 0.057$	+8%	-6%

Table D.17:

In different rapidity intervals. $0 < p_T < 12$ and 20–40 % centrality

rapidity	$N_{J/\psi}$	$A\epsilon$	$R_{AA}(3.96\% \text{ corr. sys})$	$R_{AA}^{Prompt,Max}$	$R_{AA}^{Prompt,Min}$
2.5,2.75	$4906 \pm 296 \pm 150$	4.35	$0.735 \pm 0.044 \pm 0.085$	+11%	-4%
2.75,3	$15195 \pm 461 \pm 439$	15.35	$0.682 \pm 0.021 \pm 0.057$	+11%	-5%
3,3.25	$18638 \pm 524 \pm 378$	22.16	$0.631 \pm 0.018 \pm 0.047$	+10%	-6%
3.25,3.5	$16414 \pm 442 \pm 351$	22.29	$0.605 \pm 0.016 \pm 0.043$	+10%	-6%
3.5,3.75	$10127 \pm 299 \pm 193$	16.73	$0.585 \pm 0.017 \pm 0.044$	+8%	-6%
3.75,4	$3245 \pm 169 \pm 111$	6.32	$0.610 \pm 0.032 \pm 0.064$	+8%	-5%

Table D.18:

In different rapidity intervals. $0 < p_T < 12$ and 40–90 % centrality

rapidity	$N_{J/\psi}$	$A\epsilon$	$R_{AA}(4.97\% \text{ corr. sys})$	$R_{AA}^{Prompt,Max}$	$R_{AA}^{Prompt,Min}$
2.5,2.75	$2023 \pm 103 \pm 74$	4.44	$0.838 \pm 0.043 \pm 0.098$	+11%	-2%
2.75,3	$6307 \pm 189 \pm 154$	16.02	$0.766 \pm 0.023 \pm 0.063$	+11%	-3%
3,3.25	$7998 \pm 210 \pm 178$	23.18	$0.731 \pm 0.019 \pm 0.055$	+10%	-3%
3.25,3.5	$7263 \pm 199 \pm 126$	23.29	$0.724 \pm 0.020 \pm 0.051$	+10%	-4%
3.5,3.75	$4728 \pm 136 \pm 95$	17.45	$0.740 \pm 0.021 \pm 0.056$	+8%	-3%
3.75,4	$1413 \pm 59 \pm 43$	6.60	$0.718 \pm 0.030 \pm 0.074$	+8%	-3%

Table D.19:

LIST OF TABLES

2.1	Intrinsic properties of Z-boson.	16
2.2	Intrinsic properties of charmonium states.	18
2.3	Properties of some nPDF sets.	24
2.4	Dissociation temperature of different charmonium states.	32
4.1	CMUL7-B events in p-Pb and Pb-Pb collisions at $\sqrt{s_{NN}} = 5.02 \text{ TeV}$	74
4.2	F_{norm} in p-Pb and Pb-Pb collisions at $\sqrt{s_{NN}} = 5.02 \text{ TeV}$	78
4.3	ALICE integrated Luminosity in p-Pb collisions at $\sqrt{s_{NN}} = 5.02 \text{ TeV}$	79
4.4	Effects of different muon selections in p-Pb and Pb-Pb collisions at $\sqrt{s_{NN}} = 5.02 \text{ TeV}$	81
4.5	Number of Z-boson candidates in p-Pb and Pb-Pb collisions at $\sqrt{s_{NN}} = 5.02 \text{ TeV}$	89
4.6	Average number of J/ψ in different centrality intervals.	107
5.1	Systematics on the Z-boson cross section in p-Pb collisions at $\sqrt{s_{NN}} = 5.02 \text{ TeV}$	128
5.2	Z-boson cross section in p-Pb collisions at $\sqrt{s_{NN}} = 5.02 \text{ TeV}$	129
5.3	Centrality variables in Pb-Pb collisions at $\sqrt{s_{NN}} = 5.02 \text{ TeV}$	136
5.4	Z-boson production cross section in pp collisions at $\sqrt{s} = 5.02 \text{ TeV}$	136
5.5	Systematic uncertainties in Z-boson analysis in Pb-Pb collisions at $\sqrt{s_{NN}} = 5.02 \text{ TeV}$	138
5.6	Z-boson invariant yield and R_{AA} in Pb-Pb collisions at $\sqrt{s_{NN}} = 5.02 \text{ TeV}$	142
5.7	Z-boson invariant yield and R_{AA} as a function of rapidity in Pb-Pb collisions at $\sqrt{s_{NN}} = 5.02 \text{ TeV}$	142
5.8	Z-boson invariant yield and R_{AA} as a function of centrality in Pb-Pb collisions at $\sqrt{s_{NN}} = 5.02 \text{ TeV}$	142

6.1	Systematic uncertainties in the J/ψ analysis in Pb-Pb collisions at $\sqrt{s_{\text{NN}}} = 5.02 \text{ TeV}$	147
6.2	$\langle T_{\text{AA}} \rangle$ and $\langle N_{\text{part}} \rangle$ values in Pb-Pb collisions at $\sqrt{s_{\text{NN}}} = 5.02 \text{ TeV}$	155
6.3	J/ψ integrated R_{AA}	157
6.4	Prompt J/ψ R_{AA} in different p_{T} ranges.	164
6.5	Prompt J/ψ R_{AA} in different centrality ranges.	167
D.1	J/ψ pp cross section as function of p_{T}	205
D.2	J/ψ pp cross section as function of rapidity.	206
D.3	206
D.4	206
D.5	J/ψ $\langle p_{\text{T}} \rangle$, $\langle p_{\text{T}}^2 \rangle$, and r_{AA} in Pb-Pb collisions at $\sqrt{s_{\text{NN}}} = 5.02 \text{ TeV}$	207
D.6	J/ψ R_{AA} results in different centrality intervals. $2.5 < y < 4$ and $0.3 < p_{\text{T}} < 8$	207
D.7	J/ψ R_{AA} results in different centrality intervals. $2.5 < y < 4$ and $0.3 < p_{\text{T}} < 2$	208
D.8	J/ψ R_{AA} results in different centrality intervals. $2.5 < y < 4$ and $2 < p_{\text{T}} < 5$	208
D.9	J/ψ R_{AA} results in different centrality intervals. $2.5 < y < 4$ and $5 < p_{\text{T}} < 8$	208
D.10	J/ψ R_{AA} results in different centrality intervals. $2.5 < y < 4$ and $8 < p_{\text{T}} < 12$	208
D.11	J/ψ R_{AA} results in different p_{T} intervals. $2.5 < y < 4$ and 0–20 % centrality	209
D.12	J/ψ R_{AA} results in different p_{T} intervals. $2.5 < y < 3.25$ and 0–20 % centrality	209
D.13	J/ψ R_{AA} results in different p_{T} intervals. $3.25 < y < 4$ and 0–20 % centrality	209
D.14	J/ψ R_{AA} results in different p_{T} intervals. $2.5 < y < 4$ and 20–40 % centrality	209
D.15	J/ψ R_{AA} results in different p_{T} intervals. $2.5 < y < 4$ and 40–90 % centrality	210
D.16	J/ψ R_{AA} results in different rapidity intervals. $0 < p_{\text{T}} < 12$ and 0–90 % centrality	210

D.17 J/ψ R_{AA} results in different rapidity intervals. $0 < p_T < 12$ and 0–20 %	
centrality	210
D.18 J/ψ R_{AA} results in different rapidity intervals. $0 < p_T < 12$ and 20–40 %	
centrality	210
D.19 J/ψ R_{AA} results in different rapidity intervals. $0 < p_T < 12$ and 40–90 %	
centrality	210
TABLE	Page

LIST OF FIGURES

1.1 Elementary particles of the standard model.	5
1.2 Experimental measurements of α_s	6
1.3 T, μ_b phase space diagram.	8
1.4 Space-time evolution of heavy-ion collision.	10
1.5 Initial geometry of heavy-ion collision.	11
1.6 Schematic view of an elliptic flow.	13
2.1 Examples of Z-boson production Feynman diagrams.	17
2.2 Schematic illustration for the different charmonium \rightarrow charmonium decay channels.	19
2.3 Examples of J/ψ production Feynman diagrams.	20
2.4 Example of Feynman diagram for b-hadron decay to J/ψ	21
2.5 Illustration of the J/ψ photoproduction mechanism in an ultra peripheral nucleus-nucleus collision.	22
2.6 Examples of CT14 parton distribution functions.	23
2.7 Typical nPDF distribution.	25
2.8 EPS09 prediction for the Z-boson production in Pb-Pb collisions at $\sqrt{s_{NN}} = 5.5$ TeV.	26
2.9 Examples of EPS09 nPDFs at the charm mass scale.	27
2.10 Energy dependence of the nuclear absorption cross section.	29
2.11 Lattice QCD method for determining charmonium dissociation temperature.	32
2.12 Effects color screening, interaction with comovers and regeneration to the J/ψ production.	34

2.13	Experimental results on Z-boson production in Pb-Pb collisions by ATLAS and CMS.	37
2.14	Experimental results on Z-boson production in p-Pb collisions by ATLAS and CMS.	38
2.15	Experimental results on Z-boson production in p-Pb collisions by LHCb.	39
2.16	Experimental results on J/ψ production in Pb-Pb collisions at SPS. . .	40
2.17	Experimental results on J/ψ production in heavy-ion collisions collisions at RHIC and SPS.	41
2.18	J/ψ production cross sections in pp collisions at different energies. . .	42
2.19	J/ψ R_{pPb} at $\sqrt{s_{NN}} = 5.02\text{TeV}$	43
3.1	LHC injection chain.	46
3.2	J/ψ acceptance in the LHC experiments.	49
3.3	Illustration of ALICE detector.	50
3.4	Pseudo-rapidity coverage of the different ALICE sub-detectors.	51
3.5	Illustration of the ALICE V0 detector.	52
3.6	Illustration of the ALICE ITS detector.	54
3.7	Illustration of the ALICE TPC detector.	55
3.8	Illustration of the ALICE TRD detector.	55
3.9	Illustration of the ALICE electromagnetic calorimeters.	57
3.10	Illustration of the ALICE muon spectrometer.	59
3.11	Muon spectrometer front absorber.	60
3.12	Muon tracking chamber-quadrant.	61
3.13	Muon tracking chamber-slat.	61
3.14	Muon tracking chamber-CPC	62
3.15	Muon trigger chamber resistive plate chamber.	63
3.16	Muon trigger algorithm.	64
3.17	Muon QA plot. Muon trigger efficiency.	68
3.18	Muon QA plot. Number of tracks per event.	68
3.19	Muon QA plot. Average number of clusters.	69
3.20	Muon QA plot. Percentage of accepted events.	70
4.1	Beam configurations in p-Pb collisions.	73
4.2	F_{norm} in p-Pb collisions at $\sqrt{s_{NN}} = 5.02\text{TeV}$	77

4.3	F_{norm} in Pb-Pb collisions at $\sqrt{s_{\text{NN}}} = 5.02 \text{ TeV}$	78
4.4	A Muon track traversing the front absorber.	81
4.5	Dimuon invariant mass distribution in Pb-Pb collisions at $\sqrt{s_{\text{NN}}} = 5.02 \text{ TeV}$. Range 0-140 GeV/c^2	82
4.6	A Feynman diagram for the process of semi-leptonic decay of heavy hadrons.	84
4.7	Dimuon pairs from semileptonic decay of $b\bar{b}$ pairs at $\sqrt{s_{\text{NN}}} = 5.02 \text{ TeV}$ using PYTHIA.6.	84
4.8	$Z/\gamma^* \rightarrow \tau\tau \rightarrow \mu\mu$, and $t\bar{t} \rightarrow \mu\mu$ MC samples using POWHEG.	86
4.9	Z-boson signal in p-Pb collisions at $\sqrt{s_{\text{NN}}} = 5.02 \text{ TeV}$	87
4.10	Z-boson signal in Pb-Pb collisions at $\sqrt{s_{\text{NN}}} = 5.02 \text{ TeV}$, 0-90% centrality.	89
4.11	Z-boson signal in Pb-Pb collisions at $\sqrt{s_{\text{NN}}} = 5.02 \text{ TeV}$, 0-20% and 20-90% centrality.	90
4.12	Z-boson signal in Pb-Pb collisions at $\sqrt{s_{\text{NN}}} = 5.02 \text{ TeV}$ compared to POWHEG.	91
4.13	High p_{T} J/ψ and Υ estimation.	92
4.14	Illustration of the event-mixing procedure.	95
4.15	Example of mixed opposite-charge dimuon invariant distribution.	95
4.16	Effect of vertex position on the event mixing.	96
4.17	Event mixing R_{acc}	97
4.18	Event mixing control plots.	98
4.19	Event mixing subtraction.	99
4.20	J/ψ signal extraction tails parameters.	101
4.21	Example of J/ψ fit after background subtraction.	102
4.22	Example of J/ψ without background subtraction.	104
4.23	J/ψ signal extraction systematic uncertainty.	106
4.24	Z-boson $A\epsilon$ as a function of the run number in p-Pb collisions at $\sqrt{s_{\text{NN}}} = 5.02 \text{ TeV}$	109
4.25	Z-boson and J/ψ $A\epsilon$ as a function of the run number in Pb-Pb collisions at $\sqrt{s_{\text{NN}}} = 5.02 \text{ TeV}$	110
4.26	Z-boson and J/ψ $A\epsilon$ as a function of centrality in Pb-Pb collisions at $\sqrt{s_{\text{NN}}} = 5.02 \text{ TeV}$	111
4.27	J/ψ $A\epsilon$ as a function of p_{T} and y in Pb-Pb collisions at $\sqrt{s_{\text{NN}}} = 5.02 \text{ TeV}$	112

4.28	J/ψ yield distribution as a function of p_T and y in Pb-Pb collisions at $\sqrt{s_{NN}} = 5.02 \text{ TeV}$	113
4.29	Tracking efficiency determination.	114
4.30	Tracking efficiency in Pb-Pb collisions at $\sqrt{s_{NN}} = 5.02 \text{ TeV}$	116
4.31	Misalignment of the muon spectrometer.	117
4.32	Effect of the muon spectrometer misalignment on the Z-boson signal.	118
4.33	Effect of the muon spectrometer cluster resolution on the Z-boson signal.	119
4.34	Muon trigger response in Pb-Pb collisions at $\sqrt{s_{NN}} = 5.02 \text{ TeV}$	121
4.35	122
4.36	Dimuon invariant mass distribution in pp collisions at $\sqrt{s} = 5.02 \text{ TeV}$. Range 0-140 GeV/c^2	124
4.37	J/ψ production cross section in pp collisions at $\sqrt{s} = 5.02 \text{ TeV}$	124
5.1	Bjorken x regions in p-Pb and Pb-Pb collisions.	127
5.2	Z-boson cross section in p-Pb collisions at $\sqrt{s_{NN}} = 5.02 \text{ TeV}$	128
5.3	Z-boson cross section in p-Pb collisions at $\sqrt{s_{NN}} = 5.02 \text{ TeV}$ compared to models.	130
5.4	Z-boson cross section in p-Pb collisions at $\sqrt{s_{NN}} = 5.02 \text{ TeV}$ by all the LHC experiments.	132
5.5	W-bosons cross sections in p-Pb collisions at $\sqrt{s_{NN}} = 5.02 \text{ TeV}$	133
5.6	Invariant yield and R_{AA} of the Z-boson in in Pb-Pb collisions at $\sqrt{s_{NN}} = 5.02 \text{ TeV}$	138
5.7	Rapidity dependence of the invariant yield and R_{AA} of the Z-boson in in Pb-Pb collisions at $\sqrt{s_{NN}} = 5.02 \text{ TeV}$	140
5.8	Centrality dependence of the invariant yield and R_{AA} of the Z-boson in in Pb-Pb collisions at $\sqrt{s_{NN}} = 5.02 \text{ TeV}$	141
6.1	J/ψ invariant yields as a function of p_T in Pb-Pb collisions at $\sqrt{s_{NN}} = 5.02 \text{ TeV}$	149
6.2	Fitted J/ψ invariant yields as a function of p_T in Pb-Pb collisions at $\sqrt{s_{NN}} = 5.02 \text{ TeV}$	150
6.3	J/ψ $\langle p_T \rangle$ and r_{AA} as a function of $\langle N_{part} \rangle$ at $\sqrt{s_{NN}} = 5.02 \text{ TeV}$	153
6.4	J/ψ r_{AA} as a function of $\langle N_{part} \rangle$ at $\sqrt{s_{NN}} = 5.02 \text{ TeV}$ and compared to theoretical calculations.	154

6.5	$J/\psi R_{AA}$ as a function of $\langle N_{\text{part}} \rangle$ at $\sqrt{s_{\text{NN}}} = 5.02 \text{ TeV}$, $p_{\text{T}} < 8 \text{ GeV}/c$. . .	158
6.6	$J/\psi R_{AA}$ as a function of $\langle N_{\text{part}} \rangle$ at $\sqrt{s_{\text{NN}}} = 5.02 \text{ TeV}$, $0 < p_{\text{T}} < 12$ and $0.3 < p_{\text{T}} < 12 \text{ GeV}/c$	159
6.7	$J/\psi R_{AA}$ as a function of $\langle N_{\text{part}} \rangle$ at $\sqrt{s_{\text{NN}}} = 5.02 \text{ TeV}$, $0 < p_{\text{T}} < 8$ compared to models.	161
6.8	$J/\psi R_{AA}^{\frac{5.02}{2.76}}$ as a function of $\langle N_{\text{part}} \rangle$, $0.3 < p_{\text{T}} < 8 \text{ GeV}/c$	162
6.9	$J/\psi R_{AA}$ as a function of $\langle N_{\text{part}} \rangle$ at $\sqrt{s_{\text{NN}}} = 5.02 \text{ TeV}$, $0.3\text{--}2$, $2\text{--}5$, $5\text{--}8$, and $8\text{--}12 \text{ GeV}/c$	164
6.10	$J/\psi R_{AA}$ as a function of $\langle N_{\text{part}} \rangle$ at $\sqrt{s_{\text{NN}}} = 5.02 \text{ TeV}$, $0.3\text{--}2$, $2\text{--}5$, $5\text{--}8$, and $8\text{--}12 \text{ GeV}/c$. compared to models.	165
6.11	$J/\psi R_{AA}$ as a function of p_{T} at $\sqrt{s_{\text{NN}}} = 5.02 \text{ TeV}$, centrality $0\text{--}20\%$, $20\text{--}40\%$, and $40\text{--}90\%$	166
6.12	$J/\psi R_{AA}$ as a function of p_{T} at $\sqrt{s_{\text{NN}}} = 5.02 \text{ TeV}$, $0\text{--}20\%$ centrality. . . .	168
6.13	$J/\psi R_{AA}$ as a function of p_{T} at $\sqrt{s_{\text{NN}}} = 5.02 \text{ TeV}$, $20\text{--}40\%$ and $40\text{--}90\%$ centrality.	169
6.14	$J/\psi R_{AA}$ as a function of rapidity at $\sqrt{s_{\text{NN}}} = 5.02 \text{ TeV}$	171
7.1	Z-boson and $J/\psi R_{AA}$ in Pb-Pb collisions at $\sqrt{s_{\text{NN}}} = 5.02 \text{ TeV}$	177
8.1	183
8.2	184
8.3	185
8.4	186
A.1	Crystal ball function.	188
B.1	Fraction of non-prompt J/ψ to prompt J/ψ as function of p_{T} measured by LHCb.	193
C.1	J/ψ signal extraction in different centrality intervals. $2.5 < y < 4$ and $0 < p_{\text{T}} < 8$	196
C.2	J/ψ signal extraction in different centrality intervals. $2.5 < y < 4$ and $0.3 < p_{\text{T}} < 8$	197
C.3	J/ψ signal extraction in different centrality intervals. $2.5 < y < 4$ and $0 < p_{\text{T}} < 2$	198

C.4	J/ψ signal extraction in different centrality intervals. $2.5 < y < 4$ and $2 < p_T < 5$	199
C.5	J/ψ signal extraction in different centrality intervals. $2.5 < y < 4$ and $5 < p_T < 8$	200
C.6	J/ψ signal extraction in different centrality intervals. $2.5 < y < 4$ and $8 < p_T < 12$	201
C.7	J/ψ signal extraction in different p_T intervals. $2.5 < y < 4$ and centrality 0–20 %.	202
C.8	J/ψ signal extraction in different rapidity intervals. Centrality 0–90 % and $0 < p_T < 12$	203

FIGURE	Page
---------------	-------------

BIBLIOGRAPHY

- [1] C. Patrignani and P. D. Group, “Review of particle physics”, *Chinese Physics C* **40** (2016), no. 10, 100001. [Cited on pages 3, 5, 16, 18, 19, 21, 85, 123, and 148.]
- [2] **Belle Collaboration** Collaboration, S.-K. Choi *et al.*, “Observation of a resonancelike structure in the $\pi^{+-}\psi'$ mass distribution in exclusive $b \rightarrow k\pi^{+-}\psi'$ decays”, *Phys. Rev. Lett.* **100** Apr (2008) 142001. [Cited on page 4.]
- [3] **LHCb Collaboration** Collaboration, R. Aaij *et al.*, “Observation of $j/\psi p$ resonances consistent with pentaquark states in $\Lambda_b^0 \rightarrow j/\psi K^- p$ decays”, *Phys. Rev. Lett.* **115** Aug (2015) 072001. [Cited on page 4.]
- [4] **ATLAS Collaboration**, G. Aad *et al.*, “Observation of a new particle in the search for the Standard Model Higgs boson with the ATLAS detector at the LHC”, *Phys. Lett.* **B716** (2012) 1–29, arXiv:1207.7214. [Cited on page 5.]
- [5] **CMS Collaboration**, S. Chatrchyan *et al.*, “Observation of a new boson at a mass of 125 GeV with the CMS experiment at the LHC”, *Phys. Lett.* **B716** (2012) 30–61, arXiv:1207.7235. [Cited on page 5.]
- [6] S. Bethke, “World Summary of α_s (2012)”, arXiv:1210.0325, [Nucl. Phys. Proc. Suppl.234,229(2013)]. [Cited on page 6.]
- [7] A. Bazavov *et al.*, “Equation of state and QCD transition at finite temperature”, *Phys. Rev.* **D80** (2009) 014504, arXiv:0903.4379. [Cited on page 7.]

- [8] S. Sarkar, H. Satz, and B. Sinha, “The physics of the quark-gluon plasma”, *Lect. Notes Phys.* **785** (2010) pp.1–369. [Cited on page 7.]
- [9] Z. Fodor and S. D. Katz, “Critical point of QCD at finite T and mu, lattice results for physical quark masses”, *JHEP* **04** (2004) 050, arXiv:hep-lat/0402006. [Cited on page 7.]
- [10] J. D. Bjorken, “Highly Relativistic Nucleus-Nucleus Collisions: The Central Rapidity Region”, *Phys. Rev.* **D27** (1983) 140–151. [Cited on page 8.]
- [11] M. Strickland, “Anisotropic Hydrodynamics: Three lectures”, *Acta Phys. Polon.* **B45** (2014), no. 12, 2355–2394, arXiv:1410.5786. [Cited on pages 8 and 10.]
- [12] M. L. Miller, K. Reygers, S. J. Sanders, and P. Steinberg, “Glauber modeling in high energy nuclear collisions”, *Ann. Rev. Nucl. Part. Sci.* **57** (2007) 205–243, arXiv:nucl-ex/0701025. [Cited on pages 9 and 11.]
- [13] A. Andronic, P. Braun-Munzinger, and J. Stachel, “Thermal hadron production in relativistic nuclear collisions: The Hadron mass spectrum, the horn, and the QCD phase transition”, *Phys. Lett.* **B673** (2009) 142–145, arXiv:0812.1186, [Erratum: *Phys. Lett.* **B678**,516(2009)]. [Cited on pages 12, 34, 160, 161, and 173.]
- [14] J. Rafelski and B. Muller, “Strangeness production in the quark-gluon plasma”, *Phys. Rev. Lett.* **48** Apr (1982) 1066–1069. [Cited on page 12.]
- [15] E. Andersen *et al.*, “Strangeness enhancement at mid-rapidity in pb-pb collisions at 158 a gev/c”, *Physics Letters B* **449** (1999), no. 3, 401 – 406. [Cited on page 12.]
- [16] F. Antinori *et al.*, “Energy dependence of hyperon production in nucleus-nucleus collisions at sps”, *Physics Letters B* **595** (2004), no. 1, 68 – 74. [Cited on page 12.]
- [17] **STAR Collaboration** Collaboration, B. I. Abelev *et al.*, “Enhanced strange baryon production in au+au collisions compared to $p + p$ at $\sqrt{s_{NN}} = 200$ gev”, *Phys. Rev. C* **77** Apr (2008) 044908. [Cited on page 12.]

-
- [18] A. Collaboration, “Enhanced production of multi-strange hadrons in high-multiplicity proton-proton collisions”, *Nat Phys* **13** 06 (2017) 535–539. [[Cited on page 12.](#)]
- [19] **CMS** Collaboration, V. Khachatryan *et al.*, “Evidence for collectivity in pp collisions at the LHC”, *Phys. Lett.* **B765** (2017) 193–220, arXiv:1606.06198. [[Cited on page 13.](#)]
- [20] **CMS** Collaboration, V. Khachatryan *et al.*, “Observation of Long-Range Near-Side Angular Correlations in Proton-Proton Collisions at the LHC”, *JHEP* **09** (2010) 091, arXiv:1009.4122. [[Cited on page 13.](#)]
- [21] **PHENIX** Collaboration, A. Adare *et al.*, “Measurements of Higher-Order Flow Harmonics in Au+Au Collisions at $\sqrt{s_{NN}} = 200$ GeV”, *Phys. Rev. Lett.* **107** (2011) 252301, arXiv:1105.3928. [[Cited on page 13.](#)]
- [22] **ALICE** Collaboration, K. Aamodt *et al.*, “Harmonic decomposition of two-particle angular correlations in Pb-Pb collisions at $\sqrt{s_{NN}} = 2.76$ TeV”, *Phys. Lett.* **B708** (2012) 249–264, arXiv:1109.2501. [[Cited on page 13.](#)]
- [23] **ATLAS** Collaboration, G. Aad *et al.*, “Measurement of the pseudorapidity and transverse momentum dependence of the elliptic flow of charged particles in lead-lead collisions at $\sqrt{s_{NN}} = 2.76$ TeV with the ATLAS detector”, *Phys. Lett.* **B707** (2012) 330–348, arXiv:1108.6018. [[Cited on page 13.](#)]
- [24] **CMS** Collaboration, S. Chatrchyan *et al.*, “Centrality dependence of dihadron correlations and azimuthal anisotropy harmonics in PbPb collisions at $\sqrt{s_{NN}} = 2.76$ TeV”, *Eur. Phys. J.* **C72** (2012) 2012, arXiv:1201.3158. [[Cited on page 13.](#)]
- [25] R. Nouicer, “New State of Nuclear Matter: Nearly Perfect Fluid of Quarks and Gluons in Heavy Ion Collisions at RHIC Energies”, *Eur. Phys. J. Plus* **131** (2016), no. 3, 70, arXiv:1512.08993. [[Cited on page 13.](#)]
- [26] P. Bagnaia and Others, “Evidence for z_0 boson at the cern pp collider”, *Physics Letters B* **129** (1983), no. 1, 130 – 140. [[Cited on page 15.](#)]

- [27] **SLD Electroweak Group, DELPHI, ALEPH, SLD, SLD Heavy Flavour Group, OPAL, LEP Electroweak Working Group, L3 Collaboration**, S. Schael *et al.*, “Precision electroweak measurements on the Z resonance”, *Phys. Rept.* **427** (2006) 257–454, arXiv:hep-ex/0509008. [Cited on page 15.]
- [28] **CDF Collaboration**, D. Acosta *et al.*, “First measurements of inclusive W and Z cross sections from Run II of the Tevatron collider”, *Phys. Rev. Lett.* **94** (2005) 091803, arXiv:hep-ex/0406078. [Cited on page 15.]
- [29] **ATLAS Collaboration**, G. Aad *et al.*, “Measurement of the $W \rightarrow \ell\nu$ and $Z/\gamma^* \rightarrow \ell\ell$ production cross sections in proton-proton collisions at $\sqrt{s} = 7$ TeV with the ATLAS detector”, *JHEP* **12** (2010) 060, arXiv:1010.2130. [Cited on page 15.]
- [30] **ATLAS Collaboration**, G. Aad *et al.*, “Electron and photon energy calibration with the ATLAS detector using LHC Run 1 data”, *Eur. Phys. J.* **C74** (2014), no. 10, 3071, arXiv:1407.5063. [Cited on page 16.]
- [31] R. Gavin, Y. Li, F. Petriello, and S. Quackenbush, “FEWZ 2.0: A code for hadronic Z production at Next-to-Next-to-Leading order”, *Comput. Phys. Commun.* **182** (2011) 2388–2403, arXiv:1011.3540. [Cited on pages 16, 129, and 182.]
- [32] S. D. Drell and T.-M. Yan, “Massive lepton-pair production in hadron-hadron collisions at high energies”, *Phys. Rev. Lett.* **25** Aug (1970) 316–320. [Cited on page 16.]
- [33] J. C. Collins, D. E. Soper, and G. F. Sterman, “Factorization of Hard Processes in QCD”, *Adv. Ser. Direct. High Energy Phys.* **5** (1989) 1–91, arXiv:hep-ph/0409313. [Cited on page 16.]
- [34] R. K. Ellis, W. J. Stirling, and B. R. Webber, “QCD and collider physics”, *Camb. Monogr. Part. Phys. Nucl. Phys. Cosmol.* **8** (1996) 1–435. [Cited on page 16.]

-
- [35] J. E. Augustin *et al.*, “Discovery of a narrow resonance in e^+e^- annihilation”, *Phys. Rev. Lett.* **33** Dec (1974) 1406–1408. [Cited on page 17.]
- [36] J. J. Aubert *et al.*, “Experimental observation of a heavy particle j ”, *Phys. Rev. Lett.* **33** Dec (1974) 1404–1406. [Cited on page 17.]
- [37] E. Eichten, K. Gottfried, T. Kinoshita, J. B. Kogut, K. D. Lane, and T.-M. Yan, “The Spectrum of Charmonium”, *Phys. Rev. Lett.* **34** (1975) 369–372, [Erratum: *Phys. Rev. Lett.* 36,1276(1976)]. [Cited on page 17.]
- [38] F. Karsch, M. T. Mehr, and H. Satz, “Color screening and deconfinement for bound states of heavy quarks”, *Zeitschrift fur Physik C Particles and Fields* **37** (1988), no. 4, 617–622. [Cited on page 17.]
- [39] K. G. Wilson, “Confinement of quarks”, *Phys. Rev. D* **10** Oct (1974) 2445–2459. [Cited on page 18.]
- [40] C.-H. Chang, “Hadronic Production of J/ψ Associated With a Gluon”, *Nucl. Phys.* **B172** (1980) 425–434. [Cited on page 18.]
- [41] J. P. Lansberg, “ J/ψ , ψ' and ν production at hadron colliders: A Review”, *Int. J. Mod. Phys.* **A21** (2006) 3857–3916, arXiv:hep-ph/0602091. [Cited on page 19.]
- [42] G. A. Schuler, “Quarkonium production and decays”, PhD thesis, CERN, 1994. arXiv:hep-ph/9403387. [Cited on page 19.]
- [43] **CDF Collaboration** Collaboration, F. Abe *et al.*, “Production of J/ψ mesons from χ_c meson decays in $p\bar{p}$ collisions at $\sqrt{s} = 1.8\text{TeV}$ ”, *Phys. Rev. Lett.* **79** Jul (1997) 578–583. [Cited on page 19.]
- [44] G. T. Bodwin, E. Braaten, and G. P. Lepage, “Rigorous QCD analysis of inclusive annihilation and production of heavy quarkonium”, *Phys. Rev.* **D51** (1995) 1125–1171, arXiv:hep-ph/9407339, [Erratum: *Phys. Rev.* D55,5853(1997)]. [Cited on pages 20 and 42.]

- [45] N. Brambilla *et al.*, “Heavy quarkonium: progress, puzzles, and opportunities”, *Eur. Phys. J.* **C71** (2011) 1534, arXiv:1010.5827. [Cited on pages 20, 22, and 41.]
- [46] **CDF Collaboration** Collaboration, A. Abulencia and Others, “Polarizations of j/ψ and $\psi(2s)$ mesons produced in $p\bar{p}$ collisions at $\sqrt{s} = 1.96$ TeV”, *Phys. Rev. Lett.* **99** Sep (2007) 132001. [Cited on page 20.]
- [47] J. P. Lansberg, “On the mechanisms of heavy-quarkonium hadroproduction”, *Eur. Phys. J.* **C61** (2009) 693–703, arXiv:0811.4005. [Cited on page 20.]
- [48] M. Cacciari, S. Frixione, and P. Nason, “The $p(T)$ spectrum in heavy flavor photoproduction”, *JHEP* **03** (2001) 006, arXiv:hep-ph/0102134. [Cited on pages 21, 83, and 159.]
- [49] M. Cacciari, S. Frixione, M. L. Mangano, P. Nason, and G. Ridolfi, “QCD analysis of first b cross-section data at 1.96-TeV”, *JHEP* **07** (2004) 033, arXiv:hep-ph/0312132. [Cited on page 21.]
- [50] Y. L. Dokshitzer, “Calculation of the Structure Functions for Deep Inelastic Scattering and e^+e^- Annihilation by Perturbation Theory in Quantum Chromodynamics.”, *Sov. Phys. JETP* **46** (1977) 641–653, [Zh. Eksp. Teor. Fiz.73,1216(1977)]. [Cited on page 23.]
- [51] V. N. Gribov and L. N. Lipatov, “Deep inelastic $e p$ scattering in perturbation theory”, *Sov. J. Nucl. Phys.* **15** (1972) 438–450, [Yad. Fiz.15,781(1972)]. [Cited on page 23.]
- [52] G. Altarelli and G. Parisi, “Asymptotic Freedom in Parton Language”, *Nucl. Phys.* **B126** (1977) 298–318. [Cited on page 23.]
- [53] A. D. Martin, W. J. Stirling, R. S. Thorne, and G. Watt, “Parton distributions for the LHC”, *Eur. Phys. J.* **C63** (2009) 189–285, arXiv:0901.0002. [Cited on pages 23 and 129.]
- [54] P. Nadolsky, J. Gao, M. Guzzi, J. Huston, H.-L. Lai, Z. Li, J. Pumplin, D. Stump, and C. P. Yuan, “Progress in CTEQ-TEA PDF Analysis”, in

- “Proceedings, 20th International Workshop on Deep-Inelastic Scattering and Related Subjects (DIS 2012): Bonn, Germany, March 26-30, 2012”, pp. 417–420. 2012. arXiv:1206.3321. [,417(2012)], [Cited on pages 129 and 135.]
- [55] S. Dulat, T.-J. Hou, J. Gao, M. Guzzi, J. Huston, P. Nadolsky, J. Pumplin, C. Schmidt, D. Stump, and C. P. Yuan, “New parton distribution functions from a global analysis of quantum chromodynamics”, *Phys. Rev.* **D93** (2016), no. 3, 033006, arXiv:1506.07443. [Cited on pages 23 and 135.]
- [56] **European Muon** Collaboration, J. J. Aubert *et al.*, “The ratio of the nucleon structure functions F_2^n for iron and deuterium”, *Phys. Lett.* **B123** (1983) 275–278. [Cited on page 23.]
- [57] K. J. Eskola, H. Paukkunen, and C. A. Salgado, “EPS09: A New Generation of NLO and LO Nuclear Parton Distribution Functions”, *JHEP* **04** (2009) 065, arXiv:0902.4154. [Cited on pages 23, 24, 27, 43, 128, 131, 137, 159, and 183.]
- [58] D. de Florian, R. Sassot, P. Zurita, and M. Stratmann, “Global analysis of nuclear parton distributions”, *Phys. Rev. D* **85** Apr (2012) 074028. [Cited on page 24.]
- [59] H. Khanpour and S. Atashbar Tehrani, “Global analysis of nuclear parton distribution functions and their uncertainties at next-to-next-to-leading order”, *Phys. Rev. D* **93** Jan (2016) 014026. [Cited on page 24.]
- [60] D. de Florian and R. Sassot, “Nuclear parton distributions at next to leading order”, *Phys. Rev. D* **69** Apr (2004) 074028. [Cited on page 24.]
- [61] K. J. Eskola, P. Paakkinen, H. Paukkunen, and C. A. Salgado, “EPPS16: Nuclear parton distributions with LHC data”, arXiv:1612.05741. [Cited on pages 24, 38, and 137.]
- [62] H. Paukkunen, “Status of nuclear pdfs after the first lhc p-pb run”.
<https://indico.cern.ch/event/433345/contributions/2321624/>

- attachments/1410954/2158061/QM2017_Paukkunen.pdf, 2017. [Quark matter;2017]. [Cited on page 24.]
- [63] N. Armesto, “Nuclear shadowing”, *J. Phys.* **G32** (2006) R367–R394, arXiv:hep-ph/0604108. [Cited on pages 24 and 25.]
- [64] M. Arneodo, “Nuclear effects in structure functions”, *Physics Reports* **240** (1994), no. 5, 301 – 393. [Cited on page 25.]
- [65] H. Paukkunen and C. A. Salgado, “Constraints for the nuclear parton distributions from z and w_{\pm} production at the LHC”, *Journal of High Energy Physics* **2011** (2011), no. 3, 71. [Cited on pages 26, 122, 129, 135, and 182.]
- [66] I. Vitev, “Non-Abelian energy loss in cold nuclear matter”, *Phys. Rev.* **C75** (2007) 064906, arXiv:hep-ph/0703002. [Cited on page 27.]
- [67] F. Arleo, S. Peigne, and T. Sami, “Revisiting scaling properties of medium-induced gluon radiation”, *Phys. Rev.* **D83** (2011) 114036, arXiv:1006.0818. [Cited on pages 28 and 43.]
- [68] F. Arleo and S. Peigne, “Quarkonium suppression in heavy-ion collisions from coherent energy loss in cold nuclear matter”, *JHEP* **10** (2014) 73, arXiv:1407.5054. [Cited on page 28.]
- [69] C. Lourenco, R. Vogt, and H. K. Wohri, “Energy dependence of J/ψ absorption in proton-nucleus collisions”, *Journal of High Energy Physics* **2009** (2009), no. 02, 014. [Cited on pages 28 and 29.]
- [70] J.-P. Blaizot and E. Iancu, “The quark-gluon plasma: collective dynamics and hard thermal loops”, *Physics Reports* **359** (2002), no. 5, 355 – 528. [Cited on page 30.]
- [71] Z. Conesa del Valle, “Vector bosons in heavy-ion collisions at the LHC”, *Eur. Phys. J.* **C61** (2009) 729–733, arXiv:0903.1432. [Cited on page 30.]
- [72] T. Matsui and H. Satz, “ J/ψ suppression by quark-gluon plasma formation”, *Physics Letters B* **178** (1986), no. 4, 416 – 422. [Cited on page 30.]

- [73] H. Satz, “Colour deconfinement and quarkonium binding”, *J. Phys.* **G32** (2006) R25, arXiv:hep-ph/0512217. [Cited on pages 31 and 32.]
- [74] F. Karsch, M. T. Mehr, and H. Satz, “Color screening and deconfinement for bound states of heavy quarks”, *Zeitschrift fur Physik C Particles and Fields* **37** (1988), no. 4, 617–622. [Cited on page 31.]
- [75] S. Digal, P. Petreczky, and H. Satz, “String breaking and quarkonium dissociation at finite temperatures”, *Phys. Lett.* **B514** (2001) 57–62, arXiv:hep-ph/0105234. [Cited on page 31.]
- [76] A. Jakovac, P. Petreczky, K. Petrov, and A. Velytsky, “Quarkonium correlators and spectral functions at zero and finite temperature”, *Phys. Rev.* **D75** (2007) 014506, arXiv:hep-lat/0611017. [Cited on page 31.]
- [77] S. Gavin and R. Vogt, “ J/ψ Suppression From Hadron - Nucleus to Nucleus-nucleus Collisions”, *Nucl. Phys.* **B345** (1990) 104–124. [Cited on page 33.]
- [78] E. G. Ferreira, “Charmonium dissociation and recombination at LHC: Revisiting comovers”, *Phys. Lett.* **B731** (2014) 57–63, arXiv:1210.3209. [Cited on pages 33, 36, 160, 161, and 173.]
- [79] P. Braun-Munzinger and J. Stachel, “On charm production near the phase boundary”, *Nucl. Phys.* **A690** (2001) 119–126, arXiv:nucl-th/0012064. [Cited on pages 35 and 39.]
- [80] P. Braun-Munzinger and J. Stachel, “(Non)thermal aspects of charmonium production and a new look at J/ψ suppression”, *Phys. Lett.* **B490** (2000) 196–202, arXiv:nucl-th/0007059. [Cited on page 35.]
- [81] X. Zhao and R. Rapp, “Medium Modifications and Production of Charmonia at LHC”, *Nucl. Phys.* **A859** (2011) 114–125, arXiv:1102.2194. [Cited on pages 35, 152, 154, 158, 161, 163, 165, 167, 173, and 185.]
- [82] K. Zhou, N. Xu, Z. Xu, and P. Zhuang, “Medium effects on charmonium production at ultrarelativistic energies available at the CERN Large

- Hadron Collider”, *Phys. Rev.* **C89** (2014), no. 5, 054911, arXiv:1401.5845. [Cited on pages 159, 161, and 173.]
- [83] R. L. Thews, “Quarkonium formation at high-energy”, *Nucl. Phys.* **A702** (2002) 341–345, arXiv:hep-ph/0111015. [Cited on pages 35 and 39.]
- [84] G. Bhanot and M. E. Peskin, “Short-distance analysis for heavy-quark systems”, *Nuclear Physics B* **156** (1979), no. 3, 391 – 416. [Cited on page 35.]
- [85] N. Armesto, A. Capella, and E. G. Ferreira, “Charmonium suppression in lead-lead collisions: Is there a break in the J/ψ cross section”, *Phys. Rev. C* **59** Jan (1999) 395–404. [Cited on pages 35 and 36.]
- [86] **NA50** Collaboration, M. Gonin *et al.*, “Anomalous J/ψ suppression in Pb + Pb collisions at 158-A-GeV/c”, *Nucl. Phys.* **A610** (1996) 404C–417C. [Cited on pages 35, 39, and 40.]
- [87] D. P. Dewangan, “A glauber-type approximation in impact parameter treatment”, *Journal of Physics B: Atomic and Molecular Physics* **8** (1975), no. 7, L119. [Cited on pages 36 and 160.]
- [88] **ATLAS** Collaboration, G. Aad *et al.*, “Measurement of Z boson Production in Pb+Pb Collisions at $\sqrt{s_{NN}} = 2.76$ TeV with the ATLAS Detector”, *Phys. Rev. Lett.* **110** (2013), no. 2, 022301, arXiv:1210.6486. [Cited on pages 36 and 37.]
- [89] T. Sjostrand, S. Mrenna, and P. Z. Skands, “PYTHIA 6.4 Physics and Manual”, *JHEP* **05** (2006) 026, arXiv:hep-ph/0603175. [Cited on pages 36, 83, 85, and 181.]
- [90] **CMS** Collaboration, S. Chatrchyan *et al.*, “Study of Z production in PbPb and pp collisions at $\sqrt{s_{NN}} = 2.76$ TeV in the dimuon and dielectron decay channels”, *JHEP* **03** (2015) 022, arXiv:1410.4825. [Cited on page 37.]
- [91] **ATLAS** Collaboration, G. Aad *et al.*, “Z boson production in p+Pb collisions at $\sqrt{s_{NN}} = 5.02$ TeV measured with the ATLAS detector”, *Phys. Rev.* **C92** (2015), no. 4, 044915, arXiv:1507.06232. [Cited on pages 37, 38, and 137.]

- [92] **CMS** Collaboration, V. Khachatryan *et al.*, “Study of Z boson production in pPb collisions at $\sqrt{s_{NN}}=5.02\text{TeV}$ ”, *Phys. Lett.* **B759** (2016) 36–57, arXiv:1512.06461. [Cited on pages 37, 38, and 137.]
- [93] **LHCb** Collaboration, R. Aaij *et al.*, “Observation of Z production in proton-lead collisions at LHCb”, *JHEP* **09** (2014) 030, arXiv:1406.2885. [Cited on pages 38 and 39.]
- [94] **NA50** Collaboration, M. C. Abreu *et al.*, “Evidence for deconfinement of quarks and gluons from the J/ψ suppression pattern measured in Pb + Pb collisions at the CERN SPS”, *Phys. Lett.* **B477** (2000) 28–36. [Cited on pages 39 and 41.]
- [95] **PHENIX** Collaboration, A. Adare *et al.*, “ J/ψ suppression at forward rapidity in Au+Au collisions at $\sqrt{s_{NN}} = 200$ GeV”, *Phys. Rev.* **C84** (2011) 054912, arXiv:1103.6269. [Cited on pages 39 and 41.]
- [96] A. P. Kostyuk, “Statistical J/ψ production and open charm enhancement in Pb + Pb collisions at CERN SPS”, *J. Phys.* **G28** (2002) 2047–2050, arXiv:hep-ph/0111096. [Cited on page 39.]
- [97] L. Grandchamp and R. Rapp, “Thermal versus direct J/ψ production in ultrarelativistic heavy-ion collisions”, *Physics Letters B* **523** (2001), no. 12, 60 – 66. [Cited on page 39.]
- [98] **ALICE** Collaboration, S. Acharya *et al.*, “Energy dependence of forward-rapidity J/ψ and $\psi(2s)$ production in pp collisions at the LHC”, arXiv:1702.00557. [Cited on pages 42, 100, 124, 151, 155, 205, 206, and 207.]
- [99] **ALICE** Collaboration, B. B. Abelev *et al.*, “ J/ψ production and nuclear effects in p-Pb collisions at $\sqrt{s_{NN}} = 5.02$ TeV”, *JHEP* **02** (2014) 073, arXiv:1308.6726. [Cited on page 43.]
- [100] O. S. Bruning, P. Collier, P. Lebrun, S. Myers, R. Ostojic, J. Poole, and P. Proudlock, “LHC Design Report”, CERN, Geneva, 2004. [Cited on page 45.]

- [101] A. Beuret and Others, “The LHC Lead Injector Chain”, Aug 2004, revised version submitted on 2004-09-23 14:33:06. [Cited on page 46.]
- [102] L. Evans and P. Bryant, “Lhc machine”, *Journal of Instrumentation* **3** (2008), no. 08, S08001. [Cited on page 47.]
- [103] K. Aamodt *et al.*, “The alice experiment at the cern lhc”, *Journal of Instrumentation* **3** (2008), no. 08, S08002. [Cited on pages 47, 48, 52, 54, 55, and 63.]
- [104] G. Aad *et al.*, “The atlas experiment at the cern large hadron collider”, *Journal of Instrumentation* **3** (2008), no. 08, S08003. [Cited on page 47.]
- [105] S. Chatrchyan *et al.*, “The cms experiment at the cern lhc”, *Journal of Instrumentation* **3** (2008), no. 08, S08004. [Cited on page 47.]
- [106] A. A. A. Jr *et al.*, “The lhcb detector at the lhc”, *Journal of Instrumentation* **3** (2008), no. 08, S08005. [Cited on page 48.]
- [107] M. Winn, “Prospects for quarkonium measurements in p-A and A-A collisions at the LHC”, *Few Body Syst.* **58** (2017), no. 2, 53, arXiv:1609.01135. [Cited on page 49.]
- [108] **ALICE** Collaboration, P. Cortese *et al.*, “ALICE technical design report on forward detectors: FMD, T0 and V0”, 2004. [Cited on pages 51 and 52.]
- [109] **ALICE Collaboration** Collaboration, “ALICE Photon Multiplicity Detector (PMD): Technical Design Report”, CERN, Geneva, 1999. [Cited on page 51.]
- [110] **ALICE Collaboration** Collaboration, M. Gallio, W. Klempt, L. Leistam, J. De Groot, and J. Schukraft, “ALICE Zero-Degree Calorimeter (ZDC): Technical Design Report”, CERN, Geneva, 1999. [Cited on page 53.]
- [111] **ALICE Collaboration** Collaboration, M. Gallio, W. Klempt, L. Leistam, J. De Groot, and J. Schukraft, “ALICE Inner Tracking System (ITS): Technical Design Report”, CERN, Geneva, 1999. [Cited on page 53.]
- [112] **ALICE** Collaboration, G. Dellacasa *et al.*, “ALICE: Technical design report of the time projection chamber”, 2000. [Cited on page 54.]

- [113] **ALICE Collaboration** Collaboration, P. Cortese, “ALICE transition-radiation detector: Technical Design Report”, CERN, Geneva, 2001. [[Cited on page 54.](#)]
- [114] **ALICE Collaboration**, G. Dellacasa *et al.*, “ALICE technical design report of the time-of-flight system (TOF)”, 2000. [[Cited on page 56.](#)]
- [115] **ALICE Collaboration** Collaboration, F. Piuz, W. Klempt, L. Leistam, J. De Groot, and J. Schukraft, “ALICE high-momentum particle identification: Technical Design Report”, CERN, Geneva, 1998. [[Cited on page 56.](#)]
- [116] **ALICE Collaboration** Collaboration, V. I. Man’ko, W. Klempt, L. Leistam, J. De Groot, and J. Schukraft, “ALICE Photon Spectrometer (PHOS): Technical Design Report”, CERN, Geneva, 1999. [[Cited on page 56.](#)]
- [117] **ALICE Collaboration** Collaboration, P. Cortese *et al.*, “ALICE Electromagnetic Calorimeter Technical Design Report”, Tech. Rep. CERN-LHCC-2008-014. ALICE-TDR-14, Aug 2008. [[Cited on page 57.](#)]
- [118] J. Allen *et al.*, “ALICE DCal: An Addendum to the EMCAL Technical Design Report Di-Jet and Hadron-Jet correlation measurements in ALICE”, Tech. Rep. CERN-LHCC-2010-011. ALICE-TDR-14-add-1, Jun 2010. [[Cited on page 57.](#)]
- [119] **ALICE Collaboration** Collaboration, “ALICE dimuon forward spectrometer: Technical Design Report”, CERN, Geneva, 1999. [[Cited on pages 58 and 62.](#)]
- [120] **ALICE Collaboration** Collaboration, “ALICE dimuon forward spectrometer: addendum to the Technical Design Report”, CERN, Geneva, 2000. [[Cited on page 58.](#)]
- [121] A. TWiki.
<https://twiki.cern.ch/twiki/bin/viewauth/ALICE/MuonTracking>.
[[Cited on page 59.](#)]

- [122] D. Stocco, “Development of the ALICE Muon Spectrometer: Preparation for data taking and heavy flavor measurement”, PhD thesis, Turin U., 2008. [Cited on page 64.]
- [123] **ALICE** Collaboration, B. Abelev *et al.*, “Measurement of the Cross Section for Electromagnetic Dissociation with Neutron Emission in Pb-Pb Collisions at $\sqrt{s_{NN}} = 2.76$ TeV”, *Phys. Rev. Lett.* **109** (2012) 252302, arXiv:1203.2436. [Cited on page 74.]
- [124] **ALICE** Collaboration, J. Adam *et al.*, “Centrality dependence of the pseudorapidity density distribution for charged particles in Pb-Pb collisions at 5 TeV”, arXiv:1612.08966. [Cited on page 74.]
- [125] S. van der Meer, “Calibration of the effective beam height in the ISR”, Tech. Rep. CERN-ISR-PO-68-31. ISR-PO-68-31, CERN, Geneva, 1968. [Cited on page 78.]
- [126] T. A. collaboration, “Measurement of visible cross sections in p-pb collisions at 5.02 tev in van der meer scans with the alice detector”, *Journal of Instrumentation* **9** (2014), no. 11, P11003. [Cited on page 79.]
- [127] S. Alioli, P. Nason, C. Oleari, and E. Re, “NLO vector-boson production matched with shower in POWHEG”, *JHEP* **07** (2008) 060, arXiv:0805.4802. [Cited on pages 85 and 181.]
- [128] **ALICE** Collaboration, J. Adam *et al.*, “W and Z boson production in p-Pb collisions at $\sqrt{s_{NN}} = 5.02$ TeV”, *JHEP* **02** (2017) 077, arXiv:1611.03002. [Cited on pages 87, 130, 132, 133, and 183.]
- [129] R. Brun, F. Carminati, and S. Giani, “GEANT Detector Description and Simulation Tool”, *CERN-W-5013*, 1994. [Cited on pages 100 and 108.]
- [130] **GEANT4** Collaboration, S. Agostinelli *et al.*, “GEANT4: A Simulation toolkit”, *Nucl. Instrum. Meth.* **A506** (2003) 250–303. [Cited on pages 100 and 108.]
- [131] A. Ferrari, P. R. Sala, A. Fasso, and J. Ranft, “FLUKA: A multi-particle transport code (Program version 2005)”, 2005. [Cited on page 108.]

-
- [132] M. Lenhardt, “Étude du taux de production des J/ψ et muons simples en collisions proton-proton à l’aide du spectromètre à muons de l’expérience ALICE au LHC”, PhD thesis, SUBATECH, Nantes, 2011. [Cited on page 113.]
- [133] P. Pillot. private communication. [Cited on pages 116 and 121.]
- [134] D. Stocco. private communication. [Cited on page 120.]
- [135] B. Audurier. private communication. [Cited on page 120.]
- [136] **ALICE Collaboration** Collaboration, “ALICE luminosity determination for pp collisions at $\sqrt{s} = 5$ TeV”, Jul 2016. [Cited on page 123.]
- [137] **CHORUS** Collaboration, G. Onengut *et al.*, “Measurement of nucleon structure functions in neutrino scattering”, *Phys. Lett.* **B632** (2006) 65–75. [Cited on page 137.]
- [138] **CMS** Collaboration, V. Khachatryan *et al.*, “Study of W boson production in pPb collisions at $\sqrt{s_{NN}} = 5.02$ TeV”, *Phys. Lett.* **B750** (2015) 565–586, arXiv:1503.05825. [Cited on page 137.]
- [139] **CMS** Collaboration, S. Chatrchyan *et al.*, “Studies of dijet transverse momentum balance and pseudorapidity distributions in pPb collisions at $\sqrt{s_{NN}} = 5.02$ TeV”, *Eur. Phys. J.* **C74** (2014), no. 7, 2951, arXiv:1401.4433. [Cited on page 137.]
- [140] K. Kovarik *et al.*, “nCTEQ15 - Global analysis of nuclear parton distributions with uncertainties in the CTEQ framework”, *Phys. Rev.* **D93** (2016), no. 8, 085037, arXiv:1509.00792. [Cited on page 137.]
- [141] A. Kusina, F. Lyonnet, D. B. Clark, E. Godat, T. Jezo, K. Kovarik, F. I. Olness, I. Schienbein, and J. Y. Yu, “Vector boson production in proton-lead and lead-lead collisions at the LHC and its impact on nCTEQ15 PDFs”, arXiv:1610.02925. [Cited on page 137.]

- [142] **ALICE** Collaboration, S. Acharya *et al.*, “Measurement of Z^0 -boson production at large rapidities in Pb-Pb collisions at $\sqrt{s_{NN}} = 5.02$ TeV”, arXiv:1711.10753. [Cited on pages 138, 140, 141, and 184.]
- [143] **ALICE** Collaboration, J. Adam *et al.*, “Measurement of an excess in the yield of J/ψ at very low p_T in Pb-Pb collisions at $\sqrt{s_{NN}} = 2.76$ TeV”, *Phys. Rev. Lett.* **116** (2016), no. 22, 222301, arXiv:1509.08802. [Cited on page 148.]
- [144] **ALICE** Collaboration, J. Adam *et al.* *Phys. Lett.* **B766** (2017) 212–224, arXiv:1606.08197. [Cited on pages 148, 158, 168, and 186.]
- [145] **ALICE** Collaboration, J. Adam *et al.*, “Differential studies of inclusive J/ψ and $\psi(2S)$ production at forward rapidity in Pb-Pb collisions at $\sqrt{s_{NN}} = 2.76$ TeV”, *JHEP* **05** (2016) 179, arXiv:1506.08804. [Cited on pages 152, 154, 168, 169, 170, 171, and 185.]
- [146] **PHENIX** Collaboration, A. Adare *et al.*, “ J/ψ Production in $\sqrt{s_{NN}} = 200$ -GeV Cu+Cu Collisions”, *Phys. Rev. Lett.* **101** (2008) 122301, arXiv:0801.0220. [Cited on page 152.]
- [147] M. Abreu *et al.*, “Transverse momentum distributions of J/ψ , drell-yan and continuum dimuons produced in pb-pb interactions at the sps”, *Physics Letters B* **499** (2001), no. 1–2, 85–96. [Cited on page 152.]
- [148] **LHCb** Collaboration, R. Aaij *et al.*, “Measurement of J/ψ production in pp collisions at $\sqrt{s} = 2.76$ TeV”, *JHEP* **02** (2013) 041, arXiv:1212.1045. [Cited on pages 156 and 192.]
- [149] **LHCb** Collaboration, R. Aaij *et al.*, “Measurement of J/ψ production in pp collisions at $\sqrt{s} = 7$ TeV”, *Eur. Phys. J.* **C71** (2011) 1645, arXiv:1103.0423. [Cited on pages 156, 160, and 192.]
- [150] **ALICE** Collaboration, B. Abelev *et al.* *Phys. Lett.* **B734** (2014) 314–327, arXiv:1311.0214. [Cited on pages 157 and 158.]

- [151] **ALICE** Collaboration, D. Weiser, “Centrality and transverse momentum dependence of J/ψ production in Pb-Pb collisions at $\sqrt{s_{NN}} = 5.02$ TeV at mid-rapidity with ALICE”, in “17th International Conference on Strangeness in Quark Matter (SQM 2017) Utrecht, the Netherlands, July 10-15, 2017”. 2017. arXiv:1710.05678. [Cited on page 172.]
- [152] **ALICE** Collaboration, S. Acharya *et al.*, “ J/ψ elliptic flow in Pb-Pb collisions at $\sqrt{s_{NN}} = 5.02$ TeV”, arXiv:1709.05260. [Cited on pages 172 and 173.]
- [153] “Technical Design Report for the Muon Forward Tracker”, Tech. Rep. CERN-LHCC-2015-001. ALICE-TDR-018, Jan 2015. [Cited on page 177.]
- [154] **LHCb**, **ALICE** Collaboration, ALICE and L. Collaborations, “Reference pp cross-sections for J/ψ studies in proton-lead collisions at $\sqrt{s_{NN}} = 5.02$ TeV and comparisons between ALICE and LHCb results”, 2013. [Cited on page 192.]
- [155] **CMS** Collaboration, S. Chatrchyan *et al.*, “Suppression of non-prompt J/ψ , prompt J/ψ , and $Y(1S)$ in PbPb collisions at $\sqrt{s_{NN}} = 2.76$ TeV”, *JHEP* **05** (2012) 063, arXiv:1201.5069. [Cited on page 194.]
- [156] S. Chatrchyan *et al.*, “Suppression of non-prompt j/ψ , prompt j/ψ , and $y(1s)$ in pbpb collisions at 2.76 tev”, *Journal of High Energy Physics* **2012** May (2012) 63. [Cited on page 194.]
- [157] **ALICE** Collaboration, B. Abelev *et al.*, “Suppression of high transverse momentum D mesons in central Pb-Pb collisions at $\sqrt{s_{NN}} = 2.76$ TeV”, *JHEP* **09** (2012) 112, arXiv:1203.2160. [Cited on page 194.]

